Modelling magnetized accretion columns of young stars in the laboratory

Guilhem Revet

▶ To cite this version:

HAL Id: tel-02100492

https://pastel.hal.science/tel-02100492v2

Submitted on 30 Apr 2019

Thèse de doctorat

Modelling magnetized young stars' accretion dynamic in the laboratory

Thèse de doctorat de l'Université Paris-Saclay
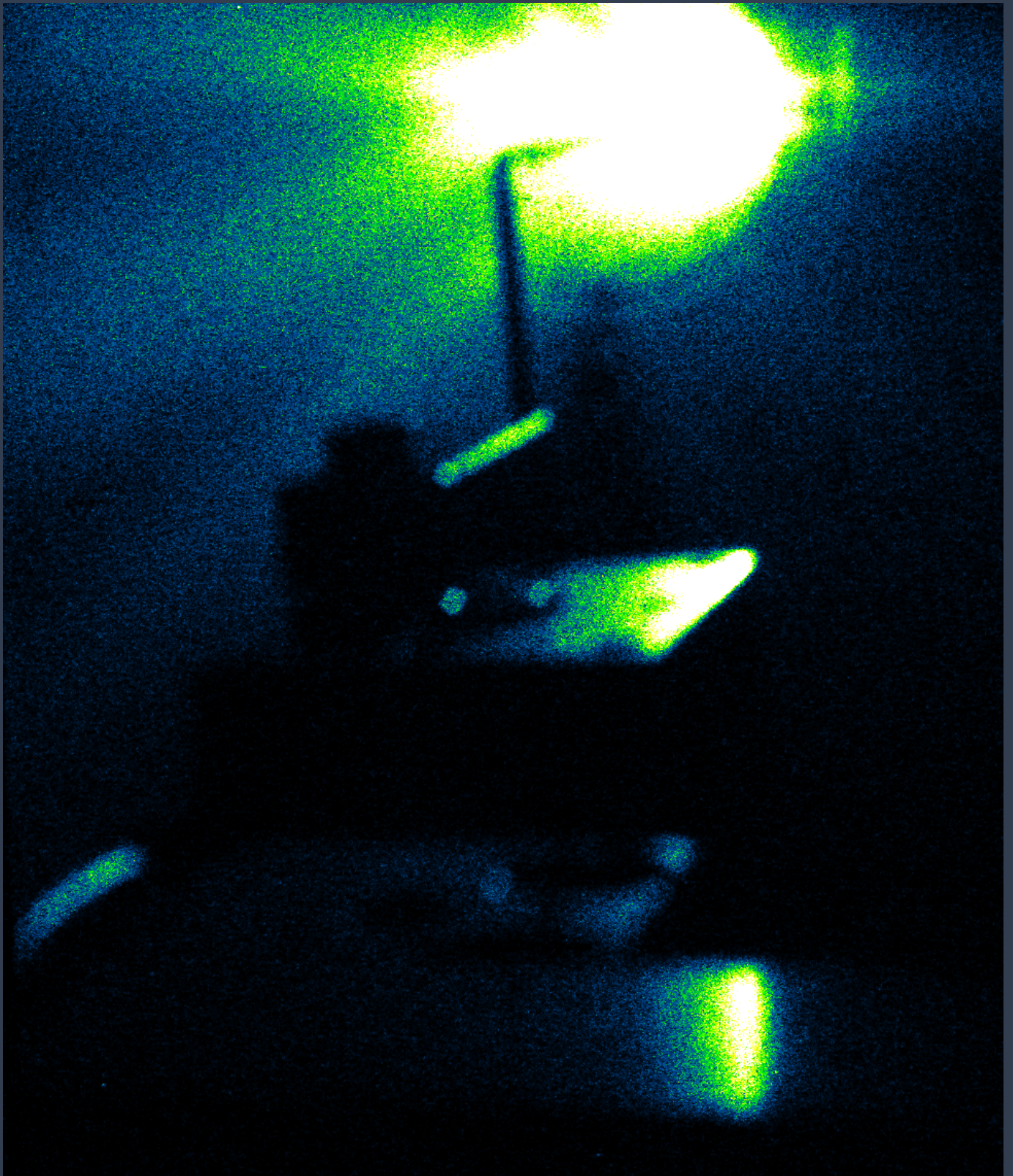préparée à L' École Polytechnique

Ecole doctorale n°572 Ondes et Matières (EDOM)
Spécialité de doctorat : Physique des Plasmas

Thèse présentée et soutenue à Palaiseau, le 30 Juillet 2018, par

GUILHEM REVET

Composition du Jury :

Mme Riconda Caterina Professeure des Universités, UPMC (UMR 7605)	Présidente
Mme Kuranz Carolyn Associate Professor, University of Michigan	Rapporteure
Mme Sthelé Chantal Directrice de recherche, CNRS (UMR 8112)	Rapporteure
M. D'Humières Emmanuel Professeur des Universités, Université de Bordeaux (UMR 5107)	Examinateur
M. Rax Jean-Marcel Professeur, Ecole Polytechnique (UMR 7639)	Examinateur
M. Fuchs Julien Directeur de recherche, CNRS (UMR 7605)	Directeur de thèse

Camera Obscura by laser-created plasma lighting source.

Using the long pulse of the ELFIE Facility, LULI, Ecole Polytechnique, FRANCE (2015)

___The light escapes from a 20 Tesla pulsed coil, and illuminates a target holder mechanical assembly___

Laser energy: 40 J @ 1054 nm; Target composition: Teflon (CF_2)

Plasma temperature: up to few hundreds of eV

Detector: Fuji Bas IP TR2040; Exposure time: less than 1 μs.

Contents

Introduction

The astrophysical environment often exhibits phenomena involving matter in the state of plasma. This state is characterized by positively charged ions evolving nearby previously extracted negatively charged electrons, within a fluid-like state. This fluid, in addition to some of the specificity of fluids, is thus highly responsive to electromagnetic excitation due to the separated charges that are present within it.

Astrophysical jets (from the early star formation process up to active galactic nucleus); Herbig-Haro objects (jet collision with an ambient); supernova remnants (the Crab Nebula being a very well-know example); planetary interiors (as Jupiter's one, for which the state of its core is still debated nowadays); solar flares (these intense ejecta at the surface of the Sun that loop along magnetic field lines); various shocks dynamic having consequences in particle acceleration or even in the start of pre stellar core collapses; all the astrophysical objects in this non-exhaustive list involve ionized matter in the state of plasma.

In the Earth environment, for all to see, plasma is not as ubiquitous than everywhere else in the universe. We have however a spectacular example of plasmas nearby us: the *Auroras*, for which are needed charged particles emitted by our Sun. Plasmas can however be artificially created. The binding energy of the electron within a Hydrogen atom is $13.6\,\mathrm{eV}$ ($2.2 \times 10^{-18}\,\mathrm{J}$), while as an example the use of a hammer, without specifically forcing on it can easily exceed $2.5\,\mathrm{J}$ (for a $200\,\mathrm{grams}$ hammer, going at the velocity of $5\,\mathrm{m/s}$). Going to heavier atoms (to increase the number of bound electrons) will give even lower binding energies for the more external electrons. In practice, a hammer is not often used to hit matter in order to ionize it. Let us make a simple estimation for the use of hammer as an ionization tool, taking our $2.5\,\mathrm{J}$ kinetic energy hammer, and presenting a "hitting surface" of $5 \times 5 = 25\,\mathrm{cm}^2$. In the solid state, matter is present in about $10^{23}\,\mathrm{atom/cm}^3$ (as for the graphite for instance). Then, let us assume the hammer kinetic energy is spread equally in between the hammer itself and the material it is hitting. In order to ionize the solid matter, we need at least to deliver per atom the energy necessary for breaking the bound between molecules (i.e. the enthalpy of fusion, $\sim 1\,\mathrm{eV}$ for the carbon), the enthalpy of vaporization ($\sim 4\,\mathrm{eV}$ for the carbon), and the ionization energy ($13.6\,\mathrm{eV}$ for the Hydrogen bound electron). Consequently, in order to ionize the matter, the kinetic energy of the hammer has to be deposited within a depth:
$$d = (2.5/2)\,\mathrm{J}/((13.6 + 1 + 4) \times 1.6 \times 10^{-19}\,\mathrm{J/atom} \times 25\,\mathrm{cm}^2 \times 10^{23}\,\mathrm{atom/cm}^3) \sim 2\,\mathrm{nm}.$$

Intuitively, this is way too small, and it is expected the energy to be spread over a much larger depth (as a simple example in support of that statement, the possibility to break into two with a hammer, a rock of several centimeters). Then, we can state that a human-use of a hammer is not sufficient to ionize our bound electron. However, the idea of using directed kinetic energy (or ram energy) in order to heat materials is very common and was at the base of impact experiments already performed during the 1960s under the direction of the NASA in order to study and evaluate the effect of micro-meteoroid at hypervelocity (up to $\sim 100\,\mathrm{km/s}$) impacting into satellites (see Friichtenicht and Slattery (1963) as the first report on that topic, with impact velocities up to $\sim 16\,\mathrm{km/s}$, or see Ratcliff *et al.* (1997) for a review). The velocity at which the projectile travels and impacts an obstacle is simply higher than in our hammer example.

Among other ways to heat materials and specifically to create plasma, one can cite discharge machines or plasma guns that create relatively low density and low temperature plasmas, but in a controlled manner that allows repeatability and the setup of diagnostics in a laboratory context for studying the plasma properties. If one wants to get higher density and temperature plasmas, the use of machines delivering more energy, or at least more density of energy, is necessary, and we get closer to the High Energy Density (HED) field of physics.

Compared to plasma physics in general, HED physics is a rather new field that became possible to investigate due to technological advances (in the mid 20th century) that allows for depositing a sufficiently large amount of energy within matter. The matter in a high energy density state is characterized by having a pressure above $\sim 1\,\mathrm{Mbar} = 10^{11}\,\mathrm{Pa} = 10^{11}\,\mathrm{J/m^3}$, which corresponds to one million atmosphere. This threshold represents enough applied energy into the system for it to become compressible. This is due to the fact that $1\,\mathrm{Mbar}$ starts to equalize the internal energy of molecules of matter (the internal energy of the Hydrogen molecule is $\sim 5\,\mathrm{Mbar}$, taking the Coulomb potential energy interaction within a sphere of radius $1\,\mathrm{\AA} = 100\,\mathrm{pm}$). This definition of a high energy density state is the one given by the National Academy of Sciences of the U.S. in 2002 in a report which noted the new available tools, suitable for academical physics investigations, that allow for reaching the HED state (for a detailed description of the HED field, the reader should refer to Drake (2008)). In this context, the Z-pinch machine, developed in the 1950s, allowed for reaching such state of matter, by the use of very intense electrical currents (tens of mega Amps) injected in wires. The amount of energy released in the wire allows for the creation of a plasma on which strong toroidal self-generated magnetic fields act in compressing the plasma. Later on, during the 1960s, the Laser (Light Amplification by Stimulated Emission of Radiation) is created (Ted Maiman makes the first prototype in May 1960). From the stimulated emission description, proposed by Einstein in 1917, through the first Maser (Microwaves Amplification by Stimulated Emission of Radiation -actually the first laser in the principle), developed in April 1954 by Jim Gordon (student of Charles H.

Townes), up to the development of very energetic lasers (and powerful lasers by the use of the Chirped Pulse Amplification mechanism (CPA) - conceptualized by Gerard Mourou and Donna Strickland in the 1980s), the lasers have become precious tools in the HED context, as they allow for the deposition of a large amount of energy within a small volume and in a short time.

The junction of the laser technology and of the HED context with astrophysical concerns have made possible the development of the laboratory astrophysics field. The very first laboratory experiments performed in this area were made by Remington *et al.* (1997); Kane *et al.* (1997), and consisted of studying laser-created shock propagation that was directly linked to the hydrodynamic process at play in supernovae, and specifically the Rayleigh-Taylor instability development. In general, laboratory astrophysics consists of studying, in the laboratory, physical processes that could be similarly happening in astrophysical objects. Because matter in such objects is mostly composed of plasma, these experiments must involve plasma generation. But the HED regime is not strictly necessary for laboratory astrophysics experiments to be relevant. The general condition in order to build a parallel between astrophysical objects (at the astronomical unit scale, or more, and over hundred of seconds, or more) and laboratory objects (which are millimetric and over hundred ns -for laser experiments), is that the physics equations at play during the processes are the same. Here, the pioneer works of Ryutov et al. [Ryutov *et al.* (1999); Ryutov, Drake, and Remington (2000); Ryutov *et al.* (2001)] have demonstrated the scalability between two systems obeying the Euler hydrodynamic equations. The validity of this can be demonstrated, although there are constraints on the plasma localization, heat and viscosity. Regarding the localization, in order for the hydrodynamic description of a plasma to be correct, the dissipative effects should stay on a microscopic scale in order for the fluid, macroscopic description of the dynamic (through fluid macro-particles), to be exact. Hence, we need the dissipation to stay localized and the thermal mean free path to be much smaller than the characteristic size of the system. This is to say, the fluid description must prevail over the kinetic description. Regarding the viscosity and the heat, *diffusion* processes must be negligible with respect to the *advection* transport mechanism. In order to quantify this, the Reynolds, and Peclet number are estimated. Including the magnetic field in the fluid equations, the same reasoning must apply. Then, the magnetic diffusion must be negligeable compared to the magnetic advection (here the magnetic Reynold number is estimated) for the Magneto-Hydro-Dynamic (MHD) equation to be scalable between the laboratory and the astrophysics situation. This regime is often called the *ideal* MHD regime.

In this manuscript, will be treated issues related to laboratory astrophysics that include the interaction of a laser-created plasma expanding into vacuum within an ambient magnetic field. The presence of a magnetic field in a variety of astrophysical phenomena makes the inclusion of this component in the laboratory necessary for the experiments to be relevant.

However, the generation of large scale, stable and homogeneous magnetic field, which is externally applied in a laboratory astrophysics experimental environment (and specifically in a laser experiment environment), was hardly achievable until recently. The difficulty lies in producing sufficiently intense magnetic field (for its strength to compete with the plasma energy density) in a non-destructive manner, such that the optical environment of laser environment can be safe. We note however that very impressive effort were performed in this sense very early on, during some of the first laser experiments with relatively high laser intensity. Indeed, already in the 1970s, Bruneteau et al. at the *Laboratoire de Physique des Milieux Ionisés* at *Ecole Polytechnique*, performed very interesting pioneering works using a laser of focused intensity about $\sim 10^{11}\,\mathrm{W/cm^2}$ and an externally applied magnetic field of $6\,\mathrm{T}$ [Bruneteau *et al.* (1970)]. Nowadays, and notably through previous work of the *Laboratoire National des Champs Magnétiques Intenses* (LNCMI) and the team I was working with during this thesis (the *SPRINT* team at the *Laboratoire pour l'Utilisation des Lasers Intenses* -LULI), a split Helmholtz coil, specifically designed in order to work in a laser environment was developed, that allows for reaching a magnetic field strength up to $30\,\mathrm{T}$, at a rate compatible with the shot rate of laser facilities (up to 1 shot every 20 min).

The interaction laser used during the experiments presented in this thesis is a laser of *moderate* intensity ($I_{max} = 10^{13}\,\mathrm{W/cm^3}$), consisting of a $40\,\mathrm{J}$ pulse at 1ω ($\lambda_{laser} = 1054\,\mathrm{nm}$; critical density, $n_c = 10^{21}\,\mathrm{cm^{-3}}$), spread over $0.6\,\mathrm{ns}$ and focused into a $700\,\mu\mathrm{m}$ diameter focal spot. As a raw estimate, and for a deposition of the laser energy up to $100\,\mu\mathrm{m}$ (corresponding to the observed ablated depth) deep within the target, one can find a maximum generated pressure of the front-target-face plasma of $2.6 \times 10^{11}\,\mathrm{Pa}$, this is to say above the HED threshold. However, this is an estimate without taking into account a proper laser energy absorption or the rapid leakage of energy out of the generated plasma, via radiations for instance. Hence, we do not expect our plasma conditions, at least for the major part of the observed dynamic duration, to by strictly speaking in the HED regime. Then, the specificity of this work is situated in the use of the externally applied magnetic field, and the link with astrophysical objects is made through the context of plasma flow interaction with an ambient magnetic field.

The astrophysical objects on which this study is focused are Young Stellar Objects (YSOs), for which the interaction of plasma flow with a magnetic field is important all along their formation. Several steps of the star formation process will be here investigated: (i) the generation of very long range, bright jets, (ii) the accretion dynamic involving, in the standard representation, matter falling down on the star in the shape of magnetically confined columns, and (iii) more exotic accretion channels, as the equatorial accretion that implies propagation of plasma perpendicularly to magnetic field lines. In this sense, Fig. 0.1 is a very good representation of the kind of objects this work deals with. It represents the HH-30 object, typical of a star surrounded by an accretion disk visible on the Hubble

picture via the absence of light in the center of the system due to light absorption by the accretion disk itself. Spectacular jets developing at each poles of the system are also observable.
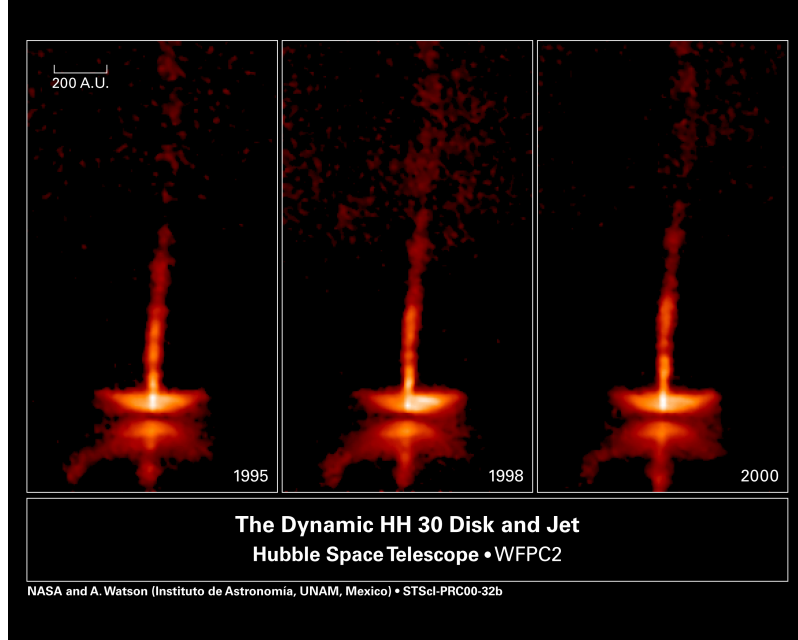

Figure 0.1.: HH 30 jet evolution over a five-years period in the disk and jets. The newborn star, to which it is associated, is situated at 450 light-years and is about half a million years old. From NASA, Hubble Space Telescope.

The manuscript will be split as follows. In chapter 1, the *jet formation* dynamic will be discussed. A first part is dedicated to the jet formation mechanism in a poloidal magnetic field (aligned with respect to the main plasma expansion axis). A second part is dealing with the distortion of such jet formation via the interaction of the same expanding plasma with a misaligned magnetic field (i.e. presenting an angle with respect to the plasma expansion axis). Finally, a third part details the propagation of the plasma within a perpendicular magnetic field. This last part allows us to investigate *exotic* channels of matter accretion onto the stars, consisting of equatorial accretion from the disk to the star, through orthogonal magnetic field lines. In chapter 2, we address the topic of the *standard* accretion dynamic via magnetically confined columns of matter, falling down onto the stellar surface. Using the same experimental setup as in chapter 1, the formed jet (in the case of the perfectly aligned magnetic field) is used to mimic the accretion column, and is launched onto a secondary target that acts as the stellar surface. The shock dynamic at the obstacle location is carefully studied and links with astrophysical accretion observations are built. A plasma cocoon, shaped around the impact region via the interaction with the magnetic field, is found to be similar to the one found in astrophysical simulations. This cocoon is an important element as a potential X-ray absorptive medium in order to explain discrepancies between observed UV/Optical and X-ray emissions emitted from

accreting stars.

Furthermore, as an opening, we stress on the fact that the experimental setup, from which results of the thesis are extracted, is a unique tool (from the coupling with the magnetic field and the laser interaction environment to the highly adaptive setup configuration that it offers). It allows in exploring a variety of laboratory astrophysics configurations including the presence of a magnetic field. Jet collision with an ambient; tilted accretion column impact; accretion within a gradually densifying obstacle; collisionless phenomena implying external magnetic field; this list gives examples of potential astrophysical configurations that can be explored via the present setup.

1. Laser-created plasma expansion in a magnetic field

Introduction

Investigating the possibility of influencing and guiding the hydrodynamics of high-temperature laser-produced plasmas has been the subject of many investigations, including some very early studies [Sucov *et al.* (1967); Bruneteau *et al.* (1970)]. Most experiments investigated plasma dynamics across B-field, revealing a fraction of the plasma to be confined while another part can move across the B-field via an $\boldsymbol{E} \times \boldsymbol{B}$ drift allowed by the development of polarization E-field in the plasma [Bruneteau *et al.* (1970); Peyser *et al.* (1992); Mostovych, Ripin, and Stamper (1989); Plechaty, Presura, and Esaulov (2013)]. The growth of flute-like instabilities affecting the plasma dynamics at intermediate levels of magnetization was also demonstrated [Ripin *et al.* (1993); Zakharov *et al.* (2006)]. We should note however that all these studies were conducted in a regime where only the electrons in the plasma were magnetized, the ions being not or weakly magnetized.

Strong plasma magnetization of laser-produced plasmas has become possible only recently with the development of adequate systems, e.g. at the Laboratory for Laser Energetics [Gotchev *et al.* (2009b,a); Chang *et al.* (2011)] (Rochester, NY, USA) and at the Institute of Laser Engineering [Fujioka *et al.* (2013)] (Osaka, Japan). However, the B-fields they develop have short spatial (mm) and temporal ($10 - 100\,\text{ns}$) scales. The platform [Albertazzi *et al.* (2013)] developed in collaboration between LNCMI and LULI laboratories (France), and which is used in the frame of this thesis, lifts these limitations by allowing magnetization of laser produced plasmas up to $40\,\text{T}$ over much larger ($> cm$) and longer ($> \mu s$) scales. Such homogeneous and stationary field generation is a key factor in allowing the observations that will be presented and discussed in this chapter, as it ensures that a homogeneous magnetic field exists over several cm.

This field is obtained through the use of large-scale pulsed coils, similarly as what had been done earlier at the Institute of Plasma Physics and Laser Microfusion [Faenov *et al.* (1994)] (Warsaw, Poland) and at the Lawrence Livermore National Laboratory [Pollock *et al.* (2008)] (Livermore, CA, USA), but using larger scales and higher-strength B-field so to induce stronger plasma magnetization. Importantly, with such a system, plasma

magnetization can be arbitrarily varied in magnitude or direction. Another significant advantage of this system is that it is not explosive and hence debris-free.

With this system, the collaborative group, in which the present work was performed, showed that by strongly magnetizing a laser-ablated plasma along its expansion axis, they could produce for the first time long, stable, and dense plasma jets without any supporting media [Albertazzi *et al.* (2014)]. This allowed to test the validity of a proposed theoretical shaping mechanism of astrophysical narrow jets (see sec. 1.2). The 20 T B-field could significantly influence the plasma dynamics since the plasma is strongly dominated by the applied B-field at distances greater than $\sim 1\,\mathrm{mm}$ from the target. This is possible since self-generated B-fields (e.g. Biermann battery, $\nabla n_e \times \nabla T_e$) do not influence the plasma anymore as they are confined [Lancia *et al.* (2014)] to $< 0.5\,\mathrm{mm}$ from the target surface, i.e. over very short scales compared to the typical plasma expansion scale.

We note that many other plasma configurations have been used in the laboratory to investigate jet formation and dynamics [Remington, Drake, and Ryutov (2006)], spheromak-like jets [Hsu and Bellan (2003); Bellan, You, and Hsu (2005)], pulsed power pinches [Lebedev *et al.* (2005); Ampleford *et al.* (2008); Ciardi *et al.* (2009)] and (un-magnetized) laser-plasmas [Farley *et al.* (1999); Foster *et al.* (2002); Nicola *et al.* (2010); Loupias *et al.* (2007); Yurchak *et al.* (2014)].

In this chapter, we will first briefly recall the solid-laser interaction within the moderate laser intensity regime we are situated in $(10^{13}\,\mathrm{W/cm^{-2}})$. The plasma expansion in the vacuum that follows that interaction is discussed, following the work of Landau and Lifshitz (1987). The adiabatic and isothermal expansion regimes are presented. This is the aim of sec. 1.1.

Thereafter, experiments of a laser-created plasma interaction with an externally applied 20 T magnetic field are presented. sec. 1.2 presents the case where the main expansion axis of the plasma plume is co-aligned with the ambient magnetic filed. sec. 1.3 presents the case where a misalignment between this expansion axis and the external magnetic field direction exists. Finally, sec. 1.4 will discuss the propagation of such a plasma within a perpendicular magnetic field.

1.1. Basics of the laser-created plasma expansion

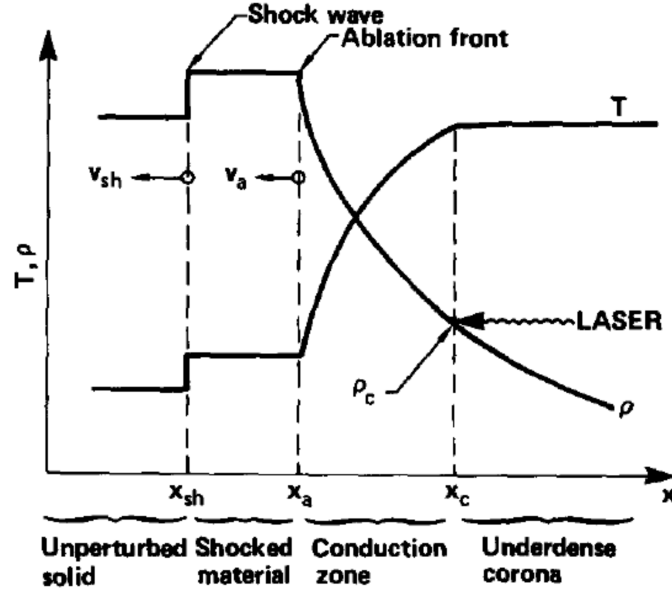### 1.1.1. Laser-matter interaction in a *ns* regime (moderate intensities)

Figure 1.1.: Schematic representation of a solid target expansion dynamic, due to a laser pulse absorption. Extracted from Fabbro, Max, and Fabre (1985).

In this section, and in general in this thesis, the appellation "moderate" intensities designates the intensities situated within 10^{12} and 10^{14} W/cm^2. This is to say, intensities that allow sufficient solid ablation in order to generate plasma flows with expansion velocities $v_{exp} > 100$ km/s (where v_{exp} is estimated via $v_{exp}(\text{cm.s}^{-1}) = 4.6 \times 10^7 I_{laser}^{1/3} \lambda_{laser}^{2/3}$ taken from Tabak *et al.* (1994)), and not intense enough so that the flow does not stay for a long time in the isothermal expansion regime (at it will be shown hereafter). Within this range, the laser light absorption by the solid is about $50 - 60\,\%$, for a light wavelength of $1\,\mu$m [Tabak *et al.* (1994)], and is predominantly due to the inverse Bremsstrahlung absorption mechanism. The very high intensity regime ($> 10^{18}$ W/cm^{-2}) (with enhanced laser absorption due to new absorption mechanisms, such as the Brunel effect or $\boldsymbol{J} \times \boldsymbol{B}$ mechanisms), which generates kinetic particles with energy up to tens of MeV, is not the focus of this thesis.

Within our moderate intensity range, a standard representation of the laser absorption and of the subsequent plasma dynamic is represented in Fig. 1.1. Following the density profile in this figure, the laser light propagates (from right to left on the figure) up to the critical density, ρ_c, which corresponds to the point where the electron plasma frequency equalizes the laser light frequency, so that the transfer of energy from the laser to the matter (via the electrons) is very efficient ; the electron density corresponding to the critical density

is given by $n_c = \frac{\varepsilon_0 m_e \omega_{laser}}{e^2} \sim \frac{1.11 \times 10^{21}}{\lambda_{laser\,[\mu m]}}$. Most of the laser energy is then deposited at that point, while some part of the laser light is also reflected back from that point. Beyond that energy deposition point at ρ_c, extends a conduction zone that allows energy deposition even deeper in the solid. This conduction zone is composed of an electron conduction zone (via an electron heat flux), and can be composed of a second radiative conduction zone (not represented in the figure), more or less important depending on the kind of material irradiated. Finally, this conduction zone leads to an ablation front at its border, continuously ablating matter from the solid. The ablation pressure thus generated launches a shock that propagates within the unperturbed solid. In short, from the solid to the vacuum, we have the unperturbed solid, the shocked material, the conduction zone (that terminates at the critical density ρ_c), and the under-dense expanding plasma.

In addition to the density profile, the temperature profile is also represented in Fig. 1.1. As one can see, the temperature remains constant in the under-dense, expanding region, which corresponds to an isothermal expansion. The condition for such regime is that a sufficient outward heat flux (i.e. going away from the target) could be generated at the critical density point in order to feed in energy the under-dense plasma, allowing to keep a constant temperature while expanding. Such a heat flux can be generated, at the first instant, by the strong temperature gradient at ρ_c, which is quite localized at that point. However, this regime cannot stand for long, and intuitively, one can understand that the time over which this regime holds is linked to the laser duration.

Fabbro, Max, and Fabre (1985) determined a criterion for an expansion to be able to reach the isothermal regime. Without entering in the details here, through considerations about the heat flux (Spitzer-Härm) and the temperature reached at the critical density location for a given absorbed intensity (I_a), they derived such a criterion for the laser intensity, pulse duration and wavelength for the isothermal assumption to hold:

$$I_a \gtrsim 5 \times 10^{12} \left(\frac{\tau_L}{1\,\text{ns}} \right) \left(\frac{1\,\mu\text{m}}{\lambda_L} \right)^4 \left(\frac{2\,Z}{A} \right)^{3/2} \text{W/cm}^2$$

where I_a is the absorbed laser intensity, τ_L the laser pulse duration, λ_L the laser wavelength, and Z and A respectively the atomic number and mass number of the target material. Such intensity (knowing the laser duration and the laser wavelength) is the one for which the heat flux generated is sufficient for supporting the isothermal regime. Then, in our experimental case, for $\lambda_L = 1\,\mu\text{m}$ and $\tau_L \sim 1\,\text{ns}$, we find $I_a \sim 5 \times 10^{12}\,\text{W/cm}^2$. The experimental laser intensity used for the work presented in this thesis is $I^{experiment} \sim 1 \times 10^{13}\,\text{W/cm}^2$. Taking a 60 % absorption [Tabak $et\ al.$ (1994)], one finds $I_a^{experiment} \sim 6 \times 10^{12}\,\text{W/cm}^2$. $I_a^{experiment} > I_a$, but still both intensities stay quite close to each other. Thus, one can think that if an isothermal regime can effectively exist in our experiments, at the first

instant of the expansion, this regime will rapidly vanish (when the laser will turn off) transiting to an adiabatic expansion regime (see hereafter).

1.1.2. 1D self-similar plasma expansion

Adiabatic expansion

Starting from the continuity equations for the mass and the momentum:

$$\frac{\partial \rho}{\partial t} + \rho \frac{\partial v}{\partial x} + v \frac{\partial \rho}{\partial x} = 0$$
$$\frac{\partial v}{\partial t} + v \frac{\partial v}{\partial x} = -\frac{1}{\rho} \frac{\partial p}{\partial x}$$

Landau and Lifshitz (1987) make the variable change $\xi = x/t$ in order to solve the above Euler equations. Such a trick results from the observation that the above equations describe the evolution of the velocity, the density and the pressure. No combinations of the latest quantities can lead to a fourth quantity having either the dimension of a length or a time. However, a quantity having the dimension of a velocity can be easily built. Hence, the density and the pressure will depend on the space and time coordinates only through the ratio $x/t = \xi$ (having the dimension of a velocity). Such a kind of solutions is called self-similar solutions due to the fact that starting from an initial profile, the quantities described by the self-similar solution will evolve temporally similarly to this initial profile, with the scale of the spatial axis, x, being simply "expanded" (or "compressed") by a factor proportional to the time evolution, t.

Rewriting the continuity equations in terms of $\xi = x/t$ one finds:

$$(v - \xi) \frac{\partial \rho}{\partial \xi} + \rho \frac{\partial v}{\partial \xi} = 0$$
$$(v - \xi) \frac{\partial v}{\partial \xi} = -\frac{1}{\rho} \frac{\partial p}{\partial \xi} = -\frac{c^2}{\rho} \frac{\partial \rho}{\partial \xi}$$

where c is the sound speed defined as $c^2 = \left. \frac{\partial p}{\partial \rho} \right|_s$, where the s subscript stands for the derivative for a constant entropy. We note here that Landau and Lifshitz (1987) show that the similarity flow (described following such transformation $\xi = x/t$) is necessary isentropic, unless the solution leads to a constant velocity flow, which is not the physically expected solution. Then, in order to find a non-trivial solution to the set of modified continuity equations (this to says a solution other than $v = constant$ and $\rho = constant$),

it is possible to show that the system should satisfy the following equality:

$$x/t = v + c \tag{1.1}$$

This is done by removing the $\frac{\partial \rho}{\partial \xi}$ and $\frac{\partial p}{\partial \xi}$ terms from the equations (by a simple substitution of the mass conservation equation within the momentum conservation). This latest expression, while inserting it in the mass conservation equation leads to:

$$c\frac{\partial \rho}{\partial \xi} = \rho\frac{\partial v}{\partial \xi} \implies cd\rho = \rho dv \implies v = \int c\frac{d\rho}{\rho} \tag{1.2}$$

Landau and Lifshitz (1987) then characterize the flow by a polytropic flow. Hence we have $P = s(r,t)\rho^{\gamma}$. Because it has been shown that the entropy must be a constant, such a flow is then an adiabatic flow, and we have $P = s_0\rho^{\gamma}$, where s_0 is the constant entropy. Later on, the only assumption made by Landau and Lifshitz (1987) is to consider a perfect gas, so that $P = \rho T/m$. From the polytopic relation, the perfect gas assumption leads to $\rho = \rho_0(c/c_0)^{2/(\gamma-1)}$. Finally, using the conservation of mass equation and the equation for the velocity Eq. 1.2 (which comes from the mass conservation), it is possible to show that $c = c_0 - \frac{1}{2}(\gamma - 1)|v|$. This leads to:

$$\rho = \rho_0 \left[1 - \frac{1}{2}(\gamma - 1)\frac{|v|}{c_0}\right]^{2/(\gamma-1)}$$
$$p = \rho_0 \left[1 - \frac{1}{2}(\gamma - 1)\frac{|v|}{c_0}\right]^{2\gamma/(\gamma-1)}$$

with,

$$|v| = \frac{2}{\gamma + 1}\left(c_0 - \frac{x}{t}\right)$$

A last consideration consists in refusing the sound speed to get negatives values (and so the temperature). Such a consideration leads to a maximum flow velocity, where the later should satisfy $|v| \leq 2c_0/(\gamma - 1)$. It also corresponds to the location where the density reaches zero.

As an illustration, Fig. 1.2 displays the adiabatic solution of Landau for the density and the velocity. As one can see, while the flow is expanding in the vacuum (from left to right, with a tip velocity $v_{max} = 2c_0/(\gamma - 1)$, as already mentioned), the point at which the velocity
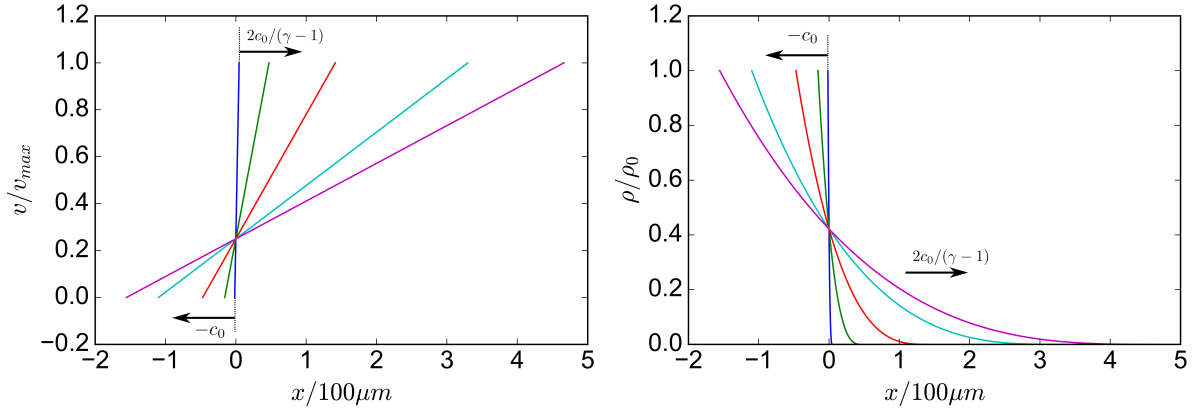
Figure 1.2.: Landau adiabatic expansion result. *Left:* The velocity profiles (normalized to the maximum velocity, i.e. $v_{max} = 2c_0/(\gamma - 1)$), as a function of the distance (normalized to $100\mu m$) for different times, going from 0 up to 1 ns. *Right:* Same for the density (normalized to the initial density, ρ_0)

reaches zero (on the left of the plot) also progresses, in the opposite direction, at the velocity $-c_0$. Everything is going on as if the expansion occurs from a *semi-infinite* plasma reservoir (situated in the x negative region). This fact is actually comprehensible and is a direct consequence of the resolution method of Landau and Lifshitz (1987), i.e. merging the space and time coordinate by setting $\xi = x/t$. Indeed, doing so, no characteristic length or time remains in the equations, and so cannot remain in the solution.

It is important to note that other ways to find self-similar solutions from the continuity equations are possible, such that some temporal and space dependence would appear within the final solution. This is for instance the case of a method using a quasi-invariant transformation of the equations (or rescaling). In it, all the solutions are found in a rescaling space and the self-similar solution can be found by setting $\partial/\partial\hat{t} = 0$ and $\hat{v} = 0$ (static solution), where $\hat{t}$ and $\hat{v}$ are the time and velocity in the rescaling space. Then, the continuity equations are found to be simplified, and no quantities are depending of the time in this new rescaling space. More important, going back to the real space (via some scaling factors $C(t)$, depending of the time, and determined for the scaling transformation), the time dependence reappears.

It is possible to see that such a solution (static solution in the rescaling space) corresponds effectively to a self-similar solution. Indeed, in the Landau solution for instance, everything reacts as if: *doing a length measurement, this length would be measured in a unit which increases proportionally to the time, so that the flow pattern does not change* [quoting Landau and Lifshitz (1987)]. This is corresponding to the static solution, from the point of view of an observer who ignores the evolution of his space unit, proportionally to the time evolution, while making his measurement. Such a solution via a rescaling is for instance intensively detailed in Falize (2008) via the Burgan-Feix-Munier transform.

However, despite the fact that a more precise/general solution can be found through this rescaling method, it will be shown that the Landau solution is already quite accurate and adequate in representing our experimental plasma expansion within a longitudinal magnetic field (see the end of sec. 1.2.5).

Isothermal expansion

The isothermal expansion is simply obtained by setting the temperature as a constant. Hence, we have $c_0^2 = \frac{\partial p}{\partial \rho}$, which differs from the previous case by the fact that the sound speed is a constant (isothermal assumption). Then, following the same method as for the adiabatic case, we obtain:

$$v = c_0 \int \frac{d\rho}{\rho}$$

for which the solution is:

$$\rho = \rho_0 exp(v/c_0)$$

with $v = c_0 - \frac{x}{t}$. The factor $\frac{2}{\gamma+1}$ disappears compared to the adiabatic case due to the constant sound speed in this case. Indeed, the equation for the velocity directly ensues from Eq. 1.1 with a constant sound speed. A schematic representation of the isothermal solution is represented in Fig. 1.3. Contrarily to the adiabatic case, where a maximum velocity can be found (by looking for the point where the sound speed reaches zero -or equivalently the temperature), no maximum speed can be found in the isothermal solution
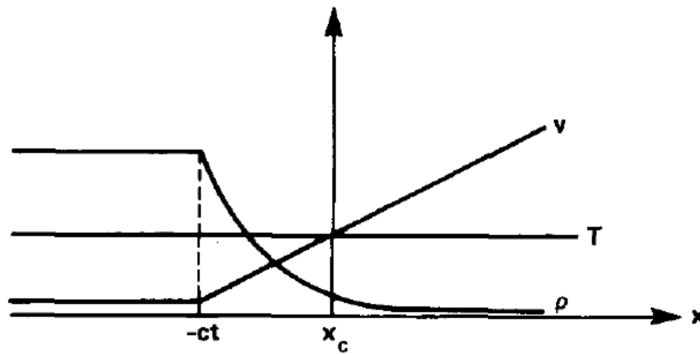

Figure 1.3.: Schematic representation of the isothermal solution for the temperature, the density and the velocity. Extracted from Fabbro, Max, and Fabre (1985).

(the sound speed being a constant). One of the consequences is the fact that the density never reaches zero ($exp(-x/t) > 0 \; \forall \; x$ and t).

1.2. Expansion in a longitudinal magnetic field

1.2.1. Introduction

Outflows of matter are general features of accreting objects, as varied as black holes, active galactic nucleus (AGNs), or star-forming regions, from which they are observed to emerge. In Young Stellar Objects (YSO), the understanding of the outflow dynamics is crucial in acquiring a complete picture of the first stages of star formation. In some YSOs, the outflows are observed to have very characteristic shapes, i.e. forming narrow and stable jets of matter that are sustained over long-ranges.

In the context of pre-stellar core collapse, and specifically in the magnetically regulated core-collapse scenario, the magnetic field take a central role in the proper collapse of the cloud, as well as in the collimation of the outflows, as we will see. Fig. 1.4 presents a sketch of the different objects at play during the core collapse in a large-scale magnetic field. The outflow genesis is widely accepted and consists of magneto-centrifugally accelerated disk or stellar winds material [Blandford and Payne (1982)] (i.e. self-collimation). The model explains the launching of wide-angle outflows, as well as the removal of angular momentum from accretion disks, allowing the matter to be accreted on the star (see chapter 2 of this thesis for a focus on the accretion dynamic); it is a mechanism that has been studied and validated both via simulations [Matsakos *et al.* (2009)] and experiments [Lebedev *et al.* (2005); Ampleford *et al.* (2008); Ciardi *et al.* (2009)]. However, the collimation process into spectacular jets is more controversial. Astrophysical observations agree that outflows, having an initial divergence of about $20-30°$, emerge from an initial region that is $\sim 3\,\mathrm{AU}$ wide, centered near the central star and Keplerian disk. In the cases of narrow jets, if formed, the collimation is observed to take place over a distance of 50 AU, leading to a jet having a small ($2-4°$) divergence angle, compatible with the expected radial expansion of a supersonic collimated jet [Dougados *et al.* (2000); Hartigan, Edwards, and Pierson (2004)].

Several scenarios have been evoked to explain jet collimation. The collimation by an external thermal pressure, induced by an ambient medium surrounding the launching region, can be rapidly discarded because of the incoherent-with-observation medium density needed for the collimation to occur. Indeed, it is possible to show that for typical outflow parameters in YSO, the collimation requires $(n_{ambient} \times T) \geq 2.4 \times 10^{10}\,\mathrm{K.cm^{-3}}$, which does not match any observables for temperature and density of the ambient [Ferreira, Dougados, and Whelan (2007)]. More likely is the collimation induced by the action of a magnetic field. This field can be a toroidal magnetic field (self-MHD collimation); however, this has been shown to rapidly lead to instabilities that dismantle the jet structure [Ciardi *et al.* (2007)]. The collimation by a poloidal magnetic field and co-aligned with the main flow expansion direction, i.e. through the pressure exerted by an external magnetic surrounding

the outflow, is another plausible scenario [Konigl (1982); Stone and Norman (1992); Ciardi *et al.* (2013)].

In YSOs, the required poloidal component could alternatively come from the large-scale magnetic field compressed during the pre-stellar core collapse. As a rough estimate, YSO outflows, taking into account their observed standard characteristic (10^{-8} $M_\odot.yr^{-1}$; $300\,km.s^{-1}$), should need for their ram pressure to be counter-balanced by a poloidal magnetic field, a strength of the latter about $10 - 100\,mG$.

Recent laboratory studies [Ciardi *et al.* (2013); Albertazzi *et al.* (2014); Manuel *et al.* (2015); Albertazzi (2014)] and pertinent astrophysical simulations [Raga *et al.* (1990, 2001); Rozyczka and Tenorio-Tagle (1995); Matt, Winglee, and Böhm (2003)] have confirmed this scenario and shown the viability of poloidal (i.e. axial: B_z) magnetic fields to directly result in the collimation of wide-angle outflows and the formation of jets in astrophysical accreting systems [Kwan and Tademaru (1988); Spruit, Foglizzo, and Stehle (1997)], such as young stellar objects (YSO). In particular, this mechanism has been shown to generate large aspect ratio (length:diameter > 10) jet. Moreover, through the formation of a long-standing and relatively stationary conical shock, it is suggested to be at the origin of long-time x-ray emission observed from such objects (e.g. HH 154) [Favata *et al.* (2002); Bally, Feigelson, and Reipurth (2003); Bonito *et al.* (2011)].

The dynamics of the laboratory-produced jets was shown to be scalable to YSOs jets [Ciardi *et al.* (2013); Albertazzi *et al.* (2014)] as both systems are to a first approximation well described by magnetohydrodynamics (MHD) [Ryutov *et al.* (1999); Ryutov, Drake, and Remington (2000); Ryutov *et al.* (2001)]. The laboratory evidence for the poloidal collimation of jets thus offers an explanation of the observed long range collimation of young stellar jets [Frank *et al.* (2014)]. As such, it is complementary to magneto-centrifugally launched, self-collimated disk winds [Blandford and Payne (1982)].

Shown below in Eq.1.3 is the radial Lorentz force exerted on an ideal MHD plasma in cylindrical coordinates. The force associated to self-collimation in magneto-centrifugal models is due to the toroidal magnetic field B_Φ. On the other hand, the poloidal collimation mechanism that is explored in this section is due to the presence of an initially axial magnetic field B_Z.

$$F_r = \underbrace{-j_z B_\phi}_{\text{self-collimation}} + \underbrace{j_\phi B_z}_{\text{poloidal collimation}} \tag{1.3}$$

The process of poloidal magnetic collimation of a laser-ablated plasma is illustrated in Fig. 1.5. Without a strong poloidal B-field, the plasma is heated to high temperature and expands into vacuum in all directions, creating a quasi-hemispherical expansion (Fig. 1.5a).

When a strong axial B-field is applied, as shown in Fig. 1.5b, the plasma is restricted from expanding radially by the field and expands only until reaching an equilibrium between the total plasma kinetic pressure and magnetic pressure. This causes a conical shock to form and the plasma is subsequently redirected onto the radial axis. As the plasma converges on axis, a conical jet is formed and the plasma is collimated into a high Mach-number, high aspect-ratio jet.

The focus of this section is to robustly characterize these laboratory-generated jets produced by laser-matter interaction and collimated via external axial magnetic fields, and that we have recently investigated [Ciardi *et al.* (2013); Albertazzi *et al.* (2014); Manuel *et al.* (2015)]. This will also allow us to highlight their stability over long temporal duration and under a variety of plasma conditions. Of particular interest is the conclusion that the plasma is only marginally magnetized at distances far away from the target. This indicates that the high aspect ratio of the jet is due mainly to the collimation at the base and then to the high Mach-number Lagrangian ballistic expansion of the flow at large distances. In other words, at large distances from the target, the presence of the magnetic field is unimportant to the collimation of the flow. To make this point clear, we characterize this collimation mechanism as a poloidal magnetic nozzle (PMN) in order to highlight that the collimation mechanism is active near the base of the jet. We note here that the B-fields are called poloidal due to the toroidal symmetry of a jet ejected from an accreting system. In the experimental setup, cylindrical symmetry is apparent and the fields are referred to as axial. Since the system size is very large in the poloidal astrophysical case, these two descriptions are equivalent near the base of the jet.

In sec. 1.2.2, we will explain the experimental configuration of the laser, the Helmholtz coil that drives an external magnetic field, and the suite of experimental diagnostics for observing the electron density (2D-space, time), optical self-emission (1D-space, time) and electron temperature (1D-space).

In sec. 1.2.3 we characterize the plasma based on measurements in different regions and we estimate the related plasma parameters in order to give a context to the plasma confinement and jet formation. Note that the characterization of the dynamics of laser-produced plasma expansion into vacuum has been an active subject of research for over 50 years and is on-going. Thus, this (unmagnetized) expansion will not be the focus of the present section, rather we will focus on how such a plasma is shaped into a narrow jet through its interaction with the poloidal B-field. In sec. 1.2.4, we describe the formation and evolution of the jet over 23 mm in space and over 70 ns in time when the B-field is applied. We detail the formation of a cavity near the target caused by the generation of an oblique shock along the plasma expansion front, which leads to a strong conical shock and the subsequent formation of a long-aspect-ratio jet.

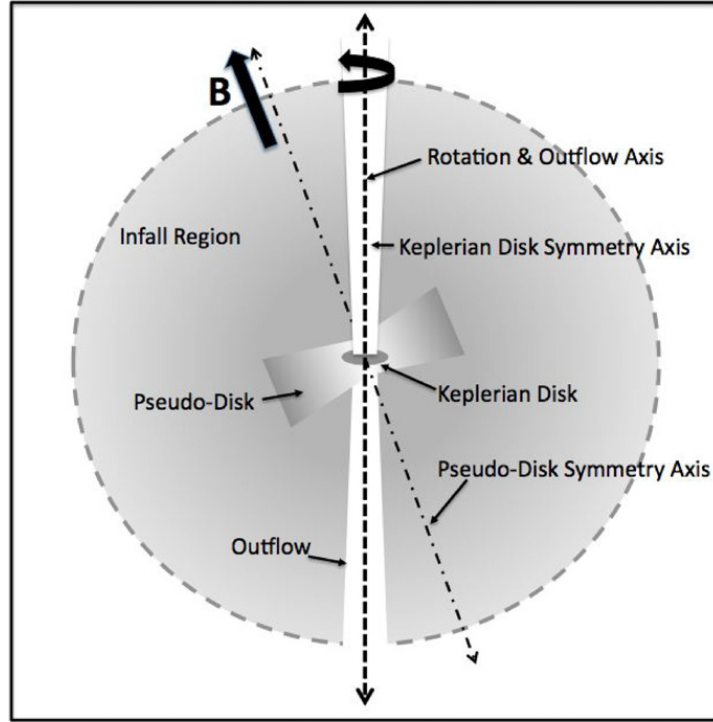In sec. 1.2.5, we give more precise insights, thanks to the help of simulated data, on

Figure 1.4.: Extracted from [Davidson *et al.* (2011)]: "Schematic summarizing the magnetically regulated core-collapse scenario. Typically, the diameter of the infall region is $\sim 10,000\,\mathrm{AU}$, the diameter of a pseudo-disk is $\sim 2000\,\mathrm{AU}$, and the diameter of a Keplerian disk is $\sim 100\,\mathrm{AU}$. In the magnetically regulated core-collapse scenario: the pseudo-disk symmetry axis is aligned with the core magnetic field; and magnetic braking tends to align the core rotation axis with the magnetic field, but this alignment may not be exact. The pseudo-disk is a dynamically collapsing object formed by the magnetic fields, not rotation. The Keplerian disk is an object formed by rotation and so its symmetry axis is aligned with the core's rotation axis, as too is the outflow axis if the outflow is driven by rotation".

the physical mechanism allowing the confinement at the base of the flow. Regarding the resulting jet, a link between a 1D adiabatic expansion model and the expansion corresponding to the collimated experimental jet is detailed.

Finally, in sec. 1.2.6, we examine the fidelity of the jets to a variety of experimental parameters: we vary the kinetic energy of the expansion by changing the laser energy incident on the target, we vary the atomic composition of the jet by varying the target material and we vary the magnetic field strength in a range going from 6 up to 30 T. We observe that those variations lead to quantitative differences in the jet formation, but shows similar overall behavior in that the plasma is confined radially and a jet is formed.
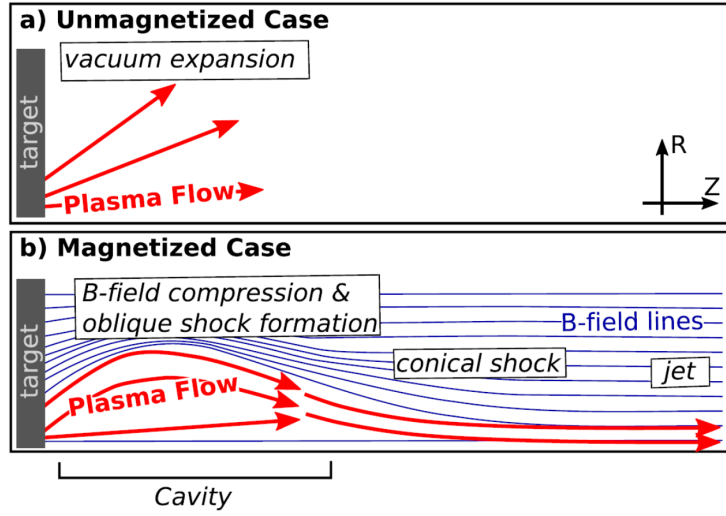
Figure 1.5.: Schematic of plasma expansion into vacuum following the laser-irradiation of the front (right) side of a target. **(a)** Without a strong B-field, the plasma expands in a wide-angle flow. **(b)** With a strong poloidal B-field, the plasma is confined laterally by the B-field, forms an oblique conical shock and is redirected onto the radial axis. The on-axis conical shock collimates the flow into a jet.

1.2.2. Experimental Setup

The experiment was performed at the ELFIE laser facility [Zou *et al.* (2008)] at the *Laboratoire pour l'Utilisation des Lasers Intenses* (LULI) in France. A schematic of the target and laser setup within the coil is shown in Fig. 1.5. This system employs a Ti:Sa ($\lambda = 1057nm$) amplification chain that normally stretches, amplifies and then recompresses to sub- picosecond duration a laser pulse via the chirped pulse amplification technique [Strickland and Mourou (1985)] . However, in our experiment we use the beam prior to recompression resulting in a frequency chirped 40 J, 0.6 ns pulse-length beam. The laser was focused through a 2.2 m focal length lens (f/22) and a random phase plate [Kato *et al.* (1984)] to achieve a 0.7 mm diameter focal spot on target. At the maximum energy of 40 J this achieved an on-target intensity of $1.6 \times 10^{13}\,\mathrm{W.cm^{-2}}$. The laser was incident at 10° on the front surface of a thick, 2 mm diameter CF_2 (Teflon) disc mounted on a glass stalk connected to an encoded motorized stage. The target surface was aligned perpendicular to the magnetic field with ±5° uncertainty.

Helmholtz coil and pulsed power driver

The Fig. 1.6a shows a schematic of the pulsed-power driven Helmholtz coil developed at the *Laboratoire National des Champs Magnétiques Intenses* (LNCMI) [Béard and Debray (2013)] in Toulouse. This device allows for a peak field strength of 40 T, though in practice it was used at 20 T to increase the lifetime of the coils. This design is similar to the
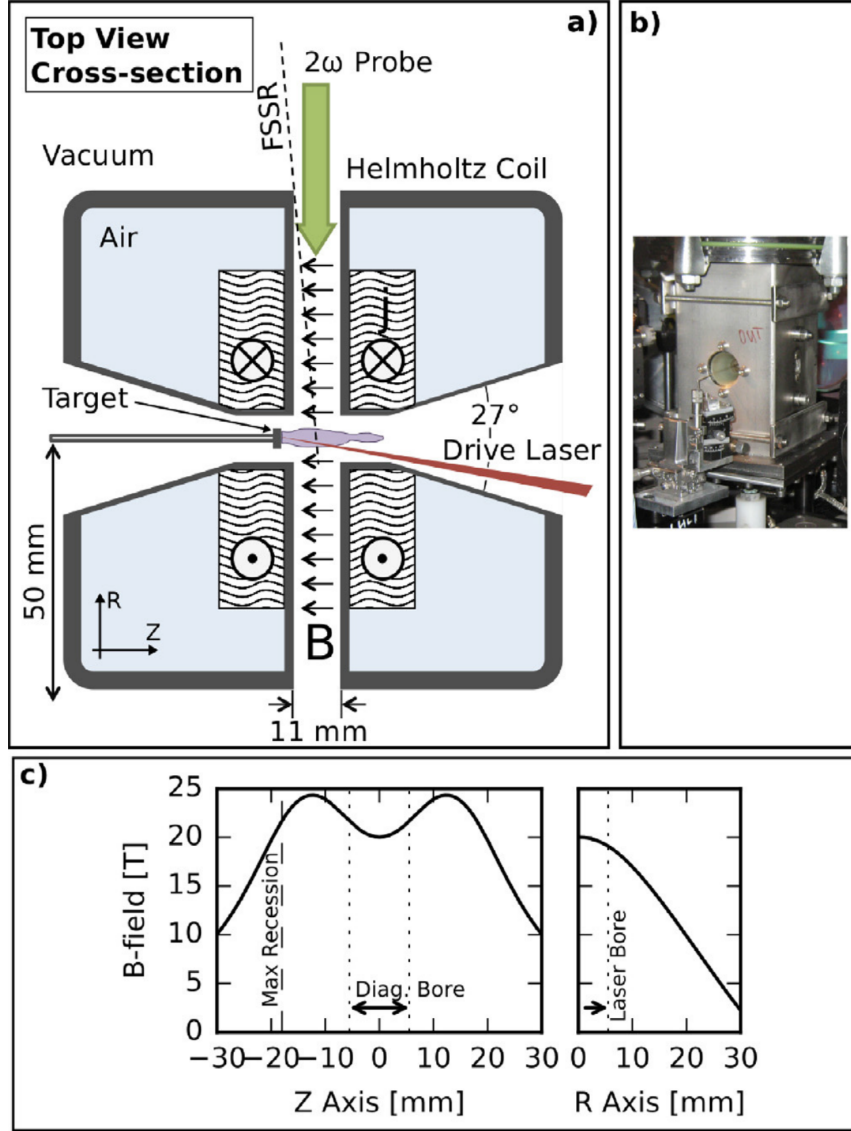
Figure 1.6.: (a) Top view schematic of the Helmholtz coil system. The "laser bore" (left-right axis) of the coil would allow a maximum of 27° full-angle beam (f/2.1) for a laser beam at normal incidence. The "diagnostic bore" (up-down axis) is of constant 11 mm diameter. **(b)** Photograph of the Helmholtz coil in the chamber looking into the "laser-bore". Motorized stages are not shown. **(c)** Magnetic field profiles along the coil central axes. The target is recessed along the longitudinal (laser bore) axis which is parallel to the field lines. Dotted and dashed lines show the extent of the coil bore and the maximum distance over which the target was recessed.

one described in Refs. [Albertazzi *et al.* (2013, 2014)] with the largest difference being increased bore sizes for diagnostic and laser access. The coil and windings are described in Ref. [Béard *et al.* (2013)]. The windings and, thus the current flow, is kept in air to avoid breakdown in the fiber-glass structure. Fig. 1.6b shows a photograph of the coil in the target chamber. The coil was supported from the top by vacuum tubes and a bellows that allowed the tilt to be aligned to align the magnetic field with the chamber.

The coils were driven by a $16\,\mathrm{kV}/250\,\mathrm{mF}/32\,\mathrm{kJ}$ pulsed power unit and delivering $20\,\mathrm{kA}$ [Albertazzi *et al.* (2013)], developed by the Dresden High Magnetic Field Lab (HLD) at Helmholtz-Zentrum Dresden-Rossendorf (HZDR). The rise time of the coil was 190 ms, meaning that the magnetic field is constant over the experiment timescale (< 0.1 ms). As shown in Fig. 1.6c, the coil was designed to have a large volume of constant magnetic field. In order to probe the jet at distances longer than the size of the bore of the coil, the target was recessed to a precise position inside the coil using the motorized target stages. The magnetic pressure of 20 T is 160 MPa and the magnetic energy in the center bore ($r = 5.5\,\mathrm{mm}$, $V = \frac{4}{3}\pi r^3$) is 56 J. This is enough to fully counter the 40 J laser pulse, considering that not all of the laser energy is absorbed and that some of the absorbed energy is lost to non-adiabatic channels (e.g. radiation, ionization).

Interferometry

Interferometry is accomplished via the Mach-Zehnder technique with a frequency doubled probe laser with a pulse length of 5 ps and $\sim 100\,\mathrm{mJ}$ of energy an at a wavelength of 1057 nm (1ω). Fig. 1.7 shows the probe beam trajectory after it has been compressed, frequency doubled and delayed with respect to the nanosecond irradiation beam. To increase the amount of data taken per shot, the probe beam was partially frequency doubled such as a similar quantity of beam at 1ω and 2ω are co-propagating after the frequency doubling crystal. Later on, the beam is split in two orthogonal polarizations, S and P, via a polarizing prism. This yields to a train of four pulses (2ω-P / 2ω-S / 1ω-P / 1ω-S) that are arranged with delay lines such that they are separated by $\sim 10\,\mathrm{ns}$ between each other, and re-injected back into the original beam path so that both beams were exactly co-aligned. This technique allows probing the plasma electron density at four different times for each laser shot on target. These four time frames allow us to access the plasma temporal dynamic without shot-to-shot laser fluctuations. At the end of the beam path, the beams were again separated using a polarizing prism and monochromatic mirror to divide the four beams evenly between the two polarizations and wavelengths, so that each beam was displayed independently on a CCD camera. The beams were imaged through a 1.2 m lens onto an Andor CCD cameras ($13 \times 13\,\mathrm{mm}$ pixels, 1024×1024 pixel chip size). This setup had a magnification of $1.2\times$, a $10.8\,\mathrm{\mu m}$ resolution and a field of view $\sim 11\,\mathrm{mm}$ to capture the entire coil window. The interference fringes were fit with a

wavelet model and unwrapped using Neutrino [Vinci and Flacco (2018)]. An Abel inversion [Bockasten (1961)] was applied to the (background-subtracted) phase to determine the electron density.

Because of the limited field of view through the magnetic field coil (11 mm), we captured the full (i.e. over several cm) plasma evolution along z by moving the target, for different shots, along the laser axis (z) and within the magnet assembly. Of course this is done only over the maximum length over which the magnetic field shows little variation (we use as a criterion that B does not vary by more than 10 %) which corresponds to a total length of $\approx 25\,\text{mm}$ within the coil. The images thus obtained are then patched in order to get the full spatial evolution of the plasma, as shown in Fig. 1.32. Due to the low-aperture of the laser beam generating the plasma (f/22), and the cm-scale homogeneous magnetic field, the plasma generation when the target location is changed does not vary in the explored range of 20 mm along the laser axis.
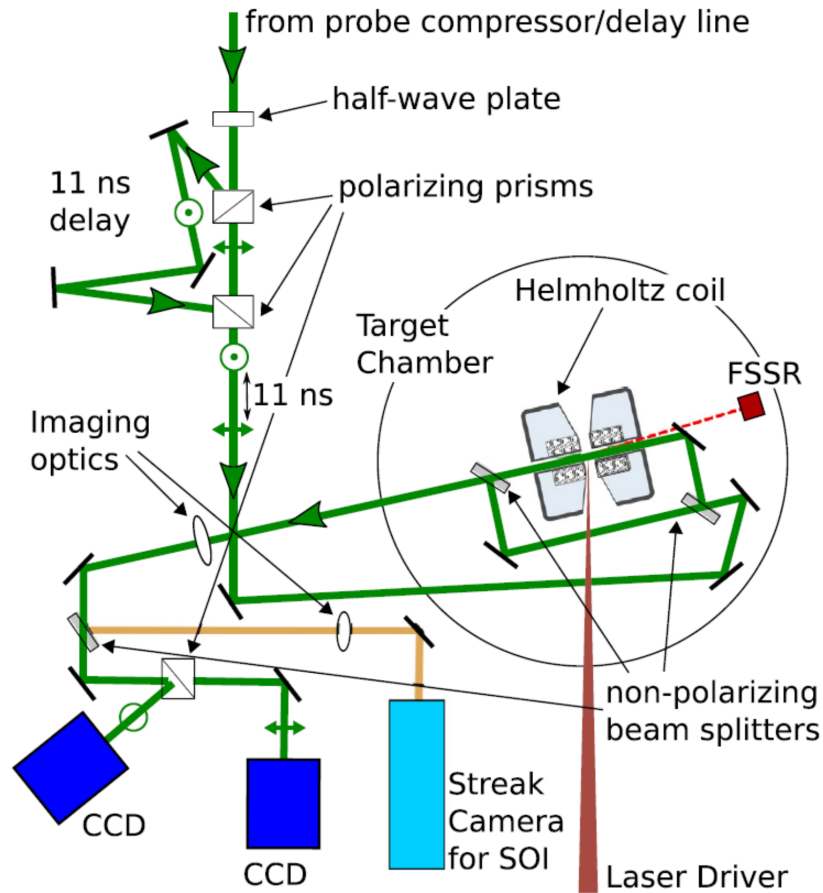

Figure 1.7.: Diagnostic diagram of the experimental setup. The probe beamline is split and recombined so that one beam is delayed by 11 ns. The SOI imaging line looks along an axis identical to the probe beam. The line-of-sight to the FSSR crystal used for x-ray spectroscopy is also shown.

Streaked optical pyrometry (SOP)

A streaked optical imager (SOI) was used to create a time-resolved 1D image of the plasma self-emission along the jet propagation axis and was centered on the middle of the laser spot. We redirect the reader to the thesis of Lévy (2008) and Antici (2007) for a detailed description of the setup using such diagnostic as well as analysis processes. As shown in Fig. 1.7, this diagnostic used the same optical pathway as the probe beam and thus imaged the plasma from the same angle as the interferometry. After the $f = 1.2\,\mathrm{m}$ imaging lens of the interferometry system, the SOI pathway was split using a non-polarizing beamsplitter and then re-imaged through a 300 mm focal length lens on to a Hamamatsu C7700 streak camera with an S20 photocathode (sensitive to 200-850 nm wavelengths). Narrow-bandwidth (notch) optical filtering was used to block the light from the probe and driver beams. The spatial variation in the cathode efficiency was taken into account using a flat-field calibration.

X-ray focusing spectrometer with spatial resolution (FSSR)

The electron temperature and dynamics of jet expansion were complementarily studied by means of X-ray spectroscopy. This diagnostic analyzes the emission of He-like and H-like Fluorine ions. A focusing spectrometer (FSSR) with high spectral and spatial resolution (about $80\,\mu\mathrm{m}$ in this experiment) was implemented to measure the X-ray spectra emitted by the multi-charged ions from the plasma, in the range 13 - 16 Å $(800 - 950\,\mathrm{eV})$ in the m = 1 order of reflection. The spectrometer was equipped with a spherically bent mica crystal with parameters $2d = 19.9376\,\text{Å}$ and curvature R = 150 mm. The time-integrated spectra were registered on Fujifilm Image Plate TR [Meadowcroft, Bentley, and Stott (2008)], which were placed in a cassette holder protected from optical radiation. For this, the aperture of the cassette was covered by two layers of filters made of polypropylene $(1\,\mu\mathrm{m})$ evaporated by aluminum $(200\,\mathrm{nm})$.

A focusing spectrometer with spatial resolution (FSSR) was used to record the temporally-integrated x-ray emission spectra of the plasma. The diagnostic was set up to resolve x-ray energies in the range of 750-950 eV in the first order of mica crystal reflection and 1500-1900 eV in the second order. The diagnostic was aligned along nearly the same line-of-sight as the interferometer with a slight angle in the upwards $(\sim 5°)$ and lateral $(\sim 2°)$ directions (i.e. small enough to neglect skewing). The relative intensities of He-like spectral lines (e.g. He_β, He_γ, He_δ) radiated by transitions in the Fluorine ions were analyzed. The ratios between multiple pairs of lines is used to constrain both the electron density n_e and temperature T_e. Since this diagnostic is not temporally resolved the values are intrinsically weighted towards times of highest emissivity, which is a function of both temperature and density. A detailed methodology of this analysis technique is presented in Ryazantsev *et al.* (2015) and Ryazantsev *et al.* (2016).

Table 1.1.: Measured and estimated plasma conditions with plasma expansion gradient length scale $L = 1\,\text{mm}$ and magnetic field $B = 20\,\text{T}$ for 3 cases: (1) the initial plasma expansion, (2a) the expanding cavity region, (2b) the collapsed cavity and (3) the jet far from the cavity. The derivation of the plasma parameters is explained in the text and in Annex sec. A.1 .

	1	2a	2b	3	(units)
z	6	2	1	22	mm
t	6	16	23	$60 - 30$	ns
Measurements					
n_e	1.10^{17}	3.10^{18}	5.10^{18}	1.10^{18}	cm^{-3}
T_e	80	20	35	10	eV
u_d	1000	120	43	$370 - 750$	km/s
Avg. Charge States					
$\bar{Z}_\text{F}$	7	5	6	4	
$\bar{Z}_\text{C}$	5	4	4	4	
$\bar{Z}_i$	6.3	4.7	5.3	4	
Ion Densities					
n_i	1.10^{16}	6.10^{17}	9.10^{17}	3.10^{17}	cm^{-3}
ρ_i	4.10^{-7}	2.10^{-5}	3.10^{-5}	7.10^{-6}	g/cm^3
Velocities					
C_s	75	33	46	22	km/s
v_{Te}	3800	1900	2500	1300	km/s
v_{Ti}	22	11	14	7.6	km/s
v_A	850	130	110	210	km/s
Length Scales					
r_{Li}	30	20	23	17	μm
λ_i	5.8	3.10^{-2}	3.10^{-2}	3.10^{-2}	μm
r_{Le}	1.1	0.5	0.7	0.4	μm
λ_e	150	0.4	0.7	0.4	μm
Time Scales					
τ_{ad}	1	8	23	1.3	ns
τ_{he}	4.5	480	220	800	ns
τ_m	140	23	48	10	ns
τ_ν	8000	3.10^6	2.10^6	4.10^6	ns
τ_r	14	4	4	5	ns
τ_{eq}	47	0.4	0.4	0.7	ns
Scaling Parameters					
M	13	0.5	1	$17 - 34$	
M_A	1.2	0.9	0.4	$1.7 - 3.4$	
β_{dy}	2.8	1.8	0.3	$6 - 25$	
β_{th}	8.10^{-3}	6.10^{-2}	0.2	1.10^{-2}	
Pe	4.5	59	9.5	$300 - 600$	
R_m	140	0.4	2	$3.5 - 7$	
Re	8000	4.10^5	9.10^4	$(1.5 - 3) \times 10^6$	
K	1.10^{-3}	2.6×10^{-5}	3.10^{-5}	3.10^{-5}	
H_i	0.2	1.10^{-3}	1.10^{-3}	2.10^{-3}	
H_e	140	0.8	0.9	1	

1.2.3. Summary of plasma and magnetization parameters

To provide a context for these magnetized jets, we will now consider the conditions of the plasma in various regions of interest using the experimentally evaluated temperatures, densities and inferred flow velocities of the plasma. These conditions are presented in Tab. 1.1. The experimental data from which we take these values will be presented in detail in sec. 1.2.4. We now define the different regions that we will evaluate and then we will derive the plasma parameters presented in Table 1. For each region we define a time t and distance of interest z ; this allows us to estimate the flow velocity $u_d = z/t$ following a Lagrangian ballistic expansion model where all of the acceleration occurs at the time of the laser irradiation at $t = 0$; a model based on previous simulations [Ciardi *et al.* (2013)] of the flow velocity in the same configuration (this assumption will be justified in sec. 1.2.5).

Region 1: Initial expansion

Region 1 considers the very initial expansion of the plasma near the target. In the first frame of the interferometry images shown in Fig. 1.5a / Fig. 1.9a we see that the fastest portion of the plasma that can be detected by our diagnostic has expanded to $\sim 6\,\mathrm{mm}$ and has an electron density of $n_e = 1 \times 10^{17}\,\mathrm{cm}^{-3}$ at a time of 6 ns. From this we conclude that this portion of the plasma is traveling at $u_d = 1000\,\mathrm{km/s}$. There may be faster portions of the plasma that are not observable to our diagnostic, but these will be of lower density and should not play a major role in the shaping of the jet. Since we expect that the plasma will reach the hottest temperatures at this initial expansion time, we use the hottest temperature measured with the FSSR, $T_e = 80\,\mathrm{eV}$ (shown in Fig. 10) for this region. We note that, as the FSSR is time-integrated, this temperature may be an underestimate.

Region 2: cavity

Region 2 defines the cavity region that can be observed in Fig. 1.9b and that will be discussed later. The cavity will be examined at two distinct periods in time and space. We first define Region 2a, as the period when the cavity is expanding, here we take the location as 2 mm and the time as 16 ns, giving $u_d = 120\,\mathrm{km/s}$. The Region 2b we define as the period when the cavity is contracting/contracted, where the location is 1 mm and the time is 23 ns, which gives $u_d = 45\,\mathrm{km/s}$. The FSSR shows $T_e \simeq 20\,\mathrm{eV}$ and $T_e \simeq 35\,\mathrm{eV}$ and the interferometry yields $n_e \simeq 3 \times 10^{18}\,\mathrm{cm}^{-3}$ and $n_e \simeq 5 \times 10^{18}\,\mathrm{cm}^{-3}$ for Region 2a and 2b, respectively.

Region 3: propagating jet

Region 3 represents the collimated jet that propagates with very high aspect ratio over long distances (see Fig. 1.9e). Following the jet in its progression thanks to the interferometer, we can infer a quasi-constant electron density of $n_e = 1 \times 10^{18}\,\mathrm{cm}^{-3}$ over space (see Fig. 1.11). The tip of this component is found to travel with a bulk velocity of 750 km/s. At 60 ns for instance, Fig. 1.9e, the jet fills all the available field of view. At these late times, we are limited by the observed range of our diagnostic of 22 mm, which corresponds to a bulk speed of 370 km/s, however we expect that the range of the jet is much longer, with a higher Mach number and larger aspect ratio than what we capture experimentally (typically, the component at $10^{18}\,\mathrm{cm}^{-3}$ is expected to have traveled 45 mm after 22 ns). In this region we determine $T_e = 15\,\mathrm{eV}$ from the FSSR (this is an upper estimate and extrapolation from the data). In order to take into account the decrease in bulk velocity of the jet, at a given distance, we present for the region 3 of Tab. 1.1 the plasma parameters for two typical speeds: the tip velocity of 750 km/s and the one corresponding to the jet at 22 mm at 60 ns, i.e. 370 km/s.

1.2.3.1. Thermodynamic quantities

To determine the average charge state $\bar{Z}$ of the plasma, we used tabular data from FLYCHK [Chung *et al.* (2005)], using the n_e and T_e values discussed above for each region. We find that these values shift less than 10% for density variations of even $10\times$ around a density of $10^{18}\,\mathrm{cm}^{-3}$. We assume a quasi-neutral plasma ($n_e = \bar{Z}_i n_i$) where the average charge state $\bar{Z}_i = \sum_\alpha S_\alpha Z_\alpha = \frac{2}{3}\bar{Z}_F + \frac{1}{3}\bar{Z}_C$ is the *stoichiometric average* of the two species, where S_α stoichiometric percentages. The mass density is found in the same manner, $\rho_i = n_i m_i = n_i \left(\sum_\alpha S_\alpha m_\alpha \right) = n_i(2m_F + m_C)/3$.

To get an idea of the relevant velocities in our system we look at the sound and thermal speeds of the plasma. We assume that $T_i = T_e$, and an adiabatic index $\gamma = 5/3$. This gives an effective sound speed $C_s = \left(\gamma T \times \left(1 + \overline{Z}_i \right) /m_i \right)^{1/2}$ and the thermal velocities $v_{T_{e/i}} = (T_{e/i}/m_{e/i})^{1/2}$. The Alfvén speed is $v_A = B/\sqrt{\mu_0 \rho_i}$, where B is the magnetic field and μ_0 is the vacuum permeability. The Mach number M and the Alfvénic Mach number M_A are defined as the ratio of the bulk velocity to the sound and Alfvén speeds, respectively.

1.2.3.2. Particles motion

We calculate the gyroradius $r_{L_{e/i}} = v_{T_{e/i}}/\omega_{c_{e/i}}$, where $\omega_{c_{e/i}} = Z_{e/i}eB/m_{e/i}$ is the gyrofrequency. As a reference value, for a 20 T B-field and charge states of $\bar{Z}_C = 4$ and $\bar{Z}_F = 7$ (stoichiometrically averaged), $\omega_{ce}^{-1} = 3 \times 10^{-4}\,\mathrm{ns/rad}$ and $\omega_{ci}^{-1} = 1.4\,\mathrm{ns/rad}$. Note that these frequencies should be roughly similar for all of the different regions considering that

the gyrofrequency is only dependent on the strength of the magnetic field and, in the case of ions, the charge state, which presents little variations.

To understand the plasma collisionality, we calculate the electron (τ_{ei}), ion (τ_{ii}), and electron-ion equilibration (τ_{eq}) inverse collision rates using values from Braginskii [Braginskii (1965)]. The mean free paths $\lambda_{e/i} = v_{T_{e/i}} \tau_{e/i}$ are calculated using the thermal speeds $v_{T_{e/i}}$ and the inverse collision rates $\tau_{e/i}$.

$$\tau_e = \tau_{ei} = \frac{3\sqrt{m_e}T_e^{3/2}}{4\sqrt{2\pi}Zn_e e^4 ln\Lambda} = \frac{3.5 \times 10^5}{ln\Lambda} \cdot \frac{T_e^{3/2}}{Zn_e} \quad ; \quad \tau_i = \tau_{ii} = \tau_{ei}\sqrt{\frac{2m_i}{m_e}}Z^{-2}$$
$$\tau_{eq} = \tau_{ii}\sqrt{\frac{m_i}{m_e}} = \tau_{ei}\frac{\sqrt{2}m_i}{m_e}Z^{-2}$$

where $ln\Lambda$ is the Coulomb logarithm that we take from Spitzer (1956) (see Annex sec. A.1 for details).

From the short electron-ion equilibration times given in Tab. 1.1, we find that for most of the plasma conditions the plasma is collisional enough to justify an equilibration between the ion and electron temperatures. The exception to this is that during the initial expansion of the plasma, there will be a hot (80 eV), low density region (10^{17} cm^{-3}), where this equilibration time may be long.

1.2.3.3. Dimension-less scaling parameters

For a detailed description of the way the dimension-less number are calculated, the reader should refer to Annex sec. A.1. We detailed here after the meaning of the main ones.

To characterize the plasma in terms of the importance of *advection* (χ_{ad}) with respect to thermal (χ_{th}), magnetic (χ_m) and viscous (χ_ν) *diffusion*, and so to understand how this experiment would scale to astrophysical phenomena, we follow the treatments of Ryutov *et al.* in [Ryutov *et al.* (1999); Ryutov, Drake, and Remington (2000)]: we calculate the non-dimensional Peclet ($P = \chi_{ad}/\chi_{he}$), magnetic Reynolds ($R_m = \chi_{ad}/\chi_m$) and Reynolds ($Re = \chi_{ad}/\chi_\nu$) numbers. These terms reveal the relative importance of advection versus heat diffusion, magnetic diffusion and viscosity, respectively. When these numbers are large, advection dominates. To quantify these numbers in the context of the experiment, we also use the gradient length scale L to determine a relative timescale $\tau = L^2/\chi$ (e.g. $\tau_{ad} = L^2/\chi_{ad}$) above which these effects will be important.

To understand the role of magnetization versus collisional effects, we calculate the Hall parameter $H_\alpha = \omega_{c\alpha}\tau_\alpha$ for the species α. This number is representative of the number of cyclotron orbits a particle performs before undergoing a collision. Thus for high Hall numbers, we consider the plasma to be strongly magnetized. We find that for these plasma

conditions the ions are not substantially magnetized ($H_i \ll 1$). On the other hand, the electrons are considerably magnetized ($H_e \gg 1$) at high temperatures and have marginal magnetization ($H_e \sim 1$) at lower temperature (i.e. in the far jet region).

Finally, we define the plasma beta. This value relates the relative importance of the total kinetic pressure of the plasma to the magnetic pressure $P_m = B^2/(2\mu_0)$. We define the plasma beta in two ways, first the dynamic beta $\beta_{dy} = P_{dy}/P_m$, which is the ratio of the ram pressure $P_{dy} = \rho_i u_d^2$ to the magnetic pressure. Secondly, the thermal beta $\beta_{th} = P_{th}/P_m$, which is the ratio of the thermal pressure $P_{th} \simeq n_e T_e$ to the magnetic pressure. Throughout the evolution of the jet, the balance between magnetic and kinetic pressure is dynamically changing.

1.2.3.4. Radiative cooling

The radiative cooling power was found using the code FLYCHK [Chung *et al.* (2005)] for different ion densities n_i in the range from 10^{17} to 10^{18} cm^{-3}. For each density the total (bound-bound, bound-free and free-free) radiation power was found for both Carbon (P_{rC}) and Fluorine (P_{rF}) considering that their densities were $\frac{1}{3}n_i$ and $\frac{2}{3}n_i$, respectively. The total radiation power density was then calculated as a summation of these two powers, $P_r = P_{rC} + P_{rF}$ at electron temperature range $T_e = 20 - 100$ eV giving the values of $\sim 5 \times 10^{-9}$ J/s/atom. We realize that a true multi-species treatment of the radiation would be the proper way to calculate this, however for an order-of-magnitude estimate we expect that this is sufficient. The radiative cooling rate is on the order of 10 eV/ns and the radiative cooling time is on the order of few ns as estimated in the same T_e range.

The cooling rate of the plasma ($\Delta T_e/\Delta t = P_r/C_v$) was found using the radiative cooling power and the heat capacity at constant volume C_v of the plasma, as determined from Livermore equation-of-state (LEOS) tables. The radiative cooling time $\tau_r = 0.1 \times T_e/(\Delta T_e/\Delta t)$ was evaluated as the amount of time for the temperature to decrease by 10% at the given cooling rate. We note here that the optical skin depth of the plasma is quite long and thus we expect the plasma to be optically thin.

However, it is necessary to note that the estimations of the radiative cooling power were made considering a plasma in the local thermodynamic equilibrium (LTE). For low-temperature (few tens of eV) recombining plasma, the radiative bound-bound transitions should provide sufficient increase in radiative cooling rate and corresponding shortening of the radiative cooling time. So the values given above represent a definite underestimation. In fact, as shown in the Tab. 1.1, one may consider the radiative cooling to play an important role in the present experiments, because the plasma is recombining all along the range of the jet propagation away from the target surface.

1.2.3.5. Plasma parameters summary

At early times (Region 1), Tab. 1.1 suggests that the plasma will be highly magnetized ($H_e \gg 1$) and that the magnetic field is effectively frozen-in with the plasma flow ($R_m \gg 1$). The β_{dy} is above unity, suggesting that at this point, the radial component of the plasma is able to push against the magnetic field and will strongly modify the topology of the field.

At later times, still close to the target (Region 2) β_{dy} drops below unity, indicating an increased ability of the magnetic field to push back against the plasma flow. The lowered $\mathbb{P}$ suggests that heat diffusion in this region can be neglected due to the cooling down of the plasma. While still greater than unity, the decreasing value of R_m suggests that magnetic diffusion may play some role in the dynamics.

Finally, at later times and distances far from the target, we find that the Mach-number is high ($M \sim 34$, $M_A \sim 3.4$) and that the strong ram pressure maintains a high β_{dy}. However, the role of the magnetic field here will be relatively small. The electrons are only marginally magnetized ($H_e \sim 1$). While $\mathbb{R}_m$ is not particularly small, the magnetic diffusion time ($\tau_m \sim 10\,\text{ns}$) is low compared to the time of interest (60 ns). This indicates that there has been plenty of time for the magnetic field to diffuse into the plasma.

Other than at very early times ($< 16\,\text{ns}$), the ion-electron equilibration time (τ_{eq}) is less than 1 ns, which suggests that our assumption of equal ion and electron temperatures is valid. Also, at all times, we find that the radiative cooling time ($\tau_r = 4 - 14\,\text{ns}$) is relatively short compared to the evolution of the plasma, which suggests that the plasma is cooling substantially as time progresses. This cooling of the plasma is important as it reduces the sound speed of the plasma and thus increases the Mach-number.

1.2.4. Characterization of a large aspect ratio jet

1.2.4.1. Electron density evolution without magnetic field

To characterize the ablation of plasma without an applied B-field, the $2 \times 10^{13}\,\text{W/cm}^2$ ($E_L = 40\,\text{J}$) laser irradiated a CF_2 target without powering the Helmholtz coil ($B = 0\,\text{T}$). Fig. 1.8 shows the electron density, as diagnosed via interferometry, for three different timings as expanding away from the initial target surface at $z = 0$. In all of the interferometry images, the electron density is found via Abel inversion, which is done separately for the top and the bottom images. As numerical errors from the Abel technique lead to a high uncertainty on-axis, the central region ± 5 pixels have been excluded from the image. Noise in the fringes leading to difficulty in the phase inversion is responsible for many of the sharp and small scale features in the images, especially at the transition between the plasma and the vacuum. One can compare the upper and lower portion of each image to get a better understanding of the features caused by this noise.

Notice that in Fig. 1.8 none of the images show any collimation of the plasma and it expands in a wide-angle flow with a half-angle of around 30°. This wide flow is expected and has been observed much earlier [Rosen *et al.* (1987)]. The expansion of such a non-magnetized flow is generally characterized as a planar (i.e. 1D) expansion close to the target ($z \sim R_{spot}$) and as a quasi-hemispherical (i.e. 3D) expansion at distances far from the target ($z \gg R_{spot}$) [Puell (1970); Pert (1989); Drake and Gregori (2012)], as observes experimentally here. We note that some previous work has referred to these flows as "jets" [Ryutov *et al.* (2011, 2012)] due to their modest directionality. However, these flows do not have high-aspect ratios and thus the authors themselves have deemed such a term inappropriate [Ryutov *et al.* (2013)]. As cited in the introduction, unmagnetized jet formation is possible using shaped targets [Farley *et al.* (1999); Loupias *et al.* (2007)] or multi-material layers [Foster *et al.* (2002); Nicola *et al.* (2010); Yurchak *et al.* (2014)] to hydro-dynamically shape the flow into a jet. However, none of these techniques were used in the present setup and thus we observe a widely diverging flow without the formation of a jet.

1.2.4.2. Electron density evolution with 20 T magnetic field

The dynamics of the plasma expansion change considerably with the addition of the z-aligned external 20 T magnetic field. Fig. 1.9 shows the electron density evolution, measured via interferometry, over many millimeters and many tens of nanoseconds in the case of the irradiation of a CF_2 target with a 1.6×10^{13} W/cm^2 laser in an 20 T applied magnetic field. The upper and lower frames in the images represent Abel inversion taken from either side of the Abel symmetry axis, and comparison between the upper and lower
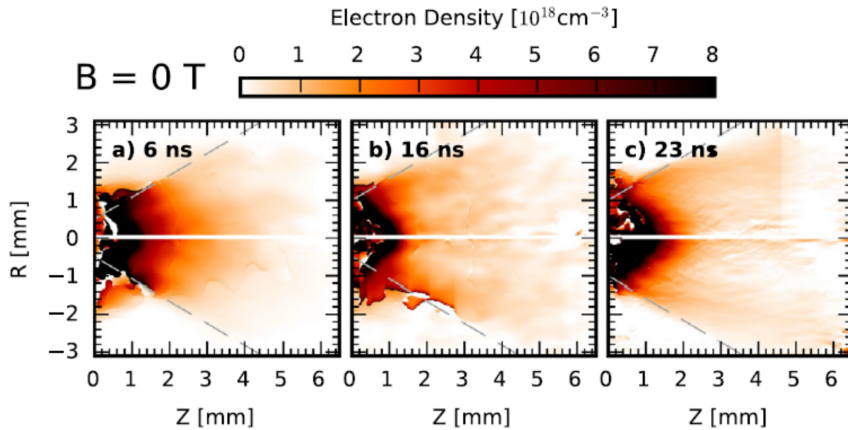
Figure 1.8.: Pseudo-color images of electron density taken via interferometry showing the electron density from a 1.6×10^{13} W.cm^{-2} laser irradiating a CF_2 target without an ambient magnetic field. The central ± 5 pixels (± 55 µm) have been removed due to the uncertainty of the Abel inversion on axis.
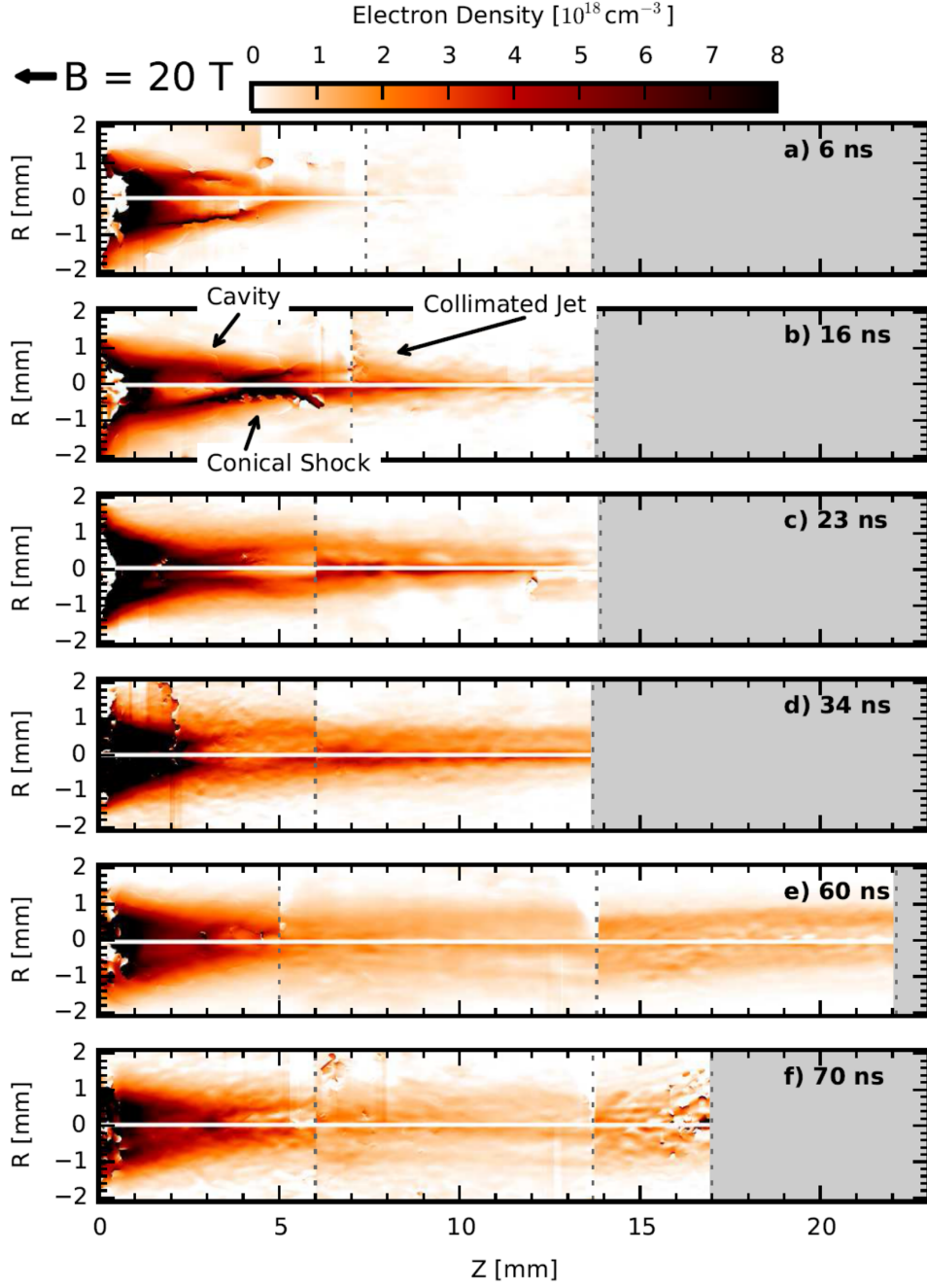
Figure 1.9.: Pseudo-color images of electron density taken via interferometry showing jet propagation from 6 to 70 ns as indicated in the plots, with $B = 20\,\mathrm{T}$. The gray background indicates a region where no data was taken or the fringes were not of sufficient quality to be unwrapped properly. The central ± 5 pixels ($\pm 55\,\mu\mathrm{m}$) have been removed due to the uncertainty of the Abel inversion on axis. Note that many of the fine structured features are due to noise in the fringes of the interferometer and thus are non-physical. These areas are most notable around the target, in (a) at $z = 3 - 5\,\mathrm{mm}$, $r = -0.5\,\mathrm{mm}$, in (d) at $z = 2\,\mathrm{mm}$, $r = 0 - 2\,\mathrm{mm}$ and in (f) at $z > 15\,\mathrm{mm}$.

portions can be used to ascertain the experimental uncertainty of the volumetric electron density. These images were taken over multiple shots with nominally identical setups. To capture different frames in time, the delay between the interferometer probe beam and the main laser pulse was varied from 6 to 70 ns. To capture long spatial scales in the plasma, the target was recessed within the coil in order to catch the plasma spatial distribution far from the source target. Then, the various spatial frames where the plasma was recorded were patched up to form the images shown in Fig. 1.9. The individual images are identified by dotted lines separations in Fig. 1.9. Comparing the cases with (Fig. 1.9) and without (Fig. 1.8) magnetic fields, it is very clear that the 20 T field drastically changes the plasma evolution, and that the field acts to confine and collimate the plasma into a narrow jet.

If we consider the front edge of the jet, we find a jet velocity $u_d \sim 1000$ km/s at early times by noticing that the plasma has progressed to 6 mm over a time of 6 ns. This is consistent with the non-magnetized case and shows that the velocity of jet is not particularly faster in the presence of the magnetic field. However, due to strong collimation, the jet has a much higher density at distances further from the initial target surface. Considering the sound speed (75 km/s) calculated previously, we find that the jet is propagating at high Mach number ($M = 13$) at this leading edge of the jet.

We now describe the forming of the jet based on direct experimental observations and from our understanding of the physics supported by simulations (similar to those in [Ciardi *et al.* (2013); Albertazzi *et al.* (2014)]). During the evolution of the jet there are three distinct spatial regions, which evolve in different ways and result from an interplay between kinetic plasma pressure and magnetic pressure. These are the cavity, the conical shock and the jet, as discussed above. We label these regions in Fig. 1.9b. Here the cavity region extends from around 1 to 4 mm from the initial target surface, the conical shock region is from 4 to 6~mm, and the collimated jet is from 6~mm and greater.

The cavity region is given its name due to the lower density on the inside compared to the high density region surrounding it, as is shown clearly in the early time frames of Fig. 1.10. We see also that the density is higher on axis as compared to the case without B-field. The sharp radial density gradient in that case is formed as the ram pressure of the plasma pushes out against the magnetic field lines to create a shock [Ciardi *et al.* (2013)]. This will transfer transverse ram pressure into thermal pressure (i.e. heating) of the ions. Fig. 1.10 shows the evolution of the radial profile of the cavity at a distance of 2 mm from the target surface. At early times there is a strong increase in density at the edges that is representative of the shock from the plasma pushing against the magnetic pressure.

This oblique shock at the edge of the cavity is then responsible for re-directing the flow of plasma along the shock so that it follows the contour of the cavity until it converges on the axis (see Fig. 1.5b). This convergence of the flow on axis generates a conical shock [Hornung (1986)] at the longitudinal tip of the cavity ($z \sim 4$ mm at 16 ns), which then
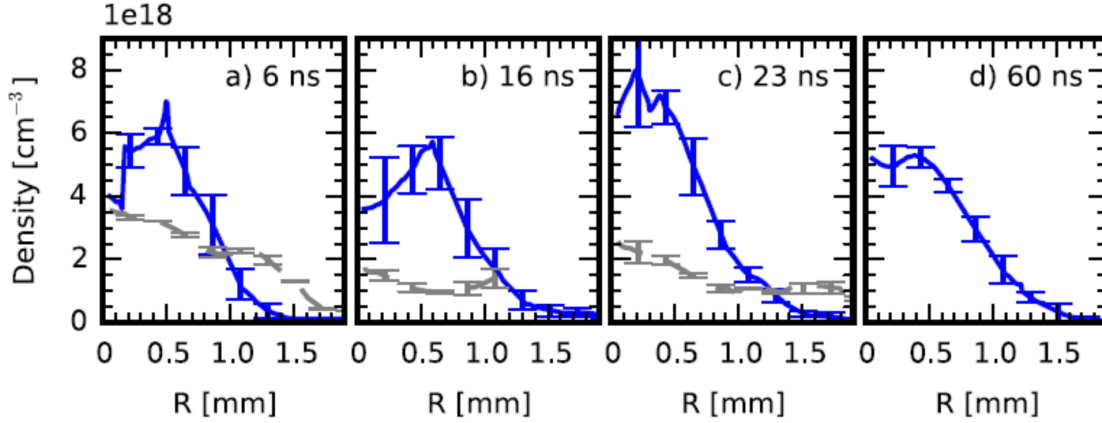
Figure 1.10.: The radial electron density profile of the jet at a distance of 2.0 mm from the initial target surface (averaged over ±55 µm). Solid (blue) lines show the case with a 20 T applied magnetic field and dotted (gray) lines show cases with no applied field. The time after laser irradiation is shown in each plot. Error bars are shown at even intervals. Those error bars are calculated via the differences in between the left and right parts (with respect to the Abel inversion axis) of the electron density maps.

re-directs the flow again. Since the plane of the conical shock is along the z-axis, the flow is symmetrically refracted along the z-axis and a collimated jet is formed. This cavity can be thought of as a nozzle, a poloidal magnetic nozzle, where the oblique shock and conical shocks create the walls of the nozzle. However, one major difference between this type of collimation and a mechanical nozzle is that the main acceleration mechanism is the initial energy from the absorbed laser and not the constriction of the flow through the throat of the nozzle, a distinction due to the fact that the experiment is not in steady-state.

At later times we see the jet propagate over long distances (> 23 mm , $> 10 : 1$ aspect ratio) and times (> 70 ns, $100\times$ the laser duration). From the plasma jet parameters at $z = 22$ mm and $t = 60$ ns, we infer a sound speed of $C_s = 22$ km/s and thus a Mach number $M = 17$ in Tab. 1.1. At this location the plasma is only marginally conductive ($R_m \sim 3.5$) and the magnetic diffusion time is around 5 ns. This suggests that strong magnetic field gradients cannot exist and that the magnetic field cannot be responsible for collimating the jet in this region. Additionally, the high β_{dy} at this point indicates that the magnetic pressure would not be able to hold in the flow if it were not already collimated. Thus the jet must be propagating hydrodynamically and we expect a divergence angle $\theta = \tan^{-1}(1/M) \simeq 3°$ (18:1), which is consistent with observations.

We now look quantitatively at the longitudinal profile of the electron density near the center of the jet in the left side of Fig. 1.11. Here the different shaded lines represent different shots taken as the target was recessed into the coil to capture a large spatial region. The overlap between the lines highlights the repeatability of the formation of the jet over different shots at the same nominal laser parameters. Unlike the case without an applied
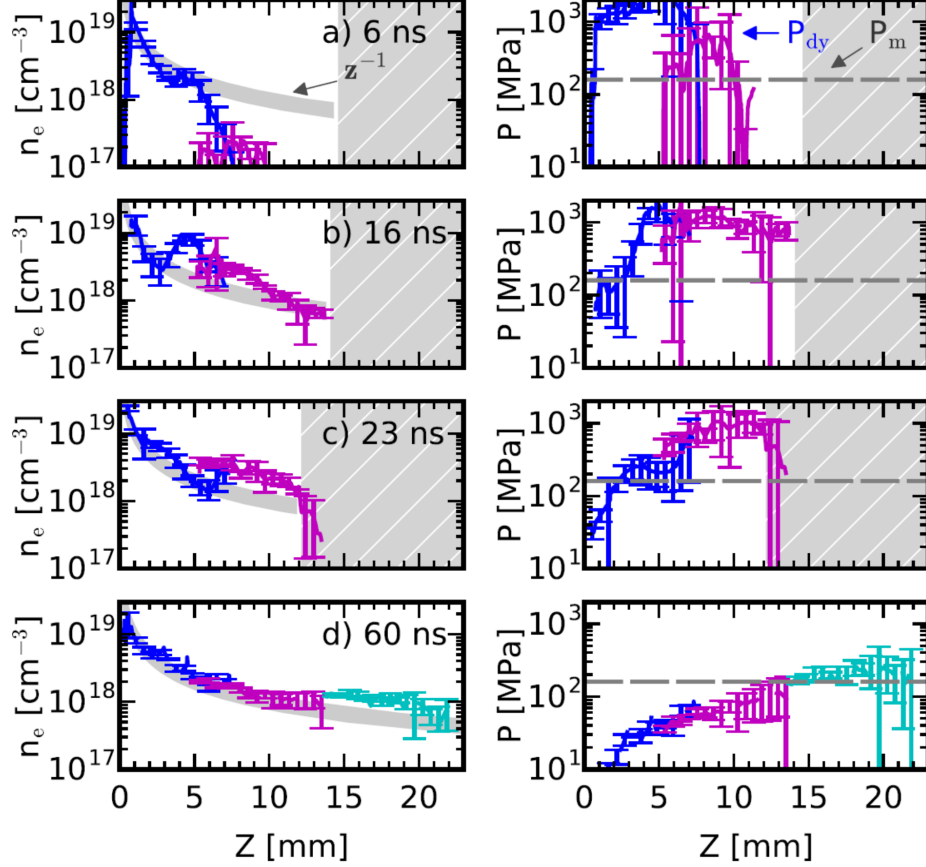
Figure 1.11.: (Left) Longitudinal electron density, n_e, near the center ($110\,\mu\mathrm{m} < r < 270\,\mu\mathrm{m}$) of the jet at times $6 - 60\,\mathrm{ns}$ after laser irradiation. The lines show the cases with an external 20 T field. The different shades of the solid lines are for different shots taken with different recession distances of the main target to look at different regions of the jet. The solid gray fill in is $n_e \propto z^{-1}$ with $\pm 20\%$ provides a reference to the fall off of the data. The solid gray hashed fill shows regions where no data was taken or the data is of poor quality. Error bars in the data are shown at even intervals. Those error bars are calculated via the differences in between the left and right parts (with respect to the Abel inversion axis) of the electron density maps. **(Right)** Ram pressure, P_{dy}, (solid lines) and nominal magnetic pressure, P_m, (dashed line) at the same times.
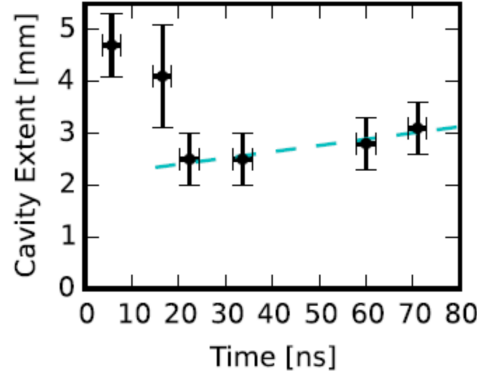
Figure 1.12.: The location, in the z-direction, of the tip of the cavity (i.e. conical shock region) at different times. The values are determined from the location of the peak density of the shock and the uncertainty is defined as the width of the shock. A linear fit of the expansion at later times is shown as the dotted line, which has a slope corresponding to 12 km/s.

field (i.e. Fig. 1.11), the profile does not show a steady monotonic decrease. Instead, with an applied field, the profile shows a strong bump in the density a few millimeters from the base of the jet. This region is the conical shock that is caused by material that is re-directed from the edges of the cavity back into the center as explained earlier. At distances far from this shock, we see an expansion that follows a scaling that is consistent with a 1D Lagrangian ballistic expansion with a constant ionization fraction. Due to the flatter falloff of the spatial dependence at distances far from the target surface we see that at 60 ns (Fig. 1.11d) the jet maintains a relatively constant density ($n_e \simeq 10^{18}\,\mathrm{cm}^{-3}$) for over a long distance ($5 - 20\,\mathrm{mm}$) and could potentially be used as a constant density medium for experiments probing plasma parameters at these conditions. However, we note the density probed here to be the electron density. The ion density is expected to have a different behavior at large distances, specifically a stronger decrease as for a quasi-adiabatic expansion (this is justified in sec. 1.2.5). The right side of Fig. 1.11 shows the ram and nominal magnetic (i.e. 20 T) pressures created by the same method as in Fig. 1.11. The ram pressure, $P_{dy} = \rho_i u_d^2$, is found assuming that the plasma expansion is ballistic (i.e. $u_d = z/t$; this is also justified in sec. 1.2.5) and that the plasma has a constant average charge state of $\overline{Z} = 6$; as consistent with the plasma parameters given earlier in Tab. 1.1. From these plots it seems clear that the ram pressure is the dominant force at the tip of the jet at all times.

To understand the interplay between the forces exerted by the plasma and those exerted by the magnetic field, we plot the longitudinal location of the tip of the cavity as a function of time in Fig. 1.12. These values are calculated from the location of the peak density of the conical shock region and taking the width of this region as the uncertainty. Considering that the plasma must initially start at the target surface (i.e. $z = 0\,\mathrm{mm}$ at $t = 0\,\mathrm{ns}$), this plot shows that the cavity expands at early times ($\leq 16\,\mathrm{ns}$), then quickly recesses ($\sim 23\,\mathrm{ns}$)

and finally expands again at a slower pace ($\geq 23\,\text{ns}$). The initial expansion and recession is consistent with the evolution of the ram pressure P_{dy} compared with the nominal magnetic pressure P_m considered in the unmagnetized case in Fig. 1.11. At early times ($< 10\,\text{ns}$), P_{dy} is large as it corresponds to the fastest leading edge of the plasma expansion. Thus at this time P_{dy} exceeds P_m and the plasma pushes out against the magnetic field to reach a peak of around 4.5 mm at $5 - 15\,\text{ns}$. As time goes on ($> 10\,\text{ns}$), the velocity of the outflow near the cavity decreases and P_{dy} falls below P_m causing the cavity to be pushed back by the magnetic field to a position of around 2 mm at 20 ns.

We note once again that while the initial force from the B-field will be in the radial direction (i.e. due to the longitudinal field lines), the field line topology will be significantly modified as the plasma evolves. This will create a radial component to the magnetic field and will result in a significant force in the longitudinal direction. Our simulations suggest that this radial force will result in an effective pressure of $10 - 50\%$ of the nominal (160 MPa) value. The final ($> 20\,\text{ns}$) expansion is quite slow and a best fit to the data corresponds to an expansion velocity of $12 \pm 10\,\text{km/s}$. The dynamics behind this late time evolution should be driven by both the plasma ram and thermal pressure considering that u_d and C_s are of the same order (i.e. from Tab. 1.1, Region 2b). This dynamic is also complicated by the fact that R_m is near unity suggesting that magnetic diffusion may be of some importance during this period (i.e. from 20 to 60 ns).

1.2.4.3. Optical emission from the jet

The optical emission originating from the central region ($r < 100\,\mu\text{m}$) of the jet is shown in the case without (Fig. 1.13a) and with (Fig. 1.13b) an applied 20 T magnetic field. The emission is streaked so that the downward direction is the time from the main pulse irradiation and the horizontal axis is the longitudinal direction away from the target in space. A dashed line is plotted on top of the images that shows a velocity of 10 km/s, which seems to roughly correspond with the darkening of the image at distances near to the target surface. The reason for this darkening is likely due to the expansion of high density plasma that is optically thick and thus blocks emission coming from the center of the plasma.

The emission in the case without a magnetic field decreases monotonically both in time and in space. By around 50 ns the emission has fallen below the noise level of the diagnostic, and in the longitudinal direction the emission has decreased to below the noise level at a distance of 2 mm.

On the other hand, with an applied magnetic field, the emission extends to both longer times ($\sim 80\,\text{ns}$) and over larger distances ($\sim 3\,\text{mm}$). Also, in contrast to the case without field, the emission does not decrease monotonically. In fact, the emission at distances greater than 1.5 mm starts to increase at around 25 ns. This can be attributed to heating
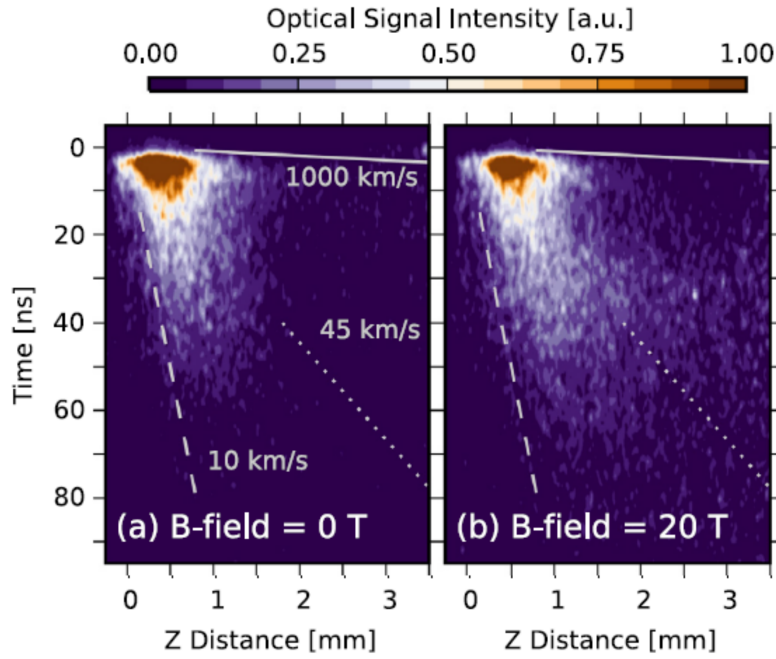
Figure 1.13.: Optical emission from the streaked optical imager (SOI) showing the cases (a) without and (b) with a 20 T applied magnetic field. The vertical axis is the time from the main pulse irradiation and the horizontal axis is the longitudinal distance from the target surface. The signal intensity units are arbitrary but are the same on both images. The peak intensities are (a) 2.6 and (b) 1.6 for the cases with and the without applied field, respectively. The overlaid dashed, dotted and solid lines are the same on both plots and have velocities of 10, 45 and 1000 km/s, respectively, and pass through the origin.

from the conical shock as it relaxes backwards towards the target. This is consistent with both the timing and the position of the tip of the cavity shown in Fig. 1.12.

1.2.4.4. Electron temperature via FSSR X-ray spectrometry

The time-integrated electron temperatures and densities from the FSSR are shown in Fig. 1.15 for the cases with and without an applied 20 T B-field. A schematic representation of the FSSR setup is displayed in Fig. 1.14. It indicates the field of view with which the spectrometer was looking at the plasma dynamic, this is to say transversally. First of all, we note that Fig. 1.15b gives electron densities that are consistent with those observed via interferometry, thus giving us confidence in our diagnostics and analysis techniques. As in the interferometry data, the electron density decreases monotonically in the case without B-field, but shows an extended density profile up to 10 mm in the case with an applied 20 T field.

The electron temperature in Fig. 1.15a peaks at $50-80\,\mathrm{eV}$ and then decreases with distance from the target. In the case without B-field, the temperature drops below the diagnostic
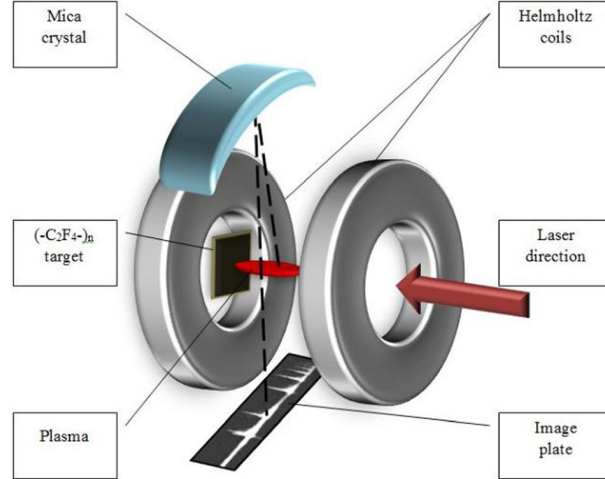
Figure 1.14.: Schematic representation of the FSSR X-ray spectrometer field of view with respect to the plasma dynamic. The FSSR is looking at the plasma dynamic transversally with respect to the magnetic field lines orientation (aligned with the laser axis) and so the jet propagation.

resolution around 3 mm. On the other hand, with a 20 T B-field the electron temperature drops to ~ 10 eV around 4 mm and then stays relatively constant for many millimeters. Another feature in the 20 T case is a small increase in temperature around $1.5 - 2$ mm as compared to the 0 T case. This location is similar to the location of the cavity after its early collapse around 20 ns as seen from interferometry (see Fig. 1.15) and with the increased optical emission from the SOI; this is consistent with the idea that the conical shock at the tip of the cavity leads to increased radiation emissions [Albertazzi *et al.* (2014)].
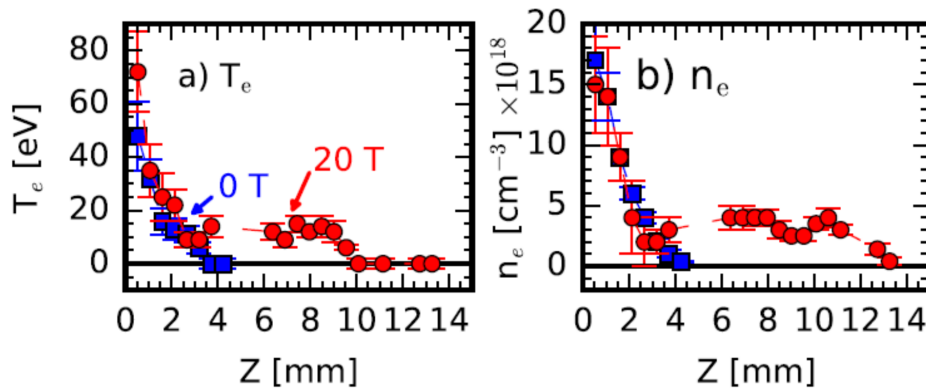
Figure 1.15.: Experimental data from the FSSR showing emission-weighted a) electron temperature and b) electron density for the cases without (squares) and with (circles) a 20 T magnetic field.

1.2.5. Insights in the collimation mechanism by a poloidal magnetic field

Having characterized the global jet structure, we further detail in this section, the mechanism responsible for this jet formation. Through the light of 3D MHD simulations using the GORGON code [Ciardi *et al.* (2007); Chittenden *et al.* (2004); Khiar (2017)], we support the previous description made on the flow collimation following the cavity formation.

Fig. 1.16 shows experimental electron density maps of laser created plasma with (left column) and without (right column) 20 T magnetic field. The bottom row present the integrated electron density, while the top row present the volumetric electron density after Abel inversion. This result is similar to the ones presented in the previous sections, but has been made during another experimental campaign, in the same laser irradiation conditions, i.e. $\lambda_{laser} = 1053$ nm; $E_{laser} = 40$ J; $t_{laser} = 0.6$ ns; $I_{max} = 1.6 \times 10^{13}$ W.cm^{-2}. It allows to stress the very good reproducibility of the mechanism, and the setup itself, when comparing those maps with the one of Fig. 1.9 and Fig. 1.8. We also note, in this case, a cleaner interferometer, with much less fringes artifact in the unwrapped electron density. The present maps exhibit, at $t = 11$ ns, the same divergent flow forming an expanding cone of $\sim 30°$ half angle, within which a decreasing electron density is observed with the distance from the target surface. This is clearly different from the $B = 20$ T case where, easily distinguishable are the shocks drawing the cavity border, as well as the conical or diamond shock at the tip of the cavity launching the long range, narrow, collimated jet.

We put these experimental maps in relation with the simulated ones presented in Fig. 1.17. They present simulations from the 3D Eulerian, radiative (optically thin approximation), resistive Magneto-Hydro-Dynamic (MHD) code GORGON with an initially uniform 20 T magnetic field in the direction perpendicular to the target surface plane. The initial laser deposition (up to 1 ns on a carbon target) is modeled in axisymmetric, cylindrical geometry with the two-dimensional, three-temperature, radiative (diffusion approximation), Lagrangian, hydrodynamic code DUED [Atzeni *et al.* (2005)], which is then passed to GORGON. The purpose of this hand-off is to take advantage of the capability of the Lagrangian code to achieve very high resolution in modeling the laser-target interaction. In Fig. 1.17, the volumetric electron density is represented in $log_{10}(ne)$ [cm^{-3}] at three different times, 2, 10, and 30 ns. We note the striking morphology similarity between the middle map, at $t = 10$ ns, and the experimental result presented in Fig. 1.16a. Here again, the formation of a cavity, delimited by a shock (visible in those maps by an enhanced electron density), is clearly seen. This cavity redirects the flow to a conical shock at the tip of the cavity.

Fig. 1.18(a) allows to show the pressure equalization at the border of the cavity, where the dynamical pressure $\beta_{dyn} = \rho v^2 / \frac{B^2}{2\mu_0}$ is represented with the blue colormap, while the
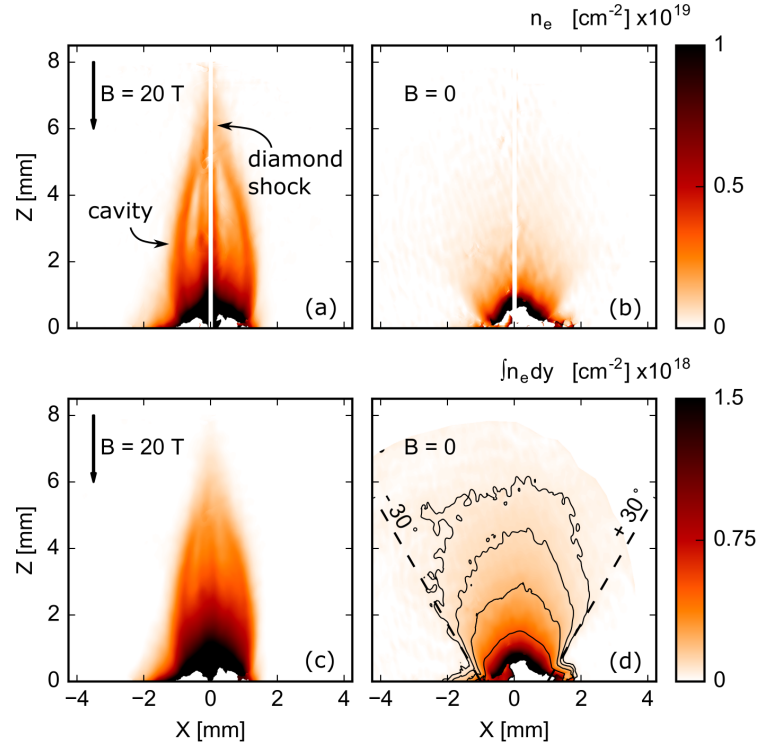
Figure 1.16.: (a) and **(b)** Laboratory electron volumetric density maps, in [cm^{-3}], after Abel inversion of the electron integrated density retrieved via interferometric measurement, at 11 ns after the start of the plasma expansion. A 150 μm diameter central region is voluntarily removed from the maps because of the unphysical values created by the Abel inversion near the inversion axis. **(a)** With a 20 T poloidal magnetic field parallel to the main plasma expansion axis (i.e. along z ; z = 0 being the target surface). **(b)** Without any magnetic field applied. **(c)** and **(d)** Same as (a) and (b) but displaying the integrated density in [cm^{-2}]. In **(d)**, the four contours display, going from bottom to top, integrated electron density of 5×10^{17}, 2×10^{17}, 1×10^{17} and 5×10^{16} cm^{-2} respectively. The straight black dashed lines are representative of a 30 degrees half angle expansion flow. The vertical black arrows indicate the magnetic field direction.
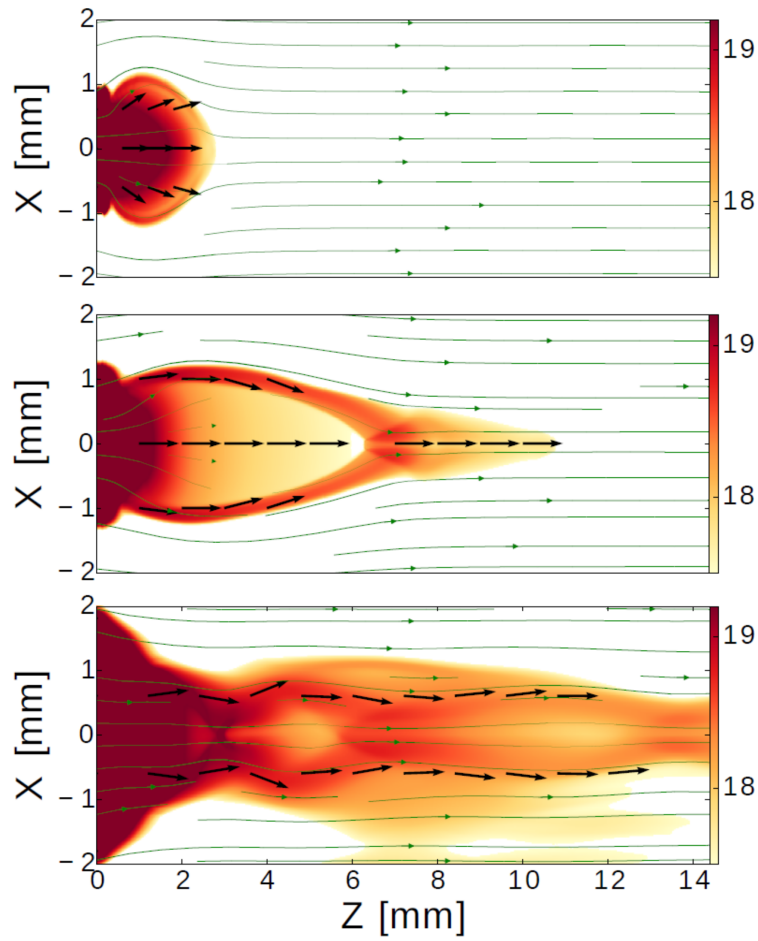
Figure 1.17.: GORGON simulated volumetric electron density maps at three different times: from top to bottom, 2, 10 and 30 ns after the start of the plasma expansion. The scale is in $log_{10}(ne)$ [cm^{-3}]. These simulations have been made by B. Khiar, and are presented in his Ph.D. thesis [Khiar (2017)].
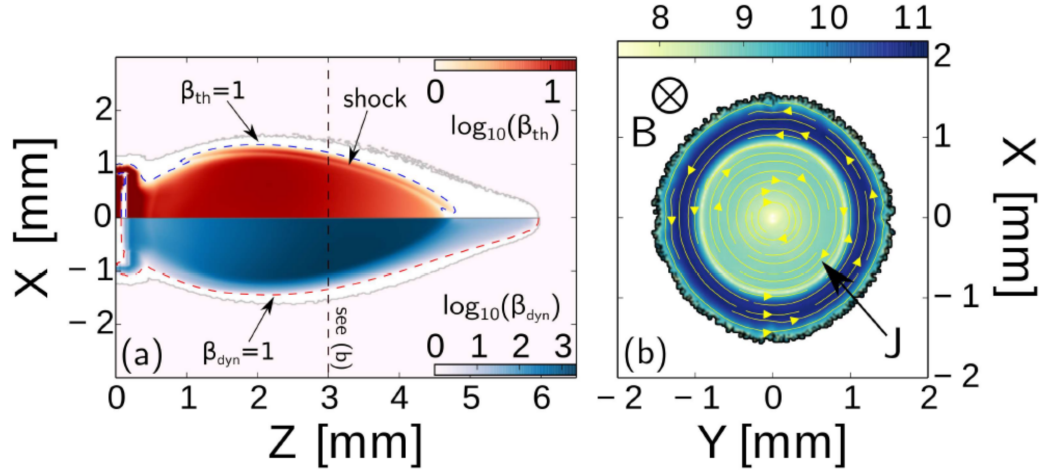
Figure 1.18.: Pressure and electrical current within the diamagnetic cavity at $t = 8\,\text{ns}$. **(a)** Side map of the thermal beta $\beta_{th} = {P_{therm}}/{P_{mag}}$ (red colormap) and dynamic beta $\beta_{dyn} = {P_{dyn}}/{P_{mag}}$ (blue colormap). **(b)** Front map of the electrical currents in $log_{10}(j)\,[\text{A.m}^{-2}]$. This work has been made by B. Khiar, and is presented in his Ph.D. thesis [Khiar (2017)].

thermal pressure $\beta_{th} = {n(Z+1)kT}/{\frac{B^2}{2\mu_0}}$ is represented with the red colormap. It is clearly seen in Fig. 1.18(a) that the border of the cavity corresponds to the pressure balanced point $\beta_{dyn} = 1$ and $\beta_{th} = 1$, highlighted by the red and blue dashed lines respectively. This pressure equilibration is made possible by the transport of the magnetic field lines with the plasma flow. Indeed, the hot expanding plasma has a relatively high conductivity, and thus a high magnetic Reynolds number ($\mathbb{R}_m > 100$); thus, the magnetic diffusion is low and the magnetic field is "frozen-in" the plasma as predicted by ideal MHD. The dynamic beta being above unity at the early expansion stage (see for instance Tab. 1.1), the plasma carries in its motion the magnetic field line. Inside the cavity, the betas are large due to the low magnitude of the magnetic field, which is expelled out of this region. Here, we shall note that the "frozen-in" regime is a purely MHD effect, for a highly conductive plasma. This regime consists of saying that MHD fluid particles are linked to the magnetic field lines such a way that the former stay on the same field line all along the evolution of the system. The Alfvén theorems (the first one - through the constant magnetic flux theorem, and the second one -through the advection term of the magnetic field induction equation) allows to highlight the notions of magnetic field lines and "frozen-in" regime within such highly conductive plasmas. In the present description, the highly conductive characteristic of the plasma is ensured by having a large magnetic Reynold number.

The key parameter to look at in such a regime is then the β parameter (dynamic and/or thermal one) in order to understand which one, from the plasma or the magnetic field, is advecting the other (i.e. $\beta > 0$: the plasma advects the magnetic field lines. $\beta < 0$: the magnetic field lines advects the plasma). When carrying the magnetic field lines in its

motion, the plasma bends them (creating magnetic tension through rotational of the field $(\boldsymbol{B} \cdot \boldsymbol{\nabla}) \times \boldsymbol{B}/\mu_0$) and compresses them (creating magnetic pressure, $-\boldsymbol{\nabla} \parallel \boldsymbol{B} \parallel^2 /2\mu_0$), thus it participates in creating a magnetic gradient that participates in slowing down the plasma flow. Indeed, through the magnetic gradient, strong electrical currents are created $\boldsymbol{J} = (\boldsymbol{\nabla} \times \boldsymbol{B})/\mu_0$. In return, this creates strong magnetic forces $\boldsymbol{F}_m = \boldsymbol{J} \times \boldsymbol{B}$ that act against the plasma propagation. Those strong electrical currents are displayed in Fig. 1.18b. Finally, the plasma flow, stopped at the cavity wall, creates a shock (see the second peak of β_{th} near $\beta_{th} = 1$, inside the cavity of Fig. 1.18).

A signature of the shock is the electron density increase at the cavity edge shown in Fig. 1.16 or Fig. 1.17.It is also seen as an electron temperature increase measured with the FSSR (see Fig. 1.27 gray $\times$ -without B field- and black $\bullet$ -with B field- in a lower laser energy cases. This figure allows, due to the zoom, to appreciate the electron temperature difference between *with* and *without* B-field in the $z = 0 - 4\,\mathrm{mm}$ region). Finally the plasma slides along the cavity border to finally be redirected (following the pressure balanced point) at the tip of the cavity. It results from this diamagnetic cavity formation that a conical shock forms (well visible at $x = 0$; $z = 6 - 7\,\mathrm{mm}$ of Fig. 1.17 middle). It launches a flow, the momentum of which is henceforth directed along z.

The radius of the cavity can be evaluated by reasoning on the pressure balanced. This has already been done by Matt, Winglee, and Böhm (2003) in the context of an astrophysical central wind collimated by a poloidal magnetic field and has been transposed to a laser plasma expansion context by Ciardi *et al.* (2013). For an initial plasma, diluting hemispherically in the vacuum, we expect that the maximum radial extent of the cavity, R_c, will vary as a function of the total plasma pressure $P_k = f\mathcal{E}_L/V$, where f is the laser absorption, $\mathcal{E}_L$ is the laser energy and $V = \frac{2}{3}\pi R_c^3$ is the volume of a hemisphere, versus the magnetic pressure P_m. Here the laser absorption f is simply the ratio of the radially directed kinetic energy to the laser energy and does not include other energy channels (e.g. radiation) and thus should not be used to understand the absolute laser absorption. Considering a hemispherical expansion, this gives a relationship of $B^2/2\mu_0 = f\mathcal{E}_L/\frac{2}{3}\pi R_c^3$ and the solution for the radial extent R_c:

$$R_c = \left(\frac{f\mathcal{E}_L}{\frac{2}{3}\pi}\frac{2\mu_0}{B^2}\right)^{1/3} \tag{1.4}$$

The time necessary for the collimation to occur can be found as $t_c \sim R_c/v_{flow}$. As a raw estimate, the expansion speed of the laser-created flow can be taken from [Tabak *et al.* (1994)]: $v_{flow}(\mathrm{cm.s}^{-1}) = 4.6 \times 10^7 I^{1/3}\lambda^{2/3}$ (where I is the Laser Intensity in units of $10^{14}\,\mathrm{W.cm}^{-2}$ and λ is the laser wavelength in μm).

Looking at this magnetic constraint on the plasma in forcing it to flow along a preferential
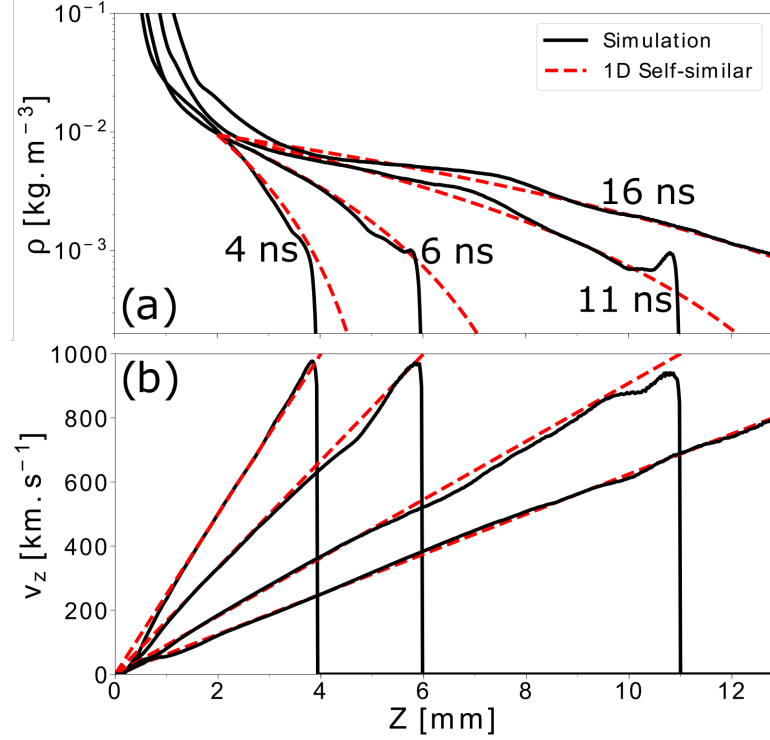
Figure 1.19.: GORGON longitudinal density profiles (top) and velocity (bottom) compared to a 1D self similar expansion, at different times. The profiles are made via an averaged around the z-axis over a radius of $700\,\mu$m. This work has been made by B. Khiar.

direction (z), one could think about a reduction of an initial 3D expansion within a simply 1D expansion. It is striking to understand how good is this intuition. Fig. 1.19 represents, with solid black lines, longitudinal (along z) density and velocity profiles taken from the GORGON simulations and averaged around the z-axis over a radius of $700\,\mu$m. The red dashed lines represent a 1D self-similar analytical solution. As one can see, the GORGON results and 1D results match quite well. However, it necessary to precise that the 1D solution presented here is neither a purely adiabatic solution, nor a purely ballistic expansion. It is actually made of a combination of both approaches. Indeed, while the density profiles are taken from the self-similar adiabatic solution ($\rho = \rho_0 \left(1 - \frac{\gamma-1}{\gamma+1}(1 + \frac{z}{c_{s0}t})\right)^{2/(\gamma-1)}$), the velocity profiles take their origin within a Lagrangian ballistic solution ($v = z/t$). This combination of both should be attributed, somehow, to the specificity of the laser heating of the target, as well as to the non infinite plasma reservoir created by the way of the laser and the boundary conditions (in the z negatives) associated to it, while the self-similar solutions, by definition, assume the target to be a semi-infinite reservoir. We also stress that the adiabatic solution for the density matches well the simulated data starting from $z = 2$ mm, i.e. z in the adiabatic solution described above should be replaced by $z + 2$ [mm]. Moreover, the initial density ρ_0 start at $\sim 10^{-2}\,$kg.m^{-3}, far below the solid density ($\sim 3.5 \times 10^3\,$kg.m^{-3} for the carbon). The

density upstream abruptly increases to reach the solid density (N.B. the initial target surface in the simulation is situated at $z = 0.5\,\text{mm}$). Actually, regarding the density, it reacts as if the initial reservoir was situated between $z = 0$ and $z = 2\,\text{mm}$, with a behavior below that latter point being obviously different from the self similar solution. It is likely in this area that the boundary condition acts on the density profiles, as well as provides an acceleration mechanism that finally results in this combination of ballistic ($v = z/t$) and adiabatic solutions.

1.2.6. Fidelity of jet creation across a variety of plasma condition

To explore the fidelity of plasma collimation across a variety of plasma conditions, we varied the laser energy incident on the target, the magnetic field strength, the target material, and finally by implementing a second heating via a second laser pulse delayed in time compared to the main laser pulse. Each of these variations show quantitative differences in jet and cavity formation, however the qualitative behavior is similar across the variety of conditions, which thus highlights that the collimation of plasma with strong axial magnetic field is a consistent and repeatable phenomenon.

1.2.6.1. Variable laser intensity

The laser intensity was adjusted by varying the laser energy from 3, 6 and 16 J corresponding to laser intensities of 1.3, 2.6 and $6.9 \times 10^{12}\,\text{W/cm}^2$, respectively. The electron densities of these different irradiation conditions are shown in Fig. 1.20 at 10 and 28 ns. At early times (10 ns) the differences between the pulses are clear as both the radial and lateral extents of the cavity increase as a function of the laser intensity. At the later time (28 ns), all of the plasmas have formed a high-density region close to the target with a collimated jet extending over a long distance. Thus while there are quantitative differences among the jets, the qualitative form remains the same.

To understand how increasing the kinetic energy of the plasma changes its expansion in the magnetic field, the radial extents of the cavity for the different cases are plotted as a function of laser energy in Fig. 1.21. The values are taken at the location where the density reaches 10% of the peak density at a distance of $z = 1\,\text{mm}$ from the target at 10 ns. The solid line in Fig. 1.21 represents eq.1.4 with a constant absorption fraction of 12%, in agreement with our previous expectations [Ciardi *et al.* (2013)].

Here, even for a laser energy varying from one case to the other, the cavity radius is examined at the same time (i.e. 10 ns). This can be justified by the fact that varying the laser energy will vary the internal energy of the plasma, and then the point for which the pressure balanced occurs, $R_c \propto \mathcal{E}_L^{1/3}$, but this is done by varying the expansion velocity:
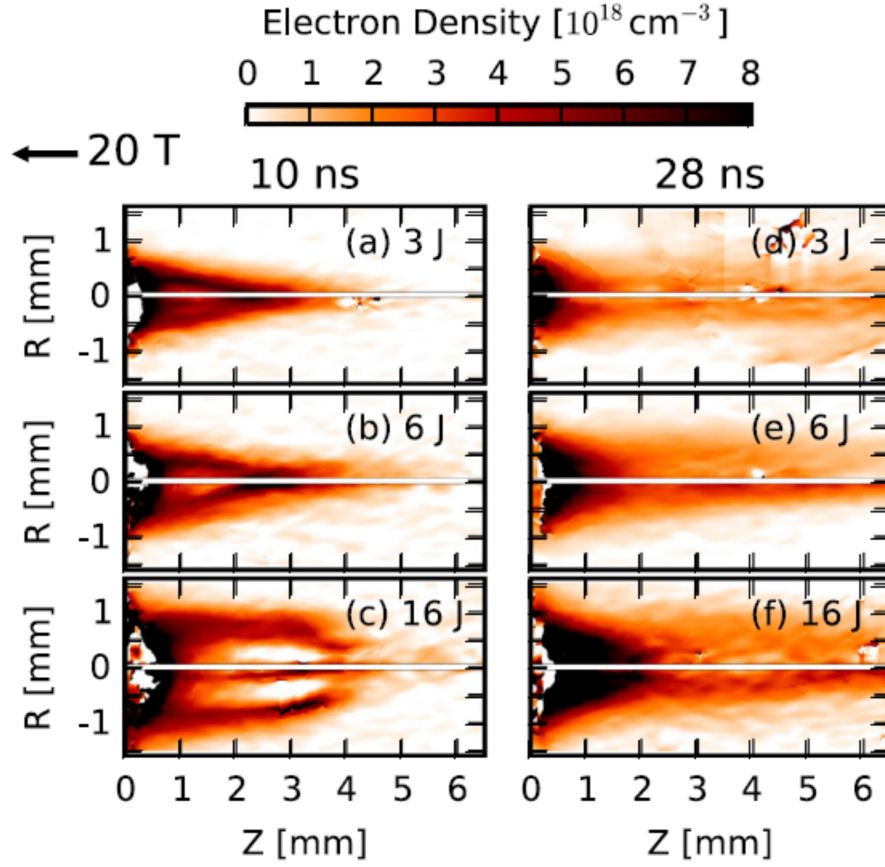
Figure 1.20.: Electron density for laser irradiation energies of (top) 3 J, (middle) 6 J and (bottom) 16 J. The left side corresponds to 10 ns and the right side to 28 ns after the main pulse irradiation.
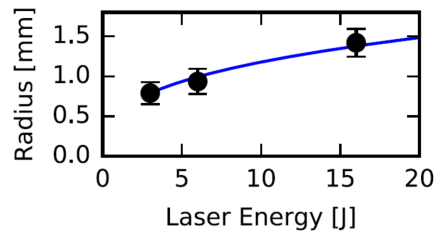

Figure 1.21.: The radius of the cavity (at 10% of the peak density) at $z = 1\,\mathrm{mm}$ from the target for different laser irradiation energies. Error bars are defined as the difference between the radius at 50% and 10% of the peak density. The solid line is from eq.1.4 with a constant absorption of $f = 12\%$.

$v_{flow}(\text{cm.s}^{-1}) = 4.6 \times 10^7 I^{1/3} \lambda^{2/3} \propto \mathcal{E}_L^{1/3}$ if τ_{laser} is a constant. Thus, if we look at the time necessary for the collimation to occurs, $t_c \sim R_c/v_{flow}$, we have $t_c \propto \mathcal{E}_L^{1/3}/\mathcal{E}_L^{1/3} = constant$.

1.2.6.2. Variable magnetic field strength

By varying the applied voltage in the coil assembly with the capacitor bank, we can vary the ambient magnetic field strength. We explore in this section 6, 20 and 30 T, for which electron density maps are presented in Fig. 1.22. Here, the laser irradiation conditions are similar between the three cases, and thus, the expansion velocity are similar: $v_{flow}(\text{cm.s}^{-1}) = 4.6 \times 10^7 I^{1/3} \lambda^{2/3}$. This is why the electron maps in Fig. 1.22 are presented at different times. Indeed, because we expect, from eq.1.4, the cavity radius to evolve as $B^{-2/3}$, and that B is the only parameter to vary here, the time necessary for the collimation to occurs is $t_c \sim R_c/v_{flow} \propto B^{-2/3}$. For instance, the collimation time at $B = 6$ T is 2.2 times longer than at $B = 20$ T, i.e. $(\frac{20}{6})^{-2/3}$. In the same way, the collimation time at $B = 30$ T is 1.3 times longer than at $B = 20$ T, i.e. $(\frac{30}{20})^{-2/3}$. Then starting from the case at $B = 20$ T (Fig. 1.22b) presented at $t_{20T} = 11$ ns, the case at $B = 6$ T (Fig. 1.22a) is presented at $t_{6T} = 23$ ns $\approx 2.2 \times t_{20T}$. However, due to experimental constraints in the probing times, the case at $B = 30$ T (Fig. 1.22c) is presented at the same time as the 20 T case, i.e. $t_{30T} = 11$ ns instead of $t_{30T} = 11/1.3 = 8.5$ ns. This time however, stays close enough to the one effectively investigated for the cavity radius comparison that we want to realize. Fig. 1.23 presents the cavity radius measured from the interferometry maps of Fig. 1.22 (black dots) and the fit with the formula of eq.1.4 (blue curve).

Of great interest is to say that we observe similar jet characteristic on between all the cases, i.e. similar formed jet radius, density, temperature and velocity. This is due to the specific shaping of the cavity including at its tip a convergence of the plasma flow onto the axis. As a consequence, all the mass flux is redirected onto this axis (at different distance and different time depending on the chosen parameters) inducing a similar diamond shock, leading to similar flow redirection and heating.
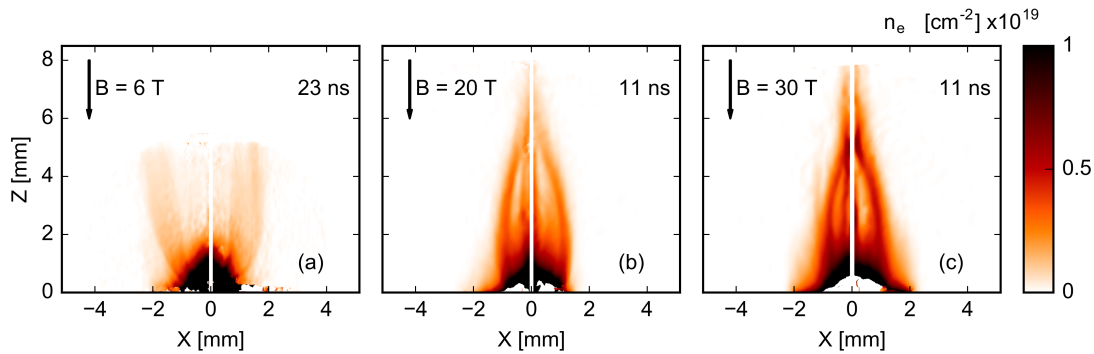
Figure 1.22.: Electron density for magnetic field strength of (a) 6 T at 23 ns, (b) 20 T at 11 ns, and (c) 30 T at 11 ns
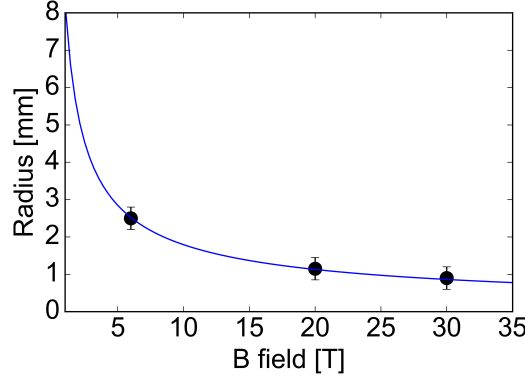
Figure 1.23.: The radius of the cavity as a function of the magnetic field strength (black dots). The blue curve follows the law described in eq.1.4.

1.2.6.3. Target composition

In order to explore the effect of the target material (Z) on the collimation mechanism it is possible to vary the target material. Fig. 1.24 shows electron density maps for two different materials. It proposes a comparison between a Lanthanum Fluoride target (LaF_3) at $t = 23\,\text{ns}$ (Fig. 1.24**(b)**), and a cavity from a Teflon target (CF_2) at $t = 24\,\text{ns}$ (Fig. 1.24**(b)**). We detail hereafter the characteristic of both materials:

CF_2: $\qquad Z_C = 6;\ Z_F = 9 \qquad \implies \overline{Z} = 8$

$\qquad\qquad A_C = 12;\ A_F = 19 \qquad \implies \overline{A} = 16.7$

LaF_3: $\qquad Z_{La} = 57;\ Z_F = 9 \qquad \implies \overline{Z} = 28$

$\qquad\qquad A_{La} = 139;\ A_F = 19 \qquad \implies \overline{A} = 65.4$

Despite the important difference in Z of both materials, the cavity does not look so different at the times displayed in Fig. 1.24. The peak density of the cavity border is approximately located at the same radius for both materials, i.e. $r = 0.75\,\text{mm}$. We note a stronger electron density in the map presented here (see in particular the cavity border) in the case of the LaF_3 target, that can be imputed to the higher Z of the La component that allows more electron to be released.

A complete time sequence (not available here) is necessary to understand the full cavity formation dynamic, and in order to highlight the differences between the two materials. We note the cavity dynamic analysis (n_e, R_c, t_c etc.) to be a very good manner to highlight some fundamental resultants of the laser-solid interaction (in the moderate laser intensity regime) for different kind of materials. Indeed, the cavity resulting from the balanced between plasma pressure (kinetic and thermal) with the magnetic pressure, for a constant applied magnetic pressure, the difference in the cavity shape for different materials should be the resultant of a difference in plasma pressure. Thus the problematic of laser absorption for varying the Z of the material, the expansion mechanism that transforms the thermal
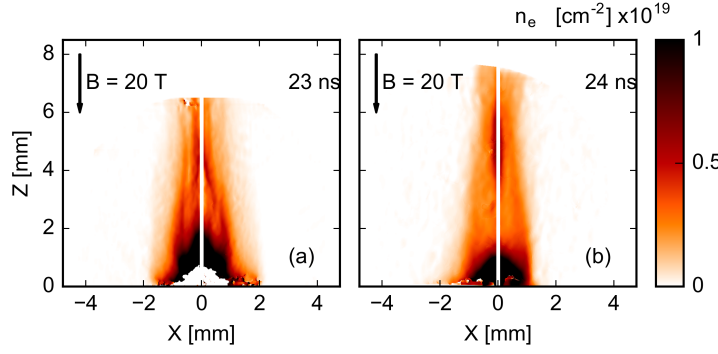
Figure 1.24.: Electron density for **(a)** a Lanthanum Fluoride target (LaF_3) at $t = 23\,$ns, and **(b)** a Teflon target (CF_2) at $t = 24\,$ns. The magnetic field strength is 20 T in both cases.

pressure into the ram pressure, or the cooling by radiation, could be investigated by analyzing in detail the cavity shape and its evolution in time.

1.2.6.4. Temporal staging of the plasma heating

We are interested in this section in introducing two separated heating sequences (still via laser irradiation) of the plasma, delayed in time, in order to study the viability of collimation under the influence of time-variable plasma ejections. The two separated heating sequences are made possible by splitting temporally the main irradiation beam. The latter was separated by either 9 or 19 ns, and subsequently recombined collinearly using nonpolarizing beam splitters and focused on target, as previously (diameter, $\phi_L = 0.7\,$mm) using the same lens and random phase plate. In the temporally staged configuration, the first beam, called the precursor, had an on-target energy (intensity) of 3 J ($1 \times 10^{12}\,$W.cm^{-2}) and the second pulse, called the main pulse, had 17 J ($7 \times 10^{12}\,$W.cm^{-2}). Additionally, a main-pulse-only setup (i.e., identical but without the precursor) was used for comparison. This staged heating setup is represented in Fig. 1.25.

The top row of Fig. 1.26 shows the plasma electron density n_e at three times in the main-pulse-only case. As already described in the previous section, the plasma dynamics consist of three distinct phases: (i) creation of a low density cavity surrounded by a shock envelope through the pressure balanced process (Fig. 1.26**a**), (ii) formation of a conical shock (Fig. 1.26**d**) at the tip of the cavity, which then (iii) recollimates the plasma plume into a jet (Fig. 1.26**g**). These phases are also captured in the MHD simulations shown in Fig. 1.29. The next two rows in Fig. 1.26 show n_e maps in the two laser-pulse cases with either 9 or 19 ns delay between the precursor and main laser pulses.

We note, in the temporally staged heating cases, a similar cavity formation as in the case without precursor. However, while the general flow structure is similar with and without precursor irradiation, it is clear that adding a precursor laser pulse crucially modifies the

dynamics and physical characteristics of the plasma in the cavity. Electron density maps taken at the same time (10 ns) after the arrival of the main pulse (Fig. 1.26**a**–**c**) show the cavity becoming more spherical when the precursor laser pulse is used. The relatively small, 14%, increase in the radial extent of the cavity is accompanied by a considerable reduction in its longitudinal extent: from 4 mm with the main pulse only to around 2.5 mm with the addition of the precursor offset by 19 ns. We notice that in the two-pulses configurations higher n_e is measured ($2 \times 10^{19} \, \text{cm}^{-3}$) along the shocks bounding the cavity (see, in particular, Fig. 1.26**d**–**f**), a clear sign that shocks are stronger. This agrees with the Te measurements shown in Fig. 1.27, which are larger with temporally staging.

Additionally, as shown in Fig. 1.28, optical emission inside the cavity ($z < 2 \, \text{mm}$) is clearly enhanced, both in intensity and duration, when adding the precursor. Non-local thermodynamic equilibrium calculations of photon absorption in the visible range (400–550 nm), corresponding to the S20 cathode response, for a CF2 plasma show that above $Te = 10 \, \text{eV}$ and below $n_e = 10^{19} \, \text{cm}^{-3}$ the photon mean-free path is greater than 30 mm, indicating an optically thin regime in this range. Given the high Te and given that optical emission decreases with temperature in this regime, the brighter areas seen in Fig. 1.28 indicate the presence of denser plasma, consistent with the interferometric data.

Differences in the plasma properties and flow dynamics when introducing the precursor pulse can be understood by considering the location in the precursor plasma where the
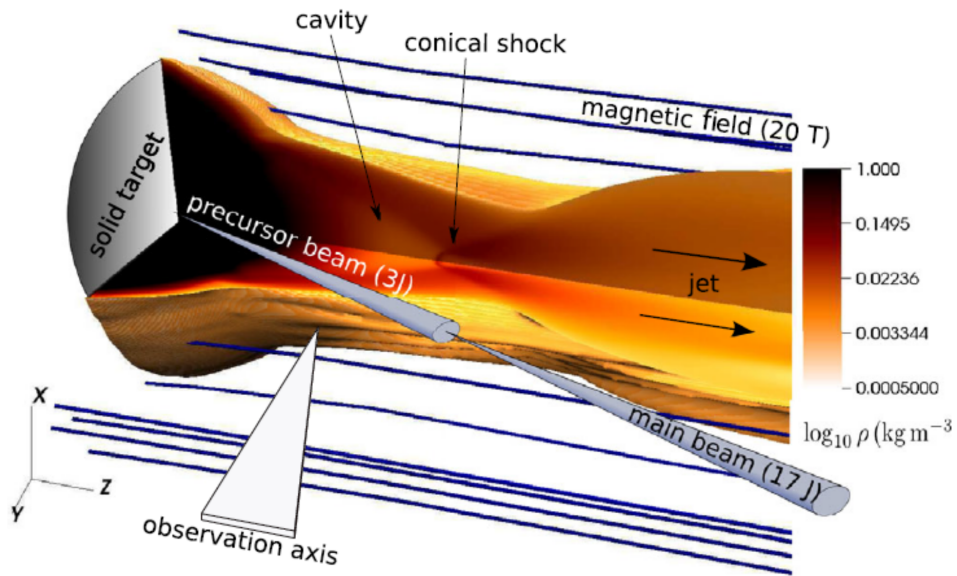
Figure 1.25.: Schematic of the staged heating experimental setup and 3D MHD simulations of the overall plasma dynamics. The volume rendering shows the simulated mass density at 22 ns, for the case of a single 17 J pulse, with 1/4 of the volume removed to show the internal flow structure. Two collinear laser pulses (3 and 17 J), that are temporally offset by either 9 or 19 ns, irradiate a CF_2 target embedded in a 20 T magnetic field. The diagnostic observation axis is also shown.
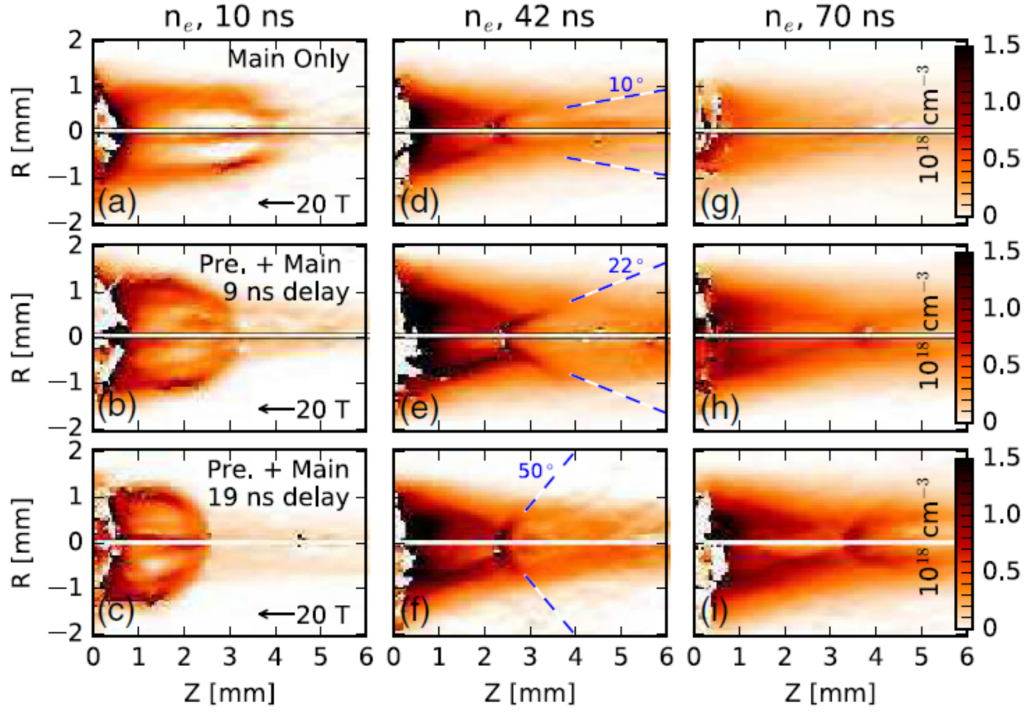
Figure 1.26.: Plasma electron density measured via interferometry, and analyzed using Abel inversion [29,30], in pseudocolor with identical color scales as shown on the right. The central pixels are removed due to the uncertainty of the Abel inversion on axis. Notice that the images appear very symmetric. The three columns show times of 10 (a–c), 42 (d–f), and 70 ns (g–i) measured from the beginning of the main pulse irradiation. The top row (a,d,g) shows the case of main pulse alone, the middle (b,e,h) and bottom (c,f,i) rows show the temporally staged cases of 9 and 19 ns delay, respectively.

energy of the main laser pulse is absorbed. Fig. 1.29(a) shows the simulated density produced by the precursor pulse at the time of the arrival of the main pulse (considering 19 ns separation). The fast expansion of the plasma in the z direction (100–500 km/s) causes rapid changes in the longitudinal n_e profiles. These are shown in Fig. 1.29(d) at three different times for both the magnetized (solid lines) and an unmagnetized (dashed lines) case of precursor irradiation. In the figure, regions where n_e is in the range from 0.1 to $1.0 n_c$, where $n_c = 10^{21}\,\mathrm{cm^{-3}}$ is the critical density of the laser, are highlighted with thicker red lines; in this region over 90% of the laser energy from the main pulse is absorbed. From this plot it is clear that the n_e profiles for the unmagnetized and magnetized cases are essentially identical up to 50 ns with substantial differences arising only in the low density regions where laser absorption is insignificant. The applied 20 T magnetic field thus does not alter the absorption of the main laser pulse and only plays a role in the plasma dynamics following the laser absorption. Nonetheless, because of the expansion of the precursor plasma, the region over which most of the main laser is absorbed moves away from the initial target surface and increases in longitudinal extent L_{abs} as well as volume, $V_{abs} \sim L_{abs}\phi^2$. Thus, the absorbing plasma becomes more cylindrical
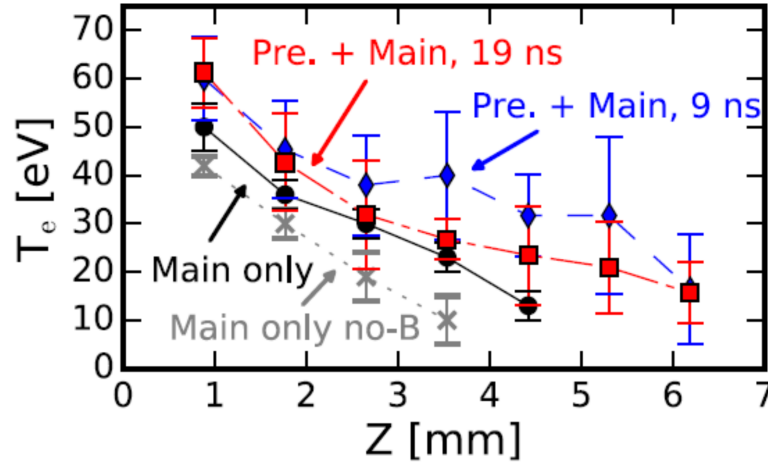
Figure 1.27.: X-ray spectrometry measurements of Te from the FSSR. Lines with circles (×'s) represent the main-pulse-only setup with (without) an applied 20 T B field. Lines with diamonds and squares show cases with a precursor of 9 and 19 ns delay, respectively.

and has lower thermal pressure ($\sim E_L/V_{abs}$), when using two pulses and for longer time delays. The longitudinal stretching of L_{abs} causes more plasma to be accelerated radially and the overall expansion to be more divergent. This is consistent with the experiments, which show a more spherical expansion for the double pulse cases and for longer time delays (Fig. 1.26(b) and (c)). Further corroboration comes from Fig. 1.29(e), which shows a reduction of the ratio of the longitudinal to radial kinetic energy in the main-pulse-only case compared to two pulses and for longer delays.

Collimation of the plasma plume into a jet takes place through a conical shock, which forms 2–4 mm from the initial target (Fig. 1.26(d)–(i)). The conical shock is the result of oblique shocks redirecting the plasma flow along the cavity walls and towards its tip. In particular, we find that the opening angle of the conical shock and jet depends on the laser irradiation conditions, increasing from around 10° with main pulse only to 50° for two pulses with 19 ns delay (see Fig. 1.26(d)–(f)). This variation is consistent with the cavity shape becoming more spherical: the flow converges at the tip of the cavity almost head-on. The more planar like collision leads to an increased thermalization of the flow's kinetic energy, higher temperatures, and thus more diverging flows. A similar effect is discussed in the astrophysical literature in the context of jet formation by the convergence of supersonic conical flows [Canto, Tenorio-Tagle, and Rozyczka (1988)]. Remarkably, the experiments show that the recollimating conical shock is quasi-steady state and independent of the presence of an ambient plasma or of the laser irradiation delay, and that the collimation is very effective even for more isotropically expanding ejections. These results strengthen the claim made in Ciardi *et al.* (2013) and Albertazzi *et al.* (2014) that the recollimating conical shock may be at the origin of the stationary x-ray emission detected in some jets
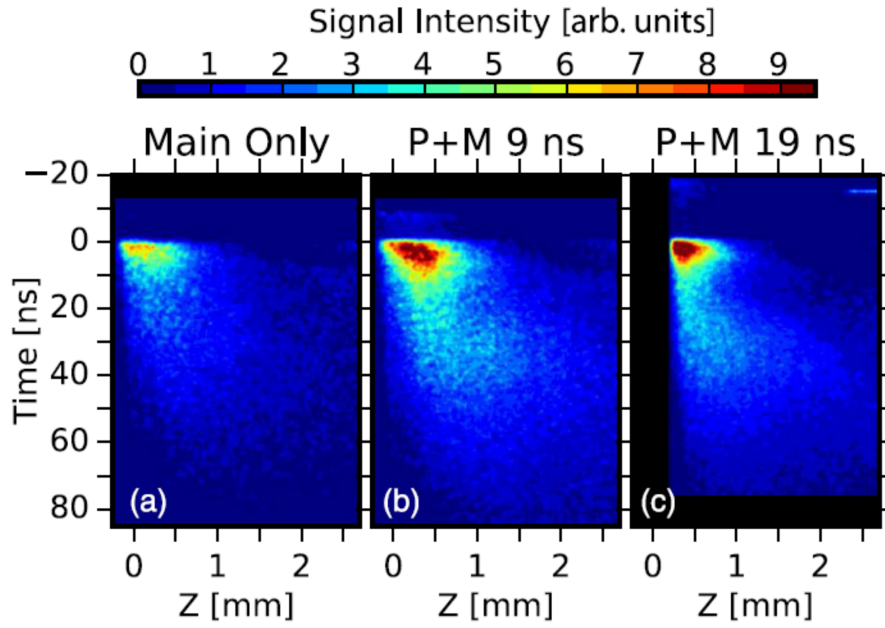
Figure 1.28.: Streaked optical emission profiles along the center of the plasma expansion axis (smoothed with a 5-pixel Gaussian) plotted with the same linear color scale for (a) the main-pulse- only case and (b) [(c)] the precursor and main pulses with a 9 ns [19 ns] delay between them. Time is measured from the beginning of the main pulse. Note the small signal from the precursor interaction in (b) [(c)] at −9 ns [−19 ns]. The profiles in (a) and (b) were taken over successive shots and with the exact same detector settings. Profile (c) was taken at a later time and thus was slightly scaled and shifted for comparison with the previous profiles. The thin streak in (c) at $t = -15\,\mathrm{ns}$, $z = 2.25\,\mathrm{mm}$ is from the interferometry probe.
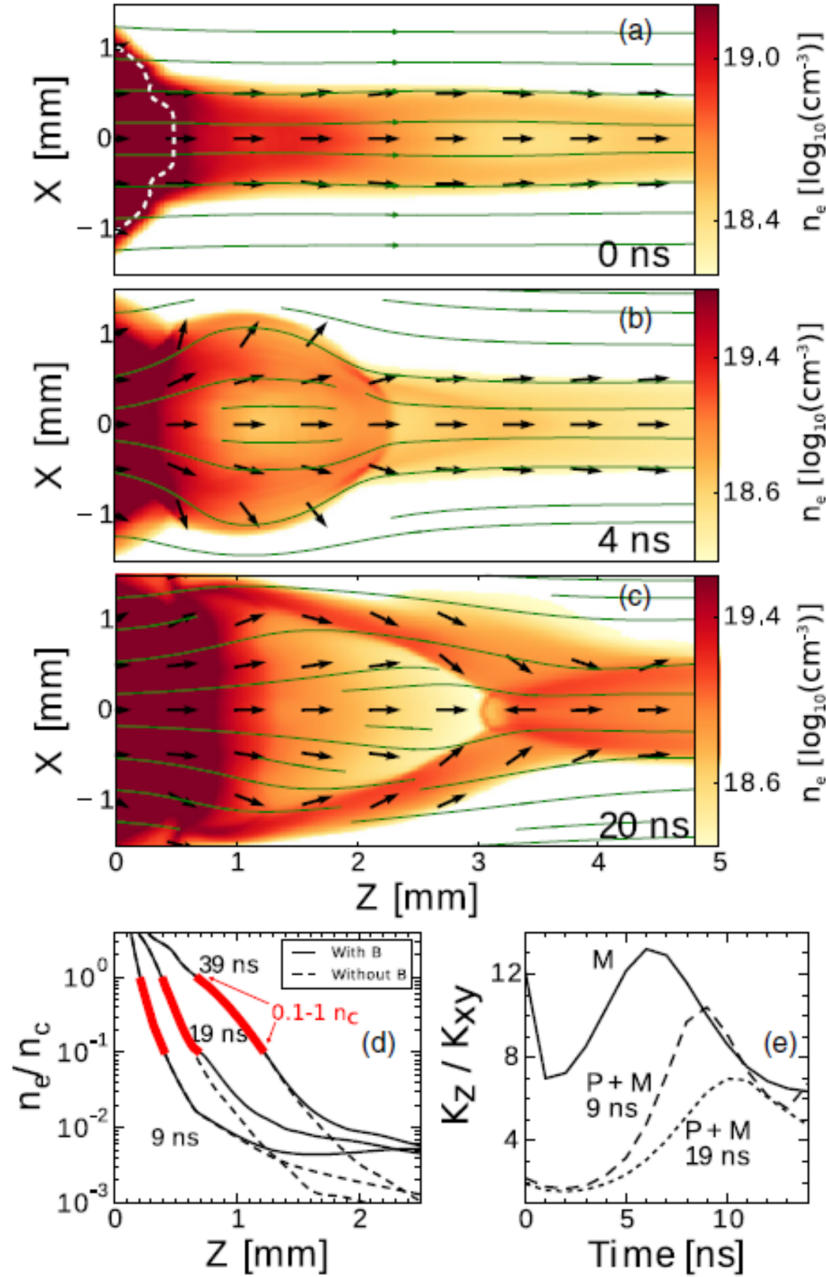
Figure 1.29.: 3D MHD simulations results. (a)–(c) Pseudocolor maps of n_e in the two-pulses configuration with a 19 ns delay. Times are measured from the main-pulse arrival. Arrows represent fluid velocity (not scaled in magnitude) and magnetic field lines are shown. Panel (a) shows the plasma created by the low energy precursor at a time just before the arrival of the main pulse. The white dashed line corresponds to the isocontour at $0.1n_c$. (d) Profiles of n_e, averaged over the laser focal spot, for a case of precursor-only irradiation at 9, 19, and 39 ns after precursor irradiation. Cases with (solid line) and without (dashed line) magnetic field are shown. (e) Ratio of longitudinal ($K_z = 0.5\rho v^2$) to radial [$K_{xy} = 0.5\rho(v_x^2 + v_z^2)$] kinetic energy integrated over the entire plasma volume, for the main-pulse-only (M) and the temporally staged cases (P + M).

from young stellar objects [Favata *et al.* (2002); Bally, Feigelson, and Reipurth (2003); Ustamujic *et al.* (2016)].

Past the conical shock, the jet properties are also modified. In addition to an increase in temperature, the simulations show that the two-pulses configuration increases the jet's mass flux (ρv_z) and kinetic energy flux ($\rho v^2 v_z/2$) by ~ 10, and create velocity variations, $\Delta v_z \sim 100$ km/s (Mach 2–3), which drive shocks within the jet itself. This is consistent with observations of astrophysical jets that indicate it is the unsteadiness of mass ejection that drives shocks (so called "knots") inside the jet body (see Frank *et al.* (2014) for a review). The results presented here thus provide a first glimpse of the effects of time variability on the formation and stability of the recollimation shock and on the jet itself.

1.2.7. Summary

The evolution of a laser-generated jet collimated via a poloidal (axial) magnetic field was investigated over long spatial and temporal scales, by observing the electron density, electron temperature and optical emission. These diagnostics were used to characterize the plasma parameters and used to identify relevant non-dimensional scaling parameters that will aid in placing these experiments in an astrophysical context and suggesting new experimental studies. We introduced the terminology of a poloidal magnetic nozzle (PMN) to clarify that, as observed experimentally, the collimation of the flow is due mostly to the formation and structure at its base, and that a magnetic field is not necessary to keep the jet collimated as it extends over long distances.

We have found that varying the laser intensity, the magnetic field strength and target material makes quantitative differences in the plasma collimation and jet formation, but that the general dynamics are very similar. We claim the cavity formation evolution to be a good experimental observable in order to establish the link with the laser absorption with a solid target (in the moderate intensity regime) as well as the mechanism of plasma expansion in a vacuum.

Regarding the temporally staged, the precursor laser pulse generates a plasma that is collimated by the magnetic field into a jet. The ensuing plasma dynamics can then be controlled by delaying the arrival of the second (main) pulse, so that its absorption occurs further away from the initial target and over larger volumes. However, even at this relatively high field strength, we see no impact of the magnetic field on the laser absorption itself, a finding that may be of particular interest to the (magnetized) inertial confinement fusion community. The time delay between the two laser pulses has clear effects on the plasma: a more divergent cavity expansion, higher electron temperatures, and stronger shocks; yet, long-lived, stable astrophysically relevant jets are still formed. This control over the flow dynamics and variability opens the door to a range of new laboratory studies related to variable accretion and ejection phenomena in astrophysics.

Finally, and in order to link better the present study to the jet formation in the general astrophysical context, it is important to discuss the magnetic field strength necessary for the collimation described in this section to occur. The experiments show that flow collimation is possible with an *initial* ram to magnetic pressure ratio of 100 (in the $B = 20\,\mathrm{T}$ case), and with a collimated jet radius of the order of the radial extension of the launching region. We could expected a similar behavior in the astrophysical case. Hence, while the magnetic field strength necessary to counter-balance the ram pressure of a typical YSO outflow should be of the order of $10 - 100\,\mathrm{mG}$ (taking standard YSO's outflow characteristics), by similarity with the experiment, we understand that a magnetic field of only $1 - 10\,\mathrm{mG}$ (reduced by a factor $10 = \sqrt{\beta = 100}$), could be enough in order to redirect the flow. Starting from a typical initial large scale magnetic field strength, before prestellar cloud compression, of $10 - 100\,\mu\mathrm{G}$, this imply an amplification, by compression of the latest during the core collapse, of only 2 order of magnitude. We note however, due to the specific shaping of the cavity (leading to similar plasma flow redirection and diamond shock at the tip of the cavity), the jet characteristic to be similar while varying the magnetic field strength. Hence, the β equal to 100 can be easily reduced when considering lower magnetic field strength, the jet radius being unchanged in the end (within the range of experimentally checked conditions going from 6 up to $30\,\mathrm{T}$).

1.3. Expansion in a tilted magnetic field: Jet formation distortion

1.3.1. Introduction

The previous section has clarified / highlighted the role that the magnetic field plays on shaping ejecta into collimated, and narrow jets of matter during the core-collapse stage of star formation. As described by Fig. 1.4, and the magnetically core-collapse scenario, we will stress here on the possible existence and influence of an angle in between the ambient magnetic field and the rotation axis of the Keplerian Disk (and so of the outflow / ejecta axis).

Recent studies suggest the necessary misalignment of the large-scale magnetic field with the core rotation axis to aid the star formation process [Hennebelle and Ciardi (2009); Joos, Hennebelle, and Ciardi (2012); Li, Krasnopolsky, and Shang (2013)]. This is because, in a perfectly aligned case, the disk formation could be completely suppressed [Li, Krasnopolsky, and Shang (2011)]. There have been thus several reported observations of an angle between outflows and the surrounding magnetic field, at different length scales [Hull *et al.* (2013); Chapman *et al.* (2013); Carrasco-González *et al.* (2010)]. Looking at the degree of collimation of the outflows, Strom *et al.* (1986) and Ménard and Duchêne (2004) highlight the preferential alignment of well collimated, bright, long-range jets with the cloud-scale (10 000 AU) magnetic field, while weaker or wider jets oppositely present a preferential misalignment. Finally, numerical studies have shown an efficiency drop regarding the ejection of mass for the systems with strong misalignment between rotation axis and large-scale magnetic field, as well as the creation, for such systems, of a clumpy outflow instead of a highly collimated jet [Ciardi and Hennebelle (2010)]. The interaction of an outflow with an ambient magnetic field, what is more when an angle exist in between both, is thus a point that requires clarification.

This is the goal of the investigations that will be reported in this section. For this, we have performed a laboratory experiment in which a wide angle expanding plasma outflow is interacting with a large-scale poloidal magnetic field having a variable orientation with respect to the outflow main axis. The overall setup is shown to be scalable to YSO outflows (see sec. 1.2 and [Albertazzi *et al.* (2014); Higginson *et al.* (2017)]). Our conclusions are that **(1)** outflows tend to align over large scales with the direction of the magnetic field, even for an initial large misalignment of their axes, and that **(2)** narrow collimation (i.e. the capability for the outflow to keep a high density over a large distance) is possible only for an initial small misalignment ($< 25°$). The latter is due to the fact that, as a result of the plasma/magnetic field interaction [Ciardi *et al.* (2013)], the generation of a diamagnetic cavity having shocked edges that redirect the flow into a narrow, long range and high density jet (Albertazzi *et al.* (2014); Higginson *et al.* (2017), and see sec. 1.2) can
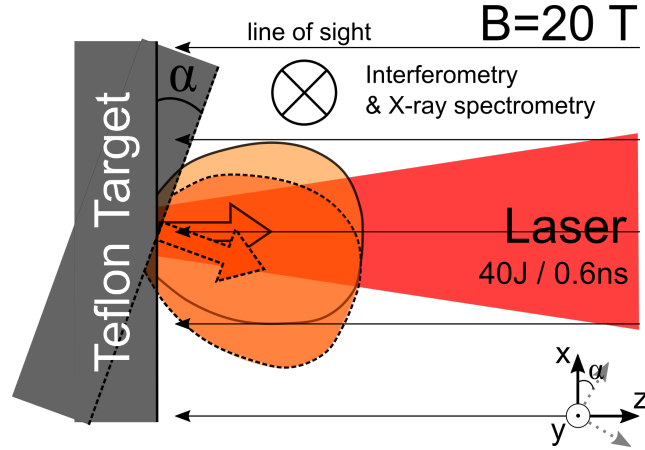
Figure 1.30.: Sketch of the tilted magnetic field experimental setup. The target is embedded in a large-scale 20 T magnetic field, and is heated by a $I_{max} = 1.6 \times 10^{13} \, \text{W.cm}^{-2}$ intensity, long pulse (0.6 ns) laser. By tilting the target, it is possible to vary the angle α between the target surface, and hence the main plasma outflow direction, with respect to the magnetic field lines. The plasma is probed along the y axis.

take place only for a small misalignment. For a large misalignment, the symmetry of the system that allows the cavity to be generated is broken and the flow cannot be redirected efficiently along the poloidal magnetic field direction. These findings are corroborated by numerical three dimensional magneto-hydrodynamic (MHD) simulations performed in the laboratory conditions and that will be detailed below. They are also consistent with the observations of the preferential alignment with the magnetic field of well collimated, long-range jets [Ménard and Duchêne (2004); Strom *et al.* (1986)], conversely to weaker and shorter jets which do not display an alignment with the magnetic field. Hence, our results provide a plausible explanation for the underlying physical mechanisms explaining the very varied morphologies (clumpy vs. collimated) of jets that have been so far observed.

1.3.2. Setup of the Laboratory Experiment

The laboratory experiment was performed at the Elfie laser facility (LULI, Ecole Polytechnique) using a chirped laser beam of 0.6 ns duration and 40 J energy, at the wavelength of 1057 nm and focused over a $\sim 700 \, \mu\text{m}$ diameter spot on a Teflon (CF_2) target. This gives a maximum intensity on target of $I_{max} = 1.6 \times 10^{13} \, \text{W.cm}^{-2}$, allowing the ablation and ionization of the Teflon (CF_2) target. The setup is identical the one presented in the previously in sec. 1.2.2. The principal modification here, as illustrated in Fig. 1.30, is the possibility by inclining the target, to vary the angle α of the magnetic field with respect to the target surface, thereby with respect to the main plasma flow direction. As previously detailed (see Fig. 1.7), in order to follow the plasma dynamics, the electron density is probed using a Mach-Zehnder interferometer and the plasma temperature is retrieved by X-ray emission spectroscopy.

1.3.3. Results of the expanding plasma density measurements

Contrarily to the *Aligned Case* (regarding the orientation of the magnetic field compared to the flow) presented in the sec. 1.2, here, by increasing the angle α, we expect the symmetry of this dynamics to be broken and hence do not use anymore Abel inversion to analyze the plasma density maps for the tilted target cases. Consequently, the maps of Fig. 1.32 for angles α of 10, 20 and 45 degrees respectively, present the electron density integrated along the probe line of sight. On these maps, a clear curvature of the expanding plasma motion is observed and two stages are clearly visible. Firstly, close to the target surface, the hot and dense plasma expands as expected, i.e. perpendicularly to the target surface, expelling out the magnetic field lines (as seen in the numerical simulations detailed below). Later on, farther from the target surface, the plasma flow is observed to be redirected along the magnetic field, the funneling tending to follow the original magnetic field axis, even at large angle, i.e. 45 degrees (Fig. 1.32(c)). The dashed white lines superimposed on the density map help guide the eyes on that redirection as they follow the center of mass, directly calculated with the density maps and assuming a constant ionization state for a given distance from the target. Even if an effective redirection of the plasma flow along the magnetic field lines is observed, however the robustness of the plasma flow collimation by the PMN mechanism(see sec. 1.2), i.e. the accumulation of matter in a jet-like structure, becomes less and less efficient. This later collimation behavior, witnessed by comparing the integrated density along the expansion axis between the with and without magnetic field cases, is investigated hereafter.

Fig. 1.31 presents experimental longitudinal lineouts of the integrated electron density (along y) and measured along the main plasma expansion axis for different magnetic field angles and at 47 ns after the laser interaction. This time is the latest time available during the experiment, and corresponds to the time when the potential jet has had the greatest chance to be stable, well formed, and well distinguishable from the magnetic free expansion. In the perfectly aligned case (Fig. 1.31(a)), the collimation along the axis is obvious, as seen by the rapid drop in electron density in the no magnetic field case (dashed lines), to compare to the flatter profile when the 20 T magnetic field is applied (solid line), which displays a higher electron density. Quantitatively, 5 mm away from the target surface, the magnetically collimated jet presents an integrated electron density 2.65 times higher than in the free expansion case, i.e. without magnetic field (see Fig. 1.31(f)). This is an indicator of the PMN efficiency in constraining the plasma to follow the magnetic field lines orientation, and so, in accumulating plasma along the central expansion axis, co-aligned with the magnetic field.

Increasing the angle α between the magnetic field lines and the target surface induces, in the magnetic field case, a decrease of the amount of plasma along the redirection axis. From Fig. 1.31(a) to (e), i.e. for increasing α, the solid lines (magnetic field cases) drop,
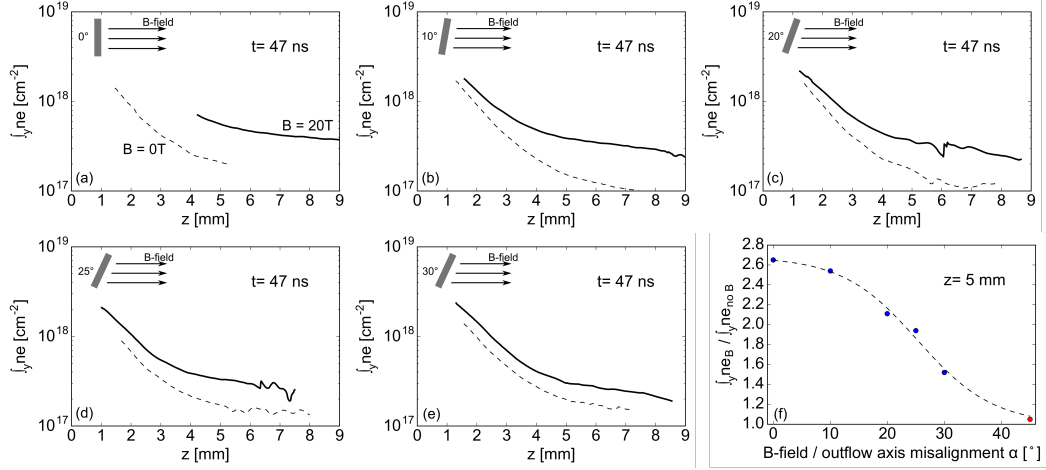
Figure 1.31.: Lineouts of the laboratory integrated plasma electron density $[\text{cm}^{-2}]$ along the plasma expansion axis (z ; $z = 0$ being the target surface) for different target angles (going from **(a)** to **(e)**, from 0 to 30 degrees respectively) with respect to the magnetic field direction, and at a time of 47 ns after the start of the plasma expansion. The axis along which the density is measured, in the case of an applied magnetic field (20 T), is voluntarily curved in order to follow the main plasma expansion direction, i.e. following the location of the center of mass (see Fig. 1.32). The solid lines show lineouts of plasma expansion in the presence of the magnetic field, while the dashed lines are lineouts without magnetic field. The profiles are voluntarily stopped for small and high z. In the first case, the high electron density is unaccessible to optical probing. In the second case, the plasma flow is out of the accessible field of view, or the fringes quality is insufficient for proper analysis. **(f)** Ratio $\int_y ne_B / \int_y ne_{no\ B}$ as a function of the magnetic field angle vs the target normal, taken at $z = 5$ mm, and at $t = 47$ ns. The dashed line represents a fit of the points by a sigmoid function.

tending progressively to join the dashed lines (no magnetic field cases), the later staying similar, as expected, irrespective of α. Fig. 1.31(f) summarizes this effect by showing the ratio $\int_y ne_B / \int_y ne_{no\ B}$ as a function of the magnetic field angle, taken at $z = 5$ mm. Starting from the perfectly aligned case, the ratio decreases progressively to finally tend to the value of 1. From this experimental evidence, we infer that the broken symmetry between the plasma expansion and the magnetic field obviously disturbs the formation of the cavity and prevents any efficient confinement and collimation of the plasma in a long-range, dense and narrow jet. Looking at the integrated density, the expansion tends to be similar to the wide angle, no-magnetic field case. We should here note that the apparent jet-like structure morphology of the plasma observed in Fig. 1.32 could be seen as contradicting the observed lack of collimation. It is due in fact to leakage of plasma in the xz plane, away from the jet axis, following the magnetic field lines. This is visible in Fig. 1.32(b), in the right of the jet from $z = 8$ mm to $z = 14$ mm, and as will be further detailed below in Fig. 1.38 in the right of the jet. By increasing α, we let the parallel-to-the-target-surface plasma momentum component to be more and more co-aligned with the magnetic field orientation. In consequence, the latter plasma momentum component is increasingly free
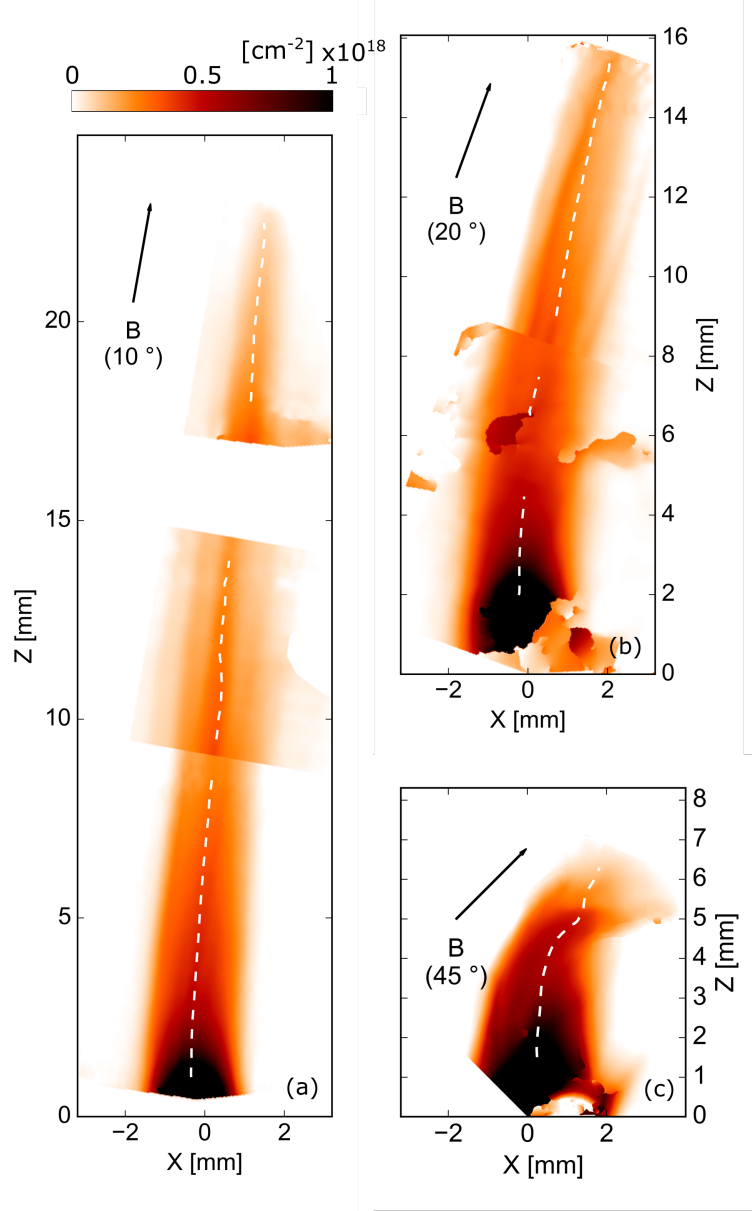
Figure 1.32.: (a) Laboratory electron integrated density in a 20 T case at 36 ns, with a misalignment of $\alpha = 10$ degrees between the target and the magnetic field. The target normal is along z. **(b)** Same as (a), with $\alpha = 20$ degrees. **(c)** Same as (a) and (b) with $\alpha = 45$ degrees, and at 16 ns after the laser interaction. In all cases, the white dashed line follow the center of mass, measured from these electron density maps, assuming a constant ionization state at a given distance from the target. The lines are interrupted when the density map is noisy or when transiting from a frame to another, in order to reconstruct the full jets. $z = 0$ represents the target surface. The black arrows indicate the magnetic field direction.

to propagate. This is discussed in more details below, in the light of 3D MHD simulations and further measurements.

1.3.4. X-ray Spectroscopy Measurement

The FSSR spectrometer (see sec. 1.2.2) was aligned to record the spectrally resolved X-ray emission of the plasma with 2D spatial resolution, though with a strong astigmatism and far larger magnification factor along the jet axis than in the transverse (spectral dispersion) direction. Knowing the scaling factors in both directions, and accounting for optical distortion of the imaging system we can reconstruct a real 2D image of the jets as recorded by the X-ray FSSR. Such images are shown in Fig. 1.33, for various values of α. These images complement and support the optical interferometry data shown in Fig. 1.32, in particular as they show the same phenomenon: the plasma initially expands normal to the source target, but later on bends, finally following the magnetic field lines direction. Similarly as for the optical interferometry diagnostic, in order to reconstruct the full plasma expansion shown in Fig. 1.33, we used different shots for which the target was located at different positions within the coil.

In Fig. 1.33, only the image retrieved from the F He 4p-1s line emission is presented, however we can state that other observed spectral lines reveal a quite similar behavior. We note that the overall plasma evolution features and distances retrieved from the interferometry diagnostic and the X-ray images, when the jet is observed to be deflected
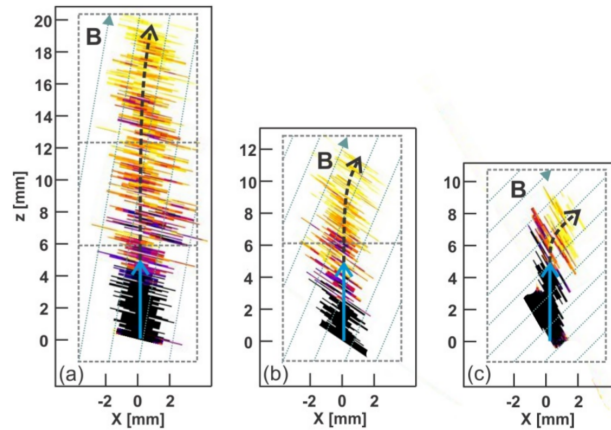
Figure 1.33.: X-ray images of the plasma jet inferred from the He line emission (transition He 4p-1s of the Fluorine ion) in a 20 T case, when the tilt of the target normal with respect to the B field lines was of **(a)** 10, **(b)** 20, and **(c)** 45 degrees. The images are the result of a combination of a few frames (shown by the dotted rectangles), each taken in a single laser shot with a target situated at different positions with respect to the diagnostic window of the magnetic coil. $z = 0$ represents the target surface. The dashed blue lines indicate the magnetic field direction.
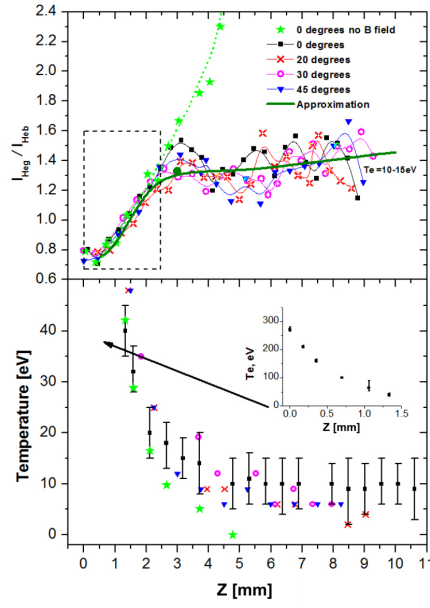
Figure 1.34.: *Top:* Fluorine $He\gamma$ to $He\beta$ lines intensity ratio measured along the jet axis for different orientations of the magnetic field, i.e. 0, 20, 30 and 45 degrees, with respect to the plane of the target and also in the case when no magnetic field is applied. The dashed rectangle delimits the range where the plasma ram pressure dominates the external B field pressure, and where the line ratios are observed to be equal for all cases, as expected.
Bottom: Corresponding time-integrated electron temperature of the jet plasma and as revealed by means of our recombining plasma model method. The inset corresponds to the region near the target surface where the temperature ranged above 50 eV.

by the magnetic field, are similar. Both diagnostics thus concur to demonstrate that the initial plasma expansion occurs normal to the target surface and is identical to the case with no B field, as detailed in sec. 1.3.3. Also, both diagnostics observe that the final jet propagation direction is imposed by the B field orientation and not by the initial outflow expansion axis.

The electron temperature along the plasma jet axis was determined analyzing the relative intensities in the F He-like line series. The method [Ryazantsev *et al.* (2016)] is based on the quasi-steady model of expanding plasmas which also takes into account a recombining plasma model with a "frozen" ion charge. The electron temperatures obtained from the relative intensities of $He\gamma$ to $He\beta$ spectral lines are shown in Fig. 1.34. While the electron temperature Te on the laser irradiated target surface is about 300 eV, it drops down to 20 eV at a 2.5 mm distance. Over this range, the lines intensity ratios and, correspondingly, the temperatures are almost the same regardless of the direction of the applied external magnetic field, or even the existence of the latest. In this initial plasma expansion zone, as was mentioned above, this can be understood as the ram pressure strongly prevails over the magnetic field pressure. Beyond this initial expansion, the presence of the magnetic field

allows in a case of perfectly aligned field and plasma expansion to keep the temperature of the formed jet almost constant in the range of 10 ± 5 eV at least for 8 mm long, consistently with our previous observations [Albertazzi *et al.* (2014); Higginson *et al.* (2017); Ryazantsev *et al.* (2016)]. This is significantly different from the case without magnetic field, in which the temperature of the jet rapidly drops below 5 eV, as the density drops below 10^{18} cm^{-3}, i.e. beyond a distance of 4 mm from the target (see Fig. 1.34). In the presence of the magnetic field, our measurements show that similar temperatures are recorded when we vary the direction of the applied magnetic field. However, we have to note that our method is not sensitive enough in the range of 0 to 10 eV temperatures, and that a high uncertainty is coming from a very low signal to noise ratio in the spectral line intensity data. Hence, although we can see that the plasma certainly stays hotter when the magnetic field is applied than without it, we can not determine with high precision significant temperature differences in the cases where the magnetic field orientation is modified.

1.3.5. Numerical Simulations

In Fig. 1.35, we show two-dimensional simulated maps of the integrated electron density along two lines of sight: perpendicular (top row: a to c), i.e. as measured in the laboratory, see Fig. 1.16, Fig. 1.32 and Fig. 1.38, and parallel (bottom row: d to f) to the magnetic field direction. The simulations are performed using the 3D MHD resistive code Gorgon [Khiar (2017); Ciardi *et al.* (2007); Chittenden *et al.* (2004)], and we present in the following, the qualitative behavior of what is observed in these simulations.

The simulated maps of Fig. 1.35 clearly highlight the fact that, as α increases, the asymmetry between the xz (top row) and yz (bottom row) planes increases. One can see the lack of collimation in the plane parallel to the magnetic field (Fig. 1.35 top row), indicating an increasingly free-expansion in this plane. This is understandable as the plasma can, in the plane containing the magnetic field, follow the magnetic field lines: the plasma momentum parallel to the target surface, which is oriented in the Y axis, is increasingly less constrained to be redirected. This is consistent with the experimental integrated electron density measurements shown in Fig. 1.32. Up to 30° (Fig. 1.35b), the flow is well redirected along the magnetic field lines, with a relatively good jet-like structure still observable. However, for larger α, i.e. 45°, the jet-like shape clearly breaks up. The momentum component the more likely to be redirected by the magnetic field being the weaker, i.e. the one parallel to the target surface (p_x), becomes unimpeded. At the same time the stronger momentum component, i.e. the one perpendicular to the target surface (p_z), increasingly encounters the magnetic field perpendicularly to it. As being the stronger momentum component, it is harder to be redirected by the magnetic field, comparatively to the weaker momentum component (p_x) in the perfectly aligned case, i.e. $\alpha = 0$. This is illustrated by the electron density maps shown in Fig. 1.35 and is further highlighted by
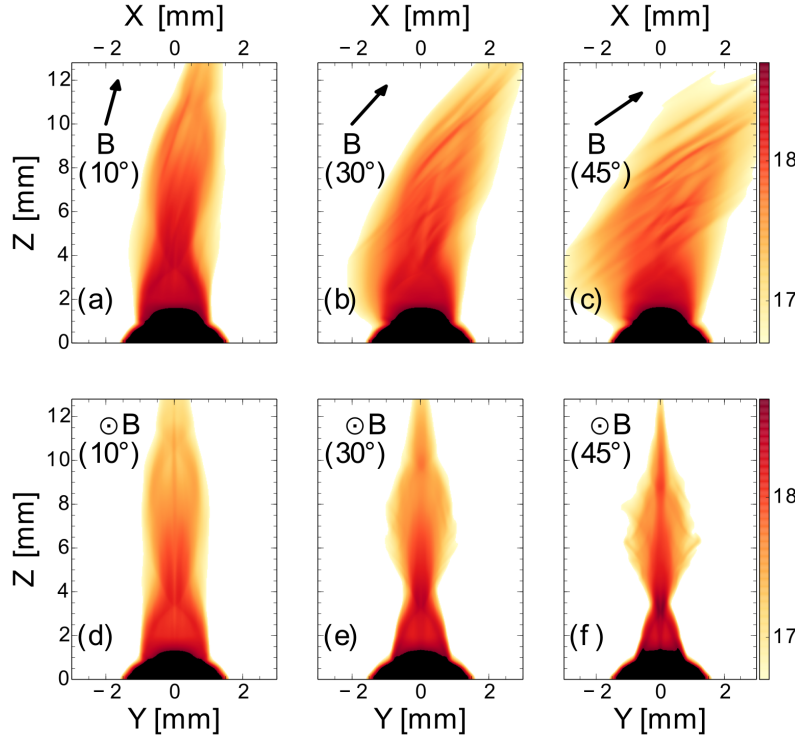
Figure 1.35.: 2D maps (in the xy and yz planes) of the decimal logarithm of the integrated electron density along either x or y of Gorgon 3D MHD numerical simulations. Figures a, b and c correspond to maps in the plane containing the magnetic field whereas figures d, e and f correspond to maps in the plane orthogonal to the magnetic field. Thus, a, b and c correspond to the laboratory measurement shown in Fig. 1.16, Fig. 1.32 and Fig. 1.38. All figures correspond to a time of 18 ns after the start of the plasma expansion. The black arrows indicate the magnetic field direction.

Fig. 1.36, where the parallel-to-the-magnetic-field momentum is plotted as a function of α. As one can see, for small α, the parallel-to-the-magnetic-field momentum is important, and the plasma flow tends to be efficiently redirected, through the PMN mechanism, along the magnetic field lines. However, for larger values of α, the rapid drop of the parallel momentum highlights the increasing lack in plasma redirection efficiency.

Looking at the plane perpendicular to the magnetic field (i.e. the yz plane of Fig. 1.35(d,e,f)), the plasma flow still looks like a collimated jet, as in this plane the fluid particles are not free to propagate across the magnetic field. Actually the jet, which is cylindrically shaped for small misalignments, as it moves away from the target progressively flattens in the plane containing the magnetic field, for increasing value of α. From a cylinder shape, clearly visible for a misalignment of $\alpha = 10$ degrees, the plasma outflow changes into a flattened sheet of plasma.

More precisely, the origin of this behavior can be understood thanks to the complete set of plasma parameters available in the simulations. First, we remark that for all angles a diamagnetic cavity is always formed during the initial expansion of the laser-produced
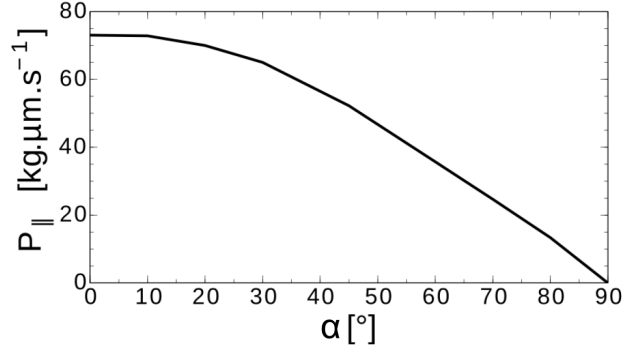
Figure 1.36.: Temporal average of the spatially integrated plasma momentum along the direction of the local magnetic field $\left(\iiint \rho \vec{v} (\frac{\vec{B}}{|\vec{B}|}) dV \right)$ as a function of the misalignment angle α, retrieved from the simulations shown in Fig. 1.35.

plasma. Then a key condition required in order for the PMN mechanism to be efficient in term of flow collimation is that the magnetic diffusion times must be large compared to the characteristic cavity crossing times of the fluid particles (few nanoseconds). Indeed, if the compressed magnetic field can diffuse fast enough inside the cavity to prevent the generation of sufficiently strong Lorentz forces, then one can expect a much less constrained expansion of the flow against the field lines. However, because we keep the same parameters for the laser-target interaction when varying the angle α, the initially created plasma is similar and there is no reason for the Reynolds numbers to vary, and for the magnetic diffusion times to change between the different cases. This is confirmed by our simulations where we have checked that the magnetic diffusion time is always at least one order of magnitude larger than the cavity crossing times. We are thus forced to look for another origin. There exists a second way to transport the field and therefore to reduce the collimating Lorentz forces: the "planar" advection of the magnetic field lines by the plasma flowing perpendicular to the B-field lines, i.e. without inducing bending of the magnetic field lines. This is what is induced by the increase of the angle α and the asymmetry in the cavity formation, as we detail just below just below.

Fig. 1.37 displays a more detailed set of data from the Gorgon simulations, showing the 2D maps of the electron density together with magnetic field lines and flow velocity vectors, for two different angles. As one can see in the two first frames (3 and 7 ns), if the case at $\alpha = 10°$ is quite similar to the case at $\alpha = 0°$ (see sec. 1.2), the case at $\alpha = 45°$ differs significantly. In this latter case, the bottom part of the flow (from $x = 0$, going to the x negative) is effectively slowed down and a shock forms in the same way as the shock at the border of the cavity in the $\alpha = 0°$ case (N.B: the shock is highlighted by an increase of the electron density). The difference being in the present case that the magnetic field lines encounter a stronger momentum (p_z) than in the $\alpha = 0°$ or $\alpha = 10°$ cases (along x or y). The fluid particles are harder to be stopped in a first time. Looking at the upper part
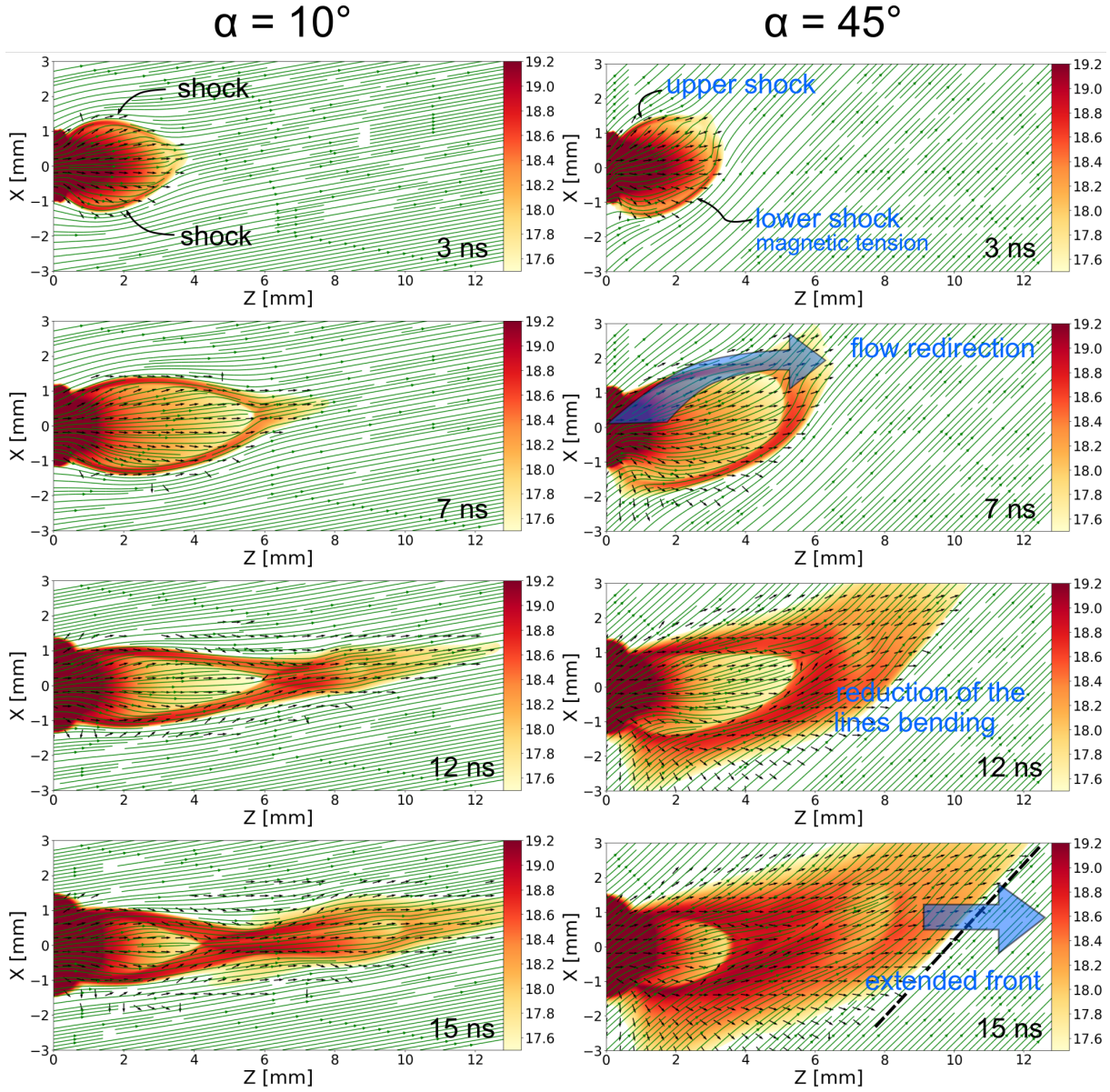
Figure 1.37.: Gorgon 3D MHD numerical simulations, in the plane xOz, of the plasma dynamic at two different angles, $\alpha = 10°$ (*left column*) and $\alpha = 45°$ (*right column*), at different times, i.e. from top to bottom 3, 7, 12 and 15 ns. The colorbar corresponds to the log_{10} of the electron density. The magnetic field lines are represented as green lines. The plasma flow speed is represented as black arrows.

of the plasma flow (from $x = 0$, going to the x positive), a part of it is unperturbed by the magnetic field as it propagates along its lines. The part of the flow going the most in the x positive direction (p_x) is however efficiently redirected in the z direction by the magnetic field (note the shock also present in that upper part of the dynamic). Globally, this results in a redirection of all the upper part of the flow in the z direction, above the end part of the lower shock. As a consequence, the distance, following the magnetic field lines, for which the B-field encounters a flow of plasma is enlarged. This upper part of the flow, this way redirected, participates in breaking the bending of the magnetic field lines initially generated by the lower shock. See for instance the frame at 7 ns of Fig. 1.37 where we clearly see the plasma situated in the region ($z = [4 - 6]$ mm ; $x = [1 - 3]$ mm) and coming from the upper part of the target, participating in relaxing the bending of the magnetic field lines, previously created in the lower shock region. The tension of the magnetic field line being reduced, it results in a much more "planar" advection of the magnetic field by the plasma, reducing efficiently the Lorentz forces acting against its propagation. In the frame at 12 ns of Fig. 1.37, we clearly see the lower shocked part of the plasma growing, being extended in the z direction.

In short, while increasing the angle α, the flow presents a stronger perpendicular (to the magnetic field) momentum. This generates internal shocks that are increasingly inefficient to stop the particles that still experience a strong post-shock speed, advecting the flow. The upper part of the flow is redirected in such a way that is participates in the release of the magnetic tension, helping in the advection of the magnetic field in a "planar" way, which implies a reduction of the magnetic forces acting against its propagation. The balance between ram pressure and magnetic pressure does not occur as rapidly as with a strong magnetic tension, and the frame at 15 ns, finally displays a shocked plasma that efficiently progresses in the z direction by advecting the magnetic filed lines within a very extended front.

We also note in the Gorgon simulation of Fig. 1.35, the formation of density striations in the plane containing the magnetic field. Those striations are perfectly aligned with respect to the magnetic field and already visible in the frame with 10 degrees of misalignment (see Fig. 1.35(a)). They become more present and contrasted while α increases, i.e. 30 degrees (b) and 45 degrees (c). Those striations take their origin in a magnetized Rayleigh-Taylor instability developing between the plasma and the magnetized vacuum [Khiar *et al.* (2018)]. That instability allows additional leakages of plasma across the magnetic field in yOz plane. Those striations are equally seen experimentally, as shown in Fig. 1.38 displaying an integrated plasma electron density map measured in the laboratory for $\alpha = 45$ degrees and for the latest probing time, i.e. 47 ns. Striations of density, aligned with respect to the magnetic field lines are clearly seen on the right of the jet.
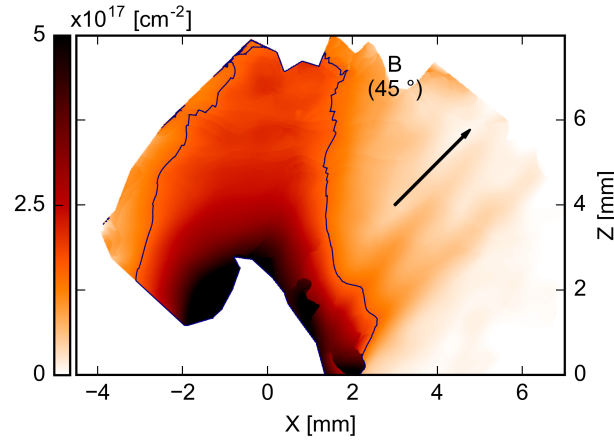
Figure 1.38.: Laboratory plasma electron density map at late time, i.e. 47 ns after the start of plasma expansion, for a magnetic field misalignment of 45 degrees. The contour follows the $1.5 \times 10^{17} \, \mathrm{cm}^{-2}$ integrated density value. The black arrow indicates the magnetic field direction.

1.3.6. Conclusion

The main conclusion we can draw from the laboratory and numerical investigations conducted here is that the presence and direction of a large-scale poloidal magnetic field with respect to the main expansion axis of an initially divergent outflow plays a major role on determining the outflow direction and on the ability of the outflow to be collimated at large distances from the outflow source. We note that the outflows investigated here in the laboratory are well scalable to YSO outflows. It has been shown in this section that the plasma flow tends to follows the magnetic field direction. However the mechanism responsible for the efficient collimation of a wide-angle outflow by a poloidal component of the magnetic field [Albertazzi *et al.* (2014); Ciardi *et al.* (2013); Higginson *et al.* (2017)], is progressively disturbed for an increasing misalignment angle α between the main plasma momentum and the magnetic field.

For $\alpha = 0°$, the plasma momentum component that enconters perpendicularly the magnetic field is rather small since it corresponds to the plasma flow along the target surface (p_x or p_y). Indeed, the plasma expands mainly normal to the target surface (see Fig. 1.16**d**). Hence, the reaction of the B-field against this normal component can be efficient. In addition, the perfect symmetry of the system in this case, implies that there is at the edge of the cavity strong magnetic tension and compression that subsists over long time, leading to an efficient slow-down and redirection of the plasma flow and an overall flow collimation. However, increasing α, the plasma momentum component that enconters perpendicularly the magnetic field becomes the stronger one ; in the limit of $\alpha = 90°$, this component corresponds to the main momentum along the target normal, i.e. p_z (see Fig. 1.16**d**). The stronger momentum component being hardly redirected by the magnetic field, this induces

a lack of slow-down of the plasma flow. In addition, the broken symmetry in this case implies a redirection of the flow that results in a relaxation of the magnetic tension initially generated. Finally, the plasma advects the magnetic field in a planar way, without efficient magnetic forces acting against it. In addition to that lack of collimation, additional leakage of matter is found to develop through a Rayleigh-Taylor type of instability, which decreases even more the amount of matter distributed in a jet-like structure.

Overall, these findings are well consistent with the findings of Ménard and Duchêne (2004) and Strom *et al.* (1986) that show a tendency for well collimated, long range, bright jets to be aligned with the magnetic field, while oppositely, weaker and shorter jets are mainly found to be misaligned with the magnetic field. As a consequence, we claim that in an astrophysical situation where there exists a too large misalignment between the outflow (rotation axis of the Keplerian disk) and the large scale magnetic field, no bright, long-range, well collimated jet should be observed.

1.4. Expansion in a transverse magnetic field

1.4.1. Experimental Setup

The experiment, the result of which will be presented in this section, was performed at three different laser facilities, the Elfie facility (LULI, Ecole Polytechnique), the PEARL facility (IAP-RAS, Russia) and the TITAN facility (Livermore). The drawing of Fig. 1.39 represents schematically the experimental configuration where a $\sim$ one nanosecond duration laser pulse impacts a Teflon (CF_2) solid target embedded in a 20 T magnetic field initially oriented parallel to the target surface. The diagnostics line of sight is set either along or across the magnetic field direction, depending on the experimental campaign, either ELFIE or TITAN. The main diagnostic is an interferometer used to probe the electron density.

At both facilities, the laser parameters are tuned so that the laser intensity is about $I_{max} = 10^{13} \ W.cm^{-2}$ (as for the experiments presented in the previous sections). At the Elfie facility, the chirped laser beam of 0.6 ns/30 J, and at the wavelength of 1057 nm, was focalized over a $\sim 700 \, \mu$m diameter focal spot, implying a laser intensity of $I_{max} = 1.6 \times 10^{13} \, \mathrm{W.cm^{-2}}$. The TITAN facility provided a long pulse of 1.2 ns/20 J, at the wavelength of 527 nm, and focalized in a $\sim 300 \, \mu$m diameter spot. This allowed to have a similar intensity onto the target surface, i.e. $I_{max} = 1.2 \times 10^{13} \, \mathrm{W.cm^{-2}}$. In both facilities, interferometry was accomplished using a Mach-Zehnder setup with a laser having a duration of the order of the ps and laser energy of about 100 mJ of energy, i.e. with negligible heating effect on the plasma dynamics (see sec. 1.2.2).
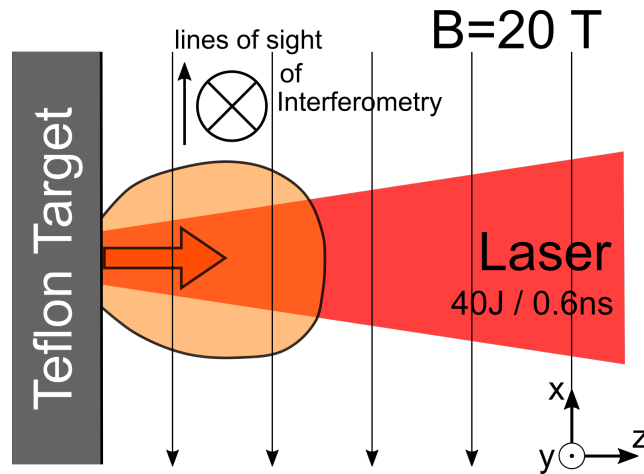
Figure 1.39.: Sketch of the perpendicular magnetic field experimental setup. The target is embedded in a large-scale 20 T magnetic field, and is heated by a $I_{max} = 1.6 \times 10^{13} \, \mathrm{W.cm^{-2}}$ laser. The plasma density is probed either along the x or y axis, i.e. along or across the magnetic field lines.
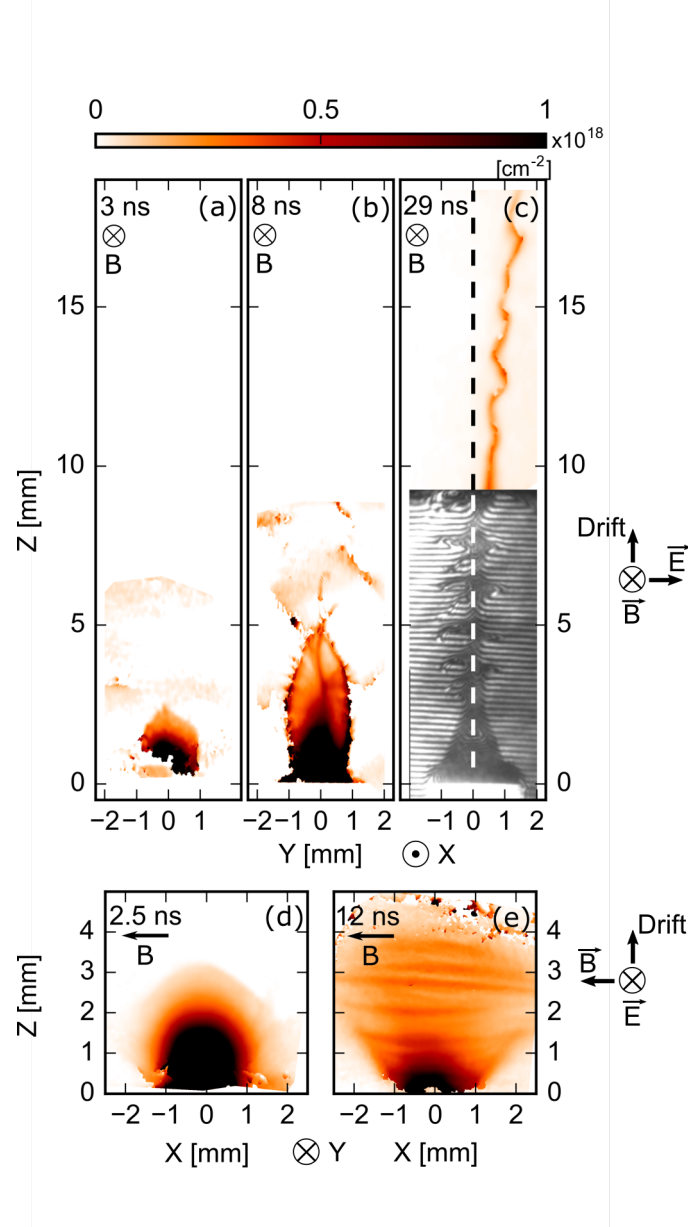
Figure 1.40.: Plasma areal electron density [cm^{-2}] measured via interferometry in the transverse magnetic field orientation setup. (a) to (c) electron density probed along x, at different times from 3 to 29 ns. (d) and (e) electron density probed along y, at $t = 2.5$ and 12 ns respectively. The magnetic field orientation is indicated in the top left corner of each maps.

1.4.2. Plasma propagation

1.4.2.1. Free expansion

Fig. 1.40 presents 2D areal electron density [cm^{-2}] maps at different times and for the two lines of sight, i.e. along the magnetic field (top maps row) and perpendicular to the magnetic field (bottom maps row). At early time, ≤ 3 ns, the expansion is found to be quite symmetric in all directions, as the plasma exhibit similar density profiles for both probing directions ((a) and (d)). The very slight asymmetry in between the lateral propagation, x or y directions, and the longitudinal, z direction, is roughly the same in both planes and found to be ~ 1.3, and exhibits a stronger propagation in the z direction compared to the x or y directions. This is simply due to the specificity of the heating source, i.e. the laser irradiating a plane target. The stronger pressure gradient in the plane getting out of the target plane, compared to the pressure gradient contained in the target plane, results in an enhanced expansion speed in the z direction. However, the similar topology in between the planes perpendicular to or containing the magnetic field demonstrates the quite free expansion of the plasma which propagates indifferently of the presence of the magnetic field. This is due to the quite hot plasma being created by the way of such laser irradiation ($I_{max} \sim 10^{13}$ W.cm^{-2}). Indeed, spectroscopy measurements of the electron plasma temperature reveal a temperature at the target surface up to $T_e = 300$ eV (see Fig. 1.34).

The initial plasma parameters are detailed in the first column of Tab. 1.1. As previously described, such a hot plasma, quite non resistive ($\eta \propto T_e^{-3/2}$), is characterized by a quite high magnetic Reynold ($R_m = V.L \times \frac{\nu_0}{\eta}$; with V and L, the flow speed and characteristic size respectively) which allows the magnetic field to be 'frozen-in' the plasma. In addition to that, the relatively fast ($\sim 1000\ km.s^{-1}$) plasma possesses a larger ram pressure compared to the magnetic one, i.e. $\beta_{dyn} = ram\ pressure/magnetic\ pressure \gg 1$, up to 140, see Tab. 1.1. Consequently, the magnetic field lines moves with the plasma flow, and the propagation of the latter is almost unimpeded at the first instants.

1.4.2.2. Cavity formation and plasma redirection

This symmetry breaks out later on, at $t \sim 10$ ns. In the plane perpendicular to the magnetic field (Fig. 1.40(b) ; $t = 8$ ns), the plasma propagation displays an obvious asymmetry in between the y and z directions. Although both directions are going across the magnetic field, the plasma expands much farther in the z direction than in the y direction. Using the physical picture developed earlier (see sec. 1.2) we can deduce that the motion of the magnetic field lines with the plasma allows the bending of the magnetic field. Consequently, at the tip of the flow, strong magnetic field tension is created. The high conductivity of the hot plasma allows the creation of intense currents, in reaction to those magnetic

gradients ($\boldsymbol{J} = \boldsymbol{\nabla} \times \boldsymbol{B}/\mu_0$). Then, a Lorentz force acts on those current slowing down the propagation of the plasma flow. It results in a diamagnetic cavity, emptied of magnetic field, at the border of which the plasma density is increased, as visible in the Fig. 1.40(b) oval-shaped cavity. The larger extension in the z direction of this cavity compared to the y direction takes its origin in the stronger plasma momentum along z than along x (and y), due to the laser irradiation. The slower flow speed in the y direction is more easily stoppable than the one in the z direction. Because of the highly conductive regime and the strong beta at that moment, the overall dynamic resembles the diamagnetic cavity formation in the longitudinal magnetic case presented in sec. 1.2. The diamagnetic cavity, thus constituted, allows the next particles to flow freely from the source (the target surface) up to the cavity border. The particles are then stopped at that location, heated up, and drift along the cavity border to reach the tip of that cavity. In the plane perpendicular to the magnetic field, all that mechanism then results in a redirection of the plasma flow along the z axis.

In the plane containing the magnetic field (Fig. 1.40(e) ; $t = 12\,\mathrm{ns}$), the topology is radically different. If along z, the dynamic is the same as the one explained above, along x, the particles are free to propagate as they move following the magnetic field lines orientation. This lateral motion along x then does not need the high conductivity (for the "frozen-in" regime to allow to push against the magnetic field lines) to develop, and no plasma slowing down is expected in this direction, as actually observed in the frame (e). Thus, in the x direction, the expansion is free and no redirection of the plasma flow along the z axis develops.

1.4.2.3. Sheet formation and propagation across the magnetic field

Let us concentrate on a late frame in the plane perpendicular to the magnetic field, i.e. Fig. 1.40(c) ; $t = 29\,\mathrm{ns}$. At 29 ns after the laser irradiation, the plasma is found to have propagated up to 20 mm. A detailed tracing of the plasma tip actually goes in the way of a constant propagation across the magnetic field, with a speed $V_{flow} \sim 650\,\mathrm{km.s^{-1}}$, as it can be seen in Fig. 1.41. This figure represents the plasma tip position as a function of time. The blue points are the one for which the plasma tip is well visible, and the propagation is quite straight as the one seen in Fig. 1.40(c). The red points are the ones for which the plasma tip is well visible, but the propagation exhibit a quite chaotic behavior leading to strong changes in the tip direction (up to 90°change in the direction on some shots). Finally, the black solid line corresponds to a fit on the blue points, and corresponds to a flow velocity of $650\,\mathrm{km.s^{-1}}$.

The plasma shape is considerably reduced in the y direction, exhibiting a thin layer of diameter $D_{layer} \sim 400\,\mu\mathrm{m}$. In the other plane, a frame at approximately the same time (as it as been measured experimentally) displays a similar topology as in the frame (e), i.e.

	Laboratory
B-Field $[T]$	20
Material	C_2H_3Cl (PVC)
Atomic number	16.7
	Sheet layer (late time)
Characteristic size (L) $[mm]$	1×10^{-1}
Charge state	4.0
Electron Density $[cm^{-3}]$	5×10^{18}
Ion density $[cm^{-3}]$	1.2×10^{18}
Density $[g.cm^{-3}]$	3.5×10^{-5}
Te $[eV]$	10
Ti $[eV]$	10
Flow velocity $[km.s^{-1}]$	650
mfp_e/L	7×10^{-4}
mfp_i/L	6×10^{-5}
Electron thermal Larmor radius $[mm]$	3.8×10^{-4}
Ion thermal Larmor radius $[mm]$	1.7×10^{-2}
Electron magnetization (mfp_e/r_{Le})	0.2
Ion magnetization (mfp_i/r_{Li})	4×10^{-4}
Magnetic diffusion time $[ns]$	0.1
Magnetic Reynolds	6.2×10^{-1}
Reynolds	7.3×10^5
Mach number	30
Alfvenic Mach number	6.6
β_{ther}	6.3×10^{-2}
β_{dyn}	93

Table 1.3.: Measured and estimated plasma conditions in the propagating plasma sheet well formed. This is to say at late time. We stress that such parameters do not correspond to the one described in the above "Free expansion" and "Cavity formation and plasma redirection" subsections.
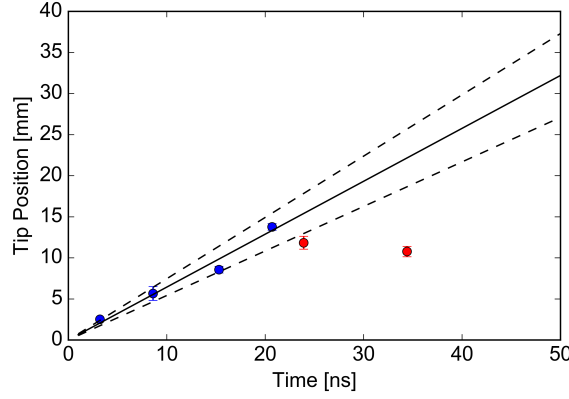
Figure 1.41.: Plasma tip position as a function of time, taken from different laser shots. See main text for a description of the different point colors.

a free expansion in the x direction with the plasma filling the entire field of view of the interferometer. The sheet plasma layer then continuously propagates along the z direction, while it expands in the x direction.

For $z < 5$ mm, the cavity visible at 8 ns (frame (b) of Fig. 1.40) is not visible anymore in the frame (c), and is instead replaced by a plasma sheet on which plasma "ripples" are clearly observed to develop and propagate perpendicularly to the plasma sheet, i.e. in the y direction. The diamagnetic cavity has collapsed. This is due to the fact that the laser irradiation, and hence the plasma creation and ejection, is limited in time. The ram pressure that initially provided the extension of the cavity in the y direction decreases progressively, leading to a situation where the magnetic pressure exceeds the ram pressure, inducing the collapse of the cavity in the y direction.

According to the thickness of the plasma layer (400 μm) and the areal density measured in the plane containing the magnetic field ($\int n_e dx \sim 2.15 \times 10^{17}$ cm^{-2}), we estimate the volumetric electron density inside the layer to be approximately $n_e = (D_{layer})^{-1} \times \int n_e dx = 5 \times 10^{18}$ cm^{-3}. Obviously, in the z direction, given the experimentally observed constant velocity propagation (see Fig. 1.41), the mechanism responsible for stopping the plasma, as in the y direction, is not or lowly efficient.

Such a behavior can be attributed to the fact that, due to the free expansion in the x direction, this configuration is very efficient in removing the magnetic tension at the front of the plasma. Quite rapidly, due to the extension of the "pushing plasma front" in the x direction, the propagation occurs in such a way that the magnetic forces acting against the plasma are only composed of the magnetic pressure, while the magnetic tension is absent. This leads to a more suitable situation for the plasma to "push" the magnetic field lines for a long time. We can add that, early in the dynamic, the redirection of the plasma along the z axis (visible in the frame (b)) would support such a propagation. Indeed, all the ram pressure initially directed in the y direction, is redirected in the z direction, thus

supporting further the propagation by increasing the ram pressure in the z direction at the tip location of the plasma sheet.

We stress here on the fact that the reasoning made above relies on the fact that the conductivity of the plasma is high enough for the diamagnetic current to be generated without hindrance ($\sigma \propto T_e^{3/2}$). This is to say, if the magnetic Reynolds number is much greater than one. This is true at the early stage of the propagation, where the plasma temperatures stay sufficiently large (see Tab. 1.1 and Fig. 1.34, where the temperature starts from 300 eV).

ExB mechanism As for the lateral expansion which has stopped (leading to the collapse of the cavity), one could expected this propagation along z to slow down, at late time, and stop. Indeed, the compression of the magnetic field lines occurring during the plasma propagation, the magnetic pressure should increase and allow it to counter-balance of the plasma ram pressure. This is effectively what is observed in the Gorgon MHD code (not shown here, see pages 164 and 170 of B. Khiar's thesis [Khiar (2017)]), where a deceleration of the plasma front is observed. In a pure magneto-hydrodynamic way, the slowing down is effectively inevitable. However, as revealed by the frame (c) of Fig. 1.40, the plasma sheet propagates quite far (up to 20 mm), with an important propagation speed, which in addition seems to stay constant (see Fig. 1.41). Moreover, as revealed by spectroscopy measurements of the electron temperature of the plasma far from the target surface, the latter considerably decreases with the distance to settle down at a typically value of $T_e = 10$ eV (see Fig. 1.34). As a consequence, the initially high magnetic diffusion time (up to 140 ns at the first instants for the hot plasma) decreases considerably to stand below the nanosecond for a plasma at 10 eV (taking into account the decrease of the characteristic size of the system, from 1 mm initially to 400 μm). In those conditions, the magnetic field can diffuse relatively rapidly in the plasma sheet, as highlighted by the relatively small magnetic magnetic Reynolds number $R_m = 6.2 \times 10^{-1}$, or the magnetic diffusion time $\tau_m = 0.1$ ns (Tab. 1.3).

Then, it is necessary to find an other explanation for propagation at those late times. In the literature, it is often evoked to be the $E \times B$ mechanism [Bostick (1956); Schmidt (1960); Bruneteau *et al.* (1970); Plechaty, Presura, and Esaulov (2013)]. The magnetic field diffusing in the plasma sheet, a polarization electric field can be generated, oriented along the y axis, due to the opposite direction with which the ions and the electrons initiate their gyro-radius around the magnetic field.

Fig. 1.42(left) shows the electrons and ions distribution along y induced by such separation, after magnetic field diffusion and taking into account the density and temperature values retrieved experimentally. Both species escape over twice their respective thermal Larmor radius (see Tab. 1.3). The charge separation induces an electric field in the plasma layer
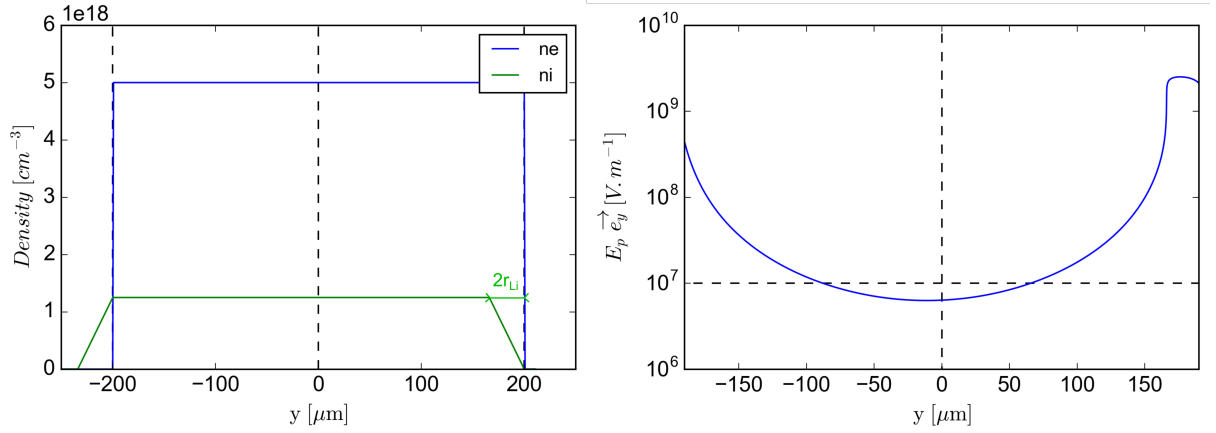
Figure 1.42.: Charges separation and induced electric field within the plasma sheet.

that is represented in Fig. 1.42(right). The latter stands, in the middle of the plasma sheet, at a typical value of $E_p \sim 10^7$ V.m^{-1} and directed along the y positive. With the 20 T magnetic field applied during the experiment, such electric field provides a drift velocity, in the z positive, of $\|\boldsymbol{v}\| = \frac{E}{B} \sim 500$ km.s^{-1}, completely compatible with the 650 km.s^{-1} experimentally measured.

The existence of such polarization field, seems to be further confirmed by the presence of a lateral shift of the plasma sheet in the y direction and visible in the frame (c) of Fig. 1.40. Taking into account the same kind of charge separation (due to thermal gyro-radius, but at the tip of the sheet, in the z direction), at the front of the plasma sheet, one can find the possible existence of another electric field oriented in the z negative direction, with a typical value of $E_p \sim 10^6$ V.m^{-1}. Such electric field will lead, after 30 ns to a lateral shift of around 1.5 mm, quite consistent with the shift measured in Fig. 1.40(c).

However, the generation of such polarization field is based on the fact that the particles are not impeded in their gyro-motion so that the Larmor radius can be completed properly. Here, the collisions can prevent the gyro-motion to occur in a lasting way. A proper parameter to look at, in order to understand which mechanism is dominant between the magnetic gyration or the collision, is the Hall parameter. The latter is the ratio of the collision time over the time necessary for a specie to complete its Larmor radius, $H_\alpha = \omega_{c\alpha} \tau_\alpha$ - this is somehow an estimation of the degree of magnetization of the species. Yet, if we look at the Hall parameters, in the plasma sheet conditions (see Tab. 1.3), we understand the ions to be unmagnetized ($H_i = 7.2 \times 10^{-4}$), while the electrons are weakly magnetized ($H_e = 1.4$). In those conditions, at least regarding the ions, no charges separation can stand in the long-term.
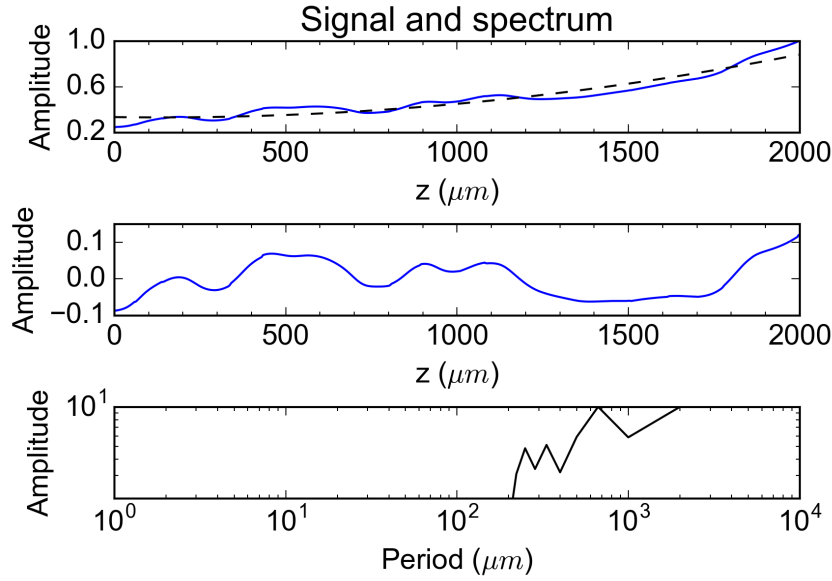
Figure 1.43.: Normalized experimental electron density variation and the associated modes in the plasma sheet. *Top:* Lineout in the z direction of a 8 ns electron density map in the xOz. Blue full curve: lineout in the z direction taken at x=0 (note that $z = 0$ is taken arbitrarily in this figure) . Black dashed curve: best power low following the global increase of the density with increasing the distance (i.e. going closer to the target surface). *Middle:* Lineout corrected from the power law. *Bottom:* Fast Fourier Transform (FFT) of the corrected lineout. Three peaks are well visible, corresponding to periods of about 250, 330 and 665 µm. The last increase in the amplitude of the FFT, corresponding to a period of about 2000 µm, should not be taken into account as is is an artifact due to the size of the "box / lineout" ($\sim 2000\,\mu$m) within which the FFT is performed.

1.4.3. Magnetized Rayleigh-Taylor instabilities

On can observe in Fig. 1.40(c) (frame at 29 ns in the plane yOz) the development of "fingers" at the base of the plasma sheet. Those fingers also correspond to the striations visible in the frame at 12 ns (Fig. 1.40(e)), then looking at the orthogonal plane, xOz. It can be seen in the latest frame that the growing modes developing are well identified as having a wavenumber, **k**, oriented in the z direction, this is to say perpendicular to the magnetic field, **B**, direction (oppositely to a mode that would have developed with a wavenumber oriented in the y direction). Those structures are identified as Rayleigh-Taylor instabilities developing at the interface plasma / magnetized vacuum [Khiar *et al.* (2018)]. Indeed, Chandrasekhar (1981) (page 466) shows that the growth rate of such magnetized Rayleigh-Taylor instabilities (MRTI) writes down: $\gamma^2 = kg_{\text{eff}} - 2(\mathbf{k} \cdot \mathbf{B})^2/(\mu_0\rho)$. With the latest formula, one can understand that the modes growing-up the faster are the ones with a wavenumber perpendicular to the magnetic field direction (i.e. **k.B** $= 0$), while the growth rate of modes with **k.B** $\neq 0$ is reduced by magnetic tension.

In the growth of such instability, the magnetic diffusivity, D_M, and the kinematic viscosity, ν, play a role of damping the MRTI. Indeed, Green and Niblett (1960) shows that $\gamma = (g_{\text{eff}}k)^{1/2} - k^2(\nu + D_M)$. Using Spitzer-Härm expression for the resistivity and Braginskii's expression for the ion dynamic viscosity (see Annex sec. A.1), it can be shown that the modes growing the faster are found to present spatial periods of several hundreds µm to 1 mm [Khiar *et al.* (2018)]. This is in good agreement with what is actually observed in the experiment and specifically in the density map probing the xOz (Fig. 1.40(e)).

For instance, taking a shot at 8 ns (not presented in Fig. 1.40, but qualitatively similar to the (e) frame), Fig. 1.43 shows that it is possible to find preferential modes of ~ 250, 330 and 665 µm. We note that, due to the way the electron density is probed, the modes developing either at the topside or underside of the plasma sheet (that should be similar regarding the period) are probably mixed within the electron map finally measured. Then, the measurement of the exact modes developing is rather complicated, and a safer information retrieved from Fig. 1.43 should be to say that *modes* with *periods* of the order of *hundreds microns* are experimentally seen to develop at the border of the plasma sheet.

1.4.4. Conclusion

It has been shown that the propagation of a laser created plasma within a perpendicular magnetic field exhibits very unique features. Due to the geometry and within the "frozen-in" regime of the ideal MHD, the experimentally observed plasma sheet formation can be understood. This sheet, once formed is found to propagate quasi unimpeded across the magnetic field lines. While Gorgon MHD simulations [Khiar (2017)] display a deceleration of the plasma front, due to an increase of the magnetic pressure, this deceleration does not seems to occur in the experimental case. Regarding this specific point, the polarization electric field (not present in the MHD simulation) could be a good candidate to explain such a constant propagation across the magnetic field. Hence, a kinetic phenomenon, at the longer times, should be at the base of the quasi-unimpeded plasma propagation. The collisionality of the plasma sheet seems to partially satisfy the conditions required to achieve such a kinetic regime. Here, a transition regime, in between the MHD and kinetic regime, should be at play for the plasma generated within that setup to propagates over such a long time and distance from the target.

Moreover, it is of interest to investigate on the instabilities developing at the base of the plasma sheet (see Fig. 1.40(c), or the striations visible in (e)). Those instabilities, identified as Rayleigh-Taylor kind of instabilities, should receive greater attention in the future [Khiar *et al.* (2018)].

2. Accretion shock experiment: supersonic plasma flow collision with a dense obstacle

2.1. Introduction

Accretion dynamic is a process that occurs in a variety of forming stellar objects, from black holes (in the center of Active Galactic Nucleus (AGNs)), pulsar, to binary stars (as for example in white dwarf accreting material from their companion star), up to isolated low mass stars (Sun-like kind of star). In the latter, from the initial rotating molecular cloud that collapses in order to form the central object, i.e. the protostar, the interplay between the accretion and ejection processes is of great importance. Indeed, it determines the exchange of mass, energy, and angular momentum between the accreting object and its surroundings, and, eventually, the formation of planetary systems around stars.

Cloud collapse

Figure 2.1 displays a schematic representation of the different evolutionary stages of a forming star in the pre-main sequence, from Class 0 (star age $\sim 0.001\,\mathrm{Myr}$), where a large molecular cloud with a radius of about $10^4\,\mathrm{AU}$ is still present, to the latest Class III stage (star age $\geq 10\,\mathrm{Myr}$), where the major part of the mass is now situated in the central protostar. The size of the initial molecular cloud can be expressed, in a very first approximation, by trying to find a cloud at initial hydrostatic equilibrium, counterbalancing gravitational forces and thermal ones. Consequently, the equilibrium for a cloud of mass M_{cl}, and a radius R_{cl} can be expressed as follows [Hartmann (2008)]:

$$\frac{GM_{cl}}{R_{cl}} \sim c_s^2 = \frac{kT}{\mu m_H} \ ,$$

where c_s is the sound speed, k is the Boltzmann constant, T is the temperature, m_H is the hydrogen mass and μ is the molecular weight. For a cloud molecular weight of 1
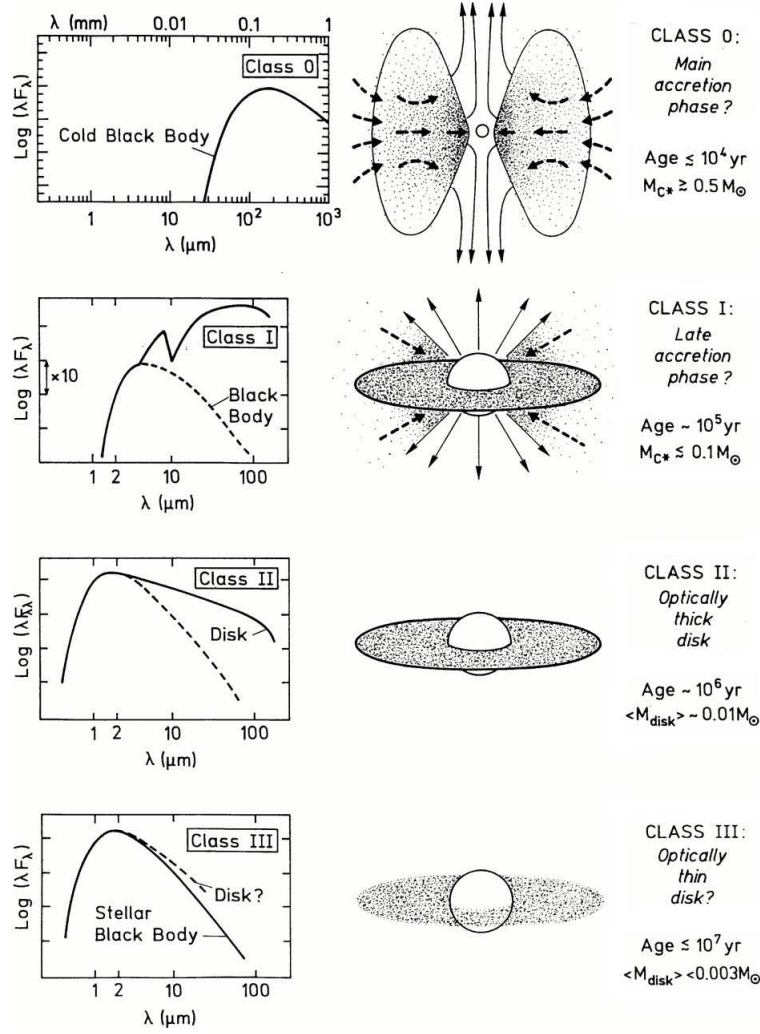
Figure 2.1.: Star formation evolutionary stages. The Class II corresponds to the classical T Tauri stars formation stage. F_λ is the total radiated flux at wavelength λ. From Argiroffi (2005).

(Hydrogen), a temperature of $10\,\mathrm{K}$ and assuming a cloud mass of the order of the solar mass, one finds a typical cloud radius $R_{cl} \sim 0.05\,\mathrm{pc} \sim 1.10^4\,\mathrm{AU}$, in very good agreement with astrophysical observations of molecular clouds. However, because of the inability of the cloud to trap the thermal energy that instead is radiated away, the cloud doesn't heat up efficiently during the contraction and becomes gravitationally unstable, leading to a rapid collapse.

Formation of a disk

Taking into account the rotation of the cloud with a constant angular velocity Ω_0, through centrifugal forces one can understand that the typical shape of the collapsed material will consist in an extended structure along the radial direction in the equatorial plane (i.e.

perpendicular to the axis of rotation). The matter closer to the center, that exhibits a small angular momentum, will reach the center first, starting the accumulation of matter giving birth later on to the protostar. However, the matter susceptible to reach that center at later time, because it starts from larger radii, experiences a larger angular momentum ($mrv_\perp = mr^2\Omega$) and will fall down in the equatorial plane at a farther distance from the center, i.e. at a radius that corresponds to its Keplerian circular orbit: $r_c = r_0^4 sin^2\theta \frac{\Omega_0^2}{GM}$; where r_0 is the starting falling down radius, Ω_0 is the initial rotational angular speed, which is a constant at the initial stage for the entire cloud (as hypothesized in Hartmann (2008)), M is the mass situated at $r < r_0$ ($\overrightarrow{r} = \overrightarrow{OM}$; where O is the center of the cloud), and θ is the angle between the rotation axis and $\overrightarrow{r}$.

A more sophisticated self-similar solution of the collapse can be build [Shu (1977)] that leads to a proper description of the temporal evolution of the mass accumulation at the center : $M(r < r_0, t) = 0.975 \frac{c_s^3 t}{G}$ which is contained within a radius $r_0 = \frac{0.975}{2} c_s t$ (we note here the apparition of the temporal dependence). Injecting that description in the previous expression of r_c, one can find the temporal evolution following which a certain equatorial radius is filled in by continuously collapsing material. This dependence is found to be $r_c(t) = 0.975^3 \frac{c_s t^3}{16} \Omega_0^2 sin^4\theta$ [Hartmann (2008)]: this is to say, from an initial collapse in the center, forming a central object, matter is spread in the equatorial plane, forming a disk-like structure which radial extension and filling progresses at a rate $\propto t^3$.

Here, we note that from an initial situation in the cloud where, the farther the matter from the center is, the faster it is circularly moving (the linear/tangential speed is $v_\perp = r\Omega_0$), we reach an opposite situation, where the farther the matter from the center within the disk is, the smaller is its linear speed (in accordance with the Keplerian motion around a central mass, $v_\perp = r\Omega_K = \sqrt{\frac{GM}{r}}$, with $\Omega_K = \sqrt{\frac{GM}{r^3}}$); see Figure 2.2. This inversion is solely due to the conservation of the angular momentum during the collapse.

Note that the disk formation will occur unless the angular speed of the cloud is very slow, i.e. $\leq 10^{-3}$ times the break-up angular speed at the outer equatorial radius of the cloud ($\Omega_{br}^2 = \Omega_K^2 = \frac{GM}{R^3}$, if R is the cloud extension) [Hartmann (2008)]. However, observations of cloud velocity gradient support the fact that most of the systems present a sufficient rotational speed to be subject to an evolution as a disk-like structure.

A gap between disk and star

Starting from that disk shape, a central object is formed and the disk is centrifugally supported in its rotation around the central object. Then, angular momentum transfer processes, from the inner part to the outer part of the disk, are necessary in order to lead to the phase where accretion occurs from the disk to the star. Among most probable transfer processes, let us cite the magnetic turbulence [Velikhov (1959)] and the gravitational instability. At approximately 1 Myr, the forming star is located in the Class II of the pre

main sequence, and is part of the so-called T Tauri star (TTS) kind of star. The mass is distributed in between the central core and a well formed accretion disk. Considering the strong magnetosphere of a Classical T Tauri star (CTTS), characterized by $\sim kG$ surface field [Johns-Krull *et al.* (1999, 2001); Guenther *et al.* (1999)], a truncation of the disk at R_{trunc} is expected, which is equal to a few stellar radii *from the stellar surface*, i.e. at a point where the ram pressure ($\frac{1}{2}\rho v^2$) of the disk material is balanced by the magnetic pressure ($\frac{B^2}{2\mu_0}$) of the magnetosphere. This magnetosphere can be complex, from strongly bipolar (as for AA Tau), to octupole component (as for TW Hya), through more exotic topology (as for V2247 Oph). It is possible to show that the more the dipolar component is dominant, i.e. the less is the magnetic topology complex, the more the disk and the solar atmosphere (the corona) are decoupled, i.e. less they overlap [Johnstone *et al.* (2014)]. This is due to the fact that the bipolar component, when strong enough, is conducive to a truncation of the disk farther from the star, simply because it is the magnetic field topology that allows the stronger magnetic field strength at large distances. Figure 2.3 right displays a standard representation of a T Tauri star. The black lines represent the magnetic field lines, here strongly bipolar. The accretion disk is truncated and is well detached from the stellar surface.

Accretion of matter onto the star

From that configuration and by the action of angular momentum transfer (through magnetic coupling, gravitational or viscous effect within the disk [Cassen and Moosman (1981)]), material in the disk spins down and accretion of disk material onto the protostar is then possible when the gravitational force from the central star overtakes the centrifugal force of the disk material. This accretion is made possible on an area in between two critical points of the accretion disk, as indicated in Figure 2.2. It starts from the inner edge of the disk, namely the truncation point (at R_{trunc}), up to the co-rotation point (at R_{co}), where the Keplerian angular velocity of the disk is equal to the stellar angular velocity. Before R_{co}, the Keplerian angular velocity is greater than the angular velocity of the protostar, and a coupling of the two objects by the way of the magnetic field lines will
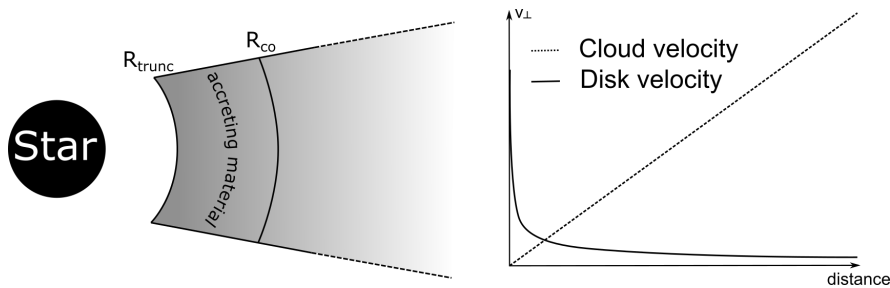
Figure 2.2.: Top view of an accreting star and tangential velocity distribution for the initial cloud and the final disk (see main text).
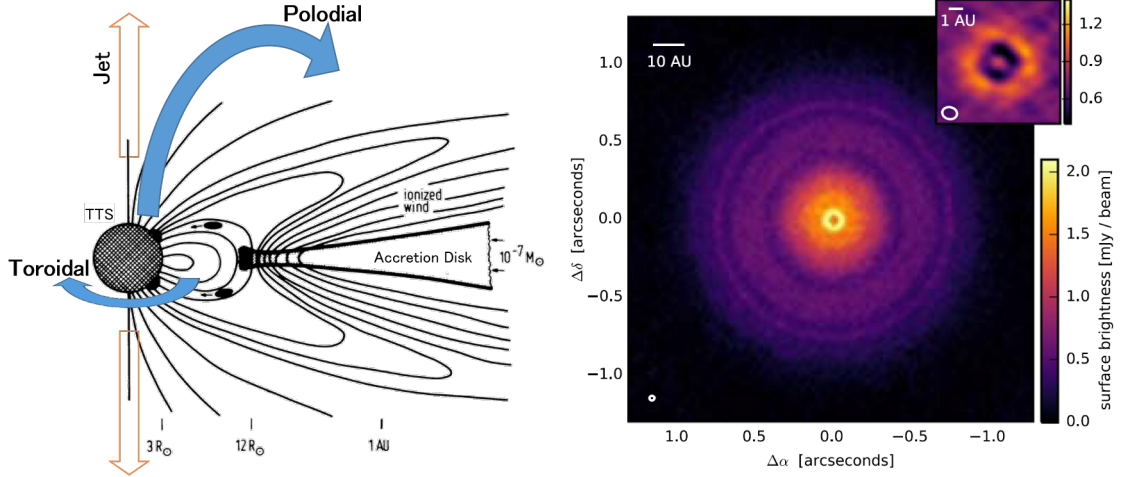
Figure 2.3.: *Left:* Schematic view of a low mass stars in its CLASS II evolutionary stage (Classical T Tauri Star - CTTS): the accretion disk is well formed and matter falls down from the truncation point to the stellar surface, forming an accretion column following the magnetic field lines. Adapted from Bouvier *et al.* (2003).
Right: ALMA (Atacama Large Millimeter/submillimeter Array) high-resolution map of the 870 μm continuum emission from the TW Hya disk (from Andrews *et al.* (2016)). TW Hydrae is an approximately 8 million years old star exhibiting emissions characteristic from accretion phenomena, and is situated at a distance of $180\,\mathrm{light-years}$ (the disk plane normal has the particularity to point towards Earth).

have for effect to spin up the central object as well as spin down the disk material in that region. However, after the co-rotation point, that coupling will have the opposite effect, i.e. spin down the central object as well as spin up the disk material. Consequently, every material coupled to the star by the magnetic field lines after the co-rotation point, will experience an increase of its angular velocity and additional centrifugal forces expelling the material away from its initial location and forming the disk winds.

The accretion process is then only possible for a region of the disk situated at $R_{trunc} < R < R_{co}$. Assuming a bipolar magnetic topology, the ionized matter will fall onto the stellar surface at the free fall velocity, guided by the magnetic field lines in the form of columns of matter to a near-pole region of the stellar surface. We note here that standard CTTS characteristics ($M_* \sim 0.5\text{-}2\,\mathrm{M_\odot}$; $R_* \sim 1\text{-}3\,\mathrm{R_\odot}$) imply a free fall velocity $v_{ff} = \sqrt{2M_*G(\frac{1}{R_*} - \frac{1}{R_{trunc}})} \sim 200\text{-}500\,\mathrm{km.s^{-1}}$, where it was assumed a typical $R_{trunc} \sim 5R_*$ truncation radius. This range of speed corresponds to acceleration of the flow up to supersonic velocities (for typical value of the incoming stream temperature, $T \sim 2500\,\mathrm{K}$, we get $Mach = v_{ff}/C_s \sim 40-100$), leading to strong shocks at the impact with the stellar surface.

Near the surface, the accretion process can then be sketched as in Figure 2.4. An accretion column, following the magnetic field lines, falls down onto the stellar surface and impacts the latter, forming a shock that goes up the incoming flow. The matter is heated up, under

the shock, at a temperature around few 10^6 K [Calvet and Gullbring (1998)], emitting radiations from optical to X-rays that are observable through astrophysical observations of CTTSs. Those radiations, measured by high resolution spectroscopy measurements in CTTSs to emanate from dense regions (typically $10^{11} - 10^{13}$ cm^{-3}) compared to more tenuous corona type of radiations (~ 10 MK; $10^{10} - 10^{11}$ cm^{-3} – [Testa, Drake, and Peres (2004); Ness *et al.* (2004)]), are then believed to be the signature of disk accretion radiations, coming from dense disk material heated up through the accretion shock while impacting the stellar surface. Typical CTTS examples revealing that behavior are TW Hya, BP Tau, and V4046 Sgr.

Present issues

That standard description of the accretion shock offers the possibility of confrontations between astrophysical observables and theoretical or simulated predictions, allowing a better understanding of this key phase in the star formation process. However, among others difficulties, the current modeling of the accretion dynamic suffers from an obvious lack of understanding when confronted to the observation of multi-band emissions coming from the shocked region. Indeed, observations from CTTSs, where the accretion process is important, show that there are significant discrepancies [e.g., Curran *et al.* (2011); Herczeg and Hillenbrand (2008)] between the observed X-ray luminosity and predictions based on the UV/visible bands from the same object. In some systems, the discrepancy is moderate (i.e. below a factor of 4; e.g. Hen 3-600, TW Hya), while in others the discrepancy is large (up to two orders of magnitude; e.g. RU Lup, T Tau), but in all cases the observed X-ray luminosity is lower than expected. Based on magnetohydrodynamic (MHD) models [e.g., Orlando *et al.* (2010); Sacco *et al.* (2010); Orlando *et al.* (2013); Matsakos *et al.* (2013); Colombo *et al.* (2016); Sacco *et al.* (2008); Costa *et al.* (2017)], so far limited to two-spatial dimensions, absorption of X-rays by an optically thick envelope of plasma surrounding the shocked plasma [Orlando *et al.* (2010)] is one of several scenarios [Reale *et al.* (2013); Bonito *et al.* (2014); Orlando *et al.* (2013)] that have been evoked to explain this discrepancy and the lower than expected observed X-ray luminosity.

Interest of laboratory experiments

However direct, finely resolved observations of such an envelope is well beyond present-day observation capabilities. Laboratory experiments can then play an important role in shedding light on important plasma dynamics coming into play in the context of accretion, and allow to validate, with the support of simulation works, one or other scenarios evoked to solve that discrepancy.

In this chapter, after a review of the state of the art in astrophysical observations, simulations and laboratory experiments in the context of accretion shocks, a novel experimental
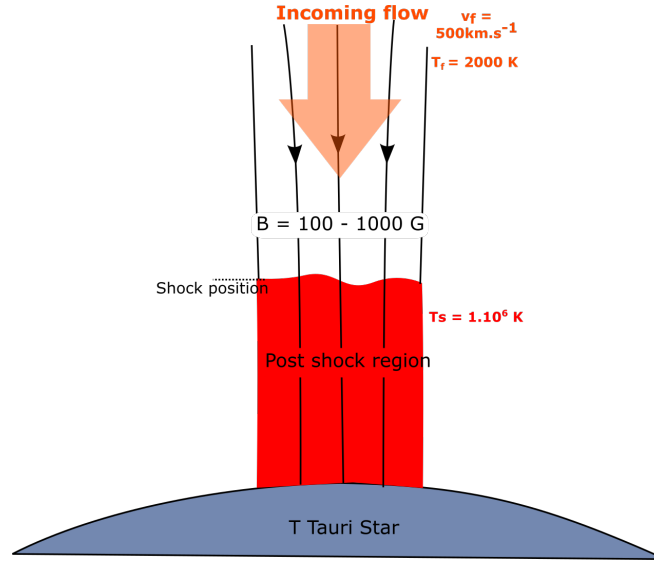
Figure 2.4.: Standard description of the accretion shock in the magnetospheric accretion model, in the context of a Classical T Tauri star.

setup coupling laser-created plasma expansion and external pulsed magnetic field will be detailed. A careful discussion on the astrophysical relevance of the setup, and its scalability with CTTS kind of accretion will be done. Using information retrieved from several diagnostics, namely interferometry, X-ray radiography, X-ray spectroscopy and streak-optical-pyrometry (SOP), it will be shown that important features of the accretion dynamic can be reproduced in the laboratory, namely an accretion shock going up the incoming flow and specific ejection of matter at the border of the flow. The magnetic field is shown to play an important role in the development of a dense plasma shell, surrounding the main shocked region, by its interaction with the ejected material. In the light of astrophysical and laboratory-condition MHD simulations, the plasma dynamic is investigated in detailed and the formation of that shell is found to be plausibly responsible for absorption of significant X-ray flux in the astrophysical context.

2.2. State of the art

What we do know, or can infer

In the context detailed above, detection and modeling of the emissions coming from the shocked material is essential because those radiations can influence several aspects of the star-disk system: from the alteration of the physical and chemical structure of the disk around the young star, which affects also the disk's lifetime [Armitage (2010)], to their influence in the formation of exoplanets. More simply, the observation of those radiations allows an insight in the accretion shock dynamic allowing to study its physics and infer important characteristics of the young star, as for instance the accretion rate, assessing our present understanding of the star formation process.

For this purpose, the accretion rate can be inferred by several ways. From the optical band, as detailed by Herczeg and Hillenbrand (2008) or Curran *et al.* (2011), the optical accretion rates can be calculated through an empirical relation between the accretion and line luminosities described as

$$logL_{acc} = a + b \times logL_{line} \tag{2.1}$$

where L_{acc} is the accretion luminosity, L_{line} is the line luminosity, and the coefficients a and b are empirical and were calculated by comparing optical emission-line fluxes and accretion luminosities measured from the UV continuum excess in a large sample of CTTSs [Herczeg and Hillenbrand (2008)]. Once the line luminosity L_{line} is derived from the observed optical spectra, the accretion luminosity, L_{acc}, is determined through Equation 2.1. Then, assuming $L_{acc} = \frac{1}{2}M\dot{v}_{ff}^2$, the mass-accretion rate $\dot{M}$ is calculated through the equation

$$\dot{M} = (1 - \frac{R_*}{R_{trunc}})^{-1} \times L_{acc}(\frac{R_*}{GM_*}) \tag{2.2}$$

where R_* and M_* are the radius and mass of the star, R_{trunc} is the truncation radius [Gullbring *et al.* (1998)]. Another way to calculate the optical accretion rate is through the H_α (Hydrogen's Ly_α) full width at 10%, using the equation [Natta *et al.* (2004)]

$$log\dot{M} \sim 12.9(\pm0.3) + 9.7(\pm0.7) \times 10^{-3}H_{\alpha\,10\%}$$

where $H_{\alpha\,10\%}$ is the H_α 10% full width in km.s^{-1} and $\dot{M}$ is in M$_\odot$/yr.

The mass-accretion rate $\dot{M}$ of CTTSs can be derived also from the soft X-ray emission (e.g. Schmitt *et al.* (2005)). In this case the method is based on the following assumptions:

1. the whole soft X-ray emission is entirely due to accreting material and not to coronal plasma

2. the post-shock zone can be described as a stationary isothermal slab of plasma at constant velocity and density

3. strong shock regime.

Under these assumptions, the X-ray mass accretion rate can be derived from the emission measure, EM, value inferred from the soft X-ray emission via

$$\dot{M} = \mu m_H EM \Lambda(T)/(3kT) \tag{2.3}$$

where μ is the mean atomic weight, m_H is the hydrogen mass, $\Lambda(T)$ is the plasma radiative losses per EM unit (emission measure : $EM = \int n_e n_H dV$ [cm^{-3}] ; with unit n_e and n_H the electron and Hydrogen density respectively), k is the Boltzmann constant, and T is the temperature of the hot, shocked slab (see Curran *et al.* (2011) for a detailed description).

We note that in those calculations of both the optical and X-ray mass accretion rates, it is assumed that the stream impacts the stellar surface with free fall velocity from a distance of few R_*. In the case where the hot slab temperature T_1 can be measured, the incoming flow velocity v_0 is inferred by Rankine-Hugoniot equations in a strong shock approximation (see Zel'dovich and Raizer (1966)):

$$N_1 = 4N_0 \; ; \; v_1 = \frac{1}{4}v_0 \; ; \; T_1 \approx \frac{3}{16}\frac{\mu m_H}{k}v_0^2 \tag{2.4}$$

where 0 and 1 denote the *pre* and *post* shock conditions respectively, and the speed are the ones determined in the shock frame, i.e. when the shock is at rest. From that velocity, and through the free-fall assumption, the inner radius is then calculated as $R_{trunc} = (1/R_* - v_{ff}^2/2GM_*)^{-1}$. If T is not measured, it is often assumed $R_{trunc} \sim 5R_*$.

The set of assumptions made above, based on the free fall of disk material from the inner edge of the disk through magnetized accretion columns, coupled with the strong shock approximation, are the basics of the 1D version of the magnetospheric accretion model. In support to that method, 1D hydrodynamic simulations,which integrate the treatment of the thermal conduction, the radiative cooling of the optically thin plasma, the gravity stratification, and a detailed description of the stellar chromosphere, can help to refine that model [Sacco *et al.* (2008, 2010)]. It was shown in particular the important

effect of the sinking of the impacting stream into the chromosphere, that could affect the observability of the accretion shock. More recently, 1D hydrodynamic simulations with the additional description of radiative transfer went in support to the previous studies [Costa *et al.* (2017)], and have shown the importance of heating of the pre-shocked plasma by absorption of X-ray radiation coming from the shocked plasma. This pointed out that most of the UV emission could originate from that heated "precursor".

Open questions

However, the inability of those models to reproduce the lower than expected X-ray flux brought up the necessity to develop more exotic situations by the way of 2D simulations. Among plausible scenarii modeled by this way we evoke the following: a clumpy structure of the accretion stream, an oblique impacting surface or an energy flux present in the chromosphere [Matsakos *et al.* (2013)]; nonuniform magnetic field topology near the shocked region [Orlando *et al.* (2013)]; the exploration of wide range of initial $\beta = \frac{Ram\ pressure}{Magnetic\ pressure}$ parameter [Orlando *et al.* (2010)]. The latter, through the 2D description of the impact region, shed light on plausible development of ejection of matter at the border of the impacting column in the case of moderate β values, while Bonito *et al.* (2014) have shown the effect of local absorption in reducing the X-ray flux by the accretion column material itself overhanging the hot slab.

However those simulations, up to now limited to 2 dimensional studies suffer, in the specific plasma dynamic that they bring to light, from a lack of effective comparison with astrophysical observation regarding that plasma dynamics. This limitation comes from the fact that, the observed stars are too far to allow the impacting column to be resolved with nowadays telescopes. For instance, the nearest T Tauri star from our Sun, TW Hydrae, is situated at $180\,light-years$ (see Figure 2.3 left). The *Chandra* telescope has a resolution of 0.2 *AU* at a distance of 0.2×10^8 *AU*, i.e. the nearest star from the sun, Proxima Centauri. It corresponds to a maximum resolution of an object of radius 20 solar radii, while CTTSs have radius of $1-2$ solar radii.

Interest of laboratory investigations

In this view, laboratory experiments, and especially laser-created plasma experiments, through the high energy density plasmas that they can create and the set of diagnostics that they can use, offer a platform to help understanding accretion plasma dynamics, with both time and space resolution.

Up to now, in the context of accretion shock, experiments were used to model the impact of a plasma flow onto an obstacle through the so-called "shock-tube" setup. This one consists in creating a plasma expansion at the rear face of a target irradiated on its front
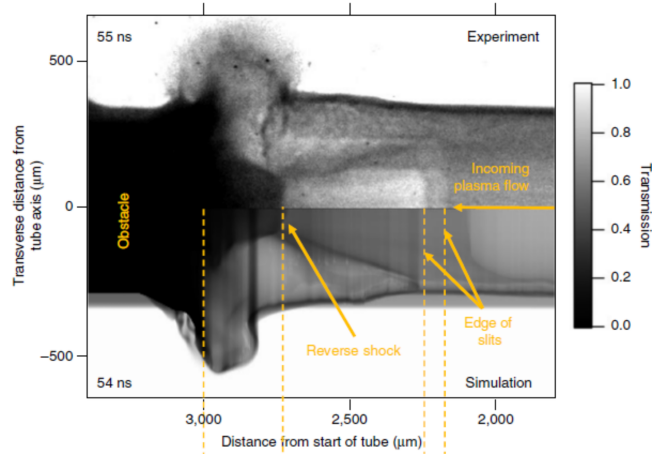
Figure 2.5.: Accretion shock experiment in the laboratory using a "shock-tube" setup at the Orion facility (UK). The plasma flow impacting the obstacle creates a reverse shock that propagate in the incoming flow. The dynamic is diagnosed using X-ray radiography. Extracted from Cross *et al.* (2016).

face by a high power laser ($I_{Laser} \sim 10^{14}\,\mathrm{W.cm}^{-2}$). This laser irradiation launches a shock that propagates in the target, comes out at its rear surface and starts an expansion of the target material. This expansion is then guided with the help of a cylindrical tube to finally hit an obstacle at the other edge of the tube. The supersonic plasma flow thus formed propagates with typical speed of $v_{flow} \sim 200\,\mathrm{km.s}^{-1}$, temperature of $T_{flow} \sim 2\,\mathrm{eV}$, and density of $\rho_{flow} \sim 3.10^{-2}\,\mathrm{g.cm}^{-3}$ [Cross *et al.* (2016)]. However if that setup presents some clear benefits as a highly collisional plasma flow, necessary for the formation of the shock, and a good scalability with astrophysical-relevant situation (especially with binary system kind of accretion: the so-called cataclysmic variables [Busschaert *et al.* (2013)]), it obviously lacks a magnetic field and tube edges apply strong constraints on the plasma dynamic especially near the shock region, as seen in Figure 2.5, where tube edges destruction is clearly visible.

An other noticeable use of the shock tube setup is in the configuration of launching the coming out shock at the rear face of the target in a gas medium filling the cylindrical tube. This shock propagates at supersonic velocity from tens to hundred of $\mathrm{km.s}^{-1}$ depending of the amount of energy deposited in the target ($60\,\mathrm{km.s}^{-1}$ for a 60J/1ns laser up to a $150\,\mathrm{km.s}^{-1}$ for 4kJ/1ns laser). The high Z gas, usually Xe gas, allows to generate strong radiations by the multiple, dominant bound-bound transitions of the high Z material, and is a common setup for the study of radiative shocks in a 1D configuration. In this configuration, the interplay between radiation and opacity changes the plasma conditions upstream of the shock and creates a "precursor" of enhanced temperature and density, in contrast to the sharp usual shock transition in standard shock propagation. This is susceptible to change the shock hydrodynamic and propagation conditions [Bouquet *et al.* (2004); Chaulagain *et al.* (2015)].

2.3. Accretion in the laboratory using a magnetically collimated jet

2.3.1. Experimental Setup

We present hereafter a new experimental setup using the magnetically collimated jet described in chapter 1. The present accretion shock experiment was performed at the ELFIE facility (Ecole Polytechnique, France). We used of the $60\,\mathrm{J}/0.6\,\mathrm{ns}$ chirped laser pulse, focused on a primary target (PVC material : C_2H_3Cl) onto a $700\,\mu\mathrm{m}$ diameter focal spot ($I_{max} = 1.6 \times 10^{13}\,\mathrm{W.cm^{-2}}$) for the plasma expansion creation. The front face, laser-created plasma expanding from the primary target, is collimated by the way of a $20\,\mathrm{T}$ externally applied magnetic field, giving birth to a plasma jet with a high aspect ratio ($length/radius$) still embedded in the homogeneous magnetic field.

The characteristics of the jet can be found in section 1.2 of the chapter 1. We hereafter, recall it principal characteristics. The jet propagates at $1000\,\mathrm{km.s^{-1}}$; that is for its smallest detectable tip density ($n_e \sim 5 \times 10^{16} - 10^{17}\,\mathrm{cm^{-3}}$ through interferometry), while the $n_e \sim 1.5 \times 10^{18}\,\mathrm{cm^{-3}}$ front propagates at $750\,\mathrm{km.s^{-1}}$. The electron density then stays quite constant with time and distance while the velocity of the jet is expected to decrease as t^{-1} and the ion density to increase as $-t^{-2/\gamma-1}$, as from a near adiabatic expansion (see chapter 1). As shown in Figure 2.6, this jet, mimicking the accretion column, is launched onto a secondary target (Teflon material : CF_2), that mimics the stellar surface. At the obstacle location, through the impact with the incoming jet, a reverse shock going up the incoming flow is expected to develop. Contrary to the shock-tube setup shown in Figure 2.5, the entire dynamic is embedded in an external magnetic field, and the edge-free propagation of the flow allows specific plasma motion to freely develop at the border of the reverse shock. The specific Helmholtz coil we used, designed to work in a laser environment, is represented in Figure 2.7. Then, by the use of the same set of diagnostics detailed in the chapter 1 for characterizing the astrophysical jet dynamic, the near obstacle
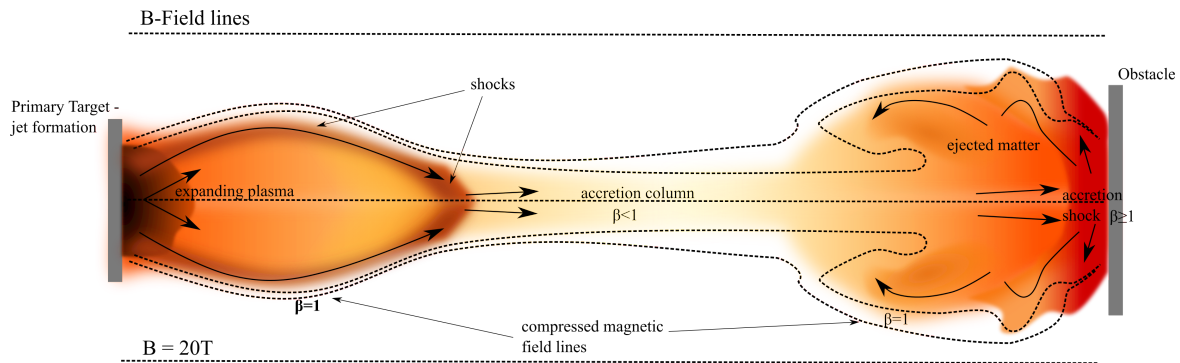
Figure 2.6.: Cartoon of the experimental accretion experiment we performed using a magnetically collimated supersonic flow generated by a laser.
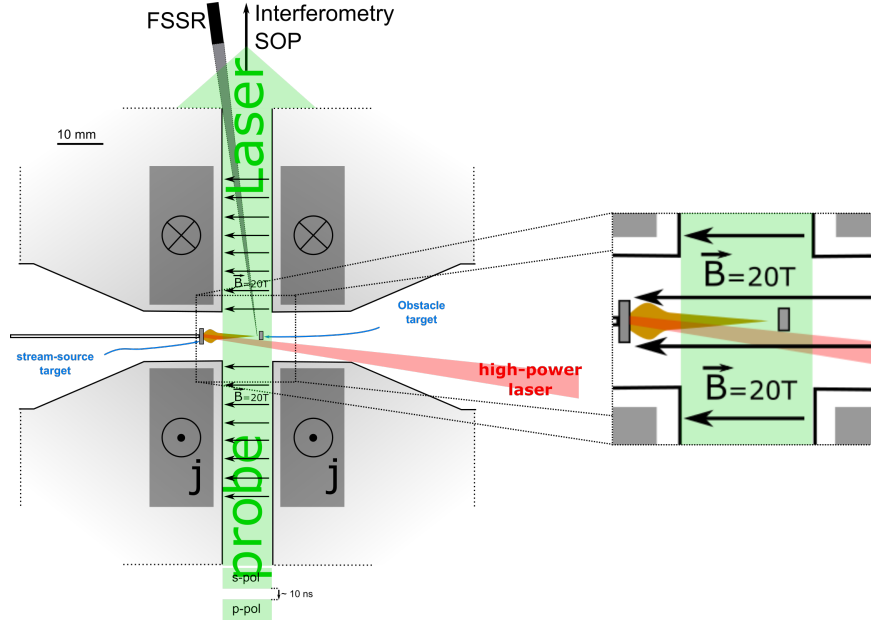
Figure 2.7.: Cartoon showing the top view of the central coil-region of the experimental set-up and the diagnostics paths. The grey rectangle represents the Helmholtz coil, inside the airtight structure, delivering a magnetic field in the central region up to 20 T [Albertazzi *et al.* (2013)]. The conical apertures allow the insertion of the stream-source target as well as the main laser beam to reach the stream-source target without clipping the obstacle target. The obstacle target is inserted from the bottom of the coil through a vertical aperture. The probe beam travels along the coil following the perpendicular aperture, going through the interaction region.

region is studied. Recalling those diagnostics, the interferometry (Mach-Zehnder) was performed using the probe laser ($100\,\mathrm{mJ}/ \sim$ ps) at 2ω ($528.5\,\mathrm{nm}$ wavelength) in order to probe the low-density region ($5.10^{16}\,\mathrm{cm}^{-3} < n_e < 10^{20}\,\mathrm{cm}^{-3}$). The Self Optical Pyrometry (Streak self emission measurement) and the X-ray spectroscopy (FSSR spectrometer) are also present.

In addition to these, X-ray radiography was performed in order to probe the denser part of the plasma dynamic ($n_e > 10^{20}\,\mathrm{cm}^{-3}$), i.e. very close to the obstacle surface. The set-up of this X-ray radiography setup can be found in the Annex (section A.2). The X-ray radiography was performed using the short pulse of the facility ($2.5\,\mathrm{J}/320\,\mathrm{fs}/10\,\mu\mathrm{m} \Rightarrow I_{max} \sim 5 \times 10^{18}\,\mathrm{W.cm}^{-2}$ at 2ω), and focused on a glass (SiO_2) stalk. The laser pulse is focused thanks to a f/3 parabola onto the stalk situated at one of the entrance of the radial tube of the magnetic coil. The X-ray generated by the hot electron created through the interaction between the glass and the laser are emitted isotropically, of short duration (ps), and strongly dominated by the Silicon cold K- emission line at $\sim 1740\,\mathrm{eV}$ [Chen *et al.* (2016)]. As the glass stalk is oriented in the same axis as the radial tube managed in the coil, and as the stalk is tapered into a point-like tip on which the short-pulse laser is shooting, the X-ray emission will originate from a point source from the point of view

of the plasma. It produces on an Image Plate [Meadowcroft, Bentley, and Stott (2008)], situated at the opposite side of the radial tube, a sharp projected 2D transmission map of the X-rays as they go through the denser plasma regions. The reader should refer to the Annexe (section A.2) for a detailed description of the X-ray radiography analysis method.

2.3.2. Scalability with the astrophysical situation

The ideal MHD regime

To understand the astrophysical relevance of the laboratory setup, we now address the scalability between the two systems. Scaling the laboratory flows to astrophysical flows relies on the two systems being described accurately enough by ideal MHD Ryutov *et al.* (2001). For the experiments this generally means to generate a relatively hot, conductive and inviscid plasma so that the relevant dimensionless parameters, namely the Reynolds number ($R_e = L \times v_{stream}/\nu$; L the characteristic size of the system ; v_{stream} the flow velocity ; ν the kinematic viscosity Ryutov *et al.* (1999)), Peclet number ($P_e = L \times v_{stream}/\chi_{th}$; χ_{th} the thermal diffusivity Ryutov *et al.* (1999)) and Magnetic Reynolds number ($R_m = L \times v_{stream}/\chi_m$; χ_m the magnetic diffusivity Ryutov, Drake, and Remington (2000)) are much greater than one. This ensures the momentum, heat and magnetic diffusion respectively to be negligible with respect to the advective transport of these quantities. In addition to these dimensionless numbers we also consider the acoustic Mach number $M = v_{stream}/c_s$, where $c_s = \sqrt{\gamma(Z k_B T_e + k_B T_i)/m_i}$ is the sound speed, and the Alfvén Mach number $M_A = v_{stream}/v_A$, where $v_A = \sqrt{B^2/(\mu_0 \rho)}$ is the Alfvén speed. We precise here that a detailed description of the way plasma parameters are calculated is given in the Annex (section A.1).

The ion mean free path (mfp) should also be smaller than the typical length scale ($L \sim 0.1\,\mathrm{cm}$) of the laboratory experiment. Regarding this mean free path, we distinguish between the ion thermal mean free path, $mfp_{i\,th}$, and ion the directed mean free path, $mfp_{i\,dir}$. These two mean free paths are defined from their respective collision rates $\nu_{i\,th}$ and $\nu_{i\,dir}$ Trubnikov (1965):

$$\nu_{i\,th} = \frac{Z_s^2 Z_i^2 e^4}{12(\pi \varepsilon_0)^2} \frac{n_i \pi^{\frac{1}{2}}}{m_i^{\frac{1}{2}} (kT_i)^{\frac{3}{2}}} ln\Lambda = 4.8 \times 10^{-8} Z_s^2 Z_i^2 n_{i\,[cm^{-3}]} \mu^{-\frac{1}{2}} T_{i\,[eV]}^{-\frac{3}{2}} ln\Lambda_{i/i} \qquad (2.5)$$

$$\nu_{i\,dir} = \sum_{s=i}^{e} \left[\left(1 + \frac{m_i}{m_s}\right) \psi(x^{i/s}) \right] \nu_0^{i/s} \qquad (2.6)$$

with

$$\psi(x^{i/s}) = \frac{2}{\sqrt{\pi}} \int\limits_{0}^{x} t^{1/2} e^{-t} dt \, ; \quad x^{i/s} = m_s v_i^2 / 2kT_s$$

and

$$\nu_0^{i/s} = \frac{Z_s^2 Z_i^2 e^4}{(4\pi\varepsilon_0)^2} \frac{4\pi n_s}{m_i^2 \Delta v^3} ln\Lambda = 2.4 \times 10^{-4} Z_s^2 Z_i^2 n_{s\,[cm^{-3}]} \mu^{-2} \Delta v_{[km\ s^{-1}]}^{-3} ln\Lambda_{i/s}$$

where s = ion or electron: the field particles on which the ion test particle is colliding. μ is the ion mass in proton mass unit ($\mu = \frac{m_i}{m_p}$), e the elementary charge, ε_0 the vacuum permittivity, Z_i and Z_s are the ion charge state of the test and field particles respectively, and $ln\Lambda_{i/s}$ is the Coulomb logarithm Huba (2016). We note $\nu_{i\,th}$ to be a limit case of $\nu_{i\,dir}$ for $x^{i/s} \ll 1$, this is to say when the thermal energy of the field particles dominates the directed energy of the test particle.

Finally, $mfp_{th} = v_{r\,th}/\nu_{i\,th}$ with $v_{r\,th} = \sqrt{\frac{2T_i}{m_i}}$ the relative ion thermal velocity, integrated over a Maxwellian velocity distribution (the factor 2 comes from the reduced mass). The thermal mean free path, measures the distance in between two collisions due to thermal motions. In order for the the fluid description of a plasma to be correct, the thermal mean free path should be much smaller than the characteristic size of the system. Similarly, $mfp_{dir} = \Delta v/\nu_{i\,dir}$ with Δv the relative stream speed, $|\boldsymbol{v_i} - \boldsymbol{v_s}|$, between the test ion and the field particles it is colliding in. The directed mean free path accounts for the distance after which a directed momentum (i.e. the stream directed speed) will undergo an isotropization, while colliding with a background of field particles with a Maxwellian velocity distribution.

The initial collision of the stream with the obstacle occurs in reality with an expanding obstacle medium that is ablated from the x-rays generated by the interaction of the laser with the first target. Interferometry and x-rays radiography measurements of the obstacle expansion, at $t = 7$ ns, exhibits electron density that consists of a very sharp gradient from the solid density (the experimental measurement is limited at $n_e \sim 10^{20}$ cm^{-3}) to $n_e = 5 \times 10^{18}$ cm^{-3} within a distance of 7.5×10^{-3} cm. Following this sharp front, the plasma has a smoother density profiles, consisting of a decrease of the electron density from 5×10^{18} cm^{-3} to 10^{17} cm^{-3} over a distance of ~ 0.13 cm. One dimensional ESTHER simulations matching the experimental expansion indicate a plasma temperature of the obstacle of a few eV ($1 - 5$ eV, corresponding to an ion charge state of about 1.5 for CF_2 in the density range $10^{18} - 10^{19}$ cm^{-3}). The initial stream collision with the obstacle material is effective at the foot of the sharp density gradient. In this region, an electron density $n_e \sim 6 \times 10^{18}$ cm^{-3} corresponds to a directed mean free $mfp_{dir} \lesssim 10^{-2}$ cm of the order of the density scale-height; we have used Equation 2.6 with $T_s = 3$ eV, $Z_i = 2.5$, $Z_s = 1.5$, and

$\Delta v = 750\,\mathrm{km\ s^{-1}}$. From that "stopping point", stream-particles are effectively collisional with the background plasma, the particles loose there directed momentum, and ram pressure is transformed into thermal one at a shock which starts to propagate up the incoming flow.
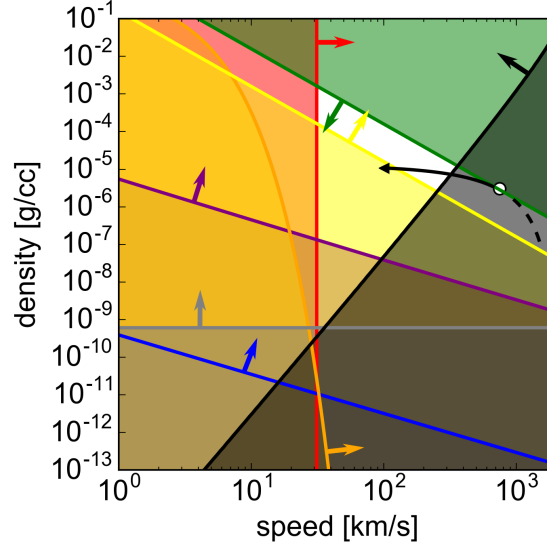
Figure 2.8.: Density-speed scalability diagram for the young star accretion experiment. Each filled-in part of the diagram displays unwanted regions regarding dimensionless numbers. Red : $Mach < 1$; Blue : $R_e < 1$; Orange : $R_m < 1$; Purple : $P_e < 1$; Gray : $mfp_{ther} > L/10$; Black : $mfp_{dir} > L/10$; Yellow : $\beta_{dyn} < 1$; Green : $\beta_{dyn} > 10$. The dimensionless numbers are calculated using the experimental plasma conditions : $L = 0.1\,\mathrm{cm}$ ($\sim$ stream radius) ; $T_e = T_i = 10\,\mathrm{eV}$ (except for the mfp_{dir}, see main text) ; $A = 10.4$; $B = 20\,\mathrm{T}$. The white area then represents the area for which the dimensionless numbers respect the scaling constraints. The white point represents the location in the diagram of our initial plasma stream ($v_{stream} = 750\,\mathrm{km\ s^{-1}}$; $\rho_{stream} \sim 3 \times 10^{-6}\,\mathrm{g.cm^{-3}}$ - $n_e \sim 1 \times 10^{18}\,\mathrm{cm^{-3}}$). The black curve associated to it, materializes the progressive change over time of the stream conditions, following the 1D self-similar expansion of a reservoir with density $\rho_0 = 3 \times 10^{-5}\,\mathrm{g.cm^{-3}}$,an adiabatic index of $\gamma = \frac{5}{3}$, and an artificially increased initial sound speed (in order to match the plasma maximum expansion speed seen experimentally) - see subsection 1.2.5. The dashed curve being the condition before the $v_{stream} = 750\,\mathrm{km\ s^{-1}}$ component. To assist the reading of the plot, the arrows anchored to the solid lines indicate the direction for which we obtain the wanted plasma conditions.

While the shock progresses within lower density values of the obstacle medium, and as soon as the density of the obstacle medium becomes sufficiently small compared to the density jump of the compressed stream ($n_{ps} = 4 \times n_{stream}$ in a strong shock approximation Zel'dovich and Raizer (1966) - the subscript ps stands for *post shock*) it is better to consider the directed mean free path for the collision between the ions of the stream and the ions and the electrons of the stream medium itself, which has already been
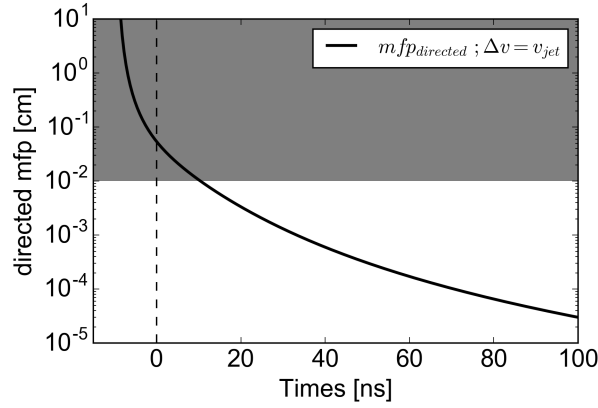
Figure 2.9.: Directed mean free path as a function of time, at the obstacle location, i.e. $\sim 1.2\,\text{cm}$ from the stream target, following the 1D self-similar model. The gray area displays the transition region for which $mfp_{dir} = L/10 = 10^{-2}\,\text{cm}$, where the shock front size over which the particle are stopped becomes sufficiently small compared to the characteristic size of the system L, i.e. the stream radius (see also discussion linked to Figure 2.8). The time in the abscissa takes its origin at the $750\,\text{km}\,\text{s}^{-1}$ plasma component arrival time, as also highlighted by the vertical dashed line.

stopped and shocked. Hence, in Equation 2.6 we take the strong shock condition for the density, i.e. $n_i = 4 \times n_{stream}$, justified by large stream sonic Mach number (see later in the text and Table Table 2.1). For the temperatures, we take $T_e \sim T_{stream} = 10\,\text{eV}$ and $T_i = (\frac{3}{16 \times (Z+1)})m_i v_i^2$, expected to be the electrons and ions temperatures just after a strong shock Zel'dovich and Raizer (1966), and before electron and ion temperature equilibration occurs. We note this temperatures equilibration time to be relatively long and to vary, regarding the density and speed evolution of the stream over time, from about 10 to 50 ns.

Figure 2.8, shows a density-speed diagram with filled-in parts representing the unwanted regions regarding the parameters detailed above, while the white area represents the region in the speed-density space for which ideal MHD conditions are satisfied. The white point represents the location in that diagram of our initial plasma conditions. Then, one can see that, while the flow is supersonic ($M_a = 24 \gg 1$ -see also Table Table 2.1 for a list of plasma parameters), the viscosity can be neglected ($R_e = 5 \times 10^6 \gg 1$), the magnetic field is preferentially advected than dissipated in the plasma ($R_m = 68 \gg 1$), the heat advection is dominant over the heat conduction ($P_e = 7 \times 10^2 \gg 1$) and that we are in presence of a collisional plasma within the stream itself ($mfp_{ther} \ll L$). This constitutes the necessary conditions for our plasma to be treated in the ideal MHD framework.

However, we understand the directed mean free path of the flowing stream particles within the shocked previously stream material (black region) to be too large in the initial condition of the stream. Figure 2.9 gives an evolution of that mean free path over time using the 1D self-similar expansion. The time in that figure takes its origin when the $750\,\text{km}\,\text{s}^{-1}$ plasma component arrives at the obstacle location. Hence, one can consider

that after 10 ns following the latter component impact, the particles are stopped over a sufficiently small distance (10^{-2} cm) in the previously shocked stream material to allow the proper shock formation and propagation. Taking into account that the first collision occurs within the very dense obstacle material, and taking into account the time needed for the shock to propagate and to leave that dense obstacle regions, we could consider the plasma conditions to be, at any time, proper for the shock to form and to propagate away from the obstacle, within the stream material.

Relevance of the experiments to the accretion in Classical T Tauri stars

As detailed in the introduction, it exists a variety of matter accretion regimes, from Classical T Tauri Stars to Cataclysmic Variables through Herbig Ae/Be objects, regarding the accretion flow density, velocity and magnetic field strength effectively present in these systems.

The laboratory and astrophysical accretion columns are well described by ideal MHD (in the astrophysical case this is often true due to the very large spatial scales involved) and in order for them to evolve similarly one should verify that the Euler ($Eu = v\sqrt{\rho/P}$) and Alfvén ($Al = B/\sqrt{\mu_0 P}$) numbers are similar in the two system Ryutov *et al.* (1999, 2001). We define these parameters in the *post-shock region*, where the interaction of the plasma with the magnetic field is largely responsible for determining the accretion shock dynamic regime Orlando *et al.* (2010). From the Rankine-Hugoniot relations for a strong shock Zel'dovich and Raizer (1966), which are valid for hypersonic flows with $M_a = v_{stream}/c_s \gg 1$ (i.e. $\rho_{stream} v_{stream}^2 \gg n_{stream} k_B T_{stream}$), the post-shock pressure is given by $P_{ps} = \frac{3}{16 \times (Z+1)} \rho_{stream} v_{stream}^2$, $\rho_{ps} = 4 \times \rho_{stream}$, $v_{ps} = v_{stream}/4$. The Euler and Alfvén numbers are then given by $Eu = \sqrt{4(Z+1)/3}$ and $Al = 4\sqrt{(Z+1)/3} \times B/(v_{stream}\sqrt{\mu_0 \rho_{stream}})$. The Euler number only depends on the ion charge state Z, which is just a property of the material used in the experiments (and the ionization reached), while the Alfvén number depends on the incoming stream properties and it is proportional to $\beta_{dyn}^{-1/2}$, the plasma dynamic-β, which is defined as the ratio of the ram to the magnetic pressure, $\beta_{dyn} = \frac{\rho_{stream} v_{stream}^2}{B^2/2\mu_0}$.

The evolution of β_{dyn} (see Figure 2.10), following the density and speed evolution given by the 1D self-similar model, indicates that the experimental stream has typical values in the range $\beta_{dyn} \sim 1-10$. In CTTSs, taking standard ion density of about $10^{11} - 10^{13}$ cm^{-3} Calvet and Gullbring (1998), a magnetic field of few hundreds of Gauss to a kiloGauss Johns-Krull (2007) and a typical free-fall speed of 500 km s^{-1}, the dynamic-β ranges from ~ 0.01 to 10. Which shows that there exists a vast variety of physical conditions in which accretion streams can be found in young stars, and our experiments at 20 T make it possible to model a high dynamic-β (i.e. $\beta_{dyn} > 1$) astrophysical case. Note that, under the same laser irradiation conditions, getting a $\beta_{dyn} = 1$ at its maximum where the whole

accretion dynamic evolves in a magnetic pressure dominated regime necessitates a magnetic field strength of $\sim 60\,T$. Such a magnetic field strength could be achievable using the same split Helmholtz coil technology used in the present setup. Oppositely, using a higher laser irradiation will give access to a higher β_{dyn} dynamic. For this purpose, one can keep in mind the expansion velocity estimate as a function of the laser intensity and wavelength: $v_{[cm.s^{-1}]}^{expansion} = 4.6 \times 10^7 I_{[10^{14}W.cm^{-2}]}^{1/3} \lambda_{[\mu m]}^{2/3}$ Tabak *et al.* (1994).

Another constraint comes into play when considering a comparison with accreting CTTSs for which accretion radiation emanating from the shocked material is effectively observable. Indeed, as the infalling stream impacts the chromosphere, the exact location for which the stream is halted and the shock starts to develop is where the stream ram pressure is equal to the chromospheric thermal pressure. The ram pressure of the impacting stream can induce important sinking of the stream onto the chromosphere before it to be stopped, if one considers a too large density in the stream. As described in the 1D simulation study of Ref. Sacco *et al.* (2010), the shock dynamic can then be buried enough for the accretion emission to be strongly absorbed, and hence hard to detect, which happens for ion stream density above $10^{12}\,cm^{-3}$. Secondly, an ion stream density below $10^{10}\,cm^{-3}$ will give a post-shock emissions that cannot be distinguished from coronal emissions. A reasonable density for which the shock dynamic is sufficiently uncovered and distinguishable is thus found to be about $10^{11}\,cm^{-3}$.

Figure 2.11 represents the ion density as a function of the magnetic field strength for the CTTSs accretion columns. The density restriction discussed above is represented by a gray horizontal rectangle, labeled "unabsorbed accretion emission". Coupling that density constraint to the $\beta_{dyn} \sim 1 - 10$ range of the experimental stream (represented by the two black diagonals), one get the green area. It represents the CTTS accretion
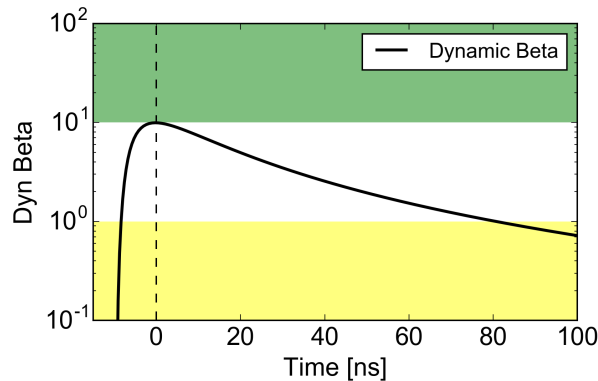
Figure 2.10.: Same as Figure 2.9 for $\beta_{dyn} = \frac{\rho_{stream} v_{stream}^2}{B^2/2\mu_0}$, calculated for $B = 20\,T$. The green area represents the region $\beta_{dyn} > 10$, and the yellow area represents the region $\beta_{dyn} < 1$ -keeping the color label of Figure 2.8. Note that an other interesting information, the ram pressure $\rho_{stream} v_{stream}^2$, is directly readable on that plot by multiplying the β_{dyn} by the magnetic pressure $B^2/2\mu_0 = 160\,MPa$.
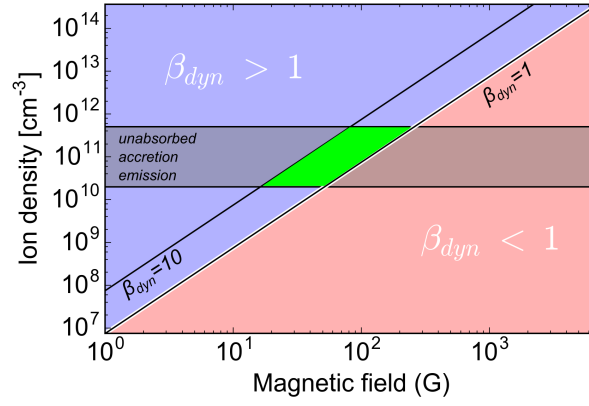
Figure 2.11.: Dynamic-β variation as a function of the magnetic field and the ion density, for a CTTS accretion column with free fall velocity of $500\,\mathrm{km\ s^{-1}}$. The red filled-in part represents the area for which the couple magnetic field - ion density gives a $\beta_{dyn} < 1$, while the blue filled-in zone represents the region for which $\beta_{dyn} > 1$. The separation line, $\beta_{dyn} = 1$, is represented by the white diagonal. Additional black diagonals display the $\beta_{dyn} = 1$ and $\beta_{dyn} = 10$ experimental range. The horizontal gray rectangle highlights the 2×10^{10} - $5 \times 10^{11}\,\mathrm{cm^{-3}}$ density range, corresponding to the observable accretion emission due to the non-absorption of their shocked emissions, through sinking into the chromospheric material (following the study of Ref. Sacco *et al.* (2010) - see text). The green area represents the CTTS ion density and the magnetic field modeled by the experiment − this leads to an accessible magnetic field strength range of $20 - 200\,\mathrm{G}$.

column parameters the experiment is relevant to model. This area already gives a good constraint on the astrophysical magnetic field strength that our experimental setup can model : $20\,\mathrm{G} \lesssim B_{CTTS} \lesssim 200\,\mathrm{G}$. For instance, working with a stream density of $n_{stream} = 1 \times 10^{11}\,\mathrm{cm^{-3}}$, a $\beta_{dyn} \sim 5$ will correspond for the astrophysical situation to a magnetic field strength of $\sim 50\,\mathrm{G}$.

	Laboratory	CTTS
B-Field $[T]$	20	50.10^{-4}
Material	C_2H_3Cl (PVC)	H
Atomic number	10.4	1.28
	Stream	**Stream**
Spatial transversal scale $[cm]$	0.1	0.5×10^{10}
Charge state	2.5	1
Electron Density $[cm^{-3}]$	1×10^{18}	1×10^{11}
Ion density $[cm^{-3}]$	1.9×10^{17}	1×10^{11}
Density $[g.cm^{-3}]$	3×10^{-6}	2×10^{-13}
Te $[eV]$	10	0.22
Ti $[eV]$	10	0.22
Flow velocity $[km\ s^{-1}]$	$100 - 1000$	500
Sound speed $[km\ s^{-1}]$	31	7.4
Alfven speed $[km\ s^{-1}]$	325	304
Electron mean free path $[cm]$	2.7×10^{-5}	0.7
Electron collision time $[ns]$	2×10^{-4}	35
Ion mean free path $[cm]$	1.4×10^{-6}	1
Ion collision time $[ns]$	1.4×10^{-3}	2.4×10^3
Magnetic diffusion time $[ns]$	45	4×10^{21}
Electron Larmor radius $[cm]$	3.8×10^{-5}	2×10^{-2}
Electron gyrofrequency $[s^{-1}]$	1.4×10^8	1.2×10^8
Ion Larmor radius $[cm]$	1×10^{-3}	1
Ion gyrofrequency $[s^{-1}]$	6×10^4	5.2×10^4
Electron magnetization	0.7	30
Ion magnetization	1.4×10^{-3}	0.9
Mach number	24	67
Alfven Mach number	2.3	1.6
Reynolds	5×10^6	6×10^{11}
Magnetic Reynolds	68	4×10^{10}
Peclet	7×10^2	6×10^9
β_{ther}	1×10^{-2}	7×10^{-4}
β_{dyn}	10	5
Euler number	2.9	1.6
Alfven number	2.5×10^{-3}	2.1×10^{-3}

Table 2.1.: Parameters of the laboratory accretion stream, with respect to the ones of the accretion stream in CTTSs, for the incoming stream. The spatial scale corresponds to the stream radius, 0.1 cm for the laboratory stream while the CTTS accretion column radius is chosen to match the MP Mus infalling radius, retrieved through X-ray measurements of the accretion dynamic Argiroffi, Maggio, and Peres (2007). The stream temperature in the astrophysical case is chosen in order to obtain a stream at thermal equilibrium with the corona. The flow velocity in the laboratory case indicates the full speed range experienced by the stream during its expansion, as described by the 1D self-similar expansion in the subsection 1.2.5. The parameters below are however calculated for a stream speed of $750\,\mathrm{km}^{-1}$, which is the speed of the $1 \times 10^{18}\,\mathrm{cm}^{-3}$ electron density front.

2.4. Experimental results and comparison with the astrophysical situation

2.4.1. Plasma dynamic

Following the accretion setup described above, we present in Figure 2.12 a comparison of the plasma dynamic at three different times in both the laboratory case and the astrophysical one. The top panel represents experimental 2D volumetric electron density maps (in $[10^{19} \, \text{cm}^{-3}]$) as recorded through interferometry measurements. The bottom panel represents the results of 2D astrophysical MHD simulation performed with the astrophysical PLUTO code [Mignone *et al.* (2007)] that solves the MHD equations following the Godunov's scheme, particularly adapted to treat the astrophysical flow in the presence of discontinuities. It takes into account optically thin radiative losses and an anisotropic thermal conduction. The simulation represents here the impact onto a chromosphere of a stream whose characteristics correspond to the parameters presented in the right column (CTTS) of Table 2.1. The left panels on those maps represent the ion (Hydrogen) density in $[\log \, \text{cm}^{-3}]$, while the left panels represent the plasma temperature in $[\log \, \text{K}]$. The experimental volumetric electron density is retrieved from Abel inversion of the integrated density, and both left-right panels on each side of the axis center of the image are treated independently. Then, the obvious similarity of both panels validate *a posteriori* the cylindrical symmetry and the proper use of the Abel inversion.

On those electron density maps, the incoming stream comes from the top and propagates to the bottom where the obstacle is located. The different times labeled on the top right corner take their origin when the $750 \, \text{km.s}^{-1}$ jet component impacts the obstacle. The jet-creation target and the obstacle one being separated by $11.7 \, \text{mm}$, this component reaches the obstacle target location $\sim 15.6 \, \text{ns}$ after the laser interaction on the first target. At the impact with the obstacle, a dense region is clearly appearing to form, labeled *Core* in the first two time frames of the astrophysical and laboratory maps.

This dense slab presents an electron density of $\sim 1.5 \times 10^{19} \, \text{cm}^{-3}$ for the laboratory case and an ion density of $\sim 2 \times 10^{11} \, \text{cm}^{-3}$ for the astrophysical simulation case. While it corresponds to a jump of factor four in density in the astrophysical case, i.e. exactly what is expected in the strong shock configuration (see Equation 2.4), it corresponds to a factor 10 in electron density in the laboratory situation. However, taking into account the additional ionization experienced by the plasma under the shock, one can find $n_1 = 4n_0 \times (Z_1/Z_0) = 4n_0 \times (5.3/2.67) = 8n_0 = 1.2 \times 10^{19} \, \text{cm}^{-3}$, in good agreement with the slab density measured experimentally. This dense slab, corresponding to the density jump expected from the strong shock approximation, is then believed to be the reverse shock, namely the accretion shock, that goes upward the incoming flow. Figure 2.13 displays that density jump in both situations, by the way of lineouts in the z direction. While
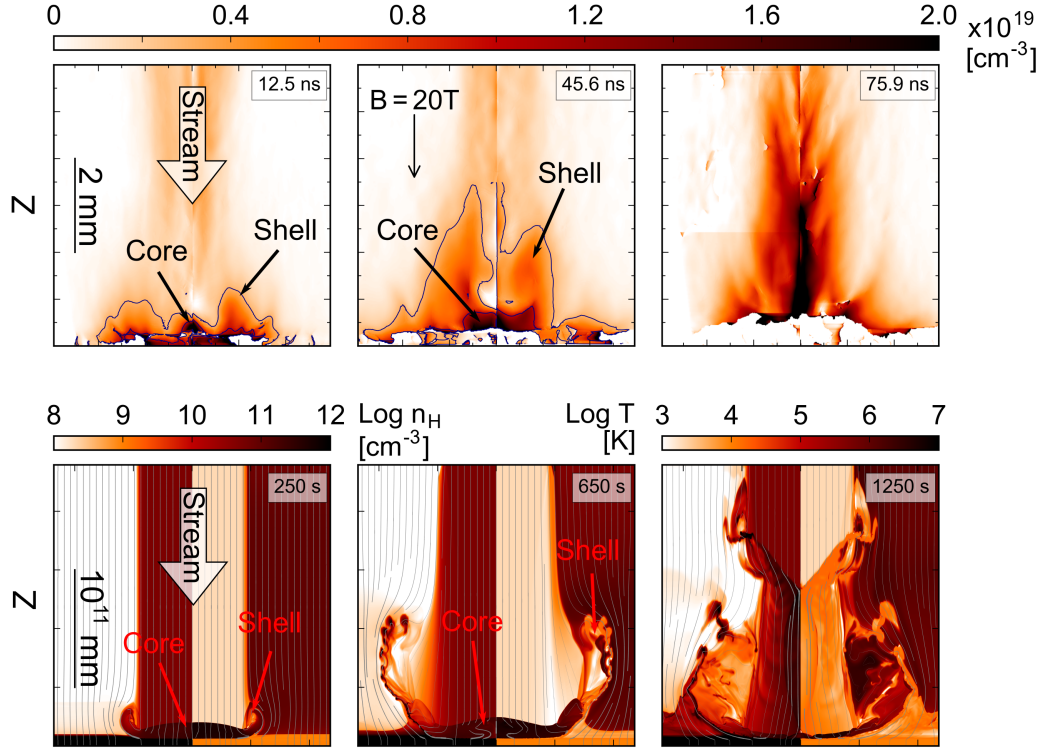
Figure 2.12.: Astro-Labo plasma temporal dynamics comparison. The *top* row represents experimental volumetric electron density maps (in cm^{-3}), which are Abel inverted from interferometry measurements. The *bottom* row displays astrophysical simulation results using the code PLUTO. Presented is the volumetric ion density maps in log cm^{-3} (left panels) and the plasma temperature in log K (right panels). On those maps, the infalling stream comes from the top to the bottom where is located the obstacle. The magnetic field, initially uniform in space, can be tracked in its evolution by the gray lines (representing the B field lines) in the astrophysical simulated maps.

averaged along 3.5×10^9 cm in the radial direction for the CTTS case, it is averaged along $100 \, \mu$m on both side of the Abel inversion axis in the laboratory case (with the $50 \, \mu$m region directly around the axis removed from the calculation because of the unphysical, divergent density values created in this region by the Abel inversion transform). In both cases, it is possible to follow the propagation of the shock front over time, which yields a velocity of $13.7 \, \mathrm{km.s}^{-1}$ and $50 \, \mathrm{km.s}^{-1}$, for the laboratory and the astrophysical shock respectively.

Then from that dense, shocked slab created at the impact, one can see on the maps of Figure 2.12 ejecta of matter at the border of the jet, labeled *Shell.* Those ejecta come from leaks at the border of the shocked slab, from which the dense plasma expels out the magnetic field lines. While being ejected out, this matter compresses the magnetic field lines (see the astrophysical simulated map of Figure 2.12 for a visualization of the magnetic field lines, and especially the 650 s frame) and is then stopped in its motion at a point
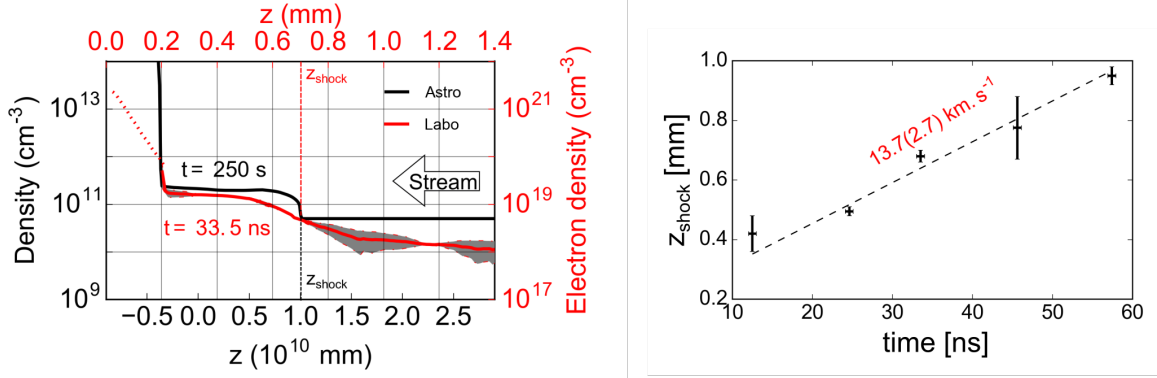
Figure 2.13.: *Left:* Laboratory and astrophysical density jump at the shock location. The laboratory profile is drawn in red (solid line: interferometry ; dashed line: X-rays radiography), and the astrophysical profile is drawn in black. The uncertainties on the experimental data are highlighted by the gray area. Those error bars are calculated via the differences between the left and right parts (with respect to the Abel inversion axis) of the electron density maps.
Right: Experimental shock front location as a function of time, determined from the interferometry data. Error bars are defined as the width of the shock.

where magnetic pressure and plasma pressure (kinetic + dynamic) are equal. It is then recollimated to the central axis of the system (see the experimental frame at 45.6 ns and the CTTS frame at 650 s) to finally enter the stream and completely disturb the incoming flow (see the experimental frame at 75.9 ns and the CTTS frame at 1250 s). One can note the striking similarity between the shock formation as well as the shell development between the astrophysical dynamic and the experimental one. As confirmed by Figure 2.14, which shows the contribution of the stream and the chromosphere separated through a specific tracer in the Pluto code, the shell is mainly made of stream material rather than chromosphere/obstacle material. This confirms the shell formation scenario from which the stream material shocked after the impact with the chromosphere/obstacle is ejected out of the infalling column to give birth to the shell, then wrapping around the dense slab.

When looking in details at the shock velocity in the context of Rankine-Hugoniot (R-H) equations, we should expect in the strong shock approximation ($M_a \gg 1 \Rightarrow v \gg c_s \Rightarrow \rho v^2 \gg nkT$), and for an adiabatic process:

$$N_1 = \frac{\gamma+1}{\gamma-1} N_0 \ ; \ v_1 = \frac{\frac{2}{\gamma-1} v_{shock} + v_0}{\frac{\gamma+1}{\gamma-1}} \ ; \ P_1 = \frac{2\rho_0}{\gamma+1} v_0^2 - \frac{\gamma+1}{\gamma-1} P_0$$

Using the adiabatic index $\gamma = 5/3$ (monatomic gas), and a perfect gas (for which the

pressure can be defined as $P = (\gamma - 1)\rho\epsilon = nkT$, where $\epsilon = \frac{3/2nkT}{\rho}$ is the specific internal energy), one gets:

$$N_1 = 4N_0 \; ; \; v_1 = \frac{3v_{shock} + v_0}{4} \; ; \; T_1 = \frac{3}{16}\frac{\mu m_H}{k}v_0^2 - \frac{T_0}{16}$$

for which the speed is here given in the reference frame of the piston, i.e. the obstacle. Again, the label "0" indicates the pre-shock conditions, while "1" indicates the post-shock conditions. Following the R-H equations for the speed, and expecting the particles to be, after the shock, at the velocity of the obstacle (i.e. the piston), one finds: $v_1 = 0 \Rightarrow |v_{shock}| = |\frac{1}{3}v_0| = 333 - 116\,\text{km.s}^{-1}$ for v_0 ranging between $1000\,\text{km.s}^{-1}$ (for the $1 \times 10^{17}\,\text{cm}^{-3}$ plasma component) to $314\,\text{km.s}^{-1}$ (for the denser plasma component). In any cases, those shock speeds are lower than the one experimentally observed ($13.7\,\text{km.s}^{-1}$), while the density jump seems in good agreement with the expectation of R-H equations. Taking the speed equation to determine the under-shock velocity, in the frame of the piston, in order to get the right shock velocity, one finds: $v_1 = 260 - 89\,\text{km.s}^{-1}$, for the same range of incoming speeds detailed just above. This means that in order to retrieve the shock speed experimentally observed, one should allow a mass flux to propagate out from the under-shock region, with an escaped speed (v_1) corresponding to the one calculated just above. Having matter flowing at such velocity could naturally be explained by the leakage of matter experimentally observed at the border of the jet that makes the creation of the shell possible. Regarding this point, one could argue that the enabled cooling by optically thin radiation of the shocked material would then make possible a greater compression (lower γ factor), and hence induce a slower shock propagation. However, the same shock speed inconsistency is found in the astrophysical simulations for which the post shock density and temperature are precisely the one expected from the strong shock R-H equations, while the γ factor is defined as a constant, equal to $5/3$. In this case, the lower shock speed observed in the simulation is likely due to the enabled leak of matter at the border of the shocked slab of stream material.

2.4.2. Temperature characterization

If the experimental shocked slab is dense, and corresponds to the density jump of the Rankine-Hugoniot strong shock equations, the temperature has also to be determined. To do so, optical emission, through Streaked Optical Pyrometer measurement (SOP), and X-ray spectroscopy, through FSSR spectrometer measurement, are performed.
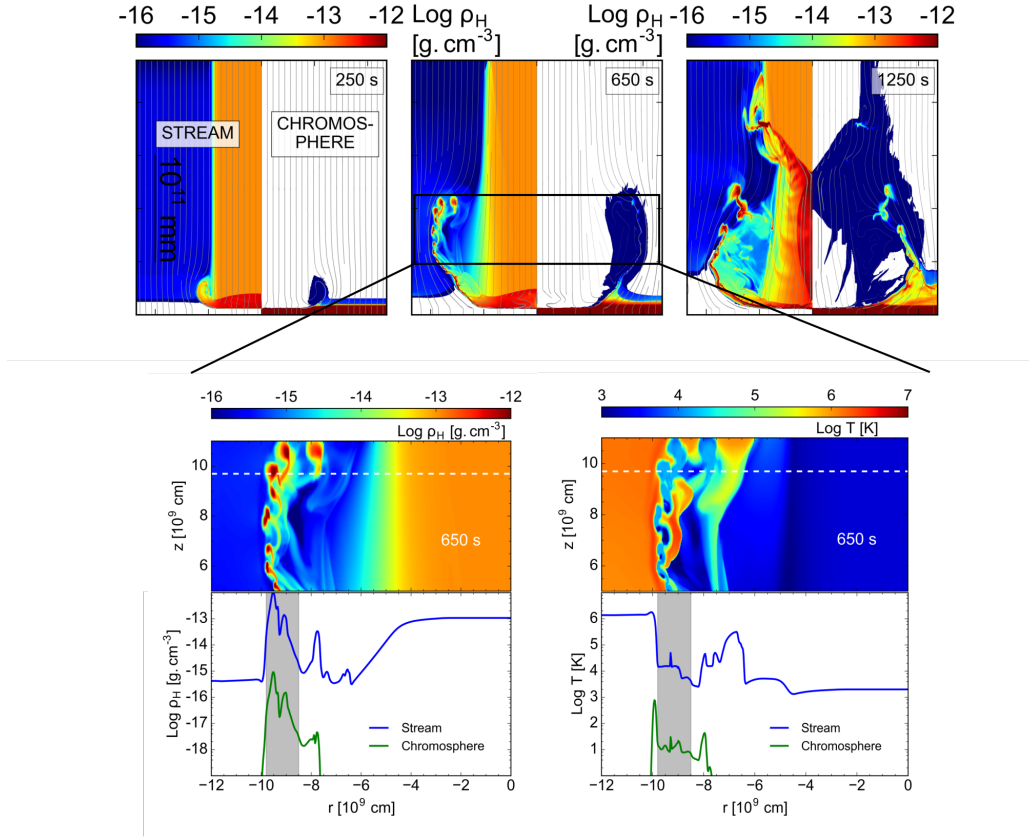
Figure 2.14.: Astrophysical simulation (Pluto code) displaying the Stream + corona (*left* panels) and chromospheric materials (*right* panels) volumetric mass density [log $g.cm^{-3}$]. A zoom in the Shell region at $t = 650\,s$ is also shown, displaying the mass density as well as the temperature. The different components are separated in the Pluto code thanks to a passive tracer.

Visible Emission

We used a streak camera, in order to collect the self emission coming from the interaction area, close to the obstacle. The different optics, N-KB7 (silica and boron trioxide glass) lenses, aluminum mirrors, neutral densities, color filters, or the response of the photocathode and CCD of the streak camera, give rise to a quite narrow accessible wavelength range ($\Delta\lambda = 200\,nm$), centered in the visible range around $\lambda = 500\,nm$, recorded by the Streaked Optical Pyrometer. This visible emission is collected by the different optics, making an image on a narrow slit at the entrance of the streak camera, which thus collects the emission from the accretion dynamic in a 1D-like shape (regarding the spatial distribution) centered around the axis of symmetry of the system which corresponds to the axis of symmetry of the Abel inverted volumetric electron density map - see Figure 2.12). This slit allows the light emitted from a zone of 80 µm only around the z axis to be collected into the streak camera. This 80 µm wide plasma region is then time resolved by the streak camera. Figure 2.15 displays a typical SOP of the accretion dynamic.
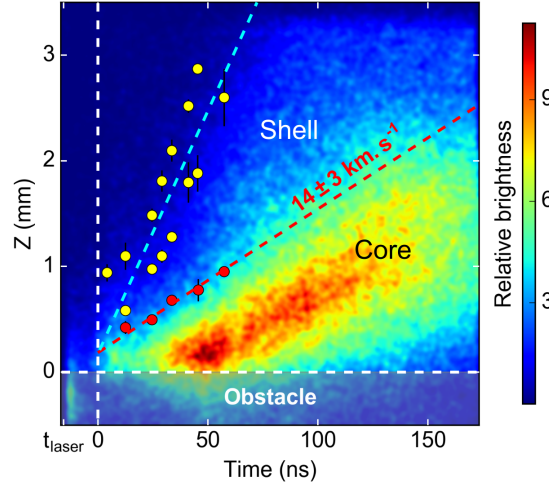
Figure 2.15.: Streaked self emission measurement of the experimental accretion dynamics. The vertical axis indicates the one dimensional spatial axis (Z, in mm), while the horizontal axis indicates the temporal one (in ns). The jet is coming from the top to the bottom where the obstacle surface is located at $z = 0$, following the vertical axis, highlighted by the horizontal dashed white line. The temporal axis takes its origin when the $750\,\mathrm{km.s^{-1}}$ jet component impacts the obstacle, highlighted by the vertical dashed white line. The red dots display the shock front location, as determined via interferometry measurement (see - Figure 2.13 *Left*). The red dashed line represents the linear fit and interpolation of the front shock motion. The yellow dots display the tip of the shell location, using the interferometry measurement. A set of two yellow points is given for a given time as it corresponds to the different locations of the shell on each side of the Abel inversion axis. The blue dashed line represents the linear fit and interpolation of the shell tip motion.

The vertical axis is the spatial one, where the distances are indicated in mm, while the horizontal axis is the temporal one, labeled in ns. Here, the jet comes from the top to the bottom, where the obstacle target is located at $z = 0$. On the horizontal axis, the time takes its origin when the $750\,\mathrm{km.s^{-1}}$ jet component impacts the obstacle. From that measurement, three distinct regions with different values of brightness are distinguishable. When taking the location in time, of the shock front and the shell tip from the interferometry measurement, one can see the striking correlation between those regions of different brightness in the SOP and the location of the regions of the *Core*, *Shell* and *Jet* also distinguishable in the interferometry. Starting from the target location ($z = 0$) and moving away from it ($z > 0$), the *Core* has a high brightness, while the *Shell*, situated further, has a moderate brightness. The *Jet*, finally, presents a lower brightness.

As the diagnostic is looking at emission situated in the visible range, we expect the Bremsstrahlung, free-free emission, to be largely dominant over the bound-free or free-free emissions. For instance, the free-free, bound-free and bound-bound radiations are represented in **Figure 2.16** *Left*. It shows the radiative power for the PVC (C_2H_3Cl) plasma in [erg/s/cm^{-3}/Hz/sr] as a function of the photon energy, zoomed around the

visible range [1.65 - 3] eV, calculated using to the atomic code FLYCHK, for each component of the PVC molecule, then averaged following the stoichiometric weight of each component in the molecule. The plasma characteristics for the calculation are the following: $n_e = 1.5 \times 10^{19}\,\text{cm}^{-3}$; $T_e = 100\,\text{eV}$. As one can see in that figure, within that photon energies range, the Bremsstrahlung emission is quite dominant over the others, bound-free and bound-bound radiations. Hence, we assume that only free-free emission participates to the recorded signal in the SOP diagnostic.

The thermal Bremsstrahlung radiation, for a plasma at thermal equilibrium (Maxwell-Boltzmann distribution on the particles speed) with electron and ion density, n_e and n^i respectively, electron temperature T_e and ionization state Z, can be expressed as follows [Rybicki and Lightman (1985)]:

$$\frac{dW}{dV\,d\nu}(\nu, n, T) = \frac{32\pi^{1/2} g_{ff} Z^2 e^6 n_e n_i}{3 m_e^2 c^3} \left(\frac{2\pi m_e}{3k T_e}\right)^{1/2} exp\left(-\frac{h\nu}{k_B T_e}\right) \ [\text{J/s/Hz/m}^{-3}] \quad (2.7)$$

which gives in CGS units:

$$\frac{dW}{dV\,d\nu}(\nu, n, T) = 6.8 \times 10^{-38} g_{ff} Z^2 n_e n_i T_e^{-1/2} exp\left(-\frac{h\nu}{k_B T_e}\right) \ [\text{egs/s/Hz/cm}^{-3}]$$

Where ν is the photon frequency, and g_{ff} is the gaunt factor, $g_{ff} = log(\frac{b_{max}}{b_{min}})$ with $b_{max} = \frac{v}{2\pi\nu}$ and $b_{min} = \frac{2Ze^2}{m_e v^2}$. For a thermal plasma, we have $v = (3k_B T_e/m_e)^{1/2}$, then it gives $g_{ff} = ln\left((3k_B T_e/m_e)^{3/2} m_e/4Ze^2\pi\nu\right)$. For $g_{ff} = 1$, when integrating Equation 2.7 over the full range of photon frequencies (i.e. from 0 to ∞) , one get $\frac{dW}{dV}(n, T) \propto n_e n_i T_e^{1/2}$, and hence, a total emitted power that increases when increasing the temperature of the emitter plasma, or its density. However, when integrating in a smaller range of photon frequencies, $[\nu_a = \nu_0 - \delta\nu,\ \nu_b = \nu_0 + \delta\nu]$, one get a decrease of the emitted power with the temperature, after a certain point that we call $T_{Br_{max}}$, point that depends on ν_a, ν_b and $\delta\nu$ (see **Figure 2.16** *right)*. It is possible to show numerically this dependency, still in the case where $g_{ff} = 1$, to be well approximated by $kT_{Br_{max}} = (0.376 \times (h\nu_b)^{-1.058} + 1.171) \times (h\nu_a) + (0.865 \times (h\nu_b) - 0.17)$, with $h\nu_a$, $h\nu_b$ and $kT_{Br_{max}}$ in eV energy unit, and $h\nu_a < h\nu_b$ (see Annex section A.3 for a detailed description). For instance, in the case of an integration between $\lambda = 400 - 600\,\text{nm}$, corresponding to the SOP range, the emitted power decreases after $T_{Br_{max}} \approx 5.1\,\text{eV}$. We also note the case where $g_{ff} = 1$ to lead, for $k_B T \gg h\nu_b$, to a decrease as $T^{-1/2}$.

From these latest considerations, we understand easily the decrease of the Bremsstrahlung power with the temperature, for $k_B T > T_{Br_{max}}$, if integrated within a finite range of photon frequencies, $[\nu_a = \nu_0 - \delta\nu,\ \nu_b = \nu_0 + \delta\nu]$. Applied to the self optical emission coming from
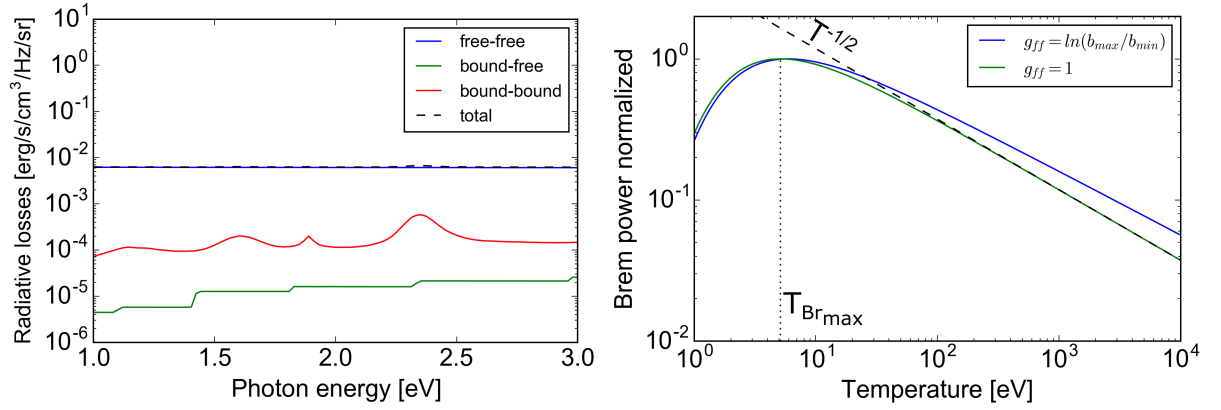
Figure 2.16.: *Left*: Radiation losses for the PVC (C_2H_3Cl) in [erg/s/cm^{-3}/Hz/sr] as a function of the photon energy, zoomed around the visible range [1.65 - 3] eV, and for a plasma with electron density $n_e = 1.5 \times 10^{19}$ cm^{-3} and an electron temperature $T_e = 100$ eV. It is calculated thanks to the atomic code FLYCHK, for each component of the PVC molecule, then averaged following the stoichiometric weight of each component in the molecule.
Right: Normalized Bremsstrahlung emitted power, integrated over a $\lambda = 400 - 600$ nm photon wavelength range, as a function of the plasma electron temperature. The green curve stands for $g_{ff} = 1$ while the blue one stands for $g_{ff} = ln(\frac{b_{max}}{b_{min}})$.

the accretion dynamics displayed in Figure 2.15, this implies a brighter region to be electronically cooler than a region presenting a lower brightness, this for a constant density. In a schematic vision, taking into account the average density of the different regions seen by the streak camera, Stream, Shell, Core, and the respective volume of each regions, that is to say their respective extended length along the axis, x, following the field of view of the SOP, we represent the accretion as in Figure 2.17 *Left*. In this simplified vision, and following the information extracted from the interferometry, each region is represented with an identical extension, R, along the axis of light collection of the SOP, while the height is different, and variable with time. We attribute to each region an average electron density: $n_{Stream} = 1.5 \times 10^{18} cm^{-3}$; $n_{Core} = 1.5 \times 10^{19} cm^{-3}$; $n_{Shell} = 3 \times 10^{18} cm^{-3}$, based on the interferometry measurements. We note also the Shell to be situated on each side of the Core and Stream, leading to a contribution multiplied by two, despite the similar radial extension of the shell compared to the Stream or Core. Then, knowing the temperature of the incoming jet to be $Te_{stream} = 15$ eV through spectroscopy measurement (see chapter 1), we take that component as a reference. Taking into account the difference in density and radial extension of each component, the temperature of Core and Shell is then determined in a relative way, looking at the brightness ratio *Shell/Stream* and *Core/Stream* (taken from the SOP measurement presented in Figure 2.15) as follows:

$$\frac{Brightness_\alpha}{Brightness_{Stream}} = \frac{\int_0^{\Delta x_\alpha} \frac{dW_\alpha}{dV} dx \, (ne_\alpha, ni_\alpha, Te_\alpha)}{\int_0^{\Delta x_{stream}} \frac{dW_{stream}}{dV} dx \, (ne_{Stream}, ni_{Stream}, Te_{Stream})}$$

with $\alpha \equiv$ Shell or Core. In the latest formula, we then impose ne, ni and Δx, following the interferometry measurement. The right electron temperature is then the one allowing the ratio of the emitted Bremsstrahlung power to correspond to the brightness ratio observed in the SOP. The SOP measurement giving $\frac{Brightness_{Shell}}{Brightness_{Stream}} = 7.4 \pm 3.4$ and $\frac{Brightnes_{Core}}{Brightness_{Stream}} = 100 \pm 1.5$, the associated Core and Shell electron temperatures are the ones presented in Figure 2.17 *Right*, i.e. $Te_{Core} = 65$ eV and $Te_{Shell} = 520$ eV. The gray areas represent the uncertainty on the brightness ratio of the SOP measurement. Note that it is only significant for the Shell to Stream ratio. Indeed, if the resulting error on the Core temperature is not significant, the SOP gives a Shell temperature ranging between $Te_{Shell} \in [250 - 2000]$ eV. We note however this approximation to be a rough estimate due to the schematic vision of the accretion region and its plasma components that have been whittled down in the present case to three: i.e. Stream, Core, Shell. Nevertheless, this description, correlated to the SOP measurement, simply suggests the following hierarchy regarding the level of electron temperature of each component: $Te_{Stream} < Te_{Core} < Te_{Shell}$, and so a shocked Core, electronically cooler than the resulting Shell at its border. The explanation for that counterintuitive result will be detailed after, and takes its origins in the thermal equilibration between ions and electrons. Before, we present in the next subsection a second temperature measurement by the way of spectroscopy, which corroborates the one we just detailed.

X-ray emission

A focusing spectrometer with spatial resolution (FSSR) in one direction (along the axis z of the incoming stream) was used to record the temporally-integrated X-ray emission spectra of the plasma [Faenov *et al.* (1994)]. The field of view of the spectrometer is the same as for the jet generation study (see Figure 1.14 of the chapter 1), this is to say the spectrometer looks at the plasma dynamic transversally. In this view, the field of view, regarding the Stream, Shell and Core is the same as the one of the SOP diagnostic (see Figure 2.17left). The spectrometer was equipped with a spherically bent mica crystal ($2d = 19.9$ Å) and set up to observe X-rays having a wavelength range of 13.5 to 15.5 Å (750–950 eV photon energies) containing the emission of $H-$ and $He-like$ fluorine ions. The diagnostic was aligned along nearly the same line-of-sight as the interferometer with a slight angle in the upwards ($\sim 5°$) and lateral ($\sim 2°$) directions, which were small enough to neglect the skewing of the image. We note that here, contrary to the previous detailed results, the obstacle is a PVC ($(C_2H_3Cl)n$) target, while the stream
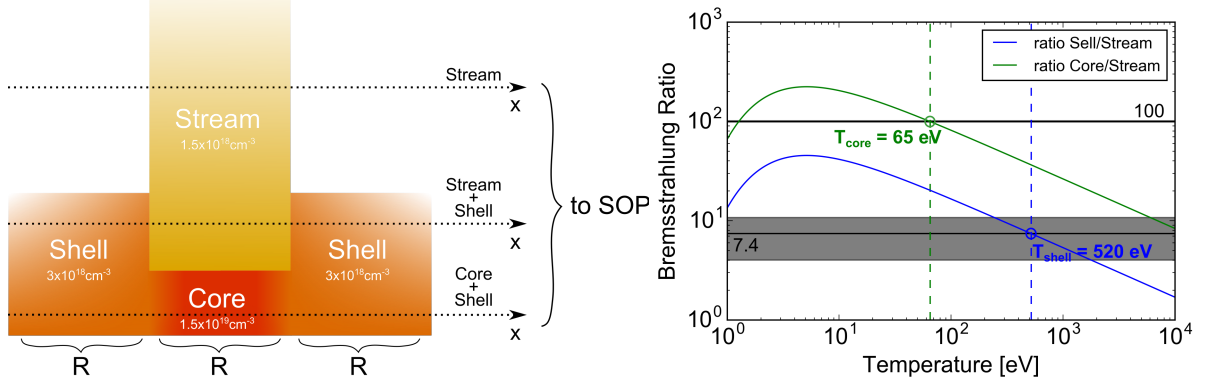
Figure 2.17.: *Left*: Schematic representation of the three regions seen by the streak camera, i.e Stream, Core, Shell.
Right: Bremsstrahlung emission ratio Shell/Stream (blue curve) and Core/Stream (green curve) as a function of the temperature. The temperature of the Stream component, in the ratio calculation, is taken as a constant, and only the Shell or core temperatures are variable. The black horizontal lines, labeled 7.4 and 100, correspond to the observed ratio of brightness in the SOP diagnostic (see - Figure 2.15), Core/Shell and Stream/Shell respectively. The gray areas around the lines reflect the uncertainties on the measurement of the brightness ratios. The respective density of each region is taken into account (retrieved from the interferometry measurements), as well as the effective "volume" of each component seen by the streak camera, Core, Shell and Stream: $\Delta x_{Stream} = \Delta x_{Core} = \frac{1}{2}\Delta x_{Shell}$

is generated from a laser-irradiated CF_2 target (this situation is the opposite compared to the previous sections of the chapter). We however observe that the plasma density dynamics and characteristics (density, temperature) are the same whenever the laser target and obstacle targets are swapped. The configuration using a CF_2 stream-source target is used since the spectrometer records the spectrum corresponding to the Fluorine ions, and that most (95 %) of the plasma seen above the obstacle is composed of stream material, as precisely analysed by recording F-ions emission solely originating from stream or obstacle material (seen when inverting the obstacle and stream target composition on some shots). Hence, such configuration leads to stronger emissions compared to when using the reverse configuration of a CF_2 obstacle target. We concentrate our analysis on the first 2 mm of the plasma along z, starting from the obstacle surface ($z = 0$), i.e. where the core and shell are present (as indicated by the interferometry and SOP data). For the analysis of the spectra, the exact spatial geometry of the plasma was inferred from the interferometer diagnostic.

As shown in Figure 2.18, the spectrum contains a remarkably intense series of high-n transitions in $He - like$ fluorine ions ($He\gamma$, $He\delta$, and $He\varepsilon$) together with a dominating $Ly\alpha$ line of $H - like$ F. In attempting to model the observed ratio between the $He\beta$ and $Ly\alpha$ lines with an atomic kinetics modeling in a steady-state approach (as can be made
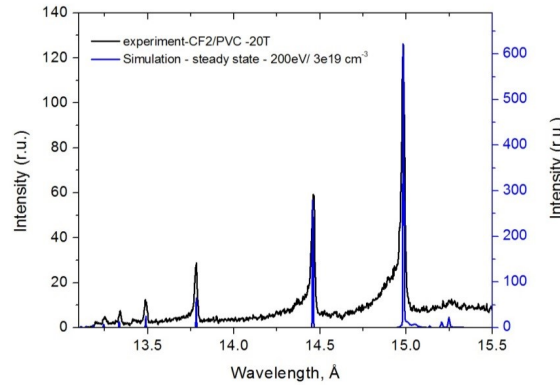
Figure 2.18.: Best fit of the X-ray spectrum measured near the obstacle (PVC target, the stream being generated from a CF2 target) in the case of a magnetic field strength of B = 20 T and as obtained by the PrismSPECT code in steady-state mode for an electron temperature of 200 eV, or 2.32 MK.

using the FLYCHK [Chung *et al.* (2005)] and/or PrismSPECT codes [MacFarlane *et al.* (2007)]), a fit can be achieved for the plasma with an electron plasma temperature of $T_e = 2.32\,\text{MK}$ (200 eV) and an electron plasma density of $n_e = 3 \times 10^{19}\,\text{cm}^{-3}$ as shown in Figure 2.18. However, such fitting yields a clear underestimation of the rest of the He series lines. In general, the observed relative intensities of the $He\gamma$, $He\delta$, $He\varepsilon$ lines can occur only in a recombining plasma, i.e. in the conditions when the recombination processes dominate ionization ones, and the electron temperature of the plasma at a given moment is rather lower than the ionization temperature. As a consequence, we can deduce that the observed spectrum of $He - like$ ions should originate from a plasma with electron temperature below 100 eV (1.16 MK) due to the fact that the ionization potential of the high-n levels in $He - like$ F is below or about this value. All together, the observed spectrum gives a clear evidence that at least two regions of plasmas (one being "hot", i.e. having temperature of hundreds of eV, and another one being a recombining "cold" plasma) with various parameters contribute to the observed spectrum, both of which are located near the obstacle surface.

In the cold plasma case, the emission of the $He - like$ series can be analysed following the procedure for recombining plasma having non-steady ionization state that is detailed in Ref. [Ryazantsev *et al.* (2016)]. The relative intensities of the transitions $1snp\ ^1P_1-^1s_2$ $^1S_0$ where n = 3 – 7 in multiple charged $He - like$ ions (He_β, He_γ, He_δ, He_ε, He_ζ lines correspondingly) are sensitive to the electron density in the range of $10^{16} - 10^{20}\,\text{cm}^{-3}$ when the temperature ranged from 10 to 100 eV (0.1 to 1 MK) for ions with nuclear charge Zn ~ 10. This allows us to retrieve the electron temperature and density of the "cold" plasma fraction. As shown in Figure 2.19, such procedure applied to the spectra recorded over the first 600 μm along the axis z from the obstacle surface yields the following estimations
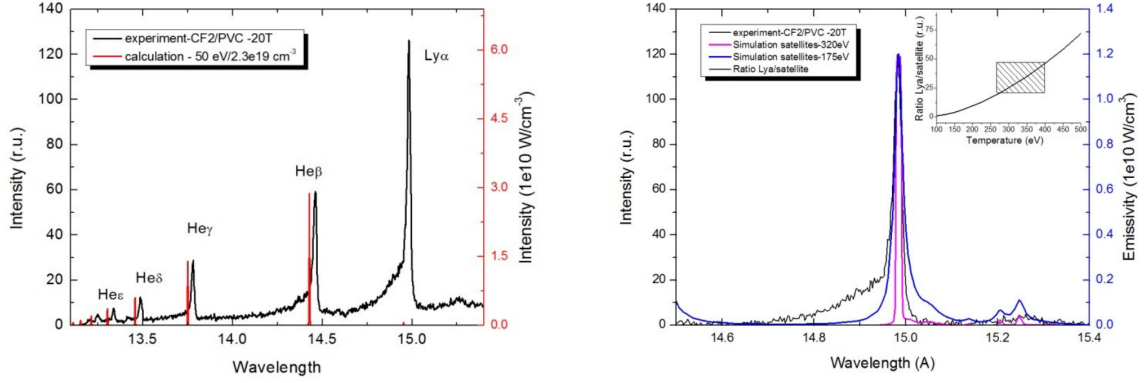
Figure 2.19.: *Left:* Comparison of experimental spectra (in black) recorded near the obstacle target, for the cases of 20 T(here the obstacle is a PVC target, while the stream is generated from a CF2 target) applied B-field, together with simulations (in red) of the He-like line series obtained using a recombination plasma model. The experimental intensity values are scaled according to instrumental functions of the spectrometer and the readout system in order to compare them to the real emissivity of the plasma in the two cases. The scale for the modeled spectra emissivity (in W/cm^3) is given on the right. Note that the simulated, red spectra are artificially shifted compared to the experimental, black spectrum for a better visibility.
Right: The spectrum measured for an applied magnetic field of 20 T (here the obstacle is a PVC target, while the stream is generated from a CF2 target), in the range from 14.5 to 15.4 Å and containing the $Ly\alpha$ line and its dielectronic satellites. The modeled spectra is calculated by PrismSPECT code in the steady-state approach for plasma temperatures of 175 eV (2 MK) and 320 eV (3.7 MK). The dependence of the ratio of the $Ly\alpha$ line intensity to the one of the satellites with respect to the plasma electron temperature is given in the inset, from which the precision on the temperature determination can be inferred.

for the "cold" plasma component near the obstacle surface:

- $T_e = 50$ eV (0.6 MK), $n_e = 2.3 \times 10^{19}$ cm^{-3}

Note that these density values retrieved from the recombining spectra modeling correspond well to the values obtained from the interferometry measurements for the inner shocked core region of the plasma.

Since at such low temperatures (~0.5 MK), the population of $H - like$ ions is low, the contribution of this "cold" plasma component to the $Ly\alpha$ line can be considered negligible. Hence, we can retrieve the electron temperature of the "hot" plasma fraction independently, analyzing the relative intensities of $Ly\alpha$ line and its dielectronic satellites, which appear at longer wavelength (see Figure 2.19). As the hot plasma is assumed to be in the range of several hundreds of eV (several MK) temperature range, the steady-state approach of the PrismSPECT code can be applied for the spectra modeling. Although the relative
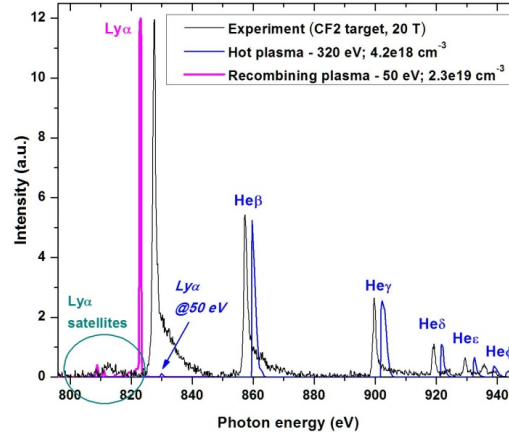
Figure 2.20.: X-ray (integrated in time, and in space over $0 < z < 1$ mm, i.e. near the obstacle, but spectrally resolved) emissions from the laboratory plasma. Overlaid are the simulations of the emissions produced by two plasma components having the densities of the core and shell respectively, and temperatures of 0.58 MK (50 eV) and 3.7 MK (320 eV) respectively. The modeled spectra are offset along the photon energy scale for better visibility. Note that the simulated, purple and blue spectra are artificially shifted compared to the experimental, black spectrum for a better visibility.

intensities between particular satellite components are strongly dependent on the plasma density, the overall intensity of the satellite group is not sensitive to the plasma density in the range considered, but to the electron temperature only. The inset of Figure 2.19 shows how the ratio between the $Ly\alpha$ line and the dielectronic satellites depends on the electron temperature. The best correspondence of the modeled ratio to the measured one is obtained for Te ~ 320 eV (3.7 MK). The quite low signal-to-noise ratio in the satellite spectrum gives us a confidence interval for the temperature of 250 - 400 eV ($2.9 – 4.6$ MK).

In summary, from what is observed in the SOP and interferometer diagnostics, along the same light of sight as the X-ray spectrometer, we observe a two components plasma: the inner cold shocked core region, surrounded by a shell region that is taller (along z), and thicker (in radius) but hotter and less dense. The analysis of the full X-ray spectra recorded for magnetic field strengths 20 T, as shown in Figure 2.20, confirms this observation as the spectra can be only modeled as the emission from two distinct plasma components having densities consistent with the interferometry measurement, and temperatures as derived from the X-ray spectrum analysis and detailed above.

2.4.3. Evolution of the plasma temperatures

The temperature measurements are further highlighted by the GORGON 3D MHD resistive code simulations. As shown in Figure 2.21, the electron temperature is effectively higher in the Shell than in the Core. However, the latest simulations also highlight the fact that
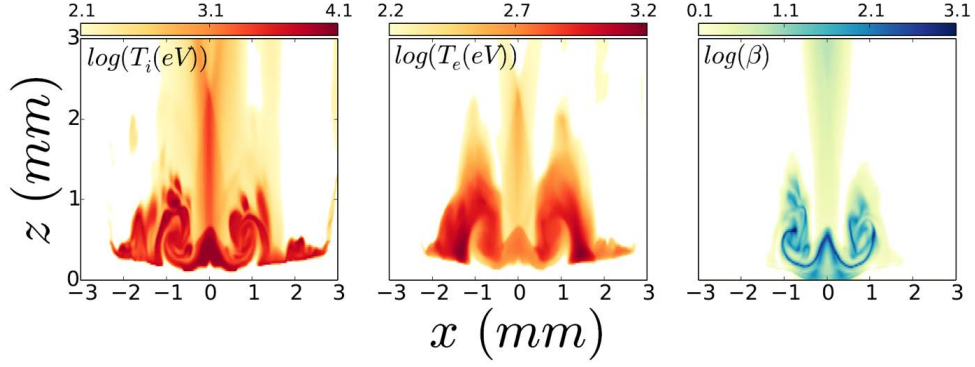
Figure 2.21.: 2D slices of ion and electron temperatures as well as plasma thermal beta at $t = 22\,\text{ns}$ (i.e. $12\,\text{ns}$ after the stream impacts the obstacle -1000 km/s jet component)

the situation is opposite for the ion temperature, where T_i is more important in the Core than in the Shell.

This can be understood if one takes into account the fact that under a shock, the ions are much more heated than the electrons. The electrons are heated up only in a second step by collision with the ions. Indeed, under a shock the directed *ram* pressure ($\frac{1}{2}\rho v^2$) of the particles is isotropized into *thermal* pressure (nkT). In a flow of plasma with the same speed for ions and electrons, if one takes into account the fact that the ions are ~ 1836 times heavier than the electrons, we understand easily the major part of the ram pressure to be carried by in the ions. Then, when this plasma flow will be shocked, the major part of the newly created thermal energy will be given to the ions. The Rankine-Hugoniot equation can actually be applied for each species in the plasma: the ions and the electrons. Hence, one gets for the temperatures:

$$T_{1\alpha} = \frac{3}{16}\frac{m_\alpha}{k}v_0^2 - \frac{T_{0\alpha}}{16} \tag{2.8}$$
$$\implies T_{1i} \approx T_{1e}\left(\frac{Am_p}{m_e}\right) \approx 1836 \times AT_{1e}$$

for electrons and ions having the same pre-shock velocity (v_0) and temperature (T_0) ; here 0 and 1 denote pre and post conditions, while α stands for either the electrons or the ions. Starting from those post-shock temperatures, two mechanisms are then at play: the electrons-ions collision and the radiative cooling. The first allows the ion energy gained under the shock to be transfered to the electrons, while the second, oppositely, allows the electrons to lose energy by radiation. The radiative losses, $\Lambda(T)\,[\text{W.cm}^3]$, are defined by the full set of transitions (free-free, bound-free and bound-bound) experienced by the electrons, which emit radiations that exit the plasma. Assuming an optically thin plasma, the radiative losses are presented in Figure 2.22 *left*. The data for the laboratory case are calculated using the FLYCHK atomic code [Chung *et al.* (2005)], while the data for the
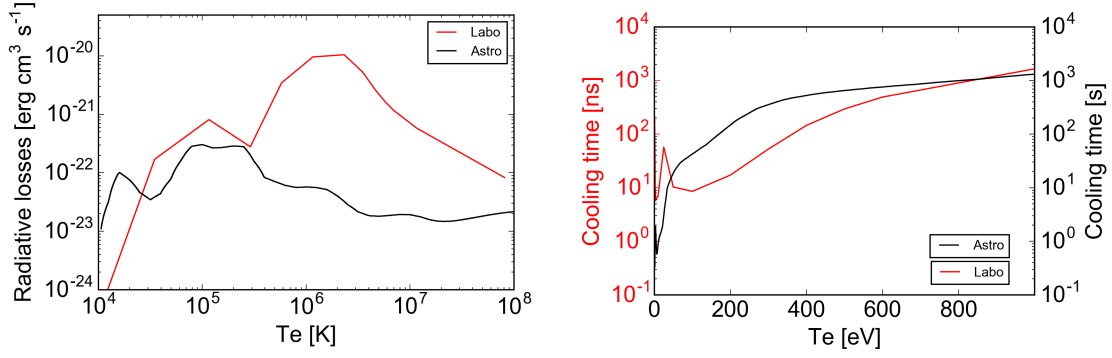
Figure 2.22.: *Left:* Radiative losses $\Lambda(T)$ in [erg.cm^3.s^{-1}] for the experimental case (red curve) and the astrophysical case (black curve). The astrophysical radiative losses are taken from Orlando *et al.* (2010), i.e. taken from the APED V1.3 atomic line database [Smith *et al.* (2001)] for an optically thin plasma, assuming the metal abundances of 0.5 of the solar values (Anders & Grevesse 1989). The laboratory radiative losses are calculated thanks to the atomic code FLYCHK [Chung *et al.* (2005)] for each element of the PVC molecule (H_3C_2Cl) and stochimetrically averaged respecting the amount of each element in the PVC, also assuming optically thin plasma. In both cases, bound-bound, bound-free and free-free emissions are taken into account.
Right: Cooling time defined as $t_{cooling} = (3/2)n_i(1 + Z)kT/n_in_e\Lambda(T)$, for both the experimental case (red curve) and the laboratory case (black curve), in the conditions of the shocked plasma: $n_i^{shocked} = 4n_i^{stream}$ and $n_e^{shocked} = 4(z^{shocked}/z^{stream})n_e^{stream}$ for the astrophysical and the experimental situation respectively. Note the change in the scale in between the laboratory cooling time [ns] and the astrophysical cooling time [s].

astrophysical case are extracted from Orlando *et al.* (2010). Figure 2.22 *right* represents the cooling time associated to the radiative losses, defined as the ratio of the plasma energy density ($(3/2)n_i(1 + Z)kT$) over the total volumetric radiative power ($n_in_e\Lambda(T)$):
$t_{cooling} = (3/2)n_i(1 + Z)kT/n_in_e\Lambda(T)$.

The exchange of energy, by collisions, between different species having different temperature can be described as follows $\frac{dT\alpha}{dt} = \sum_\beta \nu_\epsilon^{\alpha\backslash\beta} (T_\beta - T_\alpha)$, with $\nu_\epsilon^{\alpha\backslash\beta}$ the equilibration collision frequency between the species α and β defined as $\nu_\epsilon^{\alpha\backslash\beta} = 1.8 \times 10^{-19}(m_\alpha m_\beta)^{1/2}(Z_\alpha Z_\beta)^2 \times n_\beta \times ln\Lambda/(m_\alpha T_\beta + m_\beta T_\alpha)^{3/2}$; here all quantities are in cgs units except for the temperatures in eV. Taking into account the electron energy losses by radiation previously detailed, one can described the ions and electrons temperatures evolution with the following system:

$$\frac{dT_e}{dt} = \nu_\epsilon^{e\backslash i} (T_i - T_e) - \frac{n_e\Lambda(T_e)}{^3/2 \times Z}$$

$$\frac{dT_i}{dt} = \nu_\epsilon^{i\backslash e} (T_e - T_i)$$

(2.9)

Where the last term in the left part of the equation for $\frac{dT_e}{dt}$ is the electron cooling rate $\frac{\Delta T_e}{\Delta t}$. It corresponds to the ratio of the electron temperature (T_e) over the time (τ_{cool}^e) needed for the electrons to lose the corresponding energy ($\frac{3}{2}n_e T_e$) by radiation: $\frac{\Delta T_e}{\Delta t} = T_e/\tau_{cool}^e$, which corresponds well to a cooling rate in [eV.s^{-1}]. τ_{cool}^e is then defined as the ratio of the electron energy density ($\frac{3}{2}n_e T_e$) over the volumetric radiative power ($n_i n_e \Lambda(T)$): $\tau_{cool}^e = \frac{3/2 \times Z \times T_e}{n_e \Lambda(T_e)}$. Finally it comes $\frac{\Delta T_e}{\Delta t} = \frac{n_e \Lambda(T_e)}{3/2 \times Z}$. We note this reasoning to be equivalent in considering the electron cooling rate as the ratio of the radiative power over the heat capacity at constant volume, $\frac{\Delta T_e}{\Delta t} = \frac{n_i n_e \Lambda(T)}{C_v^{cm-3}}$, where C_v^{cm-3} is the volumetric heat capacity. Indeed, taking the heat capacity of a perfect gas, $C_v^{cm-3} = \frac{3}{2}k_B n$ [J.K.cm^{-3}] $\iff \frac{3}{2}n$ [eV.T(eV).cm^{-3}], and considering only the electrons to contribute in the heat exchange (as the cooling rate operates only for the electrons in Equation 2.9), we have $n = n_e \implies C_v^{cm-3} = \frac{3}{2}n_e$. Finally it comes $\frac{\Delta T_e}{\Delta t} = \frac{n_e \Lambda(T_e)}{3/2 \times Z}$.[1]

Solutions for the system of Equation 2.9 are shown in Figure 2.23, in the laboratory case, for different initial T_e and T_i and densities within the shocked core. Those initial temperatures correspond to different incoming speeds of the plasma flow before impact. From left to right, it corresponds to incoming speeds respectively of 419, 534 and 750 km.s^{-1}, implying initial temperatures respectively of (T_{i0}, T_{e0}) $\approx$ (3.5 $\times 10^3$, 10), (6 $\times 10^3$, 10) and (1.1 $\times 10^4$, 10) eV. The ion densities associated to those speeds correspond to the ones given assumed by the adiabatic expansion described in chapter 1, then compressed by a factor four as expected under the shock. This gives respectively $n_i = 1.2 \times 10^{19}$, 7.6×10^{18} and 2.6×10^{18} cm^{-3}.

As one can see, the evolution is drastically different depending on the initial conditions. In the first instants, because of the important difference between T_e and T_i, the gain (loss) in temperature of the electrons (ions) is quite important: $\frac{dT_\alpha}{dt} \propto (T_\beta - T_\alpha)$. This is to say, as long as the temperature difference between electrons and ions is important, the gain of energy of the electrons is much more important than the radiative losses. The increase of the electron temperature from 10 eV up to its maximum value is driven by that gain of energy, and it is similar between each cases presented in Figure 2.23. In order to get a rough idea of the time, t_e, for which the electron temperature increase is not significant anymore, we define the latest increase comparatively to the hydrodynamic time ($t_{hydro} = L_c/c_s$; $L_c \equiv$ characteristic size of the system), and t_e such as $\frac{dT_e}{dt}\Big|_{t_e} \times \frac{t_{hydro}}{T_e} = 0.01$. This is to say, when the increase of the electron temperature over the hydrodynamic time represents no more than an increase of 1%. This time t_e is represented on the plot of Figure 2.23 by the vertical black dashed line, where one can see that the denser the system, the faster it equilibrates, as expected. If no radiative losses were taken into account, the equilibration temperature will simply be $T_{equi} = T_e = T_i = (T_{i0} + T_{e0})/(Z + 1)$, as the total energy is spread out equally over the ions and the electrons (there is Z times more

---

[1] In section 1.2 of chapter 1 the cooling rate was defined thanks to a tabulated heat capacity, from the Livermore equation-of-state (LEOS). The perfect gas heat capacity is used here for simplicity.
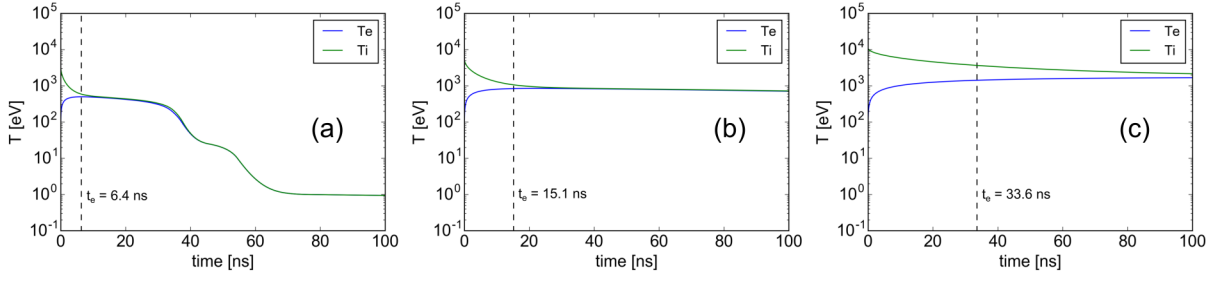
Figure 2.23.: Electron and ion temperature evolution for different initial temperatures and densities. From left to right, $(Ti_0, Te_0) \approx (3.5 \times 10^3, 10)$, $(6 \times 10^3, 10)$ and $(1.1 \times 10^4, 10)$ eV for the temperatures, and $n_i = 1.2 \times 10^{19}$, 7.6×10^{18} and 2.6×10^{18} cm^{-3} for the densities.

electrons than ions).

When the electron temperature starts to stabilize, and the difference between the electron and ion temperatures lowers, the radiative losses can act more importantly. Here, two factors have to be taken into account: the density and the temperature from which the cooling start to overtake, close to the equilibration temperature. The higher the density, the more the cooling will be important (volumetric radiative power $\propto n_i n_e \Lambda(T)$), but the radiative losses also depend on the temperature ($\Lambda(T)$), and possibly in a complex manner. As one can see in Figure 2.22, in the laboratory case, the radiative function is monotonous for electron temperatures between $100\,\mathrm{eV}$ and $1000\,\mathrm{eV}$. In this range, the higher is the electron temperature, the lower are the radiative losses. Then, the higher will be the equilibration temperature, the slower will be the radiative cooling. This is what is observed in Figure 2.23 with, from (a) to (c), an initial ion temperature after the shock increasing (and so an equilibration temperature), implying a slower cooling, from (a) to (b), after equilibration. In addition to that, and going in the same way, the density decrease from (a) to (b) contributes in slowing down the cooling rate. We note the fluctuations between 30 and $70\,\mathrm{eV}$ in the temperature evolution of Figure 2.23(a) to be due to the non-monotonicity of the radiative loses below $T = 100\,\mathrm{eV}$ (see Figure 2.22).

Within all this temperature evolution process, one should take into account, however, the medium change during the fluid particle transit from the Core to the Shell, involving a reduction of the medium density and so, a reduction of the cooling rate while entering in the Shell. This is not represented in the plots of Figure 2.23 as the density is kept as a constant during all the evolution. One can estimate the moment when the medium change occurs by $t_{core \to shell} \sim r_{core}/v_1$, with v_1 the flow speed after the shock front. This corresponds to the time needed for the particles to exit the core, starting from its center to its border. Of course, we don't expect the change of density to occur abruptly at the border of the Core region, as well as the trajectory of the particles to be directly the one from the center to the border of the particles, but this gives a rough estimate of the time spent into the Core. Assuming a Core radius ranging between $250\,\mu$m and $500\,\mu$m (see
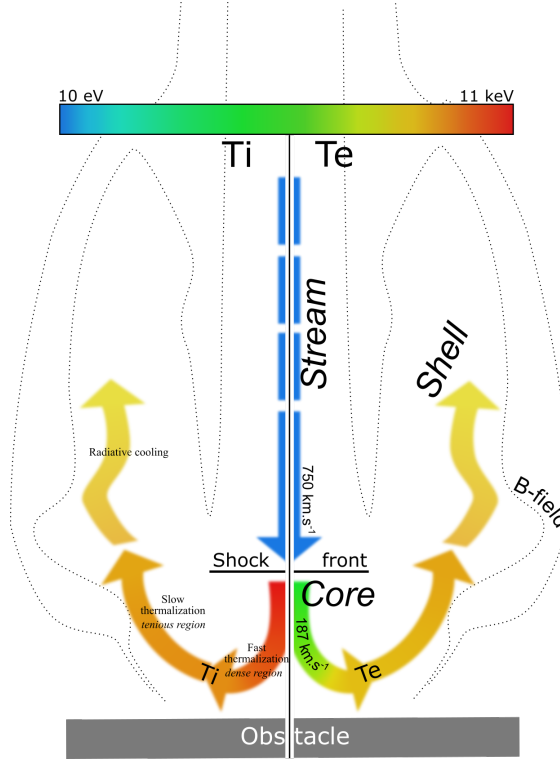
Figure 2.24.: Schematic representation of the electron and ion temperature evolution during the experimental accretion dynamics. Ions and electrons temperature are represented in the left and right side of the schema respectively. The evolution of the temperatures is here schematically represented for an incoming stream with a velocity of $750\,\mathrm{km.s^{-1}}$, consequently exhibiting a peak of ion temperature, just after the shock, of $\sim 11\,\mathrm{keV}$.

interferometry data in Figure 2.12) and flow speed ranging between about $^{750}/_4\,\mathrm{km.s^{-1}}$ and $^{400}/_4\,\mathrm{km.s^{-1}}$, we obtain a time spent in the Core ranging between $1.3\,\mathrm{ns}$ and $5\,\mathrm{ns}$. This time range is in any case below the time needed for the electrons to reach their maximum temperature, and hence, we understand here the Core to be electronically colder than the Shell. The relatively slow equilibration between electrons and ions allows this. Figure 2.24 schematically represents the evolution of T_e and T_i under the accretion shock dynamic, from the Stream to the Shell, going through the core.

For the astrophysical case however, the situation is different. Extracted from the PLUTO simulations, the temperature for the stream or chromospheric material are displayed in Figure 2.25. Here, the temperature represented is the plasma temperature as the electron and ion temperatures are equal. This is due to the fact that the equilibration time between ions and electrons is really short compared to the hydrodynamic time. In the astrophysical plasma conditions corresponding to the PLUTO simulation, $t_{hydro} \sim 100\,\mathrm{s}$ while $t_{equil} \sim 1\,\mathrm{s}$. In these conditions, one can consider the ions and the electrons to be almost instantaneously equilibrated after the shock. The radiative cooling then acting
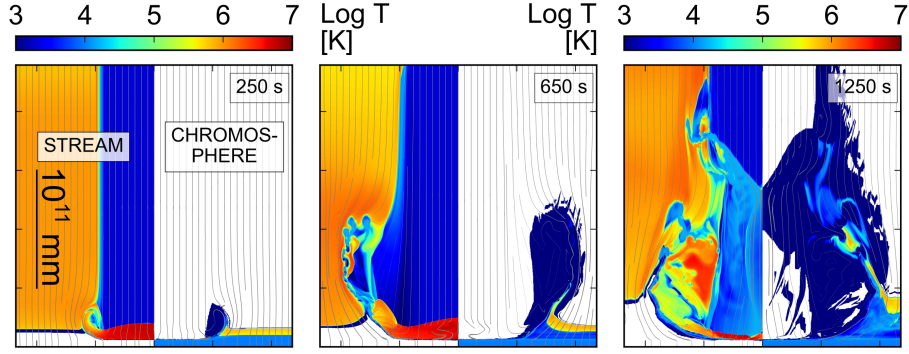
Figure 2.25.: Stream + corona (left panels) and chromospheric materials (right panels) temperature [log K]. The different components are separated in the PLUTO code thanks to a passive tracer.

on the temperature, we understand the Shell to be colder than the Core, as presented in Figure 2.25.

2.4.4. The stream, the shock, the shell: three distinct plasma regions

From those different diagnostics, allowing insight in the electron density and temperature, we are able to separate three distinct regions coexisting during the accretion dynamic: the Stream, the Core and the Shell. The stream impact onto the obstacle, launching a shock, defining the core region, from which matter escapes to create the shell. As a summary, Table 2.2 displays the plasma parameters for these three regions, for the laboratory and the astrophysical situations. The laboratory parameters comes from the experimental results coupled with the 3D MHD simulation of the laboratory situation in order to retrieve the non probed variables (e.g. the core and shell flow speeds and ion temperatures). The astrophysical parameters are extracted from the Pluto simulation. The laboratory stream velocity range indicates the variation of the stream velocity as expected during the adiabatic expansion.

For all the stream parameters calculated in the Table below the given value of the stream velocity, we use a fixed value of the velocity (750 km/s) as it corresponds to the peak velocity of the highest density part of the stream ($1.5 \times 10^{18}\,\mathrm{cm^{-3}}$). For the laboratory core, we start with the temperatures that are derived from the Rankine-Hugoniot equations, i.e. that correspond to what is expected after the shock. From the shock front where only the ions are heated, we consider that the electron and ion temperatures in the core region correspond to the ones expected after the particles have traveled 125 µm

inside the core shocked region, at the flow velocity given, in the frame of the shock, by $v_{flow-core} = v_{flow-stream}/4$.

To determine these temperatures, we use thermal equilibration equations (see Equation 2.9 of subsection 2.4.3), coupled with a Thomas-Fermi model for the ionization as well as optically-thin free-bound radiative losses. We note that the obtained temperatures are completely consistent with the ones retrieved by the 3D-MHD model of the laboratory dynamic. The temperatures in the shell region are directly extracted from the 3D-MHD code GORGON, at locations having electron densities consistent we the ones measured experimentally. Note that the stated electron temperature of 600 eV is resulting from electron-ion equilibration over a few ns as the electrons transit from the core to the shell. The indicated cooling times for the laboratory plasma are obtained by running the 0-D atomic code FLYCHK [Chung *et al.* (2005)]. In the CTTS case, the density values and temperatures in the stream and core regions are extracted from the PLUTO simulations. For the CTTS shell, the density and temperature values are taken from the shell area having for coordinate $(r_1 - r_2, \ z_1 - z_2) = (7.5 \times 10^9 - 8.5 \times 10^9 \, \mathrm{cm}, \ 3 \times 10^9 - 4 \times 10^9 \, \mathrm{cm})$ in the 1250 s frame of PLUTO astrophysical simulation. This area corresponds to the shell part being composed by the shocked stream material ejected away from the core, and not by the cold chromosphere material, for a better correspondence with the laboratory-defined shell. The similar $\beta_{dyn} \sim 1$ in the astrophysics shell and the laboratory one, reflects that correspondence. A detailed description of the way the different numbers are calculated is given in the Annex (section A.1).

	Laboratory			*CTTS*		
B-Field [T]	20			7.10^{-4}		
Material	C_2H_3Cl (PVC)			H		
Atomic number	10.4			1.28		
	Stream	*Core*	*Shell*	*Stream*	*Core*	*Shell*
Spatial transverse scale [mm]	0.7	0.5	1.55	0.5×10^{11}	0.5×10^{11}	1×10^{11}
Charge state	2.67	5.3	5.3	1	1	1
Electron Density [cm^{-3}]	1.5×10^{18}	1.5×10^{19}	2×10^{18}	0.5×10^{11}	2×10^{11}	6×10^{9}
Ion density [cm^{-3}]	5.6×10^{17}	2.9×10^{18}	2.8×10^{17}	0.5×10^{11}	2×10^{11}	6×10^{9}
Density [g.cm^{-3}]	9.7×10^{-6}	4.9×10^{-5}	6.6×10^{-6}	1×10^{-13}	4×10^{-13}	1.28×10^{-14}
Te [eV]	10	320	660	0.22	350	22
Ti [eV]	10	9000	3300	0.22	350	22
t_{equi} [ns]	—	~30	—	—	~1×10^{9}	—
Flow velocity [km.s^{-1}]	$100-1000$	177	178	500	84.5	84.5
Sound speed [km.s^{-1}]	24	405	323	7.4	295	74
Alfven speed [km.s^{-1}]	181	80	220	62	31	175
Electron mean free path [mm]	1.6×10^{-3}	0.1	2.9	17	5.2×10^{6}	6.9×10^{5}
Electron collision time [ns]	1.2×10^{-3}	1.5×10^{-2}	2.7×10^{-1}	86	6.6×10^{5}	3.5×10^{5}
Ion mean free path [mm]	1.2×10^{-4}	0.8	0.7	24	7.4×10^{6}	9.8×10^{5}
Ion collision time [ns]	1.3×10^{-2}	2.9	4	5.9×10^{3}	4.5×10^{7}	2.4×10^{7}
Magnetic diffusion time [ns]	31.7	1.9×10^{3}	1.9×10^{4}	3.5×10^{20}	1.1×10^{25}	7.4×10^{23}
Electron Larmor radius [mm]	3.8×10^{-4}	2.1×10^{-3}	3.1×10^{-3}	1.6	64	16
Electron gyrofrequency [s^{-1}]	3.5×10^{12}	3.5×10^{12}	3.5×10^{12}	1.2×10^{8}	1.2×10^{8}	1.2×10^{8}
Ion Larmor radius [mm]	2×10^{-2}	0.29	0.18	77	3.1×10^{3}	7.7×10^{2}
Ion gyrofrequency [s^{-1}]	4.9×10^{8}	9.8×10^{8}	9.8×10^{9}	5.2×10^{4}	5.2×10^{4}	5.2×10^{4}
Cooling time - thin [ns]	—	53	500	—	4.4×10^{2}	1.2×10^{11}
Electron magnetization	4.3	51	9.5×10^{2}	11	8.1×10^{4}	4.3×10^{4}
Ion magnetization	6×10^{-3}	2.9	3.9	0.31	2.4×10^{3}	1.3×10^{3}
Mach number	31.6	<1	<1	67	<1	1.1
Alfven Mach number	4.1	<1	<1	8	<1	<1
Reynolds	4.6×10^{5}	15	14	2.6×10^{11}	4.2×10^{6}	1.3×10^{8}
Magnetic Reynolds	34	6.9×10^{2}	3.4×10^{3}	3.5×10^{9}	1.9×10^{13}	6.3×10^{11}
Peclet	10	0.1	0.1	8.2×10^{8}	8.7×10^{4}	2.8×10^{6}
β_{ther}	2×10^{-2}	30	2.6	1.7×10^{-2}	107	0.2
β_{dyn}	34	9.6	1.3	128	14.6	0.5
Euler number	40.8	—	—	87	—	—
Alfven number	1.1×10^{-2}	—	—	1.2×10^{-2}	—	—

Table 2.2.: Parameters of the laboratory accretion, with respect to the ones of the accretion stream in CTTSs, for the three distinct regions, namely the incoming stream, the core and the shell.

2.5. The shell as an X-ray absorber

The dense and ionized shell, revealed here in the laboratory experiment, and also observed in the laboratory and astrophysical simulations, is seen in the latter case to modify the X-ray emission originating from the accretion region. From the X-ray emission computed from the simulation shown in Figure 2.12 for instance, and comparing the results with and without local absorption effects taken into account (Figure 2.26), we indeed observe that the X-ray flux is significantly reduced when the local absorption is included. This is done by synthesizing the X-ray maps and the spectra from the Pluto simulation, and then deriving the maps and spectra both taking into account the local absorption of the surrounding medium along the line of sight (LoS) or neglecting these effects. This approach allows us to infer the role of the local absorption on the detectability of the emission from the accretion shock.

The method to synthesize the maps and the spectra so that they can be directly compared with observations of accretion shocks consists of several steps of a tool properly developed to handle the high energy emission from shocks, as discussed in [Bonito *et al.* (2014)]. From the bi-dimensional maps of the density, velocity, and temperature of the plasma simulated with the PLUTO code, R. Bonito reconstructed the 3D maps by rotating the 2D slab around the symmetry z axis (reducing the original resolution of the numerical simulations). From the values of temperature and emission measure (EM) in each computational cell, assuming metal abundances of 0.5 of the solar values (in agreement with X-ray observations of CTTSs [Telleschi *et al.* (2007)]), we synthesize the corresponding emission using the CHIANTI atomic database [Landi *et al.* (2012)]. We take into account the local absorption by computing the X-ray spectrum from each cell and by filtering it through the absorption column density along the LoS, i.e. we take into account the emission from each cell and the absorption of each cell in front along the line of sight [Bonito *et al.* (2014)]. We use the absorption cross sections as a function of wavelength from [Balucinska-Church and McCammon (1992)] to compute the absorption, due mainly to cold material, as the soft X-ray opacity drops at high temperature (T > 106 K [Krolik and Kallman (1984)]). We also subtract the emission from the coronal component and neglect the absorption due to the interstellar medium. We synthesize the X-ray maps and spectra emerging from the shock region by integrating the absorbed X-ray spectra from the cells in the whole domain. It is worth noting that our astrophysical simulations do not include the effects of radiative transfer, so that they are not entirely self-consistent. However, the radiative transfer is expected to affect mostly the material of the pre-shock stream, developing a region of radiatively heated gas (a precursor) in the unshocked accretion column [Costa *et al.* (2017)]. As such, this heating mechanism does not affect significantly the dynamics of the post-shock plasma.

Our results thus reveal that taking into account the effect of the absorption by the
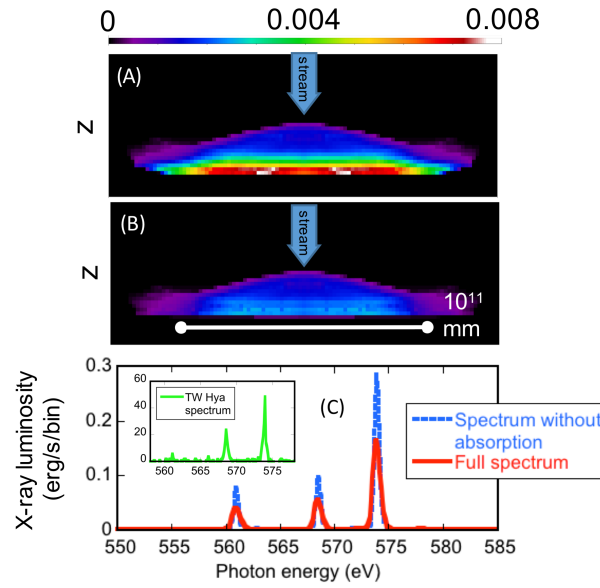
Figure 2.26.: Simulation of reduced X-ray emissivity from a young star due to local absorption in the shell. (A) Time-integrated X-ray emissivity maps [Bonito *et al.* (2014)] (the color bar is in erg/s per grid cell), as post-processed from the astrophysical simulation shown in Fig 1D, and looking along an axis perpendicular to the incident stream. (B) Same as (A), but taking into account the local absorption effect. (C) The emitted spectrum, synthesized from the numerical model used for (A-B), in the energy range of the He-like OVII triplet and using the response function of the MEG grating of the Chandra satellite, with (red) and without (blue) the local absorption. Maps such as (A-B) are out of reach of observation capability, on the contrary to spectra which can be directly compared with astrophysical data such as the one shown in the inset of (C), which displays the spectrum from the CTTS TW Hydrae, as observed by MEG/Chandra [Brickhouse *et al.* (2010)]. The unit of the ordinates of the inset are in counts/bin.

dense and cold shell indeed participates to lowering the X-ray flux that can be observed originating from such stars, and thus influences the value of the mass accretion rate that can be inferred. The set of parameters accessible in the experiment, when scaled to the astrophysical case, corresponds to a situation where the obscuration effect (Figure 2.26C) is moderate. We can expect that for accretion streams characterized by high densities, a larger amount of optically thick material will surround the X-ray emitting slab, inducing heavier obscuration of emitted X-rays.

2.6. Extended discussion and comparison limitations

2.6.1. The role of the gravity

Regarding the effect of the gravity, as it is absent in the laboratory experiment, we can state that in the laboratory case the effects of gravity on the post-shock flow (and on the plasma in general) are negligible over the duration of the experiments. In the astrophysical context however, gravitational forces are important and will tend to decelerate, over a time-scale $\tau_G \sim v_{bf} / g$, the shell plasma that escapes from the shock regions and flows back along the accretion column; where $g = GM_* / R_*^2$ is the gravitational acceleration and v_{bf} is the characteristic speed of the back-flow. The time-scale τ_G can be estimated by considering that the back-flowing plasma is driven by the thermal energy gained in the accretion shocks. Its characteristic speed will then be of the order of the sound speed in the post-shock, thus we can write $\nu_{bf} \sim c_s \sim \sqrt{k_B T/\mu m_H} \sim \frac{1}{3}\nu_{ff}$, where for the last relation we have used the fact that for a strong shock the post-shock temperature, for a Hydrogen plasma after equilibration, is given by $k_B T \sim \frac{3}{32}\mu m_H \nu_{ff}^2$ [Zel'dovich and Raizer (1966)], where v_{ff} is the free-fall speed of the accretion flow, determined by $v_{ff} = \sqrt{2M_*G(\frac{1}{R_*} - \frac{1}{R_{trunc}})}$. Considering $R_{trunc} \sim 5R_*$, we get $v_{ff} = \sqrt{1.6gR_*}$ .Thus, upon impact of the accretion flow onto the stellar surface, gravity will become important for times $\geq \tau_G \sim 1.6R_* / 3v_{ff}$. As an example, for values appropriate to the CTTS MP Mus, $R_* = 1.3R_\odot$ and $M_* = 1.2\,M_\odot$ [Argiroffi, Maggio, and Peres (2007)], this time-scale is $\tau_G \sim 900\,\mathrm{s}$, which is indeed consistent with simulations done with gravity included (see simulation in Orlando et al. (2010)) and with what can be seen in Figure 2.12 ; i.e. the gravity does not play an important role before the Core and the Shell to be fully developed.

2.6.2. The role of the velocity and density profiles

In order for the scaling between laboratory and astrophysical situation to be valid, one has to take care for the different variables to have similar initial spatial profiles [Ryutov et al. (1999)]. However, when looking to the plasma column, in the astrophysical simulation, or the jet in the laboratory, one understand this similarity to break down. Indeed, in the astrophysical situation, the density and velocity profiles of the accretion column are constant along z, while in the laboratory those profiles result from an adiabatic expansion coming from the laser-heated target that generates the jet ; i.e. a decreasing density with the distance as $n = n_0 \left(1 - \frac{\gamma-1}{\gamma+1}(1 - z/c_{s_0}t)\right)^{2/\gamma-1}$, and a velocity increasing with the distance as $v = z/t$, with γ the adiabatic index, and c_{s_0} the initial sound speed of the expanding plasma. Consequently, a perfect scaling between the astrophysical simulation and the laboratory experiment is not possible. However, one can state that the ideal case represented in the astrophysical simulation is not expected to be conform to a real
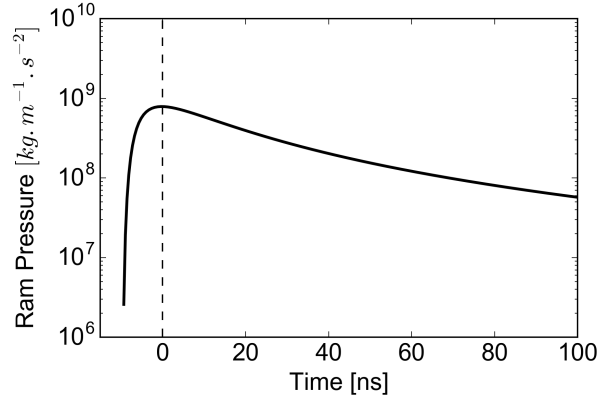
Figure 2.27.: Ram pressure ($\frac{1}{2}\rho v^2$) temporal evolution. The $t = 0$ on the x axis takes its origin from the arrival of the $750\,\text{km.s}^{-1}$ plasma component, at a distance $11.7\,\text{mm}$ from the jet-creation target (i.e. the obstacle target).

accretion impact: if the velocity will always be the one corresponding to a free fall, the density is not expected to be constant over z. Moreover, the adiabatic expansion present in the laboratory seems specific to the laser-plasma experiment.

However, taking into account the fact that, after impact, the shell development is driven by the kinetic pressure (nkT), and that the latter is a transformation of the ram pressure ($\frac{1}{2}\rho v^2$) of the flow under the shock, an important point is to look at the evolution of the ram pressure of the incoming flow. In the astrophysical simulation, it is a constant over time, as speed and density are constant. In the laboratory, the temporal evolution of the ram pressure is shown in the Figure 2.27, for different distances from the plasma source target. The $t = 0$ on the x axis takes its origin from the arrival of the $750\,\text{km.s}^{-1}$ plasma component. As one can see, the ram pressure rapidly reaches a maximum, to finally decreases slowly, i.e. of about a factor 10 within an temporal evolution of $\sim 100\,\text{ns}$. Then, if the ram pressure does not change drastically for most of the dynamic, the after-shock-thermal-pressure will not change drastically too, inducing a quasi similar similar creation of the Shell. However, this is not taking into account, for the rest of the development of the Shell, the importance of the cooling. Indeed, even for a slowly decreasing ram pressure, the incoming speed reduces much faster with time and so does the post shock temperature ($T_{post-shock} \propto v_{infall}^2$), implying a variation of the radiative losses $\Lambda(T)$ (see subsection 2.4.3).

Regarding that specific point of the velocity and density profiles, the present laboratory laser experiment then shows limitations regarding the comparison with the astrophysical simulations. For instance, the periodicity (or cyclical dynamic) pointed out by the gravity-included simulation (see Orlando *et al.* (2010)) of a rising shell followed by its collapse, and which implies a new shell rising, *etc.* (as the consequence of the steady incoming flow of matter in the simulations) will not be seen in the experiment. Consequently, the

experiment is not able to reproduce the cyclical dynamic at late times, and regarding this specific point, the lack of gravity in the experiment also plays a major role. However, the gravity-included and steady incoming flow simulations [Orlando *et al.* (2010)] shows that the same configuration is repeated, where the accretion shock and the shell coexist. Then, our experiment as well as the no-gravity astrophysical simulations presented in this manuscript both are representative of the early times of that "cyclical" situation.

2.6.3. The radiative properties

One point that could be raised regarding the accretion study presented in this chapter could be the differences between the thermodynamic and radiative properties of the laboratory and astrophysical plasma. Indeed, We do not expect, due to the very different plasma compositions (Hydrogen for the astrophysical situation; and Carbon, Chlorine, Fluorine and Hydrogen for the laboratory situation), the radiative properties to be similar between the two systems.

The important point is to distinguish two things: (a) the formation of the shell, and b) the properties (or characteristics) of that shell. The main difference between these two is that: (a) does not depend on the fact that the two plasmas (the laboratory one and the astrophysical one) do not have the same thermodynamical and radiative properties, while (b) depends on it. Hence, despite these different properties, the shell is indeed formed in both situations (laboratory and astrophysical), but does have different characteristics in the two cases. Thus, we can indeed state that the behavior observed in the experiment robustly apply to the astrophysical system.

Statement (a) is supported by the fact that the shell creation depends on the speed of extraction of the matter at the border of the stream. This speed is related to the speed under the shock, which is roughly $v_{stream}/4$ in a strong shock approximation. Note here (see the previous section) that the stream velocity is precisely quite similar between the two situations (laboratory and astrophysical), at least for one period of the "cyclical" dynamic. Then, the ram pressure under the shock has to be compared to the magnetic pressure (i.e. evaluating $\beta_{dyn} = (ram\, pressure)/(magnetic\, pressure)$) in order to understand how easily that matter can be extracted from the border of the shocked region to form the shell. Looking at β_{dyn} for the experiment and the astrophysical simulation, one can see in Table 2.2 of the subsection 2.4.4 that this parameter is effectively similar for the two situations, in the core region as well as in the shell region (only roughly a factor 2 possibly separates the parameter between the two situations).

Hence, our conclusion is that the shell formation observed in the laboratory is robustly representative of what takes place in the astrophysical situation. This is precisely because β_{dyn} is similar between the two plasmas and does not depend on each plasma radiative and thermodynamical properties.

2.6.4. The role of the magnetic field strength

The importance of the magnetic field strength was already pointed out by the simulation work made by *Orlando et al.* (see Orlando *et al.* (2010)). Figure 2.28 displays results extracted from this simulation work, and showing the impact region at the same time, $t = 530$ s, for different magnetic field strength, 50, 10 and 1 Gauss, from left to right respectively. As one can see, the shell creation is significantly affected by this change. For 50 Gauss (left map), the shell creation is almost inexistent. The magnetic field is strong enough to hold back any flowing of matter out of the stream border. Even if the beta ($2\mu_0 nkT/B^2$) value after impact is above one (i.e. the thermal pressure dominating the magnetic one), the situation rapidly reverses because of the cooling while the plasma starts to expand out of the stream. This situation leads to a very limited spread of the shell, with a radial and vertical extension that doesn't exceed the vertical extension of the core itself. The middle case (10 Gauss) is typical of the situation detailed in this chapter, where the matter can flow away from the shocked region to finally be stopped and redirected by the magnetic field. This configuration allows the ejected matter to create a cocoon (described as the shell all along the chapter) around the shocked material (described as the core). The right case, with a magnetic field strength of 1 Gauss, presents a magnetic pressure not significant enough to stop the ejected matter within the simulation box. A cocoon is not strictly speaking created, and the ejected matter is rapidly diluted because of the lack of constraints in its expansion.

Experimentally, a similar behavior has been observed when changing the magnetic field strength externally applied with the Helmholtz coil. Figure 2.29 displays electron density maps of the impact region, at $t = 31$ ns, for different magnetic field strength, 6, 20 and 30 Tesla, from left to right respectively. As for the simulation of Figure 2.28, we observe an ejected matter easily stopped as the magnetic field strength increases. As expected, the global extend of the shell decreases while increasing the magnetic field strength, inducing it to be denser.

This behavior reveals the augmentation of the magnetic pressure, shifting the point where the balance with the kinetic pressure of the plasma is achieved. However, even if the shell is constrained in its propagation when increasing the magnetic field, its existence is never suppressed. Indeed, even at 30 Tesla, the magnetic pressure is not strong enough to prevent the expansion of the shell. Looking at the typical parameter of the shocked material in the experimental case (see Table 2.2), a immediate balance between kinetic pressure (ram + thermal) and magnetic pressure at the shock location could be achieved by applying a magnetic field of 120 T. Such a value is up to now beyond the present capability in terms of non-destructive magnetic field generation. However, it is not absurd to think about getting such value for a laser-plasma experiment in a near future. Even if the constraints in terms of mechanical forces are strong, the Helmholtz coil design as it is right now is well adapted
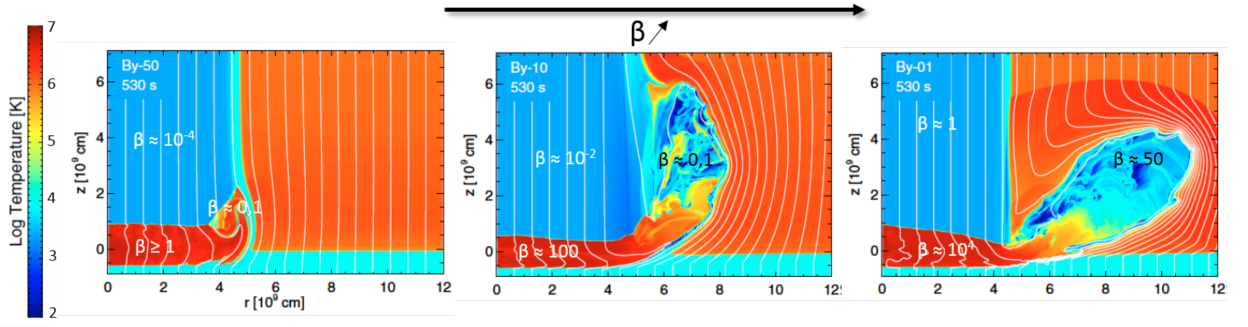
Figure 2.28.: Astrophysical simulation using the Pluto Code for different initial magnetic field values ; extracted from Orlando *et al.* (2010). The plasma dynamic is represented through the plasma temperature, displayed in Kelvin. From left to right, the initial magnetic field strength is decreased, being respectively 50, 10 and 1 Gauss. The snapshot are all taken at the same time, $t = 530\,\mathrm{s}$.

in order to get such a magnetic field value, the issue being the shot rate and the field of view to the plasma dynamic, that should both probably be reduced. Such after-shock $\beta = 1$ regime (and beyond) is of interest in order to experimentally observe fibrils creations in the shocked material. This mechanism is achieved when no matter exchanges are allowed in between tiny regions within the shocked area. This is made possible because of a magnetic field strong enough to prevent the plasma to flow "freely" by carrying the magnetic field lines. Each fibril then represents isolated tube of plasma (elongated in the direction of the magnetic field) and independent from each other. A multitude of shocks going up the falling stream are created, and having different properties (density, speed etc.) regarding the inhomogeneities initially present in the infalling stream itself. Such a configuration
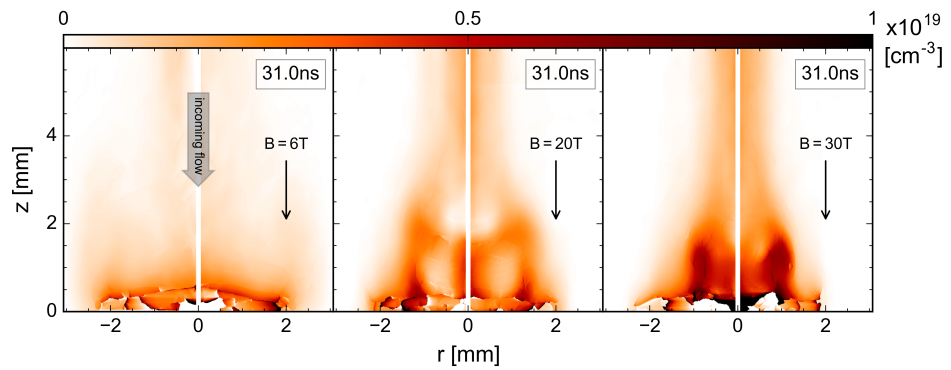
Figure 2.29.: Experimental electron density maps of the accretion dynamic for different applied magnetic field strength value. From left to right, 6, 20 and 30 Tesla respectively. Those maps are retrieved through interferometry. In the present case, is has to be noticed that contrarily to the previous accretion configuration presented in the chapter, the distance separation between the jet-creation-target and the obstacle target is 18 mm (while it was 17.7 mm before). The snapshot are all taken at the same time, $t = 31\,\mathrm{ns}$.

was already observed in simulation work, as the one of Matsakos *et al.* (2013).

2.7. Conclusions

In the context of young stars, the accretion process is a key phenomenon in the star formation process. The shock created through this mechanism generates observable radiation that helps unravelling the star formation processes. The laboratory study presented in this chapter is the first experiment that allows insight in this phenomenon by the way of magnetically confined accretion column, thanks to the coupling of an externally applied magnetic field and laser-created plasma. Oppositely to the usual shock tube setup [Cross *et al.* (2016)], this setup doesn't present the strong tube edges constraints on the plasma dynamic, as well as present the advantage for the interaction between the plasma and the magnetic field to be studied. The latter point is of importance, since the magnetic field is a key component of the star formation process in general. In this chapter we focused on a specific $\beta > 1$ case, where the total kinetic and thermal pressure after the shock is greater than the magnetic pressure. The experiments exhibit very good agreement with the astrophysical simulations, showing the accretion shock formation as well as the development, coming from the shocked plasma, of a shell wrapping up the shock region. This shell then, is found to be responsible for a non-negligible part of the absorption of the X-ray flux coming from the shocked region, reducing the X-ray luminosity effectively observable. Our results point to the crucial necessity to correctly account for plasma absorption in order to interpret and model accretion processes in young stars. Doing so allows for more accurate, with respect to alternate scenarios, modelling of observations [Orlando *et al.* (2010); Bonito *et al.* (2014); Reale *et al.* (2013)], thus supporting the plausibility of the dynamics highlighted here and suggesting that indeed such conditions are present in CTTSs.

By improving the capability of generating strong externally applied magnetic field, this setup could be suitable to get insight into accretion dynamic where the magnetic pressure dominates the plasma pressure after the shock ($\beta > 1$). This latter case, could provide experimental measurement on fibrils developments [Matsakos *et al.* (2013)]. This requires an applied magnetic field up to 120 T. The laboratory platform developed here also opens up the investigation of a number of other issues. For example, by changing the orientation of the stream with respect to the magnetic field (as for instance, what was discussed in section 1.4), or by looking at the impact of the accretion column onto an obstacle, possessing an angle with respect to the column axis, alternative channels of accretion can be explored [Casassus *et al.* (2013); Orlando *et al.* (2013); Matsakos *et al.* (2013)].

Conclusion

The work presented in this thesis is related to experimental studies dealing with laser-generated plasma flow within a magnetized environment. The plasma expansion was induced by laser irradiation of solids with a 1×10^{13} W/cm^2 laser intensity pulse, which is responsible for generating sufficiently hot (hundred of eV) and dense (about 10^{19} cm^{-3}) expanding plasma for it to be situated in a ideal MHD regime. The externally applied magnetic field was generated via a Helmholtz coil specifically designed to work in a laser chamber environment, and set up from few Tesla up to 30 Tesla. Regarding those two components, i.e. the plasma and the magnetic field, it is important to note that our experiments were situated in a moderately high plasma beta regime (where the plasma beta is the ratio of the plasma pressure over the magnetic pressure). This is to say, the plasma pressure dominates the magnetic one early in the expansion, while the dilution of the plasma implies a transition, later on and within a reasonable time scale, to a case where the magnetic pressure finally dominates the plasma pressure. Such interaction has led to experimental observations that could be linked to astrophysical situations. The framework of this thesis is then situated in the laboratory astrophysics context. We hereafter recall the main points of this manuscript.

In chapter 1 we have studied the dynamic of the plasma flow and its interaction with an externally applied magnetic field for different configurations of the magnetic field with respect to the expanding plasma. Firstly when the magnetic field is aligned with the main expansion axis of the plasma (i.e. orthogonal to the irradiated solid target). Secondly, when a misalignment angle is applied between the magnetic field and the expansion axis. And finally when the plasma is expanding perpendicularly to the magnetic field.

The first part of this chapter has shown the capability for a poloidal magnetic field (i.e. aligned with respect the plasma expansion axis) to efficiently collimate the flow. The "frozen-in" regime, provided by the ideal MHD situation, leads to a very specific dynamic where a plasma cavity is formed during the expansion. Such a cavity results from the equilibration of the magnetic pressure with the plasma ram pressure, after reduction of the latest during the expansion. The cavity shape leads to an efficient redirection of the plasma within a central axis. The plasma is found to slide along the pressure equilibration points, to finally create a conical shock at the tip of the cavity that launches a nicely directed plasma flow. This cavity collimation mechanism is described as a Poloidal

Magnetic Nozzle, for the analogy with a mechanical nozzle where, in the present case, the magnetic pressure acts as the solid border of the standard nozzles. In addition to describe the collimation mechanism, this first part was dedicated in characterizing the resulting magnetically collimated plasma jet. The electron density and flow velocity is retrieved through interferometry and the temperature via X-ray spectroscopy. Some assumptions from those experimentally measured quantities have led to the determination of an extended list of plasma parameters characterizing the plasma jet. It results from it that if the magnetic field plays a major role in the early collimation process (cavity formation), the plasma is only marginally magnetized within the well formed jet, and the magnetic field is not expected to play a major role in the jet propagation over long temporal and spatial scales. Finally, a link is built between that collimation dynamic within a poloidal magnetic field, and the jet formation process in the context of Young Stellar Objects. In the astrophysical context, the plasma outflow comes from either stellar or disk winds ejections, and the poloidal magnetic field, from the large scale, pre-cloud contracted magnetic field.

A second part of the chapter examines further the previous logic, by implementing a misalignment angle between the plasma ouflow and the magnetic field. This specific case is of direct interest for the astrophysical context, where it is believed that the symmetry axis of the star forming system (rotation axis, ans so outflow axis) can be misaligned with respect to the large scale magnetic field. Our experimental study has thus shed light on a disruption of the collimation process for a strong misalignment. The reason for the disruption can be found in the specific cavity formation process. Indeed, it is found that breaking the symmetry of the system (outflow axis / poloidal magnetic field) prevents the conical shock, at the tip of the cavity, to form properly. More important, the asymmetry in the cavity greatly reduces the confinement of the plasma. The plasma density is finally found to tend to the without-magnetic-field expansion case for important misalignments. Those experimental observations have to be linked with astrophysical observations of ouflow in Young Stellar Objects, for which is found a tendency for well collimated, long range, bright jets to be aligned with the magnetic field, while oppositely, weaker and shorter jets are mainly found to be misaligned with the magnetic field.

The last part examined the propagation of the plasma within a perpendicular magnetic field. The investigated dynamic exhibits the formation of a plasma sheet. This sheet, when formed, propagates unimpeded across the magnetic field over large distances ($> 2\,\mathrm{cm}$) compared to the initial plasma scale length. The first instants of the propagation are determined by a large plasma ram pressure, and consequently the frozen-in regime advecting the magnetic field lines. At later times, it appears that kinetic effects could play a role driving the propagation. The $E \times B$ mechanism is evoked but does not seem perfectly adequate due to the collisionality of the plasma staying important within the plasma sheet. In addition to the propagation, instabilities are found to develop at the base of the plasma

sheet. Further work is needed in order to characterize such instabilities.

In chapter 2 we took advantage of the laboratory well collimated jet (in the B-field aligned case) to study an other topic of interest within the astrophysical context: the accretion dynamic. In Classical T Tauri star, the accretion process is believed to occur from accretion columns that fall down from the accretion disk edge onto the stellar surface. The impact of these columns at the stellar surface generates a shock, from which radiations emanate and are intensively studied in astrophysics. Experimentally, it consists in launching the plasma jet onto an obstacle target. The jets acts as the accretion column, while the obstacle mimics the stellar surface.

Here again, the experiment is representative of a moderately high plasma beta. The shock formed through the impact with the obstacle is observed. From this shocked material, we observe ejecta of matter at the border of the column. These ejecta are confined by the magnetic field within a cocoon that surrounds the shocked dynamic. Finally the development of that cocoon is found to develop similarly in astrophysical simulations of the accretion dynamic. More interesting, this cocoon forms a shell that, in the astrophysical situation, is found to be a good absorptive medium for the X-rays emanating from the shocked region. Such absorptive effect is of interest in the astrophysical context, as it possibly represents a good candidate in explaining discrepancies between astrophysical observation of X-rays accretion emissions and other emission wavelengths.

Perspective

The experimental setup coupling laser-created plasma and externally applied magnetic field used here could be employed for further investigations. For example, the collimated jet formed through the Poloidal Magnetic Nozzle mechanism could be used in order to study the collision with an ambient gas (Herbig-Haro kind of objects). The collision of two counter-propagating jets could as well be investigated. Regarding the accretion process, one can think to implement an ambient medium in front of the obstacle location in order to better mimic the chromosphere of a star. Looking for a change in the topology of the impact could lead to the investigation of a plasma jet impacting a tilted obstacle. All those dynamics could likely be linked to astrophysical contexts, with the great advantage of implementing the magnetic field component. The latest being of course present in the astrophysical dynamics, and believed to play almost always a key role.

A. Annexes

A.1. Plasma Parameters

Most of the parameters defined in this section, if not indicated, come from Ryutov *et al.*' papers Ryutov *et al.* (1999); Ryutov, Drake, and Remington (2000). In the formulas below, if not specified, the quantities are expressed in the International System of Units.

The **Reynolds number**, R_e, which is the ratio of the inertial force to the viscous one is defined in the usual manner, i.e. as

$$R_e = \frac{\chi_{ad}}{\chi_\nu} = \frac{Lv}{\chi_\nu}$$

where v is the characteristic speed of the system, taken as the greater of the bulk velocity of the plasma (or flow velocity) u_d and the sound speed C_s. L is the typical scale length of the system. The distance for which gradients are observed in the plasma density, or, typically in our case the stream, core or shell radii (see Fig. 2.12 for a definition of these terms). χ_ν is the *kinematic viscosity* or bulk viscosity (also simply noted ν), taken from [Ryutov *et al.* (1999)]:

$$\nu = 2 \times 10^{19} \frac{[T(eV)]^{5/2}}{ln\Lambda\sqrt{A}Z^4 n_i\,(cm^{-3})} \quad [\text{cm}^2.\text{s}^{-1}]$$

where $ln\Lambda$ is the *Coulomb logarithm*. It can be defined following Spitzer (1956): $T_e < 50\,\text{eV}$, $ln\Lambda = 23.4 - 1.15 \times log_{10}n_e + 3.45 \times log_{10}T_e$; $T_e > 50\,\text{eV}$, $ln\Lambda = 25.43 - 1.15 \times log_{10}n_e + 2.3 \times log_{10}T_e$. (A more detailed description of the Coulomb logarithm can be found on page 34 of Huba (2016) (NRL Plasma Formulary)).

While in the case where the electrons are magnetized,

$$\nu = 2 \times 10^8 \alpha \frac{T(eV)}{ZB(G)} \quad [\text{cm}^2.\text{s}^{-1}]$$

with $\alpha = l_{magn}/r_{Li}$. Here, l_{magn} is the typical length at which the magnetic field line changes its direction by $\pi/2$; r_{Li} is the ion Larmor radius. To determine if the electrons are magnetized, or not, we calculate the following **Hall number**:

$$H_\alpha = \omega_{c\alpha}\tau_\alpha$$

where α stand for either ion or electron.

τ_α is the *electron or ion collision time* [Braginskii (1965)],

$$\tau_e = \tau_{ei} = \tau_{ie} = \frac{1}{\nu_{ei}} = \left(2.9 \times 10^{-6}Z \times n_e(cm^{-3}) \times ln\Lambda \times [T_e(eV)]^{-3/2}\right)^{-1} \quad [s]$$

$$\tau_i = \tau_{ii} = \frac{1}{\nu_i} = \left(4.8 \times 10^{-8}n_i(cm^{-3}) \times Z^4 \times A^{-1/2} \times ln\Lambda \times [T_i(eV)]^{-3/2}\right)^{-1} \quad [s]$$

(note the equality $\tau_{ii} = \tau_{ei}\sqrt{\frac{2m_i}{m_e}}Z^{-3}$).

$\omega_{c\alpha}$ is the *electron or ion cyclotron frequency,*

$$\omega_{c\alpha} = \frac{Z_\alpha \times e \times B}{m_\alpha}$$

Finally it gives,

$$H_e = 1.8 \times 10^{23} \times \frac{B \times [T_e(eV)]^{3/2}}{n_e(cm^{-3})ln\Lambda}$$

$$H_i = 6 \times 10^{21} \times \frac{B \times [T_i(eV)]^{3/2}}{Z^3 A^{1/2}n_i(cm^{-3})ln\Lambda}$$

This number, defined as the cyclotron frequency times the electron/ion collision time, is representative of the number of cyclotron orbits a particle performs before undergoing a collision. Thus for high Hall numbers (i.e. $H_\alpha \gg 1$), we consider the specie to be magnetized. It could also be useful to notice the Hall number to also simply be the ratio of the mean free path of the specie over its Larmor radius (or gyro-radius), $H_\alpha = mfp_\alpha/r_{L\alpha}$,

where $mfp_\alpha = v_{th\alpha}\tau_\alpha$, and $r_{L\alpha} = v_{th\alpha}/\omega_{c\alpha}$. This can be compared to the standard plasma collisionallity being the mean free path over the characteristic size of the system (mfp_α/L).

In order to get a system for which the ideal MHD equations apply, the viscous effects have to be negligible and then $R_e \gg 1$.

The **Peclet number**, P_e, is also defined in the usual manner, i.e. as the ratio of the heat convection to the heat conduction:

$$P_e = \frac{Lv}{\chi_{th}}$$

where χ_{th} is the *thermal diffusivity* for electrons, taken from [Ryutov *et al.* (1999)]:

$$\chi_{th} = 2 \times 10^{21} \frac{[T(eV)]^{5/2}}{ln\Lambda Z(Z+1)n_i(cm^{-3})} \quad [\text{cm}^2.\text{s}^{-1}]$$

While in the case where the electrons are magnetized,

$$\chi_{th} = 8.6 \times 10^{9} \alpha \frac{\sqrt{A}}{Z} \frac{T(eV)}{B(G)} \quad [\text{cm}^2.\text{s}^{-1}]$$

The ideal MHD equations also require, in order to be valid, the Peclet number to be large (i.e. $\gg 1$).

The **magnetic Reynolds** is also defined in the usual manner, i.e. as the ratio of the convection over Ohmic dissipation:

$$Re_M = \frac{Lv}{\chi_m}$$

where χ_m (also noted D_M in the literature) is the *magnetic diffusivity* [Ryutov, Drake, and Remington (2000)]:

$$\chi_m = \frac{1}{\mu_0\sigma} = 8.2 \times 10^5 \frac{Z \times ln\Lambda}{[T_e(eV)]^{3/2}} \quad [\text{cm}^2.\text{s}^{-1}]$$

where μ_0 is the vacuum permeability, and σ is taken as the *Spitzer conductivity*,

$$\sigma = \frac{n_e e^2 \tau_e}{m_e}$$

As for the previous dimensionless numbers, the ideal MHD equations require, in order to be valid, the Magnetic Reynolds number to be large (i.e. $\gg 1$).

We define as follows the parameters $\boldsymbol{\beta_{ther}}$, which is the ratio of the thermal pressure over the magnetic pressure:

$$\beta_{ther} = \frac{n_i k_B T_i + n_e k_B T_e}{B^2/2\mu_0}$$

and $\boldsymbol{\beta_{dyn}}$, which is the ratio of the dynamic pressure over the magnetic pressure:

$$\beta_{dyn} = \frac{\rho v^2/2}{B^2/2\mu_0}$$

The **cooling time**, τ_{cool}, is defined as:

$$\tau_{cool} = \frac{Internal\ Energy\ Density}{Volumetric\ Radiative\ Power} = \frac{(3/2)n_i(1+Z)kT}{n_i n_e \Lambda(T)}$$

where Λ are the radiative losses, taking into account free-free, bound-free and bound-bound radiation processes. Here, no opacity is taken into account, so that the plasma is considered to be in an optically thin regime (which is mostly the case for the plasma investigated here, see sec. 1.2.3.4 for a discussion on this). In the case where only Bremsstrahlung (free-free) radiations are taken into account, $\tau_{Br} = 2.4 \times 10^{-12} \frac{(1+Z)T(eV)}{Z n_i \Lambda_N}$ in $[s]$, with $\Lambda_N = 1.7 \times 10^{-25} \times Z^2 \times T(eV)^{1/2}$ in [erg.cm^3.s^{-1}] [Ryutov *et al.* (1999)]. In the case where all the kinds of radiations have to be taken into account, a correct description of those radiations, depending on the temperature and the density, has to be done, by the way of an atomic code for example, in order to get access to the radiative loses $\Lambda(T)$ (see for instance sec. 2.4.3 of this manuscript). The cooling time as described above corresponds to the time needed for the plasma temperature to decrease by 100% by radiation, at a given radiative losses. $\frac{x}{100}\tau_{cool}$ then defines the time needed for the plasma temperature to decrease by $x\%$ by radiation.

The **equilibration time**, τ_ϵ, is defined as [Braginskii (1965)]:

$$\tau_\epsilon = \tau_{ii}\sqrt{\frac{m_i}{m_e}} = \tau_{ei}\frac{\sqrt{2}m_i}{m_e}Z^{-3}$$

However, this equilibration time is a very raw estimate of the effective time for which the electron or ion temperatures stop to change significantly. It can be useful to solve the following system [Huba (2016)]:

$$\frac{dT_e}{dt} = \nu_\epsilon^{e\backslash i}\left(T_i - T_e\right) - \frac{n_e\Lambda(T_e)}{{}^{3}/_{2} \times Z}$$
$$\frac{dT_i}{dt} = \nu_\epsilon^{i\backslash e}\left(T_e - T_i\right)$$

with $\nu_\epsilon^{\alpha\backslash\beta} = 1.8 \times 10^{-19}(m_\alpha m_\beta)^{1/2}Z_\alpha^2 Z_\beta^2 n_\beta ln\Lambda/(m_\alpha T_\beta(eV) + m_\beta T_\alpha(eV))^{3/2}$. The second term (optional) in the electron equation (top) is the cooling rate, taking into account the electron radiative losses (see page 119 of this manuscript for a description of the way this term is calculated). The temperatures evolution can then be compared to a physical time, as the *hydrodynamic time* ($t_{hydro} = L_c/c_s$; $L_c \equiv$ characteristic size of the system ; $c_s = \sqrt{\gamma(ZT_e(eV)+T_i(eV))/m_i}$ the sound speed), and the equilibration time, t_e, can be defined such as $\left.\frac{dT_{e/i}}{dt}\right|_{t_e} \times \frac{t_{hydro}}{T_{e/i}} = 0.01$. That is to say, when the variation of the electron (ion) temperature over the hydrodynamic time represents no more than an increase or decrease of 1%.

———————————

For all the above quantities, the atomic number and mass number are defined as stoichiometrically averaged over the different components in the multi-ion plasma considered here, either PVC or CF_2, leading to Z_{mean} and a A_{mean}.

However, the presence of hydrogen (in PVC (C_2H_3Cl) for instance) can have a very strong effect on the bulk ion viscosity. Let us verify, in the case of the previous calculation of the plasma viscosity, that we call hereafter $\nu_{average}$, that such approach leads to similar results compared to more accurate calculations detailing the contribution of each species within a *multi-species plasma* [Dorf (2014)]:

$$\nu_{multi-species}(cm^2.s^{-1}) = \frac{4.27\times10^5}{\Lambda\rho(g.cm^{-3})}\frac{n_H\sqrt{A_H}[T(eV)]^{5/2}}{Z_{Cl}{}^2 n_{Cl} + Z_C^2 n_C}$$
$$\times\left(1 - \frac{11}{12}\left(\frac{Z_{Cl}{}^2 n_{Cl}}{A_{Cl}} + \frac{Z_C^2 n_C}{A_C}\right)\frac{A_H}{Z_{Cl}{}^2 n_{Cl} + Z_C^2 n_C}\right)$$

the formula being here specifically developed for a PVC (C_2H_3Cl) plasma. The numerical

application for our typical experimental density and electron temperatures values will give:

- $\nu_{average} = 0.7\,\text{cm}^2\text{s}^{-1}$ and $\nu_{multi-species} = 1.9\,\text{cm}^2\text{s}^{-1}$ for ($n_e = 1.5 \times 10^{18}\,\text{cm}^{-3}$; $T_e = 10\,\text{eV}$), corresponding to the laboratory stream parameters - see chapter 2.

- $\nu_{average} = 5.6 \times 10^2\,\text{cm}^2\text{s}^{-1}$ and $\nu_{multi-species} = 1.4 \times 10^3\,\text{cm}^2\text{s}^{-1}$ for ($n_e = 1.5 \times 10^{19}\,\text{cm}^{-3}$; $T_e = 320\,\text{eV}$), corresponding to the laboratory core parameters - see chapter 2.

We thus observe that a factor ~3 is separating the two approaches for the calculation of the viscosity. As a result, we can state that the use of a mean Z and A, redefining the PVC or the CF_2 plasma as a single species is quite accurate. Finally, we effectively expect the Hydrogen to have a strong effect on the viscosity while present in the middle of other high Z atoms, compared to the viscosity of a plasma in which there would be only high Z atoms. However, stoichiometrically averaging the Z and A number for our PVC plasma, already takes into account, in some way, the presence of that Hydrogen in the plasma.

A.2. X-ray Radiography

To have access to the electron density measurement at higher density values than the ones accessible by the interferometry (as shown in Fig. 2.13 of the chapter 2), X-ray radiography is performed. This is needed, not only because the plasma density will become over critical when approaching the obstacle surface, and thus will prevent the optical probe to penetrate the plasma, but also because of the large density gradients that refract the optical probe beam away from the target.
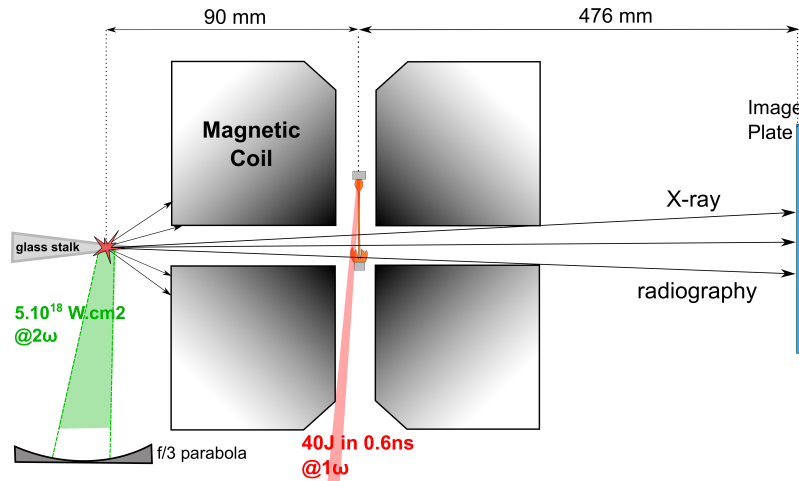
Figure A.1.: Cartoon of the X-ray radiography configuration.

The X-ray radiography is performed by focusing the 2.5 J/320 fs/528.5 nm compressed laser pulse arm of the ELFIE facility [Zou *et al.* (2008)] onto a thin SiO2 (glass) stalk situated at one of the entrance of the magnetic coil radial aperture, i.e. in the same path as the interferometry diagnostic (the two diagnostics are alternated, i.e. the X-ray probe is also transverse to the axis z, see Fig. A.1 , or Fig. 2.7 for a cartoon of the setup including the interferometry path). It generates an isotropic, short duration (ps) X-ray emission, strongly dominated by the Silicon cold K- emission line at ~ 1740 eV [Chen *et al.* (2016)]. As the glass stalk is oriented in the same axis as the radial tube managed in the coil, and as the stalk is tapered into a point-like tip on which the short-pulse laser is shooting, the X-ray emission will originate from a point source from the point of view of the plasma. It produces on an Image Plate [Meadowcroft, Bentley, and Stott (2008)], situated at the opposite side of the radial tube, a sharp projected 2D transmission map of the X-rays as they go through the denser plasma regions.

From the projected images collected on the image plates, we take a series of lineouts parallel to the axis z, passing through the stream-impacted zone and on its sides. Two typical lineouts, one taken at the center of the impact region, and one away (where the obstacle target is still cold) are shown in Fig. A.2. To quantitatively reconstruct the expanding plasma density profile, we record such lineouts all along the target surface, which are
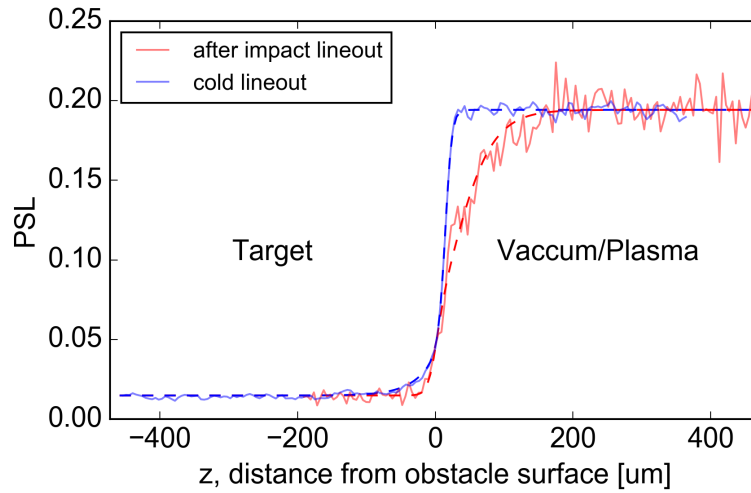
Figure A.2.: Illustration of the step transition observed in the transmitted X-rays between the target and vacuum or an ablated plasma expanding toward vacuum. The blue curves are showing the step transition of the X-ray probe transmission in a cold, non-impacted target (the target is on the left, heavily absorbing the X-rays), while the red curves show the smoother transition occurring when a plasma expands from the target surface, i.e. following the impact of the obstacle target by the incoming stream (the PSL unit in ordinates stands for "Photo Stimulated Luminescence", which is the unit of the readout instrument (FujiFilm Co.) of the Image Plate detector we used, and which can be related in absolute to the incident X-ray photon flux [Meadowcroft, Bentley, and Stott (2008)]). The solid lines are experimental lineouts while the dashed lines are the fits of the latest. The plasma transition, i.e. the red curve, is taken from a radiography occurring 35.5 ns after the stream impact on the target.

then fitted by a two-slopes sigmoid function, i.e. $Step_{\alpha_r}(z) = a \pm \frac{(a-b)}{1 \pm e^{s1(\pm z \pm l1)} + e^{s2(\pm z \pm l2)}}$. It is then possible to retrieve the transmission of the X-rays as follows: $T_r(z) = Step_{plasma}(z)/Step_{cold}(z)$.

Fig. A.3 (a) shows the deduced transmission along the target surface, at $z = 5\,\mu m$ away from the target surface. We note the drop of the transmission in a peak shape at the jet impact location, corresponding to an increased density as the jet hits the obstacle. The radial extension of this transmission drop is well corresponding with the measured incoming jet diameter, equal to 1.5 mm and which is represented by the two vertical dashed lines in Fig. A.3 (a). Fig. A.3 (b) shows the longitudinal evolution of the transmission as we go away from the target surface. It is there taken at $r = 0$, the middle of the impacted region by the incoming stream.

Because the X-ray radiation is strongly dominated by the Si K-alpha at 1740 eV, we calculate the optical depth of 1740 eV X-rays going through different couples (n_e, T_e) of plasma electron density and temperature conditions, which we chose to encompass our experimental plasma conditions, by running the 0-D atomic code FLYCHK [Chung *et al.* (2005)].
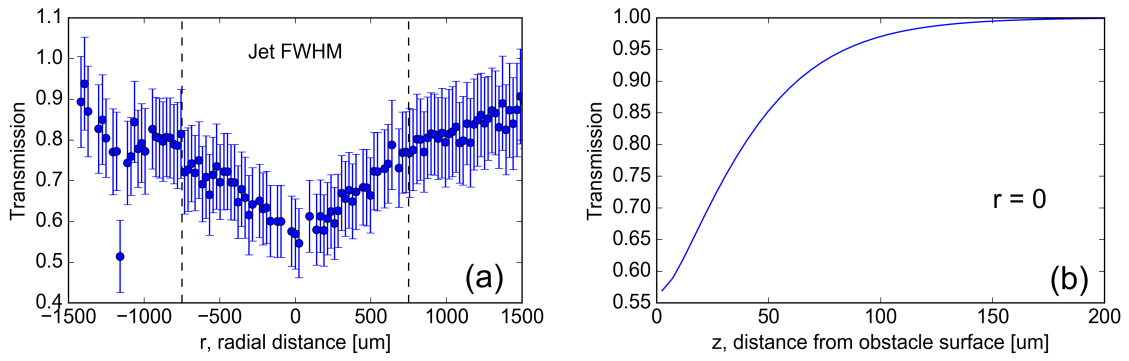
Figure A.3.: (a) Recorded radial transmission of the X-rays along the target surface, at $z = 5\mu m$ from the target surface.
(b) Longitudinal transmission of the X-rays, going away from the target surface, i.e. along the z axis, taken at $r = 0$. The transmissions are calculated here from a radiography occurring 35.5 ns after the jet impact.

Then, using the plasma electron temperature retrieved from the X-ray spectrometry measurement (see sec. 2.4.2 of the chapter 2) and analysis, the electron density is here inferred (see the dashed line in Fig. 2.13 of the chapter 2) as the one allowing to match the experimental transmission with the FLYCHK-calculated transmission.

Fig. A.4 display the 2D version of the transmission calculated following the present analysis method.
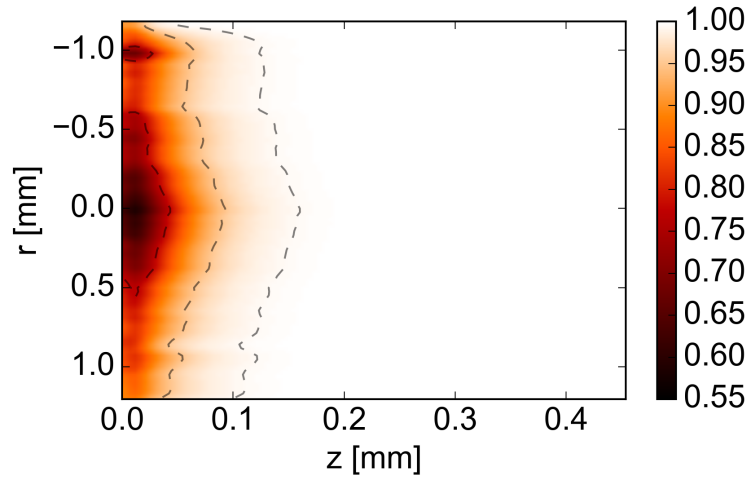
Figure A.4.: 2D map of the transmission resulting from the analysis detailed in this section. Here, $z = 0$ is the obstacle location, and the jet flows from the right to the left.

A.3. T_e of the Bremsstrahlung emission maximum ($T_{Br_{max}}$)

We present here the way how the electron temperature for the maximum of the Bremsstrahlung emission, $T_{Br_{max}}$ (in sec. 2.4.2 of the chapter 2), has been calculated.

We start from the Bremsstrahlung radiative power per unit of time and volume $\frac{dW}{dV d\nu}(\nu, n, T) = \frac{32\pi^{1/2} g_{ff} Z^2 e^6 n_e n_i}{3 m_e^2 c^3} \left(\frac{m_e}{2 k_B T_e}\right)^{1/2} exp\left(-\frac{h\nu}{k_B T_e}\right)$ in [J/s/Hz/m^{-3}] that we integrate in an interval of frequencies $[\nu_a = \nu_0 - \delta\nu, \ \nu_b = \nu_0 + \delta\nu]$. This gives $W(T) \propto T_e^{1/2} \left(exp\left(-\frac{h\nu_b}{k_B T_e}\right) - exp\left(-\frac{h\nu_a}{k_B T_e}\right)\right)$ which evolution with the electron temperature is represented in Fig. 2.16 *Right*, presenting a maximum at a temperature that we have called $T_{Br_{max}}$. Because of the shape of the function (see for instance Fig. 2.16), looking at the maximum of the function only requires to look for $\frac{dW}{dT_e} = 0$. Then, it is possible to show, that if $T_e \neq 0$ and $T_e \neq \infty$, looking at the maximum of $W(T)$ is equivalent to solve the following equation:

$$exp\left(\frac{h\nu_b - h\nu_a}{k_B T_e}\right) - \frac{k_B T_e + 2h\nu_a}{k_B T_e + 2h\nu_b} = 0 \qquad (A.1)$$

The latter equation is solved numerically for T_e.
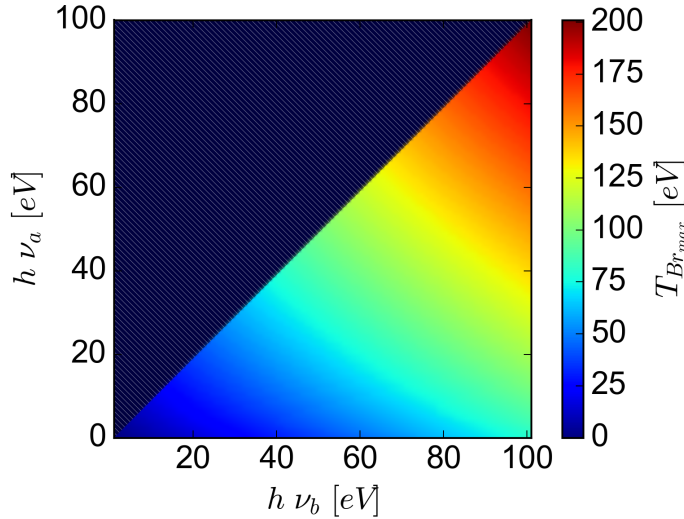
Figure A.5.: $T_e = T_{Br_{max}}$ such as it solves equation A.1 for various values of $h\nu_a$ and $h\nu_b$, with $h\nu_b > h\nu_a$ (N.B.: this is why the upper left part of the 2D map is emptied).

Fig. A.5 displays $T_e = T_{Br_{max}}$ such as it solves equation A.1 for frequencies going from 0 eV to 100 eV with $h\nu_b > h\nu_a$. Some extracted lineouts are plotted in Fig. A.6, representing $T_{Br_{max}}$ as a function of $h\nu_a$ for different $h\nu_b$.

Consequently, we assume the evolution of $T_{Br_{max}}$ with $h\nu_a$ to be well approximated by an affine relation: $T_{Br_{max}}(h\nu_a) = a \times h\nu_b + b$, with a and b, both depending on $h\nu_b$, i.e. $a(h\nu_b)$
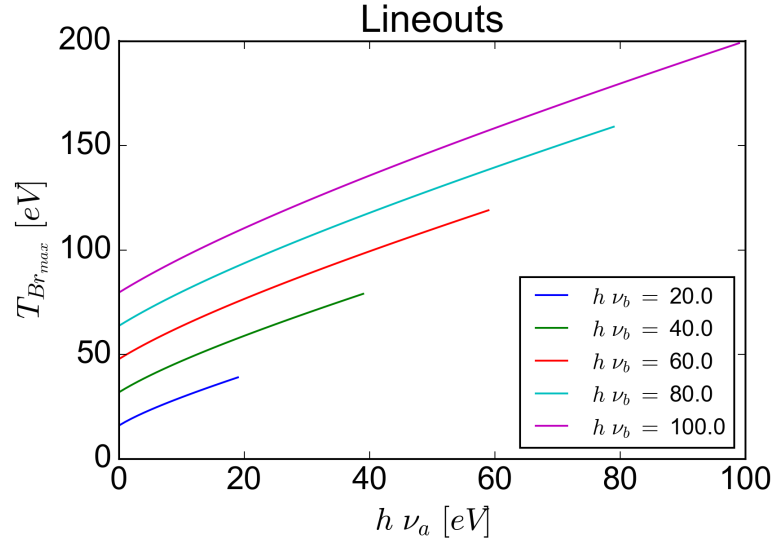
Figure A.6.: Lineouts of the map of Fig. A.5.

and $b(h\nu_b)$. This approximation however is incorrect for small $h\nu_a$ as it can be seen in Fig. A.6, but the deviation is sufficiently small for this specific shape to be chosen in order to keep a simple expression of $T_{Br_{max}}(h\nu_a)$. Fig. A.7 represents the evolution of $a(h\nu_b)$ and $b(h\nu_b)$ as well as the corresponding fits, that follow respectively a power law and an affine relation.
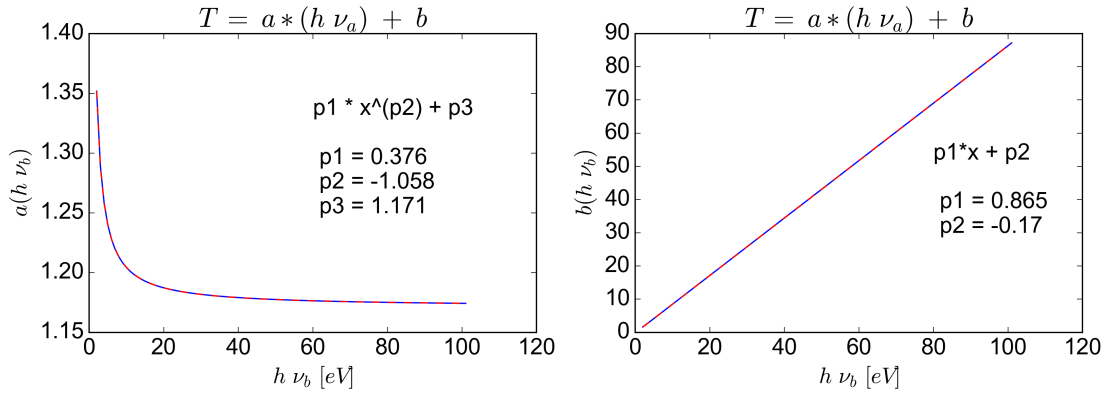
Figure A.7.: Evolution with $h\nu_b$ of the affine parameter of the $T_{Br_{max}}(h\nu_a)$ function, i.e. $a(h\nu_b)$ and $b(h\nu_b)$, and the corresponding fits. $a(h\nu_b)$ follows a power law while $b(h\nu_b)$ follows an affine relation.

From the above description, $kT_{Br_{max}}$ then reads:

$$kT_{Br_{max}} = \left(0.376 \times (h\nu_b)^{-1.058} + 1.171\right) \times (h\nu_a) + (0.865 \times (h\nu_b) - 0.17) \quad [\text{eV}]$$

with $h\nu_a$ and $h\nu_b$ in eV unit of energy.

Bibliography

Albertazzi, B., *Plasmas Lasers et Champs Magnétiques*, Ph.D. thesis, Ecole Polytechnique; INRS (2014).

Albertazzi, B., Béard, J., Ciardi, A., Vinci, T., Albrecht, J., Billette, J., Burris-Mog, T., Chen, S. N., Da Silva, D., Dittrich, S., Herrmannsdörfer, T., Hirardin, B., Kroll, F., Nakatsutsumi, M., Nitsche, S., Riconda, C., Romagnagni, L., Schlenvoigt, H. P., Simond, S., Veuillot, E., Cowan, T. E., Portugall, O., Pépin, H., and Fuchs, J., Review of Scientific Instruments **84**, 1 (2013).

Albertazzi, B., Ciardi, A., Nakatsutsumi, M., Vinci, T., Béard, J., Bonito, R., Billette, J., Borghesi, M., Burkley, Z., Chen, S. N., Cowan, T. E., Herrmannsdörfer, T., Higginson, D. P., Kroll, F., Pikuz, S. A. A., Naughton, K., Romagnani, L., Riconda, C., Revet, G., Riquier, R., Schlenvoigt, H.-P. H.-P., Skobelev, I. Y., Faenov, A. Y., Soloviev, A., Huarte-Espinosa, M., Frank, A., Portugall, O., Pépin, H., and Fuchs, J., Science **346**, 325 (2014).

Ampleford, D. J., Lebedev, S. V., Ciardi, A., Bland, S. N., Bott, S. C., Hall, G. N., Naz, N., Jennings, C. A., Sherlock, M., Chittenden, J. P., Palmer, J. B. A., Frank, A., and Blackman, E., Physical Review Letters **100**, 1 (2008), arXiv:0704.3154 .

Andrews, S. M., Wilner, D. J., Zhu, Z., Birnstiel, T., Carpenter, J. M., Perez, L. M., Bai, X.-N., Oberg, K. I., Hughes, A. M., Isella, A., and Ricci, L., The Astrophysical Journal Letters **820**, 0 (2016), arXiv:1603.09352 .

Antici, P., *Laser-acceleration of high-energy short proton beams and applications*, Ph.D. thesis, Ecole Polytechnique; Università La Sapienza (2007).

Argiroffi, C., *Coronal properties of X-ray bright stars in young associations: abundances, temperatures, and variability*, Ph.D. thesis, Universitaa degli Studi di Palermo (2005).

Argiroffi, C., Maggio, A., and Peres, G., Astronomy & Astrophysics **465**, L5 (2007).

Armitage, P. J., Annual Review of Astronomy and Astrophysics **49**, 195 (2010), arXiv:1011.1496 .

Atzeni, S., Schiavi, A., Califano, F., Cattani, F., Cornolti, F., Del Sarto, D., Liseykina, T. V., MacChi, A., and Pegoraro, F., Computer Physics Communications **169**, 153 (2005).

Bally, J., Feigelson, E., and Reipurth, B., The Astrophysical Journal **584**, 843 (2003).

Balucinska-Church, M. and McCammon, D., The Astrophysical Journal **400**, 699 (1992).

Béard, J., Billette, J., Frings, P., Suleiman, M., and Lecouturier, F., Journal of Low Temperature Physics **170**, 442 (2013).

Béard, J. and Debray, F., Journal of Low Temperature Physics **170**, 541 (2013).

Bellan, P. M., You, S., and Hsu, S. C., Astrophysics and Space Science **298**, 203 (2005).

Blandford, R. D. and Payne, D. G., Monthly Notices of the Royal Astronomical Society **199**, 883 (1982), arXiv:arXiv:1011.1669v3 .

Bockasten, K., Journal of the Optical Society of America **51**, 943 (1961).

Bonito, R., Orlando, S., Argiroffi, C., Miceli, M., Peres, G., Matsakos, T., Stehlé, C., and Ibgui, L., The Astrophysical Journal **795**, L34 (2014).

Bonito, R., Orlando, S., Miceli, M., Peres, G., Micela, G., and Favata, F., Astrophysical Journal **737** (2011), 10.1088/0004-637X/737/2/54, arXiv:1105.4081 .

Bostick, W. H., Physical Review **104**, 292 (1956).

Bouquet, S., Stéhlé, C., Koenig, M., Chièze, J. P., Benuzzi-Mounaix, A., Batani, D., Leygnac, S., Fleury, X., Merdji, H., Michaut, C., Thais, F., Grandjouan, N., Hall, T., Henry, E., Malka, V., and Lafon, J. P. J., Physical Review Letters **92**, 225001 (2004).

Bouvier, J., Alencar, S. H. P., Harries, T. J., Johns-Krull, C. M., and Romanova, M. M., EAS Publications Series **9**, 287 (2003).

Braginskii, S. I., Reviews of Plasma Physics **1**, 205 (1965).

Brickhouse, N. S., Cranmer, S. R., Dupree, A. K., Luna, G. J. M., and Wolk, S., The Astrophysical Journal **710**, 1835 (2010).

Bruneteau, J., Fabre, E., Lamain, H., and Vasseur, P., The Physics of Fluids **13** (1970), 10.1063/1.1693157.

Busschaert, C., Falize, É., Loupias, B., Michaut, C., Ravasio, A., Pelka, A., Yurchak, R., and Koenig, M., New Journal of Physics **15** (2013), 10.1088/1367-2630/15/3/035020.

Calvet, N. and Gullbring, E., The Astrophysical Journal **509**, 802 (1998), arXiv:0008203 [astro-ph] .

Canto, J., Tenorio-Tagle, G., and Rozyczka, M., Astronomy and Astrophysics **192**, 287 (1988).

Carrasco-González, C., Rodríguez, L. F., Anglada, G., Martí, J., Torrelles, J. M., and Osorio, M., Science - Reports **330**, 1209 (2010).

Casassus, S., van der Plas, G., Sebastian Perez, M., Dent, W. R. F., Fomalont, E., Hagelberg, J., Hales, A., Jordán, A., Mawet, D., Ménard, F., Wootten, A., Wilner, D., Hughes, A. M., Schreiber, M. R., Girard, J. H., Ercolano, B., Canovas, H., Román, P. E., and Salinas, V., Nature - Letters **493**, 191 (2013), arXiv:1305.6062 .

Cassen, P. and Moosman, A., Icarus **48**, 353 (1981).

Chandrasekhar, S., *Hydrodynamic and Hydromagnetic Stability*, oxford university press ed. (Dover Publications, 1981).

Chang, P. Y., Fiksel, G., Hohenberger, M., Knauer, J. P., Betti, R., Marshall, F. J., Meyerhofer, D. D., Séguin, F. H., and Petrasso, R. D., Physical Review Letters **107**, 2 (2011).

Chapman, N. L., Davidson, J. A., Goldsmith, P. F., Houde, M., Kwon, W., Li, Z.-Y., Looney, L. W., Matthews, B., Matthews, T. G., Novak, G., Peng, R., Vaillancourt, J. E., and Volgenau, N. H., The Astrophysical Journal **770**, 151 (2013), arXiv:1305.2922 .

Chaulagain, U., Stehlé, C., Larour, J., Kozlova, M., Suzuki-Vidal, F., Barroso, P., Cotelo, M., Velarde, P., Rodriguez, R., Gil, J. M., Ciardi, A., Acef, O., Nejdl, J., de Sá, L., Singh, R. L., Ibgui, L., and Champion, N., High Energy Density Physics **17**, 106 (2015).

Chen, S. N., Iwawaki, T., Morita, K., Antici, P., Baton, S. D., Filippi, F., Habara, H., Nakatsutsumi, M., Nicolaï, P., Nazarov, W., Rousseaux, C., Starodubstev, M., Tanaka, K. A., and Fuchs, J., Scientific Reports **6**, 21495 (2016).

Chittenden, J. P., Lebedev, S. V., Jennings, C. A., Bland, S. N., and Ciardi, A., Plasma Physics and Controlled Fusion **46** (2004), 10.1088/0741-3335/46/12B/039.

Chung, H. K., Chen, M. H., Morgan, W. L., Ralchenko, Y., and Lee, R. W., High Energy Density Physics **1**, 3 (2005).

Ciardi, A. and Hennebelle, P., Monthly Notices of the Royal Astronomical Society: Letters **409**, 39 (2010), arXiv:1009.0453 .

Ciardi, A., Lebedev, S. V., Frank, A., Blackman, E. G., Chittenden, J. P., Jennings, C. J., Ampleford, D. J., Bland, S. N., Bott, S. C., Rapley, J., Hall, G. N., Suzuki-Vidal, F. A., Marocchino, A., Lery, T., and Stehle, C., Physics of Plasmas **14** (2007), 10.1063/1.2436479, arXiv:0611441 [astro-ph] .

Ciardi, A., Lebedev, S. V., Frank, A., Suzuki-Vidal, F., Hall, G. N., Bland, S. N., Harvey-Thompson, A., Blackman, E. G., and Camenzind, M., The Astrophysical Journal **691**, L147 (2009), arXiv:0811.2736 .

Ciardi, A., Vinci, T., Fuchs, J., Albertazzi, B., Riconda, C., Pépin, H., and Portugall, O., Physical Review Letters **110**, 025002 (2013), arXiv:arXiv:1212.2805v1 .

Colombo, S., Orlando, S., Peres, G., Argiroffi, C., and Reale, F., Astronomy & Astrophysics **594**, A93 (2016), arXiv:1607.03009 .

Costa, G., Orlando, S., Peres, G., Argiroffi, C., and Bonito, R., Astronomy & Astrophysics **597** (2017), arXiv:1609.01059 .

Cross, J. E., Gregori, G., Foster, J. M., Graham, P., Bonnet-Bidaud, J. M., Busschaert, C., Charpentier, N., Danson, C. N., Doyle, H. W., Drake, R. P., Fyrth, J., Gumbrell, E. T., Koenig, M., Krauland, C., Kuranz, C. C., Loupias, B., Michaut, C., Mouchet, M., Patankar, S., Skidmore, J., Spindloe, C., Tubman, E. R., Woolsey, N., Yurchak, R., and Falize, É., Nature Communications **7**, ncomms11899 (2016).

Curran, R. L., Argiroffi, C., Sacco, G. G., Orlando, S., Peres, G., Reale, F., and Maggio, A., Astronomy & Astrophysics **526**, A104 (2011), arXiv:1011.5915 .

Davidson, J. A., Novak, G., Matthews, T. G., Matthews, B., Goldsmith, P. F., Chapman, N., Volgenau, N. H., Vaillancourt, J. E., and Attard, M., The Astrophysical Journal **732**, 97 (2011).

Dorf, M., Viscosity of a multispecies plasma containing hydrogen and high-Z ions (2014).

Dougados, C., Cabrit, S., Lavalley, C., and Ménard, F., Astronomy and Astrophysics **357**, L61 (2000).

Drake, R. P., *Shock Wave and High Pressure Phenomena*, edited by Y. Davison, Lee ; Horie (Springer, 2008) p. 534.

Drake, R. P. and Gregori, G., Astrophysical Journal **749** (2012), 10.1088/0004-637X/749/2/171.

Fabbro, R., Max, C., and Fabre, E., Physics of Fluids **28**, 1463 (1985).

Faenov, A. Y., Pikuz, S. A., Erko, A. I., Bryunetkin, B. A., Dyakin, V. M., Ivanenkov, G. V., Mingaleev, A. R., Pikuz, T. A., Romanova, V. M., and Shelkovenko, T. A., Physica Scripta **50**, 333 (1994).

Falize, É., *Similitude et autosimilarité en physique des hautes densité d'energie. Appliocation à l'astrophysique de laboratoire*, Ph.D. thesis, Observatoire de Paris (2008).

Farley, D. R., Estabrook, K. G., Glendinning, S. G., Glenzer, S. H., Remington, B. A., Shigemori, K., Stone, J. M., Wallace, R. J., Zimmerman, G. B., and Harte, J. A., Physical Review Letters **83**, 1982 (1999).

Favata, F., Fridlund, C. V. M., Micela, G., Sciortino, S., and Kaas, A. A., Astronomy & Astrophysics **386**, 204 (2002).

Ferreira, J., Dougados, C., and Whelan, E., eds., *Jets from Young Stars : Models and Constraints* (Springer, 2007).

Foster, J. M., Wilde, B. H., Rosen, P. A., Perry, T. S., Fell, M., Edwards, M. J., Lasinski, B. F., Turner, R. E., and Gittings, M. L., Physics of Plasmas **9**, 2251 (2002).

Frank, A., Ray, T. P., Cabrit, S., Hartigan, P., Arce, H. G., Bacciotti, F., Bally, J., Benisty, M., Eislöffel, J., Güdel, M., Lebedev, S., Nisini, B., and Raga, A., in *Protostars and Planets VI* (University of Arizona Press, 2014) pp. 451–474, arXiv:1402.3553v1 .

Friichtenicht, J. F. and Slattery, J. C., "Ionization associated with hyper velocity impact," Tech. Rep. August (National Aeronotics And Space Administration, Redondo Beach, California, 1963).

Fujioka, S., Zhang, Z., Ishihara, K., Shigemori, K., Hironaka, Y., Johzaki, T., Sunahara, A., Yamamoto, N., Nakashima, H., Watanabe, T., Shiraga, H., Nishimura, H., and Azechi, H., Scientific Reports **3**, 1 (2013).

Gotchev, O. V., Chang, P. Y., Knauer, J. P., Meyerhofer, D. D., Polomarov, O., Frenje, J., Li, C. K., Manuel, M. J., Petrasso, R. D., Rygg, J. R., Séguin, F. H., and Betti, R., Physical Review Letters **103**, 1 (2009a).

Gotchev, O. V., Knauer, J. P., Chang, P. Y., Jang, N. W., Shoup, M. J., Meyerhofer, D. D., and Betti, R., Review of Scientific Instruments **80** (2009b), 10.1063/1.3115983.

Green, T. S. and Niblett, G. B. F., Nuclear Fusion **1**, 42 (1960).

Guenther, E., Lehmann, H., Emerson, J., and Staude, J., Astronomy & Astrophysics **341**, 768 (1999).

Gullbring, E., Hartmann, L., Briceno, C., Calvet, N., Briceño, C., and Calvet, N., The Astrophysical Journal **492**, 323 (1998).

Hartigan, P., Edwards, S., and Pierson, R., The Astrophysical Journal **609**, 261 (2004).

Hartmann, L., *Accretion processes in star formation*, 2nd ed. (Cambridge University Press, 2008) p. 346.

Hennebelle, P. and Ciardi, A., Astronomy & Astrophysics - Letter to the Editor **506**, 29 (2009).

Herczeg, G. J. and Hillenbrand, L. A., The Astrophysical Journal **681**, 594 (2008), arXiv:0801.3525 .

Higginson, D. P., Revet, G., Khiar, B., Blecher, M., Borghesi, M., Burdonov, K., Chen, S. N., Filippov, E., Khaghani, D., Naughton, K., Pikuz, S., Portugall, O., Riconda, C., Riquier, R., Ryazantsev, S. N., Soloviev, A., Stardubtsev, M., Vinci, T., Willi, O., Ciardi, A., and Fuchs, J., High Energy Density Physics **23**, 48 (2017).

Hornung, H., Annual Review of Fluid Mechanics **18**, 33 (1986).

Hsu, S. C. and Bellan, P. M., Physical Review Letters **90**, 4 (2003), arXiv:0304104 [physics] .

Huba, J. D., *NRL Plasma Formulary* (Wasington, DC: Naval Reasearch Laboratory, 2016) pp. 1–70.

Hull, C. L. H., Plambeck, R. L., Bolatto, A. D., Bower, G. C., Carpenter, J. M., Crutcher, R. M., Fiege, J. D., Franzmann, E., Hakobian, N. S., Heiles, C., Houde, M., Hughes, A. M., Jameson, K., Kwon, W., Lamb, J. W., Looney, L. W., Matthews, B. C., Mundy, L., Pillai, T., Pound, M. W., Stephens, I. W., Tobin, J. J., Vaillancourt, J. E., Volgenau, N. H., and Wright, M. C. H., The Astrophysical Journal , 768 (2013).

Johns-Krull, C. M., The Astrophysical Journal **664**, 975 (2007), arXiv:0704.2923 .

Johns-Krull, C. M., Valenti, J. A., Hatzes, A. P., and Kanaan, A., The Astrophysical Journal **510**, L41 (1999).

Johns-Krull, C. M., Valenti, J. A., Saar, S. H., and Hatzes, A. P., *In Magnetic Fields Across the Hertzsprung-Russell Diagram*, edited by G. Mathys, S. K. Solanki, and D. T. Wickramasinghe (ASP Conf. Series, San Francisco, 2001) pp. 527–532.

Johnstone, C. P., Jardine, M., Gregory, S. G., Donati, J. F., and Hussain, G., Monthly Notices of the Royal Astronomical Society **437**, 3202 (2014), arXiv:arXiv:1310.8194v1 .

Joos, M., Hennebelle, P., and Ciardi, A., Astronomy and Astrophysics **543**, A128 (2012), arXiv:1203.1193 .

Kane, J., Arnett, D., Remington, B. a., Glendinning, S. G., Castor, J., Wallace, R., Rubenchik, A., and Fryxell, B. a., The Astrophysical Journal **478**, L75 (1997).

Kato, Y., Mima, K., Miyanaga, N., Arinaga, S., Kitagawa, Y., Nakatsuka, M., and Yamanaka, C., Physical Review Letters **53**, 1057 (1984).

Khiar, B., *Laboratory astrophysics with magnetized laser-produced plasmas*, Ph.D. thesis, Université Pierre et Marie Curie - Paris VI. LERMA, Observatoire de Paris (2017).

Khiar, B., Revet, G., Ciardi, A., and Fuchs, J., Physics of Plasmas, **In preparation** (2018).

Konigl, A., The Astrophysical Journal **261**, 115 (1982).

Krolik, J. H. and Kallman, T. R., The Astrophysical Journal **286**, 366 (1984).

Kwan, J. and Tademaru, E., The Astrophysical Journal **332**, L41 (1988).

Lancia, L., Albertazzi, B., Boniface, C., Grisollet, A., Riquier, R., Chaland, F., Le Thanh, K. C., Mellor, P., Antici, P., Buffechoux, S., Chen, S. N., Doria, D., Nakatsutsumi, M., Peth, C., Swantusch, M., Stardubtsev, M., Palumbo, L., Borghesi, M., Willi, O., Pépin, H., and Fuchs, J., Physical Review Letters **113**, 1 (2014).

Landau, L. and Lifshitz, E. M. ., *Fluid Mechanics*, 2nd ed., Vol. Vol. 6 (Pergamon Press, 1987) arXiv:978-0-12-381399-2 .

Landi, E., Del Zanna, G., Young, P. R., Dere, K. P., and Mason, H. E., The Astrophysical Journal **744**, 99 (2012).

Lebedev, S. V., Ciardi, A., Ampleford, D. J., Bland, S. N., Bott, S. C., Chittenden, J. P., Hall, G. N., Rapley, J., Jennings, C. A., Frank, A., Blackman, E. G., and Lery, T., Monthly Notices of the Royal Astronomical Society **361**, 97 (2005), arXiv:0505027 [astro-ph] .

Lévy, A., *Accélération d'ions par interaction laser-matière en régime de ultra haut contraste laser*, Ph.D. thesis, Université Paris XI, Orsay (2008).

Li, Z.-Y., Krasnopolsky, R., and Shang, H., The Astrophysical Journal **738**, 180 (2011), arXiv:1106.2620 .

Li, Z.-Y., Krasnopolsky, R., and Shang, H., The Astrophysical Journal **774** (2013), 10.1088/0004-637X/738/2/180, arXiv:1106.2620 .

Loupias, B., Koenig, M., Falize, E., Bouquet, S., Ozaki, N., Benuzzi-Mounaix, A., Vinci, T., Michaut, C., Rabec Le Goahec, M., Nazarov, W., Courtois, C., Aglitskiy, Y., Faenov, A. Y., and Pikuz, T., Physical Review Letters **99**, 1 (2007).

MacFarlane, J. J., Golovkin, I. E., Wang, P., Woodruff, P. R., and Pereyra, N. A., High Energy Density Physics **3**, 181 (2007).

Manuel, M. J., Kuranz, C. C., Rasmus, A. M., Klein, S. R., MacDonald, M. J., Trantham, M. R., Fein, J. R., Belancourt, P. X., Young, R. P., Keiter, P. A., Drake, R. P., Pollock, B. B., Park, J., Hazi, A. U., Williams, G. J., and Chen, H., High Energy Density Physics **17**, 52 (2015).

Matsakos, T., Chièze, J.-P., Stehlé, C., González, M., Ibgui, L., de Sá, L., Lanz, T., Orlando, S., Bonito, R., Argiroffi, C., Reale, F., and Peres, G., Astronomy & Astrophysics **557**, A69 (2013), arXiv:1307.5389 .

Matsakos, T., Massaglia, S., Trussoni, E., Tsinganos, K., Vlahakis, N., Sauty, C., and Mignone, A., Astronomy and Astrophysics **502**, 217 (2009), arXiv:0905.3519 .

Matt, S., Winglee, R., and Böhm, K.-H., Monthly Notices of the Royal Astronomical Society **345**, 660 (2003).

Meadowcroft, A. L., Bentley, C. D., and Stott, E. N., Review of Scientific Instruments **79** (2008), 10.1063/1.3013123.

Ménard, F. and Duchêne, G., Astronomy and Astrophysics **425**, 973 (2004), arXiv:0407075 [astro-ph] .

Mignone, A., Bodo, G., Massaglia, S., Matsakos, T., Tesileanu, O., Zanni, C., and Ferrari, A., The Astrophysical Journal Supplement Series **170**, 228 (2007), arXiv:0701854 [astro-ph] .

Mostovych, A. N., Ripin, B. H., and Stamper, J. A., Physical Review Letters **62**, 2837 (1989).

Natta, A., Testi, L., Muzerolle, J., Randich, S., Comerón, F., and Persi, P., Astronomy and Astrophysics **424**, 603 (2004), arXiv:0406106 [astro-ph] .

Ness, J. U., Güdel, M., Schmitt, J. H. M. M., Audard, M., and Telleschi, A., Astronomy & Astrophysics **427**, 667 (2004), arXiv:0407231 [astro-ph] .

Nicola, P., Stenz, C., Tikhonchuk, V., Kasperczuk, A., Pisarczyk, T., Juha, L., Krousky, E., Masek, K., Pfeifer, M., Rohlena, K., Skala, J., Kmetik, V., Ullschmied, J., Kalal, M., Klir, D., Kravarik, J., Kubes, P., Rezac, K., Pisarczyk, P., and Tabakhoff, E., Physics of Plasmas **17** (2010), 10.1063/1.3511774.

Orlando, S., Bonito, R., Argiroffi, C., Reale, F., Peres, G., Miceli, M., Matsakos, T., Stehlé, C., Ibgui, L., de Sá, L., Chièze, J. P., and Lanz, T., Astronomy & Astrophysics **559**, A127 (2013), arXiv:1309.5038 .

Orlando, S., Sacco, G. G., Argiroffi, C., Reale, F., and Maggio, A., Astronomy & Astrophysics **510**, A71 (2010), arXiv:arXiv:0912.1799v1 .

Pert, G. J., Journal of Plasma Physics **41**, 263 (1989).

Peyser, T. A., Manka, C. K., Ripin, B. H., and Ganguli, G., Physics of Fluids B **4**, 2448 (1992).

Plechaty, C., Presura, R., and Esaulov, A. A., Physical Review Letters **185002**, 1 (2013).

Pollock, B. B., Froula, D. H., Tynan, G. R., Divol, L., Price, D., Costa, R., Yepiz, F., Fulkerson, S., Mangini, F., and Glenzer, S. H., Review of Scientific Instruments **79**, 2006 (2008).

Puell, H., Zeitschrift fur Naturforschung - Section A Journal of Physical Sciences **25**, 1807 (1970).

Raga, A., Cabrit, S., Dougados, C., and Lavalley, C., Astronomy & Astrophysics **367**, 959 (2001).

Raga, A. C., Binette, L., Canto, J., and Calvet, N., The Astrophysical Journal **364**, 601 (1990).

Ratcliff, P. R., Burchell, M., Cole, M. J., Murphy, T. W., and Alladfadi, F., International Journal of Impact Engineering **20**, 663 (1997).

Reale, F., Orlando, S., Testa, P., Peres, G., Landi, E., and Schrijver, C. J., Science **341**, 251 (2013).

Remington, B. A., Drake, R. P., and Ryutov, D. D., Reviews of Modern Physics **78**, 755 (2006).

Remington, B. A., Kane, J., Drake, R. P., Glendinning, S. G., Estabrook, K., London, R., Castor, J., Wallace, R. J., Arnett, D., Liang, E., McCray, R., Rubenchik, A., and Fryxell, B., Physics of Plasmas **4**, 1994 (1997).

Ripin, B. H., Huba, J. D., McLean, E. A., Manka, C. K., Peyser, T., Burris, H. R., and Grun, J., Physics of Fluids B **5**, 3491 (1993).

Rosen, M. D., Price, R. H., Campbell, E. M., Phillion, D. W., Estabrook, K. G., Lasinski, B. F., Auerbach, J. M., Obenschain, S. P., McLean, E. A., Whitlock, R. R., and Ripin, B. H., Physical Review A **36**, 247 (1987).

Rozyczka, M. and Tenorio-Tagle, G., Monthly Notices of the Royal Astronomical Society **274**, 1157 (1995), arXiv:arXiv:1011.1669v3 .

Ryazantsev, S. N., Skobelev, I. Y., Faenov, A. Y., Pikuz, T. A., Grum-Grzhimailo, A. N., and Pikuz, S. A., JETP Letters **102**, 707 (2015).

Ryazantsev, S. N., Skobelev, I. Y., Faenov, A. Y., Pikuz, T. A., Grum-Grzhimailo, A. N., and Pikuz, S. A., JETP Letters **102**, 707 (2016).

Rybicki, G. B. and Lightman, A. P., *Radiative Processes in Astrophysics*, new ed ed. (Wiley-VCH, 1985) p. 400, arXiv:arXiv:1011.1669v3 .

Ryutov, D. D., Drake, R. P., Kane, J., Liang, E., Remington, B. A., and Wood-Vas,, The Astrophysical Journal **518**, 821 (1999).

Ryutov, D. D., Drake, R. P., and Remington, B. A., The Astrophysical Journal Supplement Series **127**, 465 (2000).

Ryutov, D. D., Kugland, N. L., Levy, M. C., Plechaty, C., Ross, J. S., and Park, H. S., Physics of Plasmas **20**, 1 (2013).

Ryutov, D. D., Kugland, N. L., Park, H. S., Plechaty, C., Remington, B. A., and Ross, J. S., Physics of Plasmas **19**, 1 (2012).

Ryutov, D. D., Kugland, N. L., Park, H. S., Pollaine, S. M., Remington, B. A., and Ross, J. S., Physics of Plasmas **18**, 3 (2011).

Ryutov, D. D., Remington, B. A., Robey, H. F., and Drake, R. P., Physics of Plasmas **8**, 1804 (2001).

Sacco, G. G., Argiroffi, C., Orlando, S., Maggio, A., Peres, G., and Reale, F., Astronomy & Astrophysics **491**, L17 (2008).

Sacco, G. G., Orlando, S., Argiroffi, C., Maggio, A., Peres, G., Reale, F., and Curran, R. L., Astronomy & Astrophysics **522**, A55 (2010).

Schmidt, G., Physics of Fluids **3**, 961 (1960).

Schmitt, J. H. M. M., Robrade, J., Ness, J.-U., Favata, F., and Stelzer, B., Astronomy and Astrophysics **432**, L35 (2005).

Shu, F. H., The Astrophysical Journal **214**, 488 (1977).

Smith, R. K., Brickhouse, N. S., Liedahl, D. A., and Raymond, J. C., The Astrophysical Journal **556**, L91 (2001), arXiv:0106478 [astro-ph] .

Spitzer, L., *Physics of Fully Ionized Gases* (Interscience Publisher Inc., New York ; Interscience Publisher Ltd., London, 1956).

Spruit, H. C., Foglizzo, T., and Stehle, R., Monthly Notices of the Royal Astronomical Society **288**, 333 (1997).

Stone, J. M. and Norman, M. L., The Astrophysical Journal **389**, 297 (1992).

Strickland, D. and Mourou, G., Optics Communications **55**, 447 (1985).

Strom, K. M., Strom, S. E., Wolff, S. C., Morgan, J., and Wenz, M., The Astrophysical Journal Supplement Series **62**, 39 (1986).

Sucov, E., Pack, J., Phelps, A. V., and Engelhardt, A. G., Physics of Fluids **10**, 2035 (1967).

Tabak, M., Hammer, J., Glinsky, M. E., Kruer, W. L., Wilks, S. C., Woodworth, J., Campbell, E. M., Perry, M. D., and Mason, R. J., Physics of Plasmas **1**, 1626 (1994).

Telleschi, A., Güdel, M., Briggs, K. R., Audard, M., and Scelsi, L., Astronomy & Astrophysics **468**, 443 (2007).

Testa, P., Drake, J. J., and Peres, G., The Astrophysical Journal , 508 (2004).

Trubnikov, B., in *Reviews of Plasma Physics Vol. I*, edited by M. Leontovich (Consultants Bureau, New York, 1965) p. 105.

Ustamujic, S., Orlando, S., Bonito, R., Miceli, M., Gómez de Castro, A. I., and López-Santiago, J., Astronomy & Astrophysics **596**, A99 (2016), arXiv:1607.08172 .

Velikhov, E. P., Soviet Physics Jetp **36**, 1398 (1959).

Vinci, T. and Flacco, A., Neutrino Analysis Software (2018).

Yurchak, R., Ravasio, A., Pelka, A., Pikuz, S., Falize, E., Vinci, T., Koenig, M., Loupias, B., Benuzzi-Mounaix, A., Fatenejad, M., Tzeferacos, P., Lamb, D. Q., and Blackman, E. G., Physical Review Letters **112**, 2 (2014), arXiv:1403.4885 .

Zakharov, Y. P., Antonov, V. M., Boyarintsev, E. L., Melekhov, A. V., Posukh, V. G., Shaikhislamov, I. F., and Pickalov, V. V., Plasma Physics Reports **32**, 183 (2006).

Zel'dovich, Y. B. and Raizer, Y. P., *Physics of shock waves and high-temperature hydrodynamic phenomena - I*, edited by W. D. Hayes and R. D. Probstein, Vol. I (Academic Press. New York and London., 1966).

Zou, J. P., Blanc, C. L., Audebert, P., Janicot, S., Sautivet, a. M., Martin, L., Sauteret, C., Paillard, J. L., Jacquemot, S., and Amiranoff, F., Journal of Physics: Conference Series **112**, 032021 (2008).

List of Figures

List of Tables

Role of the author

This thesis results from a collaboration between different research teams, as it presents experimental data, simulation data of the laboratory experiment, and simulation data of the astrophysical situation. Hence, this thesis was mainly done within a tight collaboration between six teams.

The LULI team (Laboratoire pour l'Utilisation des Lasers Intenses), at Ecole Polytechnique, is the experimental team I was working in during this Ph.D.

The LERMA team (Laboratoire d'Etudes du Rayonnement et de la Matière en Astrophysique et Atmosphères), at Jussieu University, is the one that was performing the GORGON MHD simulations in the laboratory conditions. Within the team, Andrea Ciardi and Benjamin Khiar were the collaborators.

The INAF team (INstituto di AstroFysica) was performing the MHD simulations in the astrophysical conditions. Within the team, Salvatore Orlando, Sara Bonito and Constanza Argiroffi were the collaborators.

The LNCMI team (Laboratoire National des Champs Magnétiques Intenses) was in charge of the conception of the magnetic field coil. Within the team, Jérome Béard was the main collaborator.

The IAP-RAS team (Institute of Applied Physics of the Russian Academy of Science) was in charge of the experiments specifically realized at the PEARL laser facility. Within the team, Konstantin Burdonov, Alexander Soloviev and Mikhail Starodubtsev were the principal collaborators.

The JIHT team (Joint Institute for High Temperatures of the Russian Academy of Sciences) was in charge of the FSSR spectrometer data analysis. Within the team, Evgeny Filippov and Sergey Pikuz were the collaborators.

As a member of the experimental LULI team, my personal work was mainly dedicated to the realization of the experiments, from which the results of this thesis are extracted. In this experimental context, I have performed during this Ph.D. several experiments at different laser "user facilities". Those include the ELFIE facility (LULI laboratory), the LULI2000 facility (LULI laboratory), the TITAN facility (LLNL laboratory), the PEARL facility (IAP-RAS laboratory), the PHELIX facility (GSI laboratory) and the Texas Petawatt Laser facility (University of Texas). Specifically for the TITAN and mainly

for the ELFIE campaigns, ahead of the work in the experimental area, I was in charge of the design of the experiments, from the arrangement of the diagnostics imaging system, up to the design of the laser beams paths (probe beam, interaction beam, protons/x-rays source high intensity beam), together with the respect of the constraints regarding the others diagnostics field of view (particles or x-ray spectrometers). During the experimental campaigns, I was in charge of the setup of the experiments (in collaboration with other team members), from laser alignment, through the diagnostics setup, up to the care taken to the targets. The work in a user facility is a team work, and I do not pretend to be able to get the results presented in this manuscript by my sole work in the laser facilities. In addition to the technical staff (laser or equipment), the experimental sessions were often realized within a ~ 5 persons group. However, I was often personally in charge of some specific diagnostics. The interferometry and the Self-Optical-Pyrometry being the diagnostics I took care more often than the others.

Apart from the experimental campaigns, my work was dedicated to the analysis of the data. For the interferometry, the Neutrino code I have used was developed by Tommaso Vinci (LULI laboratory). Other analysis were performed using personal Python routines. I have hence analyzed most of the data presented in this thesis, as well have worked on their physical interpretation and wrote significant parts of the scientific articles that were derived from them (see publication list).

The interpretation of the results, the physical insight via the Gorgon code, and the link with the astrophysical simulations and context were discussed in concert with our LULI team, the LERMA and the INAF team.

List of publications and presentations

Publications

- G. Revet, S.N. Chen, R. Bonito, B. Khiar, E. Filippov, C. Argiroffi, D. P. Higginson, S. Orlando, J. Béard, M. Blecher, M. Borghesi, K. Burdonov, D. Khaghani, K. Naughton, H. Pépin, O. Portugall, R. Riquier, R. Rodriguez, S.N. Ryazantsev, I.Yu. Skobelev, A. Soloviev, O. Willi, S. Pikuz, A. Ciardi, J. Fuchs.
  Laboratory unravelling of matter accretion in young stars. Science Advances **3**, 11 (2017).

- D. P. Higginson, G. Revet, B. Khiar, J. Béard, M. Blecher, M. Borghesi, K. Burdonov, S. N. Chen, E. Filippov, D. Khaghani, K. Naughton, H. Pépin, S. Pikuz, C. Riconda, R. Riquier, S. N. Ryazantsev, A. Soloviev, I. Yu. Skobelev, M. Stardubtsev, T. Vinci, O. Willi, A. Ciardi, and J. Fuchs
  Enhancement of Quasistationary Shocks and Heating via Temporal Staging in a Magnetized Laser-Plasma Jet. Physical Review Letters **119**, 25 (2017).

- D. P. Higginson, G. Revet, B. Khiar, J. Béard, M. Blecher, M. Borghesi, K. Burdonov, S. N. Chen, E. Filippov, D. Khaghani, K. Naughton, H. Pépin, S. Pikuz, C. Riconda, R. Riquier, S. N. Ryazantsev, A. Soloviev, I. Yu. Skobelev, M. Stardubtsev, T. Vinci, O. Willi, A. Ciardi, and J. Fuchs
  Detailed characterization of laser-produced astrophysically-relevant jets formed via a poloidal magnetic nozzle. High Energy Density Physics **23**, 48–59 (2017).

- B. Albertazzi, A. Ciardi, M. Nakatsutsumi, T. Vinci, J. Béard, R. Bonito, J. Billette, M. Borghesi, Z. Burkley, S. N. Chen, T. E. Cowan, T. Herrmannsdorfer, D. P. Higginson, F. Kroll, S. A. Pikuz, K. Naughton, L. Romagnani, C. Riconda, G. Revet, R. Riquier, H.-P. Schlenvoigt, I. Yu. Skobelev, A.Ya. Faenov, A. Soloviev, M. Huarte-Espinosa, A. Frank, O. Portugall, H. Pépin, and J. Fuchs.
  Laboratory formation of a scaled protostellar jet by coaligned poloidal magnetic field. Science **346**, 325 (2014).

In preparation

- G. Revet, B. Khiar, J. Beard, R. Bonito, S. Orlando, M. Starodubtsev, A. Ciardi, and J. Fuchs.

Laser experiment for the study of accretion dynamics of Young Stellar Objects: design and scaling. High Energy Density Physics. Submitted.

- G. Revet, B. Khiar, E. Filippov, J. Beard, M. Cerchez, S. N. Chen, T. Gangolf, D. P. Higginson, M. Ouille, S. N. Ryazantsev, I. Yu. Skobelev, M. I. Safronova, M. Starodubtsev, T. Vinci, O. Willi, S. Pikuz, A. Ciardi, and J. Fuchs.
  Laboratory Evidence for the importance of poloidal magnetic field - outflow initial alignment in collimating jets emerging from Young Stars. In preparation.

- B. Khiar, G. Revet, A. Ciardi, J. Fuchs
  Observation of the magnetic Rayleigh-Taylor instability in a laser-produced plasma. Phys. Plasmas. In preparation.

Scientific contributions - extended field from main thesis topic

- E. d'Humières, S. Chen, M. Lobet, M. Sciscio, P. Anticid, M. Bailly-Grandvaux, T. Gangolf, G. Revet, J. Santos, A.M. Schroer, O. Willi, V. Tikhonchuk, H. Pépin, J. Fuchs
  Longitudinal laser ion acceleration in low density targets: experimental optimization on the Titan laser facility and numerical investigation of the ultra-high intensity limit. Proc. SPIE **9514**, 95140B (2015).

- K.F. Burdonov, A.A. Eremeev, N.I. Ignatova, R.R. Osmanov, A.D. Sladkov, A.A. Soloviev, M.V. Starodubtsev, V.N. Ginzburg, A.A. Kuzmin, A.V. Maslennikova, G. Revet, A.M. Sergeev, J. Fuchs, E.A. Khazanov, S. Chen, A.A. Shaykin, I.A. Shaikin, I.V.Yakovlev
  Experimental stand for studying the impact of laser-accelerated protons on biological objects. Quantum Electronics **46** (4), 283–287 (2016).

- S. N. Chen, M. Gauthier, M. Bazalova-Carter, S. Bolanos, S. Glenzer, R. Riquier, G. Revet, P. Antici, A. Morabito, A. Propp, M. Starodubtsev, J. Fuchs
  Absolute dosimetric characterization of Gafchromic EBT3 and HDv2 films using commercial flat-bed scanners and evaluation of the scanner response function variability. Rev. Sci. Instrum. **87**, 073301 (2016).

- E. D. Filippov, S A Pikuz, I Yu Skobelev, S N Ryazantsev, D P Higginson, D Khaghani, G Revet, S N Chen, J Fuchs
  Parameters of supersonic astrophysically-relevant plasma jets collimating via poloidal magnetic field measured by x-ray spectroscopy method. Journal of Physics: Conference Series **774**, (2016)

- S. N. Ryazantsev, I. Yu. Skobelev, A. Ya. Faenov, T. A. Pikuz, D. P. Higginson, S. N. Chen, G. Revet, J. Béard, O. Portugall, A. A. Soloviev, A. N. Grum-Grzhimailo, J. Fuchs, S. A. Pikuz

Diagnostics of laser-produced plasmas based on the analysis of intensity ratios of Helike ions X-ray emission. Phys. Plasmas **23**, 123301 (2016).

- A. Soloviev, K. Burdonov, S. N. Chen, A. Eremeev, A. Korzhimanov, G. V. Pokrovskiy, T. A. Pikuz, G. Revet, A. Sladkov, V. Ginzburg, E. Khazanov, A. Kuzmin, R. Osmanov, I. Shaikin, A. Shaykin, I. Yakovlev, S. Pikuz, M. Starodubtsev, J. Fuchs
  Experimental evidence for short-pulse laser heating of solid-density target to high bulk temperatures. Scientific Reports **7**, 12144 (2017)

- S. N. Chen, M. Vranic, T. Gangolf, E. Boella, P. Antici, M. Bailly-Grandvaux, P. Loiseau, H. Pépin, G. Revet, J. J. Santos, A. M. Schroer, M. Starodubtsev, O. Willi, L. O. Silva, E. D'humières, J. Fuchs
  Collimated protons accelerated from an overdense gas jet irradiated by a 1 µm wavelength high-intensity short-pulse laser. Scientific Reports **7**, 13505 (2017).

- M. Barberio, M. Scisciò, S. Vallières, F. Cardelli, S. N. Chen, G. Famulari, T. Gangolf, G. Revet, A. Schiavi, M. Senzacqua, P. Antici
  Laser-accelerated particle beams for stress testing of materials. Nature Communications **9**, 372 (2018)

- M. Tarisien, J. L. Henares, C. Baccou, Th. Bonnet, F. Boulay, F. Gobet, M. Gugiu, F. Hannachi, S. Kisyov, C. Manailescu, V. Meot, F. Negoita, X. Raymond, G. Revet, L. Tudor, M. Versteegen,
  Scintillators in high-power laser driven experiments. IEEE Transactions on Nuclear Science (2018)

Presentations

- ICHED summer school, UCSD, San Diego (California), 2015

- HEDLA conference, Stanford (California), 2016

- ICHEDP conference, Shenzhen University, Shenzhen (China), 2016

- MACH meeting, Observatoire de Paris, Paris (France), 2017

- NWP conference, LaB meeting, Moscow – Saint-Petersburg (Russia), 2017 – **Invited**

- IFSA conference, Saint-Malo (France), 2017

- HEDLA conference, Kurashiki (Japan), 2018 – **Invited**

Posters

- EPS conference, Lisbon (Portugal), 2015

- ICHED conference, San Diego (California), 2015

- PLAS@PAR scientific day, Pierre-et-Marie-Curie University, Paris (France), 2016

- NIF-JLF user meeting, Livermore (California), 2016

- AAS meeting, Austin (Texas), 2017

Résumé du travail de thèse

Le travail présenté dans cette thèse s'inscrit dans le domaine de l'astrophysique de laboratoire, qui consiste à étudier en laboratoire, à des échelles de temps et d'espace réduites, des processus physiques qui se produisent dans des objets astrophysiques. Les principaux avantages ici sont que les processus peuvent être étudiés de manière contrôlée et que leur dynamique complète peut être observée. Présentement, nous avons profité des installations laser à haute intensité pour effectuer nos études.

Pour cela, dans ce manuscrit, seront traitées les questions liées à l'astrophysique de laboratoire qui impliquent l'interaction d'un plasma créé par laser en détente dans le vide avec un champ magnétique ambiant. La présence d'un champ magnétique dans une variété de phénomènes astrophysiques rend l'introduction de cette composante magnétique dans le laboratoire nécessaire afin que ces études soient pertinentes. Pour ce faire, en collaboration avec Laboratoire National des Champs Magnétiques Intenses -LNCMI, une bobine Helmholtz, spécialement conçue pour travailler dans un environnement laser a été développée, permettant d'atteindre une force de champ magnétique jusqu'à 30 T.

Les objets astrophysiques sur lesquels cette étude est centrée sont les étoiles jeunes ou « Young Stellar Objects » (YSOs). Plusieurs étapes du processus de formation de ces étoiles seront ici étudiées : (i) la génération de jets collimatés à très grande échelle, (ii) la dynamique d'accrétion impliquant, dans la représentation standard, des flux de matière tombant sur la surface de l'étoile sous forme de colonnes magnétiquement confinées, et (iii) des canaux d'accrétion plus exotiques, comme l'accrétion équatoriale qui implique la propagation du plasma perpendiculairement aux lignes de champ magnétique.

Plus précisément, dans un premier chapitre, la dynamique de formation des jets sera discutée. Une première partie est dédiée au mécanisme de formation et de collimation de jet dans un champ magnétique poloïdal (aligné par rapport à l'axe principal d'expansion du plasma). Une seconde partie traite de la distorsion d'une telle formation de jet par l'interaction du même plasma en expansion avec un champ magnétique désaligné (c'est-à-dire présentant un angle par rapport à l'axe d'expansion du plasma). Enfin, une troisième partie détaille la propagation du plasma dans un champ magnétique perpendiculaire. Cette dernière partie nous permet d'étudier des canaux exotiques d'accumulation de matière sur les étoiles, consistant en une accrétion du disque d'accrétion directement vers l'étoile, c'est-à-dire sur le plan équatorial, impliquant une propagation orthogonale aux lignes de

champ magnétiques. Il est ici mis en exergue une propagation non-inhibée à travers les lignes de champ magnétique (aux temps observés sur la durée de l'expérience), sous la forme d'une nappe (2D) de plasma. De plus, il est observé le développement d'intéressantes structures associées à des instabilités de Rayleigh-Taylor magnétisées à la base la nappe.

Le deuxième chapitre aborde le thème de la dynamique d'accrétion par l'intermédiaire de colonnes de matière magnétiquement confinées, tombant sur la surface stellaire. En utilisant la même configuration expérimentale que dans le premier chapitre, le jet formé (dans le cas du champ magnétique parfaitement aligné) est utilisé pour imiter la colonne d'accrétion et est lancé sur une cible secondaire qui agit comme la surface stellaire. La dynamique de choc à l'emplacement de l'obstacle est soigneusement étudiée et un lien avec les phénomènes d'accrétion dans le contexte des « Classical T Tauri stars » (CTTSs) est construit. Il est montré que l'expérience est en capacité de reproduire un phénomène d'accrétion où la pression cinétique dirigée du plasma domine la pression magnétique ambiante d'une manière modérée (un facteur 10 séparant les deux pressions au maximum). Dans cette situation, un cocon de plasma, formé autour de la région d'impact via l'interaction avec le champ magnétique, est observé être similaire à celui trouvé dans les simulations astrophysiques de ce type d'accrétion. Ce cocon est un élément important en tant que milieu potentiel d'absorption des émissions X. Ce milieu permettrait en effet d'expliquer les écarts observés entre les émissions UV / optiques et les émissions X provenant des étoiles lors des phases d'accrétion.

Titre : Modélisation en laboratoire de la dynamique d'accrétion des étoiles jeunes en milieux magnétisé.

Mots clés : MHD, Astrophysique de laboratoire, Accrétion, Champs magnétique

Résumé : Le travail présenté dans cette thèse s'inscrit dans le domaine de l'astrophysique de laboratoire, et en particulier l'étude de phénomènes liés aux étoiles jeunes et aux étoiles classiques de type T Tauri (CTTS). L'étude consiste à exploiter l'intérêt des plasmas créés par laser (d'intensité modérée : $\sim 10^{13}$ W.cm^{-2}) et le couplage avec un champ magnétique externe de plus de 20 Tesla. Ce genre de plasmas créés par laser, chaud (centaines d'eV) et relativement dense (autour de 10^{19} cm^{-3}) présentent des similitudes avec ceux, astrophysiques, sur lesquels la comparaison se porte (transport de la chaleur, de la masse ou du champ magnétique se faisant principalement par advection plutôt que par diffusion). De plus, l'inclusion du champ magnétique dans l'expérience, crée un lien plus direct avec l'objet astrophysique où le champ magnétique joue souvent un rôle important. Dans cette thèse, l'étude se centre sur la modélisation en laboratoire de la formation de jet dans les étoiles jeunes, leur collimation par le champs magnétique, et leur distortion par l'ajout d'un désalignement entre le champ magnétique et la direction d'expansion du plasma. Un cas extrême, où la direction d'expansion et le champ magnétique sont orthogonaux est présenté et discuté. Finalement, l'utilisation du jet expérimental bien collimaté et son envoi sur une cible obstacle permet d'étudier la génération d'un choc ainsi que la dynamique entourant se dernier. Un lien fort est construit avec la dynamique d'accrétion dans le contexte des CTTS.

Title : Modelling magnetized young stars' accretion dynamic in the laboratory

Keywords : MHD, Laboratory astrophysics, Accretion, Magnetic field

Abstract : The work presented in this thesis deals with laboratory astrophysics, and specifically with phenomena linked to young stars and classical T Tauri stars (CTTS). The study takes advantage of laser-created plasma (using a moderate laser pulse intensity: $\sim 10^{13}$ W.cm^{-2}), coupling it with an externally applied magnetic field, of strength larger than 20 Tesla. This kind of laser created plasmas, hot (hundreds of eV) and relatively dense (about 10^{19} cm^{-3}), present similar behaviors with the astrophysical ones this study aims to compare with (the transport of the heat, the mass and of the magnetic field is mainly driven by advection rather than diffusion). Moreover, the inclusion of magnetic field in our experimental setup makes a direct link with astrophysical objects, for which the magnetic field is often playing an important role. In this thesis, the study is centerd on the modelling in the laboratory of the jet formation process in young stars, their collimation by the magnetic field as well as their distortion by applying a misalignment angle between the plasma flow and the magnetic field directions. An extreme case, where the plasma is flowing orthogonally to the magnetic field is presented and discussed. Finally, the use of the well collimated jet, launched onto an obstacle target, allows the investigation in the laboratory of the accretion shock dynamic as it is believed to occur in CTTS.